NORTHWESTERN UNIVERSITY

Demystifying Rare Cosmic Transients with Multiwavelength Observations

A DISSERTATION

SUBMITTED TO THE GRADUATE SCHOOL
IN PARTIAL FULFILLMENT OF THE REQUIREMENTS

for the degree

DOCTOR OF PHILOSOPHY

Field of Astronomy

By

Aprajita Hajela

EVANSTON, ILLINOIS

August 2022

ABSTRACT

Demystifying Rare Cosmic Transients with Multiwavelength Observations

Aprajita Hajela

The field of time–domain astronomy has seen significant advancements in the latest years as increasingly sensitive, deep and wide–field surveys of the sky at all wavelengths are being carried out more and more frequently. Furthermore, the addition of gravitational wave detectors around the world has opened an entirely new window to view (or 'hear') the Universe in. With these advancements, we are positioned at an ideal time to investigate fundamental physics and produce breakthrough science. This dissertation showcases the benefits of capitalizing on these recent advancements through systematic exploration of multiwavelength observations of some rare relativistic transients, with a particular focus on X–rays and radio observations where the synchrotron emission, produced by the interaction of relativistic outflows with their ambient medium, dominates. Synchrotron emission is encoded with the information of the fundamental properties of the transient event such as the total energy of the explosion, and the density profile of the surrounding medium.

In this work, I have reported interpretation from our targeted multiwavelength campaigns of two peculiar events, namely: GW 170817, and ASASSN-15oi, along with discussing the prospects of discovering transients in blind radio surveys at sub GHz frequencies that might be missed at earlier times because of 1) dust obscuration, or 2) geometric considerations of relativistic outflows. GW 170817 is the first and the only multi–messenger event to be observed to date, with both a gravitational wave, and an electromagnetic counterpart. Multi-messenger astronomy is an emerging field and provides us with a wealth of new information that was impossible to investigate before the discovery of GW 170817. In particular, observations of multi–messenger events provide ways to constrain the poorly known equation of the state of the densest matter in the Universe, to test the principles of general relativity, and to constrain the Hubble constant independently of the conventional methods. ASASSN-15oi, on the other hand is an unusual tidal disruption event exhibiting multiple radio flares $\sim$ years after the discovery. This behavior is unprecedented. While tidal disruption events are now commonly observed at early–times, the physical processes potentially occurring at later times, such as accretion state changes, or an off–axis jet coming into our line of sight are still largely unexplored.

The following are the fundamental questions that have driven the work in this dissertation: 1) What are the different kinds of outflows produced by the different classes of relativistic transients? 2) What are the physical conditions that enable some systems to harbor a relativistic jet, while others do not? 3) What are the unique properties of an engine to power a jet? 4) What is the structure of those jets?

5) What is the makeup of the environment around the sites of these explosions? This will help towards improving our understanding of 1) the accretion physics, 2) the mechanism of launching of the jets, 3) the diversity in the energetics and structure of jets and outflows within the same class of events and also across different systems. These are all relevant and potentially universal to many other astrophysical systems as well including γ-ray bursts (GRBs), X-ray binary systems (XRBs), and, Active Galactic Nuclei(AGNs).

Acknowledgements

There are so many people I want to thank, who have been on this journey with me, and especially who have been with me on this path long before it started. First and foremost, I am indebted to my advisor Prof. Raffaella Margutti who believed in me, and encouraged me to pursue ambitious projects. She taught me how to navigate the pitfalls of academia, and to produce the best science I can regardless of the hiccups one might encounter. I want to give a special thanks to my mentors through this journey: Deanne Coppejans, Giacomo Tererran, Kate Alexander, and Joe Bright, who taught me so much of what I know, were extremely patient and some of the most kind and understanding people I have been lucky to know. It was an honor having them as collaborators, and I will look forward to continue working with them in the future. I also want to give a special thanks to my thesis committee that included Prof. Wen-fai Fong, and Prof. Shane Larson, for their encouragement, support, and thoughtful contributions to the work during my Ph.D.

I switched my fields to Astrophysics after completing my undergraduate studies in electronics engineering. Transitioning into such a different field wouldn't have been possible without the support, guidance, and excellent mentorship of Prof. A. K. Lal, and Prof. Ankush Pathania at my undergraduate institute. They helped me build important skills needed to enter the field of astronomy at the graduate level. I also want to thank them for encouraging me to attend my first Astronomy conference as an engineering student, where a random encounter with Prof. Steven Kahn from Stanford University was so positively encouraging that it ended with me applying to graduate schools in the US. My journey in the field of astronomy began with them. Without them, I wouldn't be here.

It takes a village to do anything, and so of course my journey through the graduate school wouldn't have been possible without the unconditional support of my family, friends, and colleagues. I am immensely grateful for my parents who have continually supported me in all my endeavors, whatever and wherever they are. I completely changed my career, moved to a country at 23 where neither me nor they knew anyone, and even though they were apprehensive, they did not stop me from pursuing my dream.

I want to give a special thanks to two of my closest friends, Joseph and Nicole who became family to me in this foreign land and were beside me through all the ups and downs that academia (and quarter life crisis) brings. I am grateful for my friendship with Aris who shared with me his expertise on "a Greek's way of life", an important tool to overcome all hurdles during one's Ph.D., and life.

Vishakha, Udita, Gauri, and Arshi believed in my dream long before it came true. With almost 24 years of friendship, Ishita and Urvi were the first people to know about my passion, and they never questioned my abilities to pursue it. I want to specially thank them for their understanding when I sometimes (often) failed to be in touch with them. Their encouragement, and confidence in me all this time brought me to where I am today.

Candice, Huei, Lindsay, David, Wynn, Daniel are officially my group mates, but they were the best cheer squad I had. Chase, Eve (my other fellow astronomy graduate students), Shi, and Alex (my officemates), and Danat, and Nick are so much more than just colleagues. I really appreciate all their friendships, and I want to thank them for being so welcoming, and making me feel at home at CIERA, and outside. Cheers to all the fun times we had outside work that really helped me cope with the stress of a PhD student's life!

I want to thank Prof. Vicky Kalogera, who was my first mentor at CIERA, and was extremely supportive and welcoming. She was so understanding when I told her that I want to explore more and not just stay where I first began my adventure in astronomy.

I also want to acknowledge the support of the most amazing staff in the Department of Physics and Astronomy, and CIERA throughout my seven years in Northwestern University: Bud Robinson, Gretchen Oehlschlager, Yas Shemirani, Lisa Raymond, Pam Villalovoz, Katie Curth, and Peter Anglada. I want to especially thank them for helping me navigate all the troubles of being an international student.

And, lastly but not the least, I want to acknowledge that my work during the Ph.D. was in part financially supported by a Future Investigators in NASA Earth and Space Science and Technology (FINESST) award No. 80NSSC19K1422, and also by a NRAO Summer Student Research Assistanship.

Dedication

To Maa and Papa for always providing me with a positive environment to pursue anything I wanted to

Table of Contents

List of Tables

List of Figures

CHAPTER 1

Introduction

"The universe just talks to us in so many ways, and every time you find a new way of listening, you find something else."

—Ellen Zweibel, Professor of Astronomy

This chapter serves to introduce the necessary background, the existing summary of the relevant literature to build the motivation that drives the work in this dissertation.

1.1. Multi–wavelength & Multi–messenger Astronomy

Time-domain astronomy focuses on events, known as 'transients', that evolve over a short period of time ($\sim$ hours, months, years, etc.) when compared to cosmic timescales, and form the sites for the most extreme physics in the Universe. Traditionally, the electromagnetic (EM) signatures produced by these transients provided the most efficient means of discovering them. The first discoveries in astronomy were made in the 'visible light' – the part of the spectrum accessible to our eyes. By the early 20$^{\text{th}}$ century, we started seeing objects in other different kinds of lights. In 1930s, Karl G. Jansky made the first discovery of an object outside the solar system emanating radio waves and marked the advent of radio astronomy (Jansky 1933). Radio waves are approximately 10^6 times less energetic than visible light. Soon afterwards, we discovered objects that emitted radiation such as X–rays, and gamma–rays (γ–rays) that carried energy much larger than the visible light. Each wavelength of the EM spectrum carries unique information of the different physical processes that occur during an event, and from the different regions around the transient event. One of the most effective images exemplifying the importance of multiwavelength observations is shown in Figure 1.1 . A near–by galaxy Cygnus A was observed at three different wavelengths . When observed in visible light only, nothing stands out of the ordinary, but when the same galaxy was observed at radio and X–ray wavelengths, it revealed magnificent new features unique to those wavelengths. X-rays revealed an extended bubble of hot gas (in blue), whereas the radio observations show the presence of powerful jets launched from the supermassive black hole (SMBH) in the center of the galaxy (in red). Multiwavelength observations are thus essential to reveal the true features of any cosmic event and/or object.

As showcased above, the photons at different wavelengths act like different messengers of information. There have been messengers other than photons over the years as well such as: cosmic rays, and neutrinos, but more recently, we have opened an entirely new window to observe the Universe in, i.e. through gravitational waves (GWs). All of these messengers carry complementary information and together make for a powerful tool to piece together a fuller picture of an event and to form a complete understanding of the physical processes behind it.

Gravitational waves are simply explained as ripples in space–time. These ripples are predicted to radiate away from 1) in-spiralling compact objects in a binary system

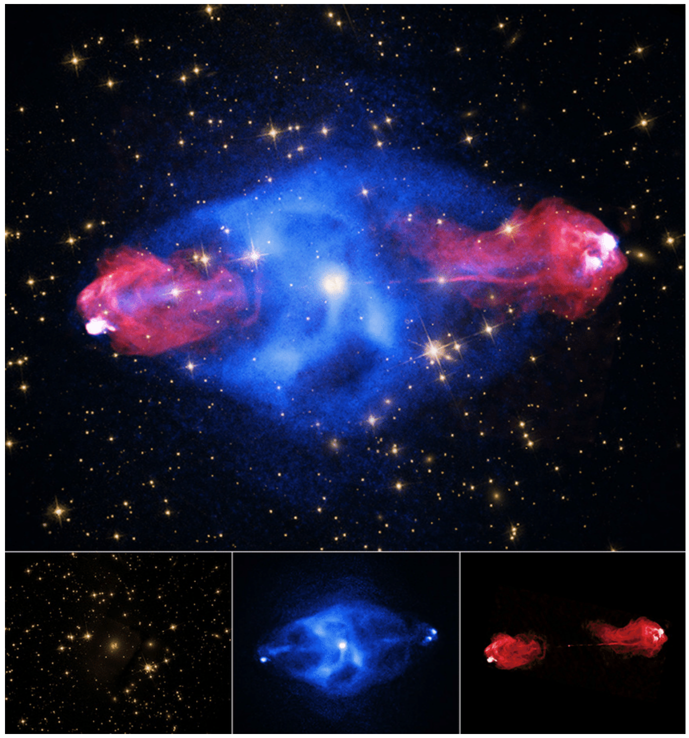

Figure 1.1 The top panel of the figure shows a combined image of the multiwavelength observations of a galaxy Cygnus A. The individual images in each wavelength are shown in the bottom panel. In gold is the image from the optical observations carried out by the *Hubble* Space Telescope, the blue represents the X–ray producing hot gas that engulfs an extended region of the galaxy as captured by the *Chandra* X–ray Observatory, and lastly in red is revealed magnificent jet features coming out of the center of the galaxy. This image exemplifies how different wavelengths carry unique information to bring together a truly complete picture. (Image Credit: X-ray: NASA/CXC/SAO; Optical: NASA/STScI; Radio: NSF/NRAO/AUI/VLA)

consisting of a) black holes (BH), b) neutron stars (NS) or c) both, or d) SMBHs, 2) events like core–collapse supernovae, and also from 3) rapidly spinning massive objects that are slightly asymmetrical such as an isolated NS with a few deformities on its surface. Although Albert Einstein predicted that the GWs will radiate away from a source with time-varying mass quadrupole moment in the year 1916 (Einstein

1916) with the help of his theory of general relativity, it was a speculative topic for most of the 20$^{\text{th}}$ century. Years of observations of a binary pulsar system, PSR B1913+16 (Hulse et al. 1975) provided the first indirect confirmation of GWs when scientists observed that the system's orbit was decaying at the rate consistent with if GWs were being radiated away (similar to what was predicted by Einstein 1916). This led to accelerating efforts for building GW detectors. Following the improvement in our understanding of the theory related to GWs, and advancements in engineering and experimental setups over the next many years, on 14$^{\text{th}}$ September 2015, the Advanced Laser Interferometer Gravitational Wave Observatory (LIGO) detectors in Livingston, Louisiana, and Hanford, Washington, made the first ever discovery of GWs from colliding black holes (also called binary black hole merger, or BBH merger). The event was named after the date of its discovery as GW 150914, this time directly confirming Einstein's predictions after nearly 100 years.

Two years later, the Advanced LIGO together with the newly added advanced VIRGO detector marked another milestone with the first ever discovery of GWs from a binary neutron star (BNS) merger, GW 170817. But this time, the GW signal spatially and temporally coincided with a detection of γ-rays with *Fermi* and *INTEGRAL* telescopes (Goldstein et al. 2017; Savchenko et al. 2017) launching us into an era of multi–messenger astronomy (MMA) with light and gravitational waves for the first time. This was soon followed by the most extensive observational campaign in the history of astronomy. GW 170817 was observed across the EM spectrum with space and ground based telescopes and it still remains the only celestial object with both a GW and an EM counterpart.

While BBH mergers are considered to be mostly dark in the EM spectrum due to the lack of matter present around the system[1], binary systems containing at least one NS are stronger candidates for multi–messenger observations. In case of binary mergers, the waveform of the gravitational wave signal informs us about the properties of the pre–merger system – for e.g., the chirp mass[2] $\mathcal{M} \equiv (M_1 M_2)^{3/5}(M_1 + M_2)^{-1/5}$, the luminosity distance (D_L), and the inclination angle (i)[3] – but also about the nature of the post–merger remnant if it also emits GWs. An EM signal on the other hand highlights the evolution of the system and the related physical processes that occur post–merger. GWs may also act as "standard sirens" (analogous to standard candles) to determine the Hubble constant H_0 (e.g. Schutz 1986). H_0 is determined by the relationship between the source luminosity distance, and its redshift. The information from a GW waveform can constrain D_L, but is also highly degenerate with the inclination angle of the system, and cannot be determined accurately for smaller values of i. EM observations of the same event will provide additional information of the inclination angle breaking the degeneracy between D_L, and i, and also provide a

[1]However, there is a possibility of an EM signal from a BBH system if there was material surrounding the system, such as an accretion disk, or if the system was present in a gas disk surrounding a SMBH in the center of the galaxy, as was proposed for GW 190521 (Graham et al. 2020)

[2]The chirp mass of a binary system determines its orbital evolution to leading order as GWs are radiated away

[3]the inclination angle is usually the angle between the line of sight and the orbital angular momentum

measurement on the source redshift, improving the measurement of H_0. The traditional approaches[4] to measure H_0 have recently seen disagreement on the final values at a level of about 4σ, and therefore multi–messenger events provide an independent way to resolve this so called 'Hubble tension'. Finally, multi–messenger observations are a valuable tool that can additionally be used to test General Relativity, and to determine the equation of state (EoS) of the densest matter in the Universe.

1.2. Transients of Interests

In this dissertation, I have focused mainly on studying relativistic transients, i.e. transients which constitute of a relativistic and collimated outflow (e.g. jets) component, in particular the EM counterparts of the GW compact object mergers (see subsection 1.2.1), and Tidal disruption events (see Section 1.2.2), through multiwavelength observations. These outflows, when launched, drive a relativistic (or sub–relativistic) shock carrying energy E_K through the ambient medium (with a density profile: Ar^{-k}, where k = 0 represents a medium with a constant density, whereas k = 2 represents a wind–like medium), accelerating the electrons with lorentz factor $\gamma > \gamma_{min}$ into a non–thermal power–law (PL) distribution, $N(\gamma) \propto \gamma^{-p}$. A fraction of its energy ϵ_e is imparted to the electrons right behind the shock, and another fraction of energy ϵ_B goes into amplifying the magnetic field. The relativistic electrons gyrate in the shock–amplified magnetic field and cool down via non–thermal synchrotron radiation spanning the entire EM spectrum(Granot et al. 2002; also see

[4]One approach uses 'standard candles', i.e. astronomical objects with known absolute magnitude to measure its distance and eventually determine H_0 (Riess et al. 2019), and the other involves accurate mapping of the cosmic microwave background (Planck Collaboration et al. 2016).

Figure 1.2 as an example). To capture the features of this broadband spectrum (i.e. the maximum flux, the peak frequency, the spectral breaks, etc.) and eventually derive the microphysical properties of shock ($\epsilon_{\rm e,B}$), the total energy carried by it, the nature of the ambient medium, the power–law index of the electron population, etc., carrying out a multiwavelength observational campaign is essential.[5]

In the following section, I discuss the general background of the relativistic transients that are included in this dissertation to place the remaining chapters in context.

1.2.1. EM Counterparts of Compact Object Mergers

Compact object mergers result from the in-spiral and eventual collision of the two components in a binary system. The components can be compact objects such as: two BHs, two NSs or a BH and a NS in a system. We mainly discuss BNS mergers in this dissertation, but this work also forms a foundation which can be extended to study any compact object mergers in the future with at least one NS. Such systems generally have four predicted outcomes: 1) gravitational waves; 2) a short γ-ray burst (sGRB), 3) a kilonova, and 4) and other physical processes that may result in production of MeV and GeV neutrinos. While it will be ideal to have access to and process the information carried by all these different messengers, this work concentrates only on the implications of the EM observations of such events (the EM components are illustrated in Figure 1.3).

[5] An important thing to note here is that while the thermal emission only provides information on the slower moving bulk of the ejected matter, the study of non-thermal emission proves to be an important tool to probe the fastest tail of the outflows and their properties in any given event with relativistic outflows

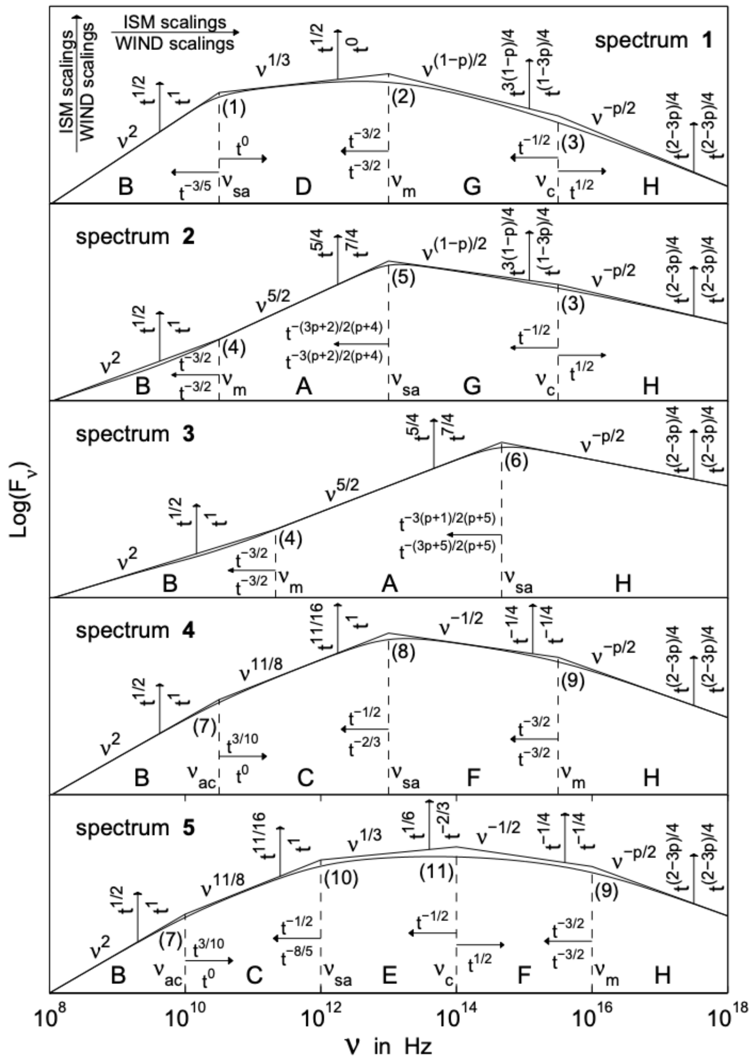

Figure 1.2 Figure from Granot et al. 2002 showing different possible broadband spectrum produced by the interaction of the relativisitic outflow with its surrounding medium.

Short GRBs had long been proposed to be produced from BNS or BH–NS mergers (Eichler et al. 1989; Narayan et al. 1992). The masses inferred from the GW signal of GW 170817 revealed that the pre–merger components in the binary system were

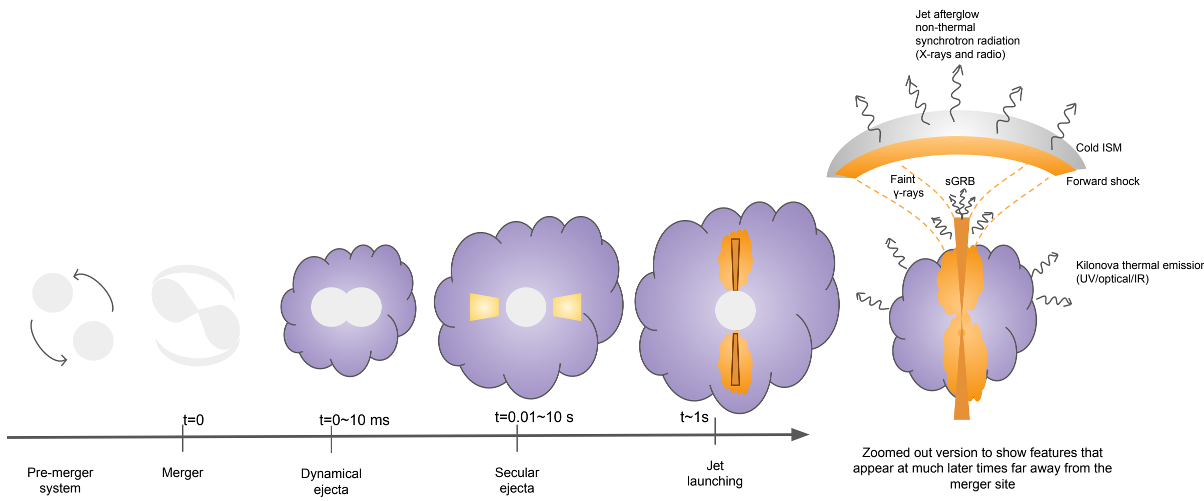

Figure 1.3 Illustration of the EM counterparts predicted at each stage from the merger of two compact objects (adapted from Nakar 2020). a) During and immediately after the merger, material is ejected at dynamical timescales due to tidal forces and shock collisions. In cases where the central object doesn't collapse to a BH promptly, a small fraction of the ejecta is accelerated to relativistic velocities that interacts with the surrounding medium to produce a kilonova afterglow. b) Within several dynamical timescales, material forms an accretion disk around the central object. Winds drive material from the accretion disk forming a secular ejecta which is more massive than the dynamical ejecta and forms the bulk of the outflow. Both dynamical and secular ejecta are neutron rich and may form the site of production of heavy r-process elements. These elements decay radioactively and power a kilonova. c) Finally an ultra–relativistic jet is launched. If the jet is powerful enough, it will successfully make it out of the ejecta and interact with the cold ISM material to produce a jet afterglow.

two neutron stars (Abbott et al. 2017a), and therefore the discovery of GW 170817 confirmed that at least a fraction of BNS mergers result in a short gamma-ray burst.

As the neutron stars are in-spiralling, some of material gets ejected on dynamical timescales but remains gravitationally bound to form an accretion disk around a rapidly rotating compact object remnant that can potentially power a strongly collimated ultrarelativistic jet. The internal shocks within the jet are primarily assumed to be responsible for the short burst of γ-ray emission ($\lesssim$ 2s), and hence the name sGRBs. GRBs are the most energetic and luminous explosions in the Universe. The jet itself might be short–lived but it produces a long–term (spanning $\sim$ weeks to years) non–thermal synchrotron emission across the EM spectrum when it interacts with its surrounding medium (as described above), known as the GRB afterglow.

The collision of the two binary components also result in the ejection of around $10^{-4} - 10^{-2}\,\mathrm{M}_{\odot}$ material moving at speeds of $0.1 - 0.3$ times the speed of light (Bauswein et al. 2013; Hotokezaka et al. 2013; Sekiguchi et al. 2016; Radice et al. 2018a), significantly slower than a jet. This material is launched over dynamical timescales, i.e. it is ejected within $\sim 0 - 10\,\mathrm{ms}$ of and immediately after the merger due to 1) the tidal forces acting between the two compact objects, and 2) shocks generated in the case of a BNS merger when the cores of two NS collide; whereas the second type of ejecta, the secular ejecta are launched over longer timescales ($\sim 0.01 - 10\,\mathrm{s}$) and are driven by the neutrino, and viscosity driven winds from the accretion disk formed around the remnant post–merger and form the bulk of the outflow with a mass $\approx 0.2M_{\odot}$. The two kinds of ejecta are neutron rich (but with different concentrations) and form one of the predominant sites for the nucleosynthesis of r-process elements, e.g. gold, in the Universe. These heavy nuclei elements undergo radioactive decay and power up a 'kilonova' (Metzger 2017). The thermal emission from the kilonova emanates radiation in the ultraviolet (UV), optical, and the near–infrared (NIR) wavelengths on hours to weeks timescale. Numerical relativity simulations have shown that if a NS is formed post–merger, the newly formed remnant bounces and drives high velocity shocks into the surrounding material, resulting in the acceleration of a small fraction of ejecta to relativistic speeds. This is known as the fast–tail of the ejecta, and it will interact with the medium in a similar way that a jet does to produce a 'kilonova afterglow' (analogous to the jet afterglow). Since this fast–tail contains less amount of energy and is slower than the jet, it will peak at very late–times and will be much fainter than the jet afterglow but will similarly dominate X–ray and radio wavelengths. The properties of the kilonova ejecta (for e.g. its mass, velocity, composition, and geometry) and the existence of a fast–tail depend on the nature of the binary (i.e., BNS or BH–NS), the masses and spins of the components, and the poorly–known NS EoS. Therefore, tracing this fast–tail of the ejecta is of utmost importance to be able to probe the NS EoS, and also reveal the nature of the merger remnant. For e.g. a lack of evidence for a fast–tail ejecta in a BNS merger event will provide evidence that the merger resulted in a prompt–collapse to a BH. In BNS mergers, whether a long–lived NS is formed, a short–lived NS that eventually collapses to BH is formed, or a BH is promptly formed as a result of the coalescence depends on the total mass of the system and NS EoS, whereas BBH and BH–NS mergers will always result in the formation of a BH.

Here, I summarize the interpretations of the earlier observations of GW 170817 to put it into context of the general review of the expectations from compact object mergers given above. GW 170817 was observed on 17$^{\text{th}}$ August, 2017 at 12:41:04.4 UTC (Abbott et al. 2017a). Around $\sim 2\,\mathrm{s}$ later, a short GRB was detected with *Fermi* and *INTEGRAL* telescopes at a location consistent with the localization region of the GW signal. The difference between GW and γ–ray signal could be attributed to either a) a delay in the launch of the jet responsible for γ–rays, or b) to the time spent by the jet within the ejecta surrounding the merger site before breaking out (also known as the cocoon shock–breakout scenario (Gottlieb et al. 2018)), or c) to the fundamental difference between the speed of GW and light. With a peak luminosity of $\sim 10^{47}\,\mathrm{erg\,s^{-1}}$, the γ–ray signal was significantly lower than what was expected from conventional sGRBs observed to date. The thermal emission from GW 170817 at optical/NIR wavelengths was observed within $\sim$ 11 hours of detection, and the first UV were detected $\sim$ 14 hours post–merger. The observations revealed features consistent with those predicted by the kilonova models. In fact, this was the first time that there was direct observation of a kilonova. Modeling the evolution of the thermal emission originating in GW 170817 led to the conclusion that there were broadly two kinds of ejecta that were launched: 1) a $\sim 0.03\,M_{\odot}$ slow–moving ($\sim 0.1 - 0.2c$) isotropic ejecta rich in lanthanides that resulted in a higher opacity material. The radioactive decay within this component dominated IR wavelengths, and therefore was called the 'red kilonova'. The properties of this ejecta component were similar to the ones expected from the material ejected over secular timescales from disk winds;

and 2) a $\sim 0.02\,M_{\odot}$ fast–moving ($\sim 0.3c$) quasi–spherical ejecta confined to non–equatorial plane with lower opacity that was responsible for the 'blue kilonova'. The origin of the blue component is less clear since it is too massive to have a dynamical origin, and too fast for a secular one. GW 170817 made its first appearance at X–ray and radio wavelengths only after 9, and 16 days respectively. The low–luminosity γ–rays, combined with rising non–thermal emission in X–ray and radio that reached a peak at ~ 160 days post–merger followed by a sharp decline confirmed the presence of an off–axis structured jet. Structured jets have Lorentz factor ($\Gamma_{\rm jet}$), and energy profile that are angle–dependent, where the core contains the maximum energy and Lorentz factor, with both of these decreasing as we move away from the axis of the jet. We continued to observe GW 170817 until ~ 1234 days post–merger, and performed a systematic exploration and interpretation of the multiwavelength observations which I report in chapters 2–3 of this dissertation.

1.2.2. Tidal Disruption Events and the Late–time Physical Processes

Tidal Disruption Events or TDEs are a rare phenomenon that occur when a star strays too close to the supermassive black hole at the center of a galaxy (Rees 1988) and gets ripped apart due to strong tidal forces. The star gets disrupted and around half of the star's mass gets siphoned off by the SMBH via accretion, producing a very bright UV/optical/soft X–ray transient (e.g. Gezari et al. 2012; Holoien et al. 2016b; Blanchard et al. 2017a), while the other half remains unbound. TDEs allow us to uniquely probe the environment around previously-dormant SMBHs, to test models of SMBH accretion, and to study the entire lifecycle of SMBH jets and outflows in real–time. Recent deep and increasingly sensitive all-sky optical surveys have increased the discovery rate of TDEs by an order of magnitude, and we are beginning to build a larger sample size required to test how the physics of jet formation depends on parameters like accretion rate, black hole mass and spin, and magnetic field strength (e.g. Alexander et al. 2020; van Velzen et al. 2020).

Recent efforts by our group and others have begun to uncover the radio properties of the bulk of the TDE population, revealing unexpected diversity. A few percent of TDEs exhibit bright γ-ray, X-ray, and radio emission, most likely from strong on-axis relativistic jets (Bloom et al. 2011; Burrows et al. 2011; Levan et al. 2011; Zauderer et al. 2011; Berger et al. 2012; Cenko et al. 2012; Zauderer et al. 2013; Brown et al. 2017; Eftekhari et al. 2018). As these jets are narrowly beamed, by purely geometric considerations we expect to observe many TDE jets from off-axis viewing angles. As time passes, however, the jets decelerate and the relativistic beaming effect weakens, allowing more and more of the jet into our line of sight. Eventually, non-thermal emission from the interaction of the jet with the ambient medium should emerge at radio and X-ray wavelengths at late-times (from $\sim$months to years post-discovery). Although not all TDEs launch jets (see Alexander et al. 2020), synchrotron emission at X-ray and radio wavelengths can also be produced in a shockwave originating in a sub-relativistic quasi-spherical outflow interacting with the ambient medium, as has been observed in a number of nearby TDEs (Alexander et al. 2020 and references therein). Observations of synchrotron emission from TDEs reveal the properties of the fastest ejecta following disruption, the magnetic field strength at the head of the shockwave, and probe the environment around the SMBH.

Systematic searches for the radio emission from the TDEs at late–times in the archival VLA Sky Survey (VLASS) data led by the team I am a part of has uncovered a population of TDEs with an unprecedented emerging radio component at $\sim$ months to years post–discovery. These same events yielded non–detections at radio wavelengths promptly after the discovery. Two of such TDEs: ASASSN-15oi, and iPTF16fnl have already been published in the literature (Horesh et al. 2021a; Horesh et al. 2021b). However, in our searches in the VLASS, we found ASASSN-15oi to have a second brightening in the radio ~ 4 years post–discovery. The second radio flare is significantly brighter than the first. The phase of these delayed radio flares in TDEs have been observed for the very first time, but ASASSN-15oi is a remarkable event to show not one, but two delayed radio flares, hinting at a previously unexplored phase in the lifetime of TDEs. These delayed radio flares can be explained by either a presence of an off–axis jet gradually coming into our line of sight (which has never been observationally confirmed before) as discussed above, or to a delayed formation of the accretion disk postponing the launch of the jet, or a transition of the accretion state of the system (e.g. from hard to soft state) similar to what is observed in many XRBs, or indicate an entirely unknown 'phase' of TDEs.

The early X–rays are commonly attributed to thermal radiation tracing the mass fall-back rate ($F_X \propto t^{-5/3}$) or disk emission ($F_X \propto t^{-5/12}$). However, the scenarios above that can explain the delayed radio flares in TDEs can also drive the emission at X–ray wavelengths at late–times, making the nature of both radio and X–ray observations at these late–times less clear. For example, in the case of *Swift* J1644+57, the early and late-time X-rays were from two distinct sources. The early X-rays were associated to the accretion process, whereas the long term monitoring of the event revealed that the evolution of X-rays and radio at late-times was in concert, both driven by the interaction of the on-axis jet with the ambient medium (Eftekhari et al. 2018; Cendes et al. 2021a).

Alternatively, in some cases like the TDE in IC3599 (Komossa et al. 1999), the difference between early- and late-time X-rays were attributed to a transition between the accretion states (hard and soft), analogous to the transitions observed in X-ray binary (XRB) systems. In these systems, the different states determine the evolution of X-ray and radio emission. In the hard state, the X-rays are dominated by the coronal emission, while the radio emission is from a collimated outflow (e.g. a jet). Whereas in the soft state, X-rays are thermal and are produced in the accretion disk, and the radio emission is suppressed due to quenching of the outflow. When the system transitions from one state to another, however, discrete knots of material are ejected responsible for short-lived radio flares.

On the other hand, some TDEs with late-time radio emission, like ASASSN-14ae and iPTF16fnl, may not show early X-rays at all. General relativistic hydrodynamic simulations of TDE accretion flows find that the debris stream forms an accretion disk at a slower rate than classically predicted (e.g. Shiokawa et al. 2015). Piran et al.

2015 further studied the dependence of jet power on the accretion rate. They found that the jet power initially follows the accretion rate but remains constant after the transition from super- to sub-Eddington rates. Combining the above two arguments, if the accretion rate peaks later, it will likely cause a delay in the formation of the jet.

Against this backdrop, in Chapter 4, we present the multiwavelength observations we acquired to study the remarkable late–time features of ASASSN-15oi to understand the true nature of physical processes that the TDE is undergoing $\sim$years post–discovery.

1.3. Searching for Transients in the Archival Survey Data

Most of the above investigation of transients employ targeted observations. In this section, and in chapter 5, I have shown how blind sky searches are the unbiased tools to uncover the true population of transients at any given frequency. While searches at GHz frequencies have yielded a rich data set of transients due to the availability of wide–field observations together with near real–time data processing and extensive follow–up observations and identification, previous surveys at sub-GHz frequencies have yielded sparse population of transients, due to limited sensitivities of the telescope and higher radio frequency interference (RFI) at lower frequencies. In Chapter 5, I carried out a search for transients and variables in the dedicated survey of SDSS Stripe 82 (S82) region performed with the Giant Metrewave Radio Telescope (GMRT) at 150 MHz driven by the motive to systematically explore the dynamic MHz sky to constrain the true rates of transient phenomenon at these frequencies. The rate of transients I am interested in (described above with an associated relativistic jet component) will be underestimated if we were to rely purely on immediate follow–up observations at earlier times, as jets are highly collimated and most of them will be missed if they are not pointing directly towards us. However, as mentioned above, as a jet decelerates, more of the material comes into our line of sight and the emission from the jet afterglow can therefore be visible at late–times with the peak of spectrum moving to lower frequencies. These transients also exhibit slower evolution, especially at MHz frequencies, if they are in high–density environment which will lead to the relevant timescale to reach peak brightness to be dictated by the synchrotron self–absorption frequency, i.e. when the optical depth is of order unity. The timescales for relevant transients are plotted in Figure 1.4. Thus motivated, and owing to the upcoming era of highly sensitive and wide–field radio interferometers, Chapter 5 in this dissertation offers a comprehensive assessment of the discovery prospects and suggestions to optimize cadences that will allow for an efficient classification of the extragalactic synchrotron radio transients to find their true intrinsic rates.

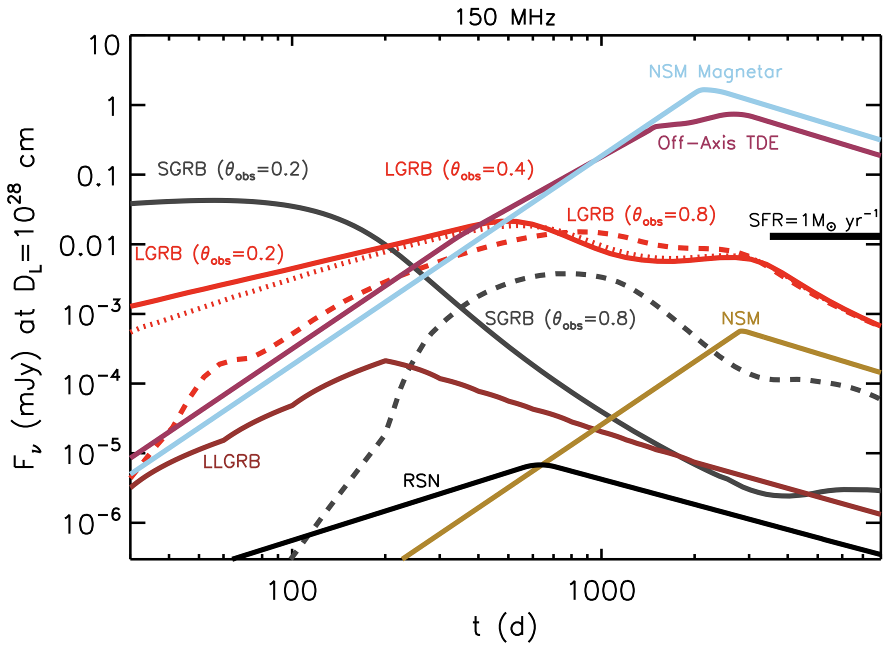

Figure 1.4 Figure from Metzger et al. 2015a showing the light curve evolution of different extragalactic transients at an observing frequency of 150 MHz. Sources considered here include: on- and off-axis long GRB afterglows for various observing angles obs (LGRB: red); low-luminosity LGRB afterglows (LLGRB; brown); Type Ib/c SNe (RSN; black); on- and off-axis short GRB afterglows (SGRB: charcoal); on-axis jetted TDEs (Sw J1644+57: green); off-axis TDEs (maroon); neutron star binary mergers with prompt black hole formation (NSM; tan) and a magnetar remnant (NSM magnetar; blue). Flux densities are normalized to DL = 1028 cm (z 0.55).

CHAPTER 2

Two Years of Non-thermal Emission from the Binary Neutron Star Merger GW 170817: Rapid Fading of the Jet Afterglow and First Constraints on the Kilonova Fastest Ejecta

This thesis chapter originally appeared in the literature as

Hajela, A., Margutti, R., Alexander, K. D., Kathirgamaraju, A., Baldeschi, A., Guidorzi, C., Giannios, D., Fong, W., Wu, Y., MacFadyen, A., Paggi, A., Berger, E., Blanchard, P. K., Chornock, R., Coppejans, D. L., Cowperthwaite, P. S., Eftekhari, T., Gomez, S., Hosseinzadeh, G., Laskar, T., Metzger, B. D., Nicholl, M., Paterson, K., Radice, D., Sironi, L., Terreran, G., Villar, V. A., Williams, P. K. G., Xie, X., & Zrake, J. (2019), ApJ, 886, L17.

We present *Chandra* and VLA observations of GW 170817 at $\sim 521-743$ days post merger, and a homogeneous analysis of the entire Chandra dataset. We find that the late-time non-thermal emission follows the expected evolution of an off-axis relativistic jet, with a steep temporal decay $F_\nu \propto t^{-1.95\pm0.15}$ and power-law spectrum

$F_\nu \propto \nu^{-0.575\pm0.007}$. We present a new method to constrain the merger environment density based on diffuse X-ray emission from hot plasma in the host galaxy and find $n \leq 9.6 \times 10^{-3}\,\mathrm{cm}^{-3}$. This measurement is independent from inferences based on jet afterglow modeling and allows us to partially solve for model degeneracies. The updated best-fitting model parameters with this density constraint are a fireball kinetic energy $E_0 = 1.5^{+3.6}_{-1.1} \times 10^{49}\,\mathrm{erg}$ ($E_{iso} = 2.1^{+6.4}_{-1.5} \times 10^{52}\,\mathrm{erg}$), jet opening angle $\theta_0 = 5.9^{+1.0}_{-0.7}\,\mathrm{deg}$ with characteristic Lorentz factor $\Gamma_j = 163^{+23}_{-43}$, expanding in a low-density medium with $n_0 = 2.5^{+4.1}_{-1.9} \times 10^{-3}\,\mathrm{cm}^{-3}$ and viewed $\theta_{obs} = 30.4^{+4.0}_{-3.4}\,\mathrm{deg}$ off-axis. The synchrotron emission originates from a power-law distribution of electrons with index $p = 2.15^{+0.01}_{-0.02}$. The shock microphysics parameters are constrained to $\epsilon_\mathrm{e} = 0.18^{+0.30}_{-0.13}$ and $\epsilon_\mathrm{B} = 2.3^{+16.0}_{-2.2} \times 10^{-3}$. Furthermore, we investigate the presence of X-ray flares and find no statistically significant evidence of $\geq 2.5\sigma$ of temporal variability at any time. Finally, we use our observations to constrain the properties of synchrotron emission from the deceleration of the fastest kilonova ejecta with energy $E_k^{KN} \propto (\Gamma\beta)^{-\alpha}$ into the environment, finding that shallow stratification indexes $\alpha \leq 6$ are disfavored. Future radio and X-ray observations will refine our inferences on the fastest kilonova ejecta properties.

2.1. Introduction

Multi-messenger observations of the binary neutron star (BNS) merger event GW 170817 ushered us into a new era of systematic exploration of our universe with gravitational waves and electromagnetic emission (Abbott et al. 2017a; Abbott et al. 2017b). Light from GW 170817 has been detected across the electromagnetic spectrum, from the γ-rays to the radio wavelengths (Alexander et al. 2017; Blanchard et al. 2017b; Chornock et al. 2017; Coulter et al. 2017; Cowperthwaite et al. 2017; Fong et al. 2017; Haggard et al. 2017; Hallinan et al. 2017; Kasliwal et al. 2017; Margutti et al. 2017; Nicholl et al. 2017; Savchenko et al. 2017; Troja et al. 2017; Valenti et al. 2017; Alexander et al. 2018; Dobie et al. 2018; Lyman et al. 2018; Margutti et al. 2018; Nynka et al. 2018; Ruan et al. 2018). While the radiation powering the thermal emission from the kilonova (KN) associated to the BNS merger peaked at $\delta t < 12$ days (e.g. Villar et al. 2017, their Fig. 1) and faded below the detection threshold of current instrumentation at $\delta t \sim 70$ days (with the latest detections in the NIR, Villar et al. 2018; Kasliwal et al. 2019) , the non-thermal emission from the off-axis structured relativistic jet is longer lived.

Here we present deep X-ray and radio observations of the non-thermal emission from GW 170817 covering the period $\delta t \sim 521 - 743$ days with the Chandra X-ray Observatory (CXO) and the Karl G. Jansky Very Large Array (VLA), together with a comprehensive re-analysis of the entire CXO data set. These observations allow us to refine previous inferences on the physical properties of the relativistic outflow launched by the BNS merger, and the density of the environment where the outflow is expanding (Alexander et al. 2018; D'Avanzo et al. 2018; Dobie et al. 2018; Granot et al. 2018; Hotokezaka et al. 2018; Lazzati et al. 2018; Margutti et al. 2018; Mooley et al. 2018a; Mooley et al. 2018b; Mooley et al. 2018c; Troja et al. 2018; Fong et al. 2019; Ghirlanda et al. 2019; Lamb et al. 2019; Troja et al. 2019). Finally, we use these observations to put the first constraints on the properties of non-thermal synchrotron emission from the deceleration of the KN fastest ejecta (i.e. the KN afterglow, e.g. Nakar et al. 2011; Kathirgamaraju et al. 2019).

This chapter is organized as follows. We present the analysis of two recent CXO observations at $\delta t \sim 582$ and $\delta t \sim 743$ days in §2.2, together with a homogeneous temporal and spectral re-analysis of the entire CXO data set acquired in two years of monitoring of GW 170817. New VLA observations of GW 170817 at $\delta t > 500$ days are presented in §2.3. §2.4 is dedicated to the broad-band modeling of the non-thermal emission from GW 170817 within the boosted fireball framework of (Wu et al. 2018). Constraints on the KN afterglow and the physical properties of the KN fastest ejecta are derived in §2.5. Conclusions are drawn in §2.6.

All times are measured with respect to the time of the gravitational-wave trigger, which is August 17th 2017 12:41:04 UT (Abbott et al. 2017a). Uncertainties are provided at the $1\,\sigma$ confidence level (c.l.) and upper limits at the $3\,\sigma$ c.l. unless otherwise stated. We adopt the luminosity distance of NGC 4993, the host galaxy of GW 170817, $d = 40.7$ Mpc inferred by Cantiello et al. 2018.

2.2. X-ray Data Analysis

The Chandra X-ray Observatory (CXO) started observing GW 170817 on 2017 August 19 (δt ~2 days after the merger). Here we use a uniform framework for data reduction to perform a temporal and spectral analysis of new observations acquired at $\delta t \sim 580 - 740$ days, and a re-analysis of the entire Chandra data set spanning $\delta t \sim 2 - 356$ days after the merger. This is fundamental to our analysis and enables us to consistently compare the fluxes, measure the ambient density of the merger environment, reliably search for temporal variability, and model the afterglow. The total exposure time across all observations is ~ 731 ks (Table 2.1). The CXO data set acquired at $\delta t \sim 582$ and ~ 743 days is presented here for the first time. Previous CXO observations of GW 170817 have been presented by Haggard et al. 2017; Margutti et al. 2017; Troja et al. 2017; Alexander et al. 2018; Margutti et al. 2018; Nynka et al. 2018; Pooley et al. 2018; Ruan et al. 2018; Troja et al. 2018; Piro et al. 2019. Our analysis consistently accounts for the low count statistics of the Chandra observations of GW 170817 to accurately determine the model parameters and their uncertainties, as described in (Margutti et al. 2017; Alexander et al. 2018; Margutti et al. 2018). We show the XMM measurements from (D'Avanzo et al. 2018; Piro et al. 2019) in Fig. 2.1 but we do not include these data in our modeling below to minimize the impact of systematic effects arising from, for instance, variability of the central AGN confused with GW 170817 in the XMM PSF.

2.2.1. X-ray Temporal Analysis of GW 170817

We homogeneously reduced the entire CXO data set acquired at $\delta t \sim 2 - 743$ days since the merger following the steps below. We reprocessed all the observations with the `repro` task within `CIAO` (v4.11, Fruscione et al. 2006) applying standard ACIS data filtering and using the latest calibration database (`CALDB`, v4.8.3). We performed blind point-source detection with `wavdetect` on individual observation

IDs. The results are reported in Table 2.1. An X-ray source is blindly detected with `wavdetect` at a location consistent with GW 170817 in all observations acquired at $9.2 \leq \delta t < 360$ days, with inferred 0.5–8 keV net count-rates reported in Table 2.1. No X-ray emission from GW 170817 is detected at $\delta t \sim 2.3$ days and our results are consistent with the earlier report by Margutti et al. 2017. The X-ray counterpart of GW 170817 is blindly detected with a very low significance ($< 3\,\sigma$) in the individual observations acquired at the epochs corresponding to $\delta t \sim 581-743$ days (IDs 21322, 22157, 22158, 21372, 22736, 22736; PIs: Margutti, Fong, Troja; programs 20500299, 20500691). However, we note that GW 170817 is blindly detected with significance $\geq 3\,\sigma$ when observations acquired around the same time are merged (grouped IDs in Table 2.1).

Motivated by the claim of significant temporal variability around ~ 160 days by (Piro et al. 2019), we searched for short time-scale variability within each observation ID and for observations acquired within $\delta t/t \leq 0.03$ (i.e. grouped IDs in Table 2.1) by applying a multinomial test to the observed photon counts. The null hypothesis that we want to test is that of a constant source count-rate in a time interval Δt_{tot}. We thus assigned to each time interval a probability proportional to the effective exposure time Δt_k within Δt_{tot}, and computed the log-likelihood of the observed photon counts with respect to a multinomial distribution with $n = N_{tot}$ (where n is the number of trials and N_{tot} is the total number of observed photons in Δt_{tot}). We then generated 10^4 realizations of N_{tot} events distributed among Δt_k following a multinomial distribution with probabilities defined as above. For each Δt_{tot}, the statistical significance of the evidence of a departure from our null hypothesis is quantified by the fraction of synthetic data sets that showed a log-likelihood value at least as extreme as the one observed. We applied the multinomial test to each observation ID and to grouped IDs in Table 2.1. For single IDs, Δt_{tot} is defined by the start and end of the CXO observations and we divided Δt_{tot} into two halves, Δt_1 and Δt_2. For grouped IDs, Δt_{tot} encompasses the time interval defined by the beginning and end time of the first and last observation, respectively, and the values of Δt_k are naturally defined as the exposure times of each ID.

We find no evidence for departures from our null hypothesis in the entire sample of CXO observations of GW 170817, with a statistical significance of short time-scale variability of the X-ray emission from GW 170817 of $\leq 2.5\sigma$ (Gaussian equivalent). In particular, our results do not confirm the claim of temporal variability at the level of $3.3\,\sigma$ in the time interval $\Delta t_{tot} = 153 - 164$ days by (Piro et al. 2019). By applying the same method as in (Piro et al. 2019) we find that we can reproduce their results only for their particular choice of time intervals ($\Delta t = 153.4 - 157.2$ days vs. $\Delta t = 159.8 - 163.8$ days, without considering data acquired in CXO ID 20937) and only if we do not account for the number of trials.[1] Properly accounting for the trials with the test above leads to a reduced statistical evidence for temporal variability in this time interval of $1.8\,\sigma$. We thus conclude that there is no statistical evidence for short-term variability in the X-ray afterglow of GW 170817 and that the

[1]Excluding the central portion of the data as in (Piro et al. 2019), but allowing for a random selection of the initial and final time intervals to compare, leads to the conclusion that only $\sim 0.4\%$ of blind choices would lead to a claim of temporal variability as significant as $\sim 3.3\sigma$ (see detailed discussion in Appendix A and Fig. A1).

current CXO data set does not quantitatively support the notion of an X-ray flare from a surviving magnetar remnant at $\delta t \sim 160$ days (Piro et al. 2019).

2.2.2. X-ray Spectral analysis of GW 170817

For each observation ID we extracted a spectrum using `specextract` and a source region of $1.5''$ centered at the location of the X-ray counterpart. We fitted each spectrum using an absorbed power-law model (`tbabs*ztbabs*pow`) within `XSPEC` (v12.9.1), adopting a Galactic neutral hydrogen column density $\mathrm{NH}_{MW} = 0.0784 \times 10^{22}$ cm^{-2} (Kalberla et al. 2005a). We employed Cash statistics and performed a series of Markov Chain Monte Carlo (MCMC) simulations to properly constrain the spectral parameters and their uncertainties in the regime of low-count statistics as in Margutti et al. 2017; Alexander et al. 2018; Margutti et al. 2018. In no case did we find any statistical evidence for significant intrinsic absorption $\mathrm{N_{H,\,int}}$, and we list the derived $3\,\sigma$ upper limits in Table 2.1. We thus assume $\mathrm{N_{H,\,int}} = 0\,\mathrm{cm^{-2}}$ in our subsequent modeling. The inferred best-fitting photon indices Γ, absorbed fluxes and (unabsorbed) luminosities are reported in Table 2.1. For observations acquired within a few days of each other, we also provide the results from a joint spectral fit and we plot the resulting light-curve in Fig. 2.1. Finally we do not find statistical evidence for spectral evolution of the source over $\delta t \sim 2 - 743$ days. From a joint-fit of all the CXO data at $\delta t \geq 9.2$ days we infer $\mathrm{N}_{H,\mathrm{int}} < 0.69 \times 10^{22}$ cm^{-2} and $\Gamma = 1.57^{+0.12}_{-0.07}$ (for $\mathrm{N}_{H,\mathrm{int}} = 0\,\mathrm{cm^{-2}}$), consistent with the spectral index inferred from broad-band radio to X-ray studies (e.g. Alexander et al. 2018; Margutti et al. 2018; Troja et al. 2018; Fong et al. 2019).

Table 2.1 Results from our homogeneous spectral analysis of all the CXO observations of GW 170817 between 2.3 and 743 days since merger. The reported photon indices, absorbed fluxes and (unabsorbed) luminosities are calculated for $N_{H,\mathrm{int}} = 0\,\mathrm{cm}^{-2}$. At $\delta t > 400$ days the photon index Γ is not well constrained and we adopt $\Gamma = 1.57$ for the spectral calibration. The reported significance is for a blind (targeted) detection for $\delta t < 360$ days ($\delta t > 360$ days).

ObsID	Time since merger (days)	Significance σ	Exposure (ks)	Net count rate (0.5-8 keV) (10^{-4} cts/s)	$N_{\mathrm{H,int}}$ 3-σ upper limit 10^{22} cm^{-2}	Photon Index Γ	Photon Index Γ (group)	Absorbed Flux (0.3 - 10 keV) 10^{-15}erg cm^{-2}s^{-1}	Absorbed Flux (group)	Luminosity (0.3-10 keV) 10^{38} erg s^{-1}	Luminosity (group)
18955	2.33	–	24.6	< 1.2	–	2 (assumed)		< 1.4		< 3.4	
19294	9.20	5.8	49.4	2.9 ± 0.8	< 17.6	$0.91^{+0.94}_{-0.39}$		$6.85^{+3.20}_{-3.04}$		$13.50^{+6.31}_{-6.00}$	
20728	15.38	7.2	46.7	3.8 ± 0.9	< 6.1	$1.55^{+0.76}_{-0.33}$	$2.22^{+0.76}_{-0.35}$	$5.99^{+2.54}_{-1.02}$	$4.32^{+1.15}_{-0.56}$	$12.53^{+5.31}_{-2.14}$	$10.35^{+2.76}_{-1.35}$
18988	15.94	5.3	46.7	3.0 ± 0.8		$3.54^{+1.49}_{-0.44}$		$5.55^{+2.11}_{-1.95}$		$19.37^{+7.37}_{-6.80}$	
20860	107.97	33.4	74.1	14.7 ± 1.4	< 1.7	$1.48^{+0.22}_{-0.14}$	$1.52^{+0.17}_{-0.12}$	$25.19^{+1.63}_{-2.04}$	$24.24^{+2.09}_{-2.87}$	$52.20^{+3.38}_{-4.22}$	$50.48^{+4.35}_{-5.98}$
20861	111.06	14.9	24.7	14.1 ± 2.4		$1.67^{+0.44}_{-0.28}$		$21.07^{+6.38}_{-3.70}$		$44.87^{+13.60}_{-7.87}$	
20936	153.55	22.5	31.8	18.6 ± 2.5	< 1.2	$1.35^{+0.31}_{-0.19}$	$1.58^{+0.26}_{-0.15}$	$32.37^{+13.89}_{-8.83}$	$24.20^{+3.60}_{-1.71}$	$66.00^{+28.33}_{-18.00}$	$50.84^{+7.57}_{-3.59}$
20938	157.12	13.5	15.9	18.5 ± 3.5		$1.75^{+0.46}_{-0.24}$		$26.46^{+4.11}_{-6.17}$		$57.14^{+8.87}_{-13.33}$	
20937	158.92	12.6	20.8	13.6 ± 2.6		$1.90^{+0.57}_{-0.26}$		$20.39^{+6.76}_{-2.00}$		$45.34^{+15.04}_{-4.44}$	
20939	159.93	10.6	22.2	10.8 ± 2.3		$1.93^{+0.61}_{-0.40}$		$14.37^{+1.42}_{-1.75}$		$32.16^{+3.19}_{-3.91}$	
20945	163.73	7.4	14.2	11.5 ± 2.9		$1.61^{+1.03}_{-0.42}$		$21.06^{+6.11}_{-7.56}$		$44.40^{+12.88}_{-15.94}$	
21080	259.20	13.8	50.8	7.8 ± 1.3	< 3.8	$1.62^{+0.44}_{-0.27}$	$1.57^{+0.29}_{-0.13}$	$11.40^{+1.86}_{-1.32}$	$12.21^{+2.88}_{-1.48}$	$24.11^{+3.93}_{-2.80}$	$25.61^{+6.04}_{-3.10}$
21090	260.78	14.8	46.0	8.3 ± 1.4		$1.52^{+0.35}_{-0.24}$		$13.06^{+4.58}_{-1.52}$		$27.22^{+9.53}_{-3.18}$	
21371	358.61	11.1	67.2	5.0 ± 0.9	< 3.9	$1.69^{+0.49}_{-0.34}$		$7.75^{+2.70}_{-0.73}$		$16.58^{+5.77}_{-1.56}$	
21322	580.99	2.3	35.6	1.5 ± 0.7	< 3.05	$0.95^{+1.73}_{-1.67}$	$1.28^{+1.04}_{-0.15}$	$5.43^{+2.54}_{-2.20}$	$3.25^{+0.85}_{-1.03}$	$11.11^{+5.19}_{-4.49}$	$7.07^{+1.86}_{-2.24}$
22157	581.94	2.7	38.2	1.6 ± 0.7		$1.38^{+1.09}_{-1.05}$		$2.75^{+2.20}_{-1.36}$		$5.82^{+2.43}_{-2.57}$	
22158	583.60	2.0	24.9	1.5 ± 0.8		$1.59^{+2.82}_{-2.57}$		$5.75^{+3.78}_{-3.01}$		$12.53^{+8.24}_{-6.57}$	
21372	740.31	2.2	40.0	<1.3	< 11.4	–	$1.23^{+1.05}_{-1.03}$	–	$2.21^{+0.85}_{-0.79}$	–	$4.82^{+1.86}_{-1.71}$
22736	742.26	3.0	33.6	1.0 ± 0.4		$2.61^{+2.66}_{-2.01}$		$2.45^{+1.39}_{-1.62}$		$6.77^{+3.85}_{-4.49}$	
22737	743.13	4.6	25.2	2.2 ± 0.9		$1.21^{+1.46}_{-1.45}$		$7.22^{+3.25}_{-2.95}$		$15.03^{+6.78}_{-6.15}$	
Joint Fit	–	–	–	–	< 0.69	$1.57^{+0.12}_{-0.07}$		–		–	

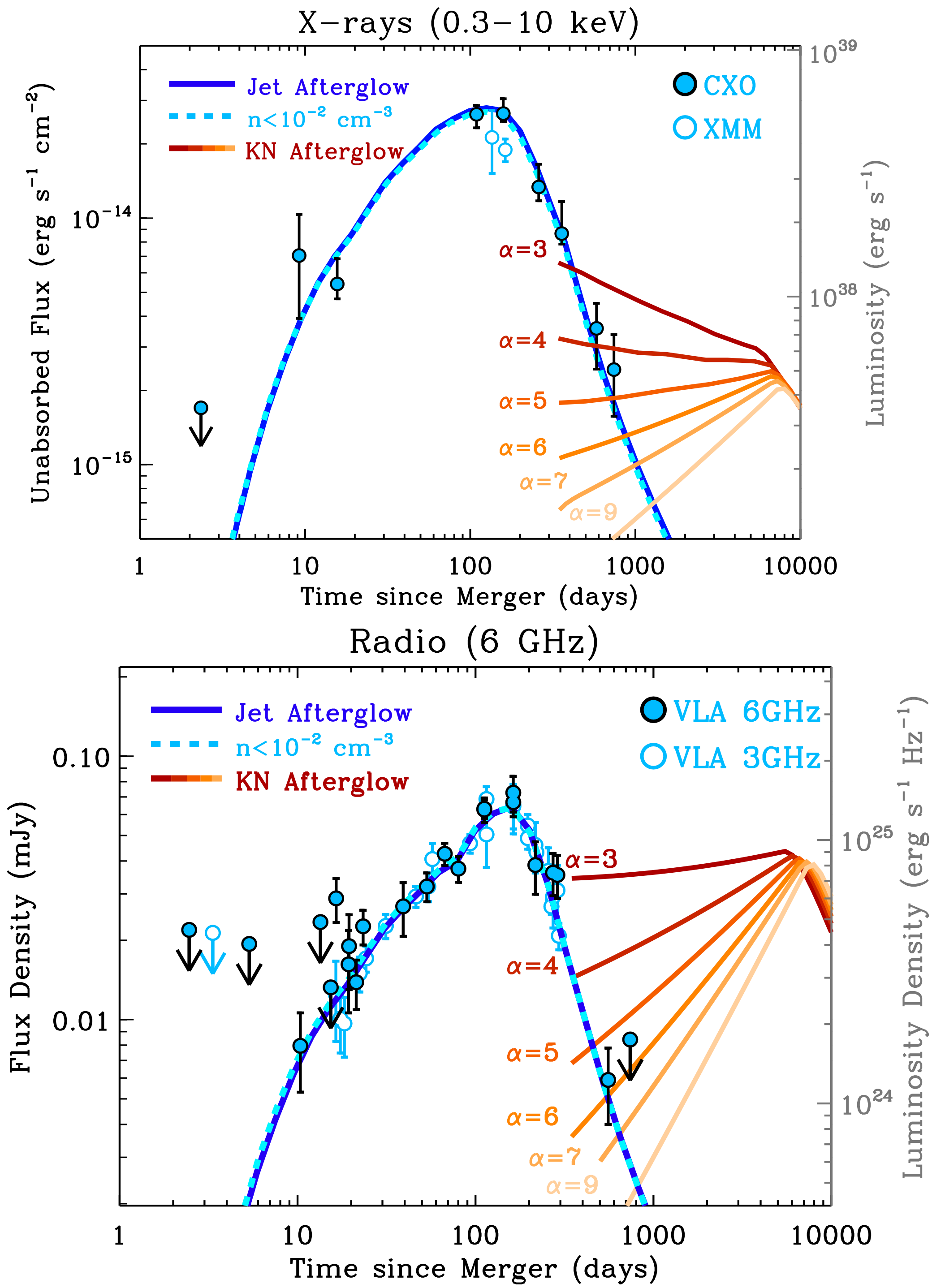
X−rays (0.3−10 keV)
Jet Afterglow
n<10^{-2} cm^{-3}
KN Afterglow
CXO
XMM
α=3
α=4
α=5
α=6
α=7
α=9
Unabsorbed Flux (erg s^{-1} cm^{-2})
10^{-14}
10^{-15}
Luminosity (erg s^{-1})
10^{39}
10^{38}
1
10
100
1000
10000
Time since Merger (days)
Radio (6 GHz)
Jet Afterglow
n<10^{-2} cm^{-3}
KN Afterglow
VLA 6GHz
VLA 3GHz
α=3
α=4
α=5
α=6
α=7
α=9
Flux Density (mJy)
0.10
0.01
Luminosity Density (erg s^{-1} Hz^{-1})
10^{25}
10^{24}
1
10
100
1000
10000
Time since Merger (days)

Figure 2.1

Figure 2.1 X-ray (upper panel) and radio (lower panel) emission from GW 170817 in the first $\sim$ 743 days since merger as constrained by the CXO (this work), XMM-Newton (D'Avanzo et al. 2018; Piro et al. 2019) and the most recent VLA observations (this work) merged with previous VLA observations (Alexander et al. 2017; Hallinan et al. 2017; Alexander et al. 2018; Margutti et al. 2018; Mooley et al. 2018a; Mooley et al. 2018c). We plot the VLA 6 GHz data (filled circles) and the 3 GHz data (empty circles) scaled at 6 GHz using an $F_\nu \propto \nu^{-0.6}$ spectrum. The broad-band emission continues to be well modeled by a structured off-axis jet (solid blue line) with best fitting energy $E_0 \sim 2 \times 10^{50}$ erg, $\theta_{obs} \sim 33°$, $\theta_0 \sim 7°$ propagating into a medium with density $n \sim 0.07$ cm^{-3} (§2.4, Fig. 2.3). Dashed light-blue lines: best fitting structured jet model for $n < 9.6 \times 10^{-3}\,\mathrm{cm}^{-3}$ as derived in §2.2.3, which leads to $E_0 \sim 1.5 \times 10^{49}$ erg, $\theta_{obs} \sim 30°$, $\theta_0 \sim 6°$ (§2.4, Fig. 2.4). Thick red-to-orange lines: expected emission originating from the deceleration of the KN ejecta into the environment (i.e. the KN afterglow). We adopt the parametrization by Kathirgamaraju et al. 2019 and show the expected KN afterglow emission for a set of representative values of the stratification index $\alpha = 3, 4, 5, 6, 7, 8, 9$ of the KN ejecta kinetic energy $E_k^{KN}(> \Gamma\beta) \propto (\Gamma\beta)^{-\alpha}$, and for fiducial values of the microphysical parameters $\epsilon_B = 10^{-3}$, $\epsilon_e = 0.1$. We further adopt an environment density $n = 0.01\,\mathrm{cm}^{-3}$ (the largest value allowed by our modeling of the diffuse X-ray emission, and a KN outflow with minimum velocity $v_0 \sim 0.3$c and total energy $\sim 10^{51}$ erg, as found from the modeling of the UV-optical-NIR KN emission, which is sensitive to the slower moving ejecta that carries the bulk of the KN kinetic energy (e.g. (Villar et al. 2017)). Current observations constrain and disfavor the shallower $\alpha \lesssim 6$ values. Future broad-band monitoring will probe a larger portion of the parameter space of the KN fastest ejecta (§2.5).

2.2.3. Spatially Resolved Spectral Analysis of the Host Galaxy Diffuse X-ray Emission

The host galaxy of GW 170817 (NGC4993) shows evidence for diffuse X-ray emission from a hot interstellar medium (ISM), in addition to harboring a weak active galactic nucleus (AGN, e.g. Blanchard et al. 2017b) and point sources of X-ray emission (Fig. 2.2). In this section we describe the results from a spatially resolved X-ray spectral analysis of NGC 4993, with the goal to constrain the physical properties of the plasma

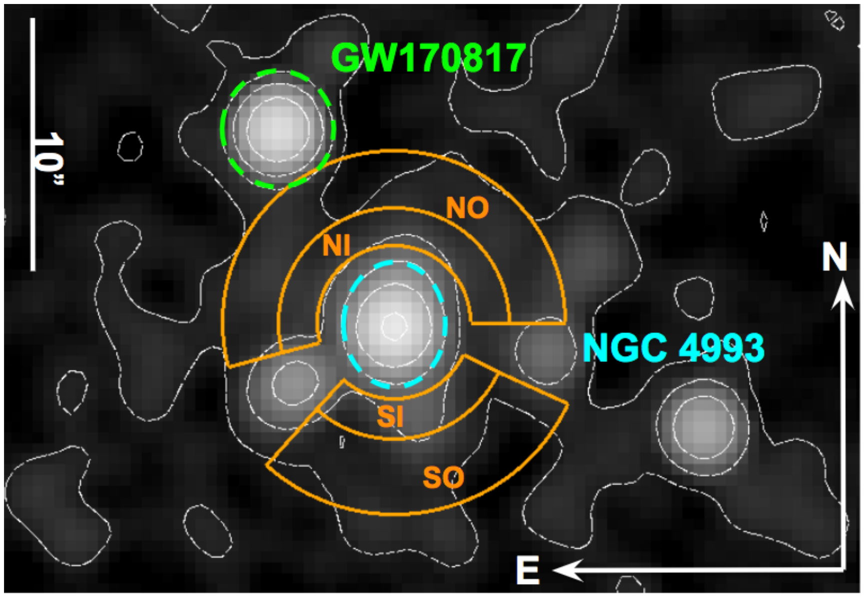

Figure 2.2 Combined X-ray image with CXO observations from δt$\sim$ 2 days - 743 days post-merger in 0.5–8 keV energy range, with contour levels in white. The four sectors in orange (NI: North Inner, NO: North Outer, SI: South Inner, SO: South Outer) mark the regions of spectra extraction for the spatially resolved X-ray spectral analysis of §2.2.3. The regions are defined so as to: (i) exclude emission from the core of the host galaxy, (ii) avoid contamination from the neighboring point-sources, and (iii) have comparable number of background subtracted counts.

responsible for the diffuse emission component, (i.e. plasma temperature T and particle density n), taking advantage of the very deep merged CXO observation.

We followed the method developed by Paggi et al. 2014 to constrain the physical properties of the hot ISM of the elliptical galaxy NGC 4649. As a first step, we merged all the observations (with a total exposure time of $\sim$ 731 ks) into a single event file using the `merge_obs` task within `CIAO`. `merge_obs` integrates two separate tasks: `reproj_obs`, which re-projects individual event files to a common astrometric solution, and `flux_obs`, which then merges the re-projected files into a single exposure-corrected event file. Other products from `merge_obs` include reprojected images, exposure maps and exposure-corrected images in a given energy band. We then combined the point spread function (PSF) maps of individual observations into a single exposure-map weighted PSF file with `dmimgcalc`. Finally, we used the exposure-map weighted PSF file from the previous step, the merged reprojected 0.5-8 keV event file, and the exposure map created by `merge_obs` as input to `wavdetect`. Our goal was to detect faint point sources that would elude searches in individual exposures. We used a false-alert probability threshold of 4×10^{-6} and a set of different wavelet scales (i.e. 1, 2, 8 and 16). Visual inspection reveals that this method reliably identifies all the sources of point-like X-ray emission in the merged image.

The end product of this process is a list of detected point sources and corresponding point-source regions.

We defined four regions for the extraction of the spectra of the diffuse X-ray emission as in Fig. 2.2. The inner sectors (NI and SI in Fig. 2.2) have an internal radius $r_{i,1} = 3.5''$ (to exclude the emission from the host galaxy core, which is dominated by the AGN), an external radius $r_{e,1} = 5.25''$, and angular extents defined to avoid the point sources identified above. The north-outer sector (NO in Fig. 2.2) has an inner radius $r_{i,2} = r_{e,1}$ and extends to $r_{e,2} = 7.8''$ (near GW 170817). The SO sector extends from $r_{e,1}$ to $r_{e,2} = 8.7''$. These regions are defined so as to contain a number of photons that lead to $\gtrsim 3\sigma$ evidence for emission in excess to the expected background counts, which corresponds to $N \sim 20 - 50$ background-subtracted counts in the different regions.

For each observation ID, we extract four spectra with `specextract` (one for each of the sectors of Fig. 2.2) with the background spectra extracted from the nearby 'blank-sky' field, generating spectral response files that are weighted by the count distribution within the aperture, as appropriate for extended sources. Finally, for each sector, we combined the spectral files obtained in the previous step using `combine_spectra`.

We modeled the emission from hot plasma in NGC 4993 with the `apec` model within *Xspec*. Due to projection effects, each 2-D sector in Fig. 2.2 collects part of the radiation from 3-D shells at larger radii. We accounted for these projection effects using the `projct` mixing model within *Xspec*, that is designed to perform a 3-D to 2-D projection of prolate ellipsoidal shells onto elliptical annuli (and respective sectors). We further adopted the solar abundances from Asplund et al. 2009 and fixed the metal abundance parameter of the `apec` model to three different values of $0.5\,Z_\odot$, $Z_\odot$, $2\,Z_\odot$, (where $Z_\odot$ is the solar metallicity). The galactic absorption column density was frozen to $\mathrm{NH}_{MW} = 0.0784 \times 10^{22}$ cm^{-2} (Kalberla et al. 2005a) for all the spectral fits. The fit was initially performed for the outermost sectors (NO and SO in Fig. 2.2) independently, and the best-fitting parameters are reported in Table 2.2. The fit of the inner sectors were then performed jointly with their respective outer sectors, with the spectral parameters of the outer sectors frozen to the best-fitting parameters obtained in the previous step. All the resulting best-fitting de-projected model parameters (i.e. plasma temperature and emission measure EM) for each sector are presented in Table 2.2 for three metallicity values.

2.2.3.1. Inferred ionized matter density at the location of GW 170817.

The best-fitting EM value of the `apec` diffuse emission model for the different shells provides a direct estimate of the host-galaxy density at that location. The EM is defined as:

$$EM = \frac{10^{-14}}{4\pi D_A^2} \int n_e n_H dV \approx \frac{10^{-14}}{4\pi D_A^2} \left(\frac{\rho}{m_p}\right)^2 \frac{X(1+X)}{2} V_{olume} \tag{2.1}$$

where D_A is the angular distance to the host galaxy (in cm); n_e and n_H are the number density of electrons and hydrogen atoms (in cm^{-3}), respectively, and $n_e \sim \frac{\rho}{2m_p}(1+X)$. ρ is the matter density, X is the fraction of hydrogen by mass, and m_p is the proton mass. The particle densities inferred from the de-projected `apec` spectral fits are reported in Table 2.2. Of particular interest are the density values inferred for the outer sector NO. We find $n \sim (5.1 - 9.6) \times 10^{-3}\,\mathrm{cm}^{-3}$, depending on the assumed gas metallicity. GW 170817 is located at larger radius (Fig. 2.2), where the gas density is likely to be lower. Additionally, unresolved point sources might contribute some of the detected emission. We thus consider $n \leq 9.6 \times 10^{-3}\,\mathrm{cm}^{-3}$ as an upper limit on the density of ionized matter in the merger environment. Our density constraint analysis is not sensitive to the presence of small-scale density variations, for instance, the presence of over-densities at the edge of a bow-shock cavity formed if the merger progenitor hosted a pulsar (e.g. (Ramirez-Ruiz et al.

2019)). Our analysis complements previous inferences of neutral hydrogen particle density $n_{HI} < 0.04\,\mathrm{cm}^{-3}$ derived from radio observations by (Hallinan et al. 2017), and it is consistent with the lower-limit on the circum-merger density $n > 2 \times 10^{-5}\,\mathrm{cm}^{-3}$ derived by (Mooley et al. 2018a).

Table 2.2 Best-fitting de-projected emission measure (EM) and temperature T derived from a bremsstrahlung spectral fit of the emission from the concentric annular regions of Fig. 2.2, and derived particle density n.

Shell	EM[2] ($\times 10^{-7}$ cm^{-5})	Temperature (T) (keV)	C-stat/dof	Density (n) ($\times 10^{-3}$ cm^{-3})
		Z = 0.5 $Z_\odot$		
NO	$4.63^{+1.33}_{-0.79}$	$0.68^{+0.07}_{-0.11}$	386/510	$9.60^{+1.38}_{-0.82}$
NI	$12.41^{+3.59}_{-3.27}$	$2.03^{+1.49}_{-0.62}$	679/1022	$28.29^{+4.09}_{-3.73}$
SO	$2.71^{+1.14}_{-1.07}$	$1.83^{+3.62}_{-0.67}$	296/510	$7.68^{+1.62}_{-1.51}$
SI	$30.74^{+6.37}_{-5.55}$	$4.28^{+8.59}_{-1.84}$	539/1022	$58.06^{+6.02}_{-5.24}$
		Z = $Z_\odot$		
NO	$2.57^{+0.69}_{-0.45}$	$0.68^{+0.07}_{-0.11}$	385/510	$7.15^{+0.97}_{-0.69}$
NI	$9.72^{+3.08}_{-3.05}$	$2.18^{+1.81}_{-0.62}$	679/1022	$25.04^{+3.96}_{-3.93}$
SO	$2.36^{+1.07}_{-1.20}$	$2.67^{+4.65}_{-1.39}$	296/510	$7.16^{+1.63}_{-1.82}$
SI	$11.59^{+2.74}_{-2.41}$	$0.74^{+0.25}_{-0.16}$	547/1022	$35.66^{+4.21}_{-3.70}$
		Z = 2 $Z_\odot$		
NO	$1.36^{+0.36}_{-0.24}$	$0.68^{+0.07}_{-0.11}$	385/510	$5.19^{+0.69}_{-0.46}$
NI	$7.03^{+2.79}_{-2.66}$	$2.43^{+2.09}_{-0.81}$	679/1022	$21.28^{+4.24}_{-4.02}$
SO	$2.15^{+0.84}_{-1.09}$	$4.29^{+3.68}_{-2.60}$	296/510	$7.37^{+1.56}_{-1.95}$
SI	$3.26^{+0.79}_{-0.64}$	$0.64^{+0.12}_{-0.11}$	490/1022	$18.90^{+2.29}_{-1.84}$

2.3. Radio Data Analysis

We observed GW170817 with the Karl G. Jansky Very Large Array (VLA) on 2019 January 21 beginning at 12:32:10 UT ($\delta t \sim 521$ days post merger), 2019 January 25 at 10:52:45 UT ($\delta t \sim 525$ days), and 2019 March 29 at 05:00:15 UT ($\delta t \sim 588$ days). The January observations lasted 2 hours each and were taken in C configuration, while the March observation lasted 4 hours and was taken in B configuration. All observations were taken at a mean frequency of 6 GHz with an observing bandwidth of 4 GHz. The data were calibrated and imaged with standard CASA routines (McMullin et al. 2007a), using 3C286 as the flux calibrator and J1258-2219 as the phase calibrator.

We do not detect GW170817 in any of the observations individually or in a combined image made from the two January observations. We therefore combine all three datasets using the CASA task `concat` and produce a single image with improved signal-to-noise. We recover a faint source at the location of GW170817 in the final joint image. We fit the emission with a point source model using the `imtool` package within `pwkit` (Williams et al. 2017a) and obtain a final flux density of 5.9 ± 1.9 μJy. This is consistent with expectations for an off-axis structured relativistic jet, Fig. 2.1 (Alexander et al. 2018; Wu et al. 2018; Xie et al. 2018).

A final epoch of radio observation was acquired at $\delta t = 724.3 - 743.2$ days since merger, and consisted of two observations, the first beginning on 2019 August 11 at 19:36:09 UT (3 hours, A configuration) and the second beginning on 2019 August 30 at 18:29:44 UT (3 hours, A configuration). For both observations the mean frequency is 6 GHz and the bandwidth is 4 GHz. Following the same data reduction and calibration procedure as above we do not find evidence of radio emission at the location of GW 170817 in the individual observations or in a combined image. We also imaged the output of the observatory-provided NRAO pipeline calibrated data and obtained similar results. We infer $F_\nu < 8.4\,\mu$Jy at $3\,\sigma$ c.l. from the combined dataset. We show the complete 6 GHz radio lightcurve of GW 170817 in Fig. 2.1.

The radio to X-ray SED at $\delta t \sim 582$ days is well modeled by a simple power-law with $F_\nu \propto \nu^{-\beta}$ and $\beta = 0.55 \pm 0.02$ consistent with Fong et al. 2019 and the inferred broad-band spectrum at earlier times (e.g. Alexander et al. 2018; D'Avanzo et al. 2018; Dobie et al. 2018; Margutti et al. 2018; Mooley et al. 2018b; Troja et al. 2018; Troja et al. 2019). We further infer a 3σ lower limit on the synchrotron cooling break frequency $\nu_c > 0.16$ keV at $\delta t \sim 582$ days. Based on data presented in this section and §2.2 we conclude that there is no evidence for spectral evolution of the non-thermal emission of GW 170817 at any time of our monitoring, from $\delta t \sim 10$ days until ~ 740 days since merger.

2.4. Updated modeling of the broad-band jet afterglow emission

We use `JetFit`, the synthetic light-curve fitting tool based on the two-parameter boosted fireball model developed by Duffell et al. 2013 and Wu et al. 2018, to fit the broad-band non-thermal emission from GW 170817 up to ~ 2 yrs since merger. `JetFit` can naturally accommodate a wide range of outflow structures ranging from mildly relativistic quasi-spherical outflows to ultra-relativistic structured jets (Wu et al. 2018; Wu et al. 2019). Specifically, our data set consists of the X-ray observations from Table 2.1, $\sim$3 GHz and $\sim$6 GHz VLA radio observations collected from Alexander et al. 2017; Hallinan et al. 2017; Alexander et al. 2018; Dobie et al. 2018; Margutti et al. 2018; Mooley et al. 2018a; Mooley et al. 2018b as well as our latest radio observations presented in Sec.2.3.

Within `JetFit` the synthetic light curves are generated using four hydrodynamical paramaters: explosion energy E_0 (one side), ambient density n, asymptotic Lorentz factor η_0, and boost Lorentz factor γ_B; four radiative parameters: spectral index p of the electron distribution $N_e(\gamma_e) \propto \gamma_e^{-p}$, the electron energy fraction ϵ_e, the magnetic energy fraction ϵ_B and the fraction of electrons accelerated in a power-law distribution by the shock ξ_N; and three observational parameters: redshift z, luminosity distance d_L and the observer angle θ_{obs} with respect to the launch direction of the fireball. Model parameters inferred from the synchrotron emission intrinsically suffer from a level of degeneracy due to the unknown ξ_N value (e.g. Eichler et al. 2005). We thus assume $\xi_N = 1$ as common practice in the Gamma-Ray Burst (GRB) literature to allow a direct comparison to parameters inferred for short GRBs. We set the bounds on priors for the remaining eight parameters similar to those of (Wu et al. 2018) as reported in Table 2.3. We perform MCMC fitting using 100 walkers and 10^4 burn-in iterations. Sampling is performed on 10^4 additional iterations. The posterior distribution of the model parameters is generated with the `emcee` package

(Foreman-Mackey et al. 2013). The one-dimensional and two-dimensional projections of the posterior distribution that result from our fits are shown in Fig. 2.3, and the best-fitting model is shown in Fig. 2.1. The median values of the fitting parameters are reported in Table 2.3 with 1σ uncertainties computed as the 16th and 84th percentiles of the one-dimensional projection of the posterior distribution. These model parameters are consistent with those inferred by (Wu et al. 2018) using data at $\delta t < 300$ days. Since the new radio and X-ray observations that we present here are consistent with the extrapolation of the model by Wu et al. 2018 at later times, this result is not surprising.

The wide distributions of E_0 and n (and ϵ_e, and ϵ_B) in Fig.2.3 indicates a high level of degeneracy between the model parameters. As a refinement of our modeling, we enforce the upper limit on the ambient density of GW 170817 derived in §2.2.3. From the posterior distribution derived above using `JetFit`, we reject all the samples with $n > 9.6 \times 10^{-3}\,\mathrm{cm}^{-3}$, and plot the revised distribution of parameters, as shown in Fig. 2.4, and the best-fitting model is shown in Fig2.1. The median values of the revised parameter distributions are reported in Table 2.3. Taking the upper bound on the environment density into consideration when modeling the afterglow emission produces tighter constraints on the model parameters. We conclude that the broad-band non-thermal emission from GW 170817 at $\sim$ 2yr since merger (Fig. 2.1) is still well described by an off-axis jetted-outflow model with angular structure. The outflow carries an explosion energy $E_0 \sim 1.5 \times 10^{49}\,\mathrm{erg}$ (corresponding to an isotropic equivalent energy $E_{iso} \sim 2 \times 10^{52}\,\mathrm{erg}$), with a jet opening angle $\theta_0 \sim 6°$, and characteristic Lorentz factor $\Gamma_j \sim 160$[3] , expanding in a low-density environment ($n_0 \sim 2.5 \times 10^{-3}\,\mathrm{cm}^{-3}$). The jet axis is located at $\theta_{obs} \sim 30°$ with respect to our line of sight. Our inferences are broadly consistent with structured jet model parameters from broad-band modeling attempts that included data extending to $\delta t \sim 300$ days (e.g Lazzati et al. 2018; Mooley et al. 2018b; Ghirlanda et al. 2019; Kathirgamaraju et al. 2019; Lamb et al. 2019; Troja et al. 2019). We find no evidence of departure from a steep post-peak light-curve decay and we infer $F_\nu \propto t^{-1.95 \pm 0.15}$ at $\delta t > 200$ days, consistent with previous findings at earlier times (e.g. Alexander et al. 2018; Mooley et al. 2018b; Troja et al. 2019) and the expectations from emission dominated by a collimated relativistic outflow seen off-axis (Lamb et al. 2018).

The outflow will eventually enter the non-relativistic phase at $t_{NR} \propto (E_{k,iso}/n)^{1/3}$ (e.g. Piran 2004), when the amount of swept-up material will be comparable to the kinetic energy of the outflow. The non-relativistic transition will lead to a flattening of the light-curve decay $F_\nu \propto t^{-\alpha}$ with $\alpha = -(15p-21)/10 \sim 1.1$ for $\nu_m < \nu < \nu_c$ and $\alpha = -(3p-4)/2 \sim 1.2$ above ν_c (e.g. Huang et al. 2003; Gao et al. 2013). For the outflow and environment density parameters listed in Table 2.3, the non-relativistic transition is expected to occur at $t_{NR} \sim 3600^{+2100}_{-2000}$ days ($t_{NR} \sim 4700^{+1700}_{-1400}$ days for the model with the $n \leq 9.6 \times 10^{-3}\,\mathrm{cm}^{-3}$ prior). Before that happens, the KN afterglow might start dominating the observed emission (§2.5).

[3]The characteristic Lorentz factor of the outflow, Γ_j, mentioned here is different from Γ that we used earlier to denote the photon index of the X-ray spectra in §2.2. When mentioned in reference to the kilonova, Γ represents the Lorentz factor of the KN ejecta (as mentioned in Sec. §2.5.)

Table 2.3 `JetFit` model parameters and inferred quantities.

Parameter	Bounds for Prior Distribution[4]	Median value of Posterior Distribution w/o density constraint	Median value of Posterior Distribution w/ density constraint
$\log_{10} E_{0,50}$ (erg)	[-6, 3]	$0.32^{+1.28}_{-1.06}$	$-0.81^{+0.53}_{-0.51}$
$\log_{10} n_0$ (cm^{-3})	[-6, 3]	$-1.13^{+1.27}_{-1.29}$	$-2.61^{+0.42}_{-0.63}$
$\log_{10} \epsilon_e$	[-6, 0]	$-1.64^{+1.04}_{-1.48}$	$-0.75^{+0.43}_{-0.62}$
$\log_{10} \epsilon_B$	[-6, 0]	$-4.38^{+1.59}_{-1.14}$	$-2.63^{+0.89}_{-1.23}$
η_0	[2, 10]	$8.11^{+1.27}_{-1.31}$	$8.16^{+1.18}_{-1.15}$
γ_B	[1, 12]	$8.60^{+2.10}_{-2.34}$	$9.73^{+1.38}_{-1.40}$
θ_{obs} (rad)	[0, 1]	$0.58^{+0.20}_{-0.09}$	$0.53^{+0.07}_{-0.06}$
p	[2, 2.5]	$2.15^{+0.01}_{-0.02}$	$2.15^{+0.01}_{-0.02}$
Derived Quantities			
θ_0[5] (deg)		$6.66^{+2.48}_{-1.31}$	$5.89^{+0.99}_{-0.73}$
$\log_{10} E_{iso,50}$[6] (erg)		$3.34^{+1.33}_{-1.07}$	$2.33^{+0.60}_{-0.55}$
Γ_j[7]		139^{+39}_{-44}	163^{+23}_{-43}

2.5. Constraints on the properties of the fastest KN ejecta

The deceleration of the KN ejecta into the ambient medium is another source of synchrotron radiation across the electromagnetic spectrum (i.e. the KN afterglow, e.g. (Nakar et al. 2011)). In close analogy to stellar explosions, the bulk of the kinetic energy in KNe is carried by "slowly" moving material that powers the detected UV-optical-NIR KN thermal emission, while the significantly lighter KN fastest ejecta rush ahead and shock the medium, accelerating electrons that cool via radiating synchrotron emission. By modeling the thermal UV-optical-NIR KN associated with GW 170817, (Villar et al. 2017) constrained the bulk velocities and masses of the post-merger ejecta to $v \sim 0.1 - 0.3c$ and total ejecta $M_{ej} \sim 0.08\,\mathrm{M}_{\odot}$, carrying a kinetic energy in excess of 10^{51} erg (see also (Arcavi et al. 2017; Cowperthwaite et al.

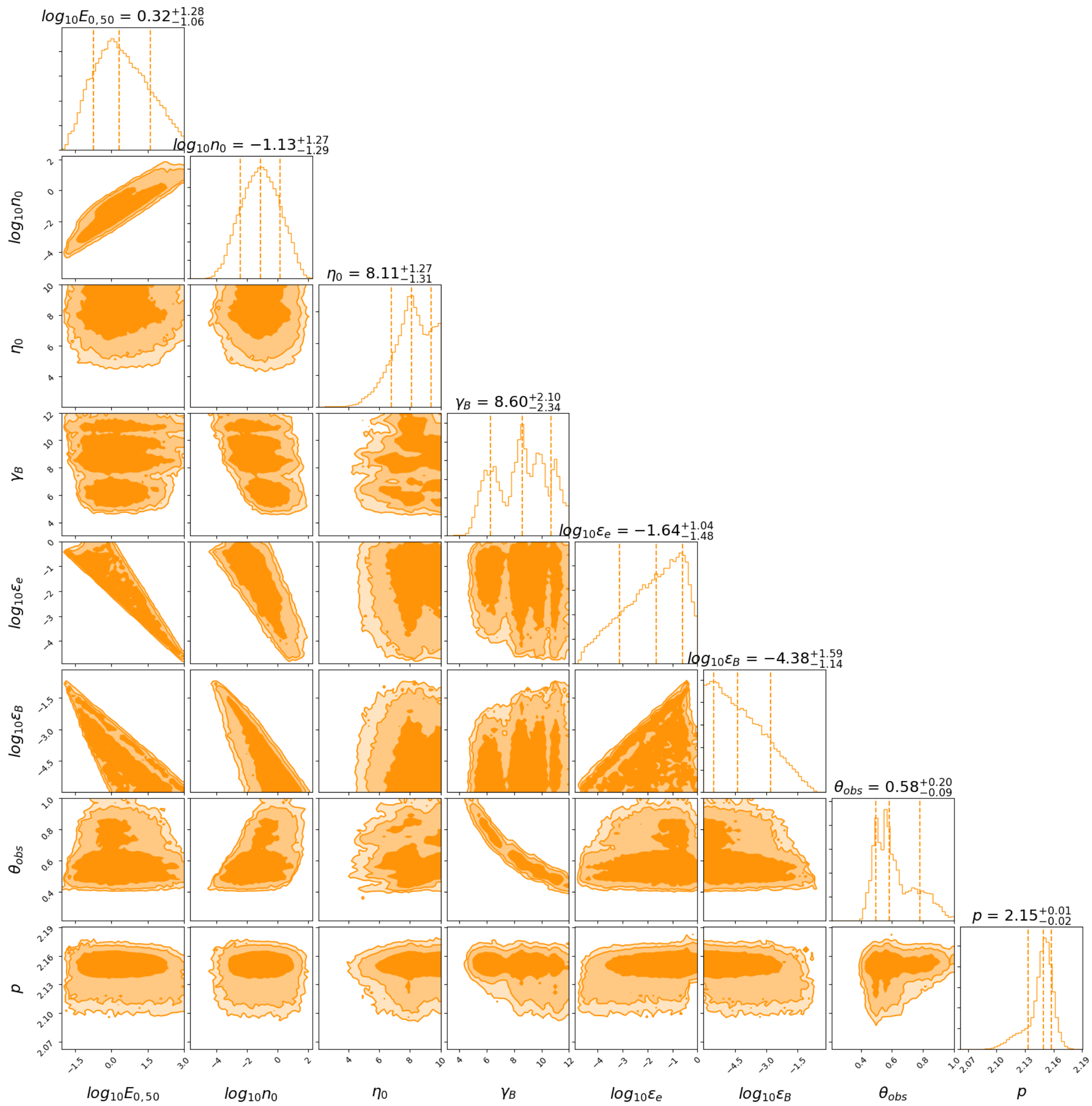

Figure 2.3 Corner plot showing the one and two dimensional projection of the posterior probability distribution of the jetted-outflow model parameters. Vertical dashed lines in the one-dimensional projections of the posterior distribution mark the 16%, 50% and 84% percentiles of the marginalized distributions, (i.e. the median value and the $1\,\sigma$ range). The contours are drawn at 68%,95%, and 99% confidence levels.

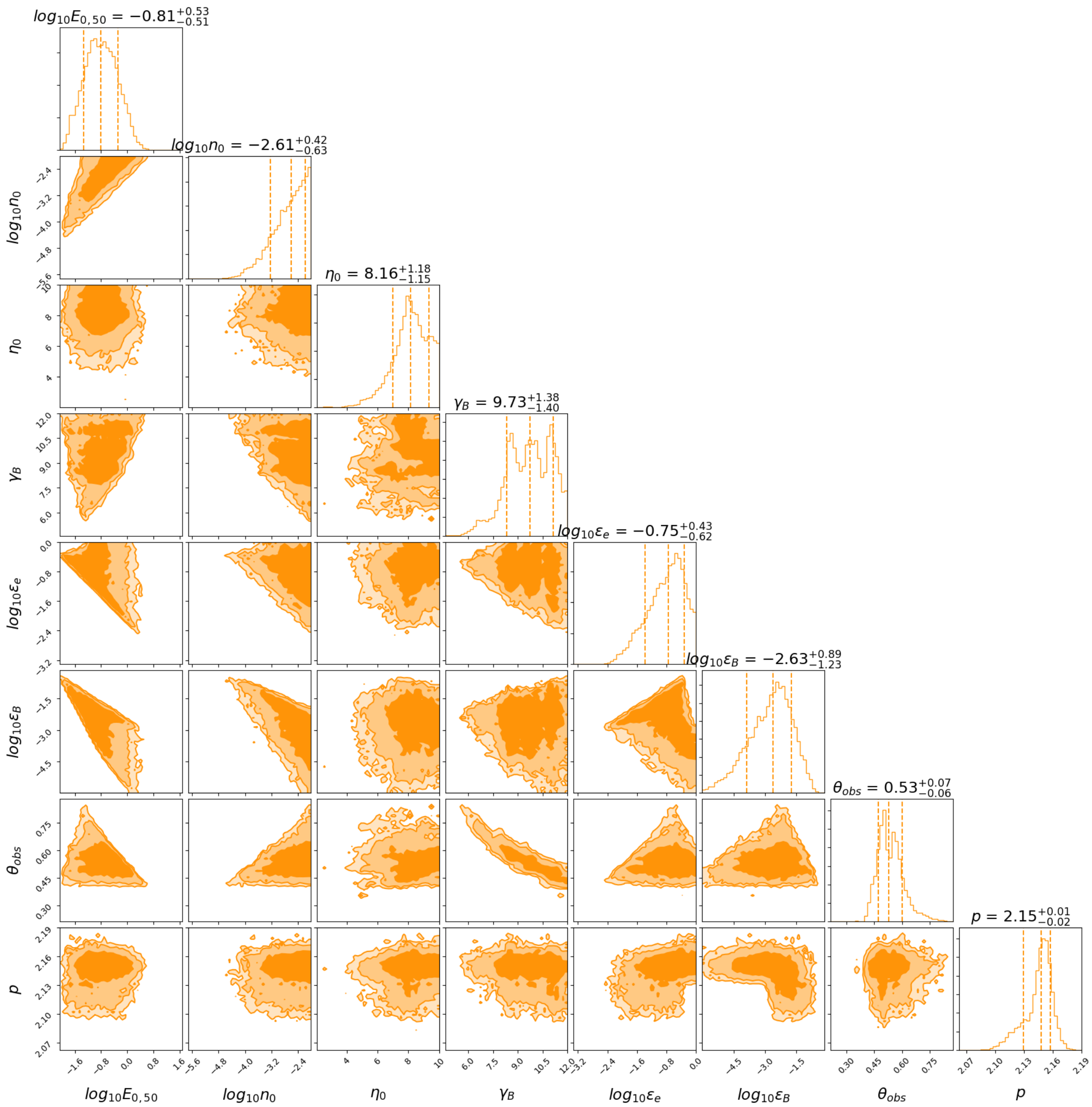

Figure 2.4 Same as Fig. 2.3 with the prior $n \leq 9.6 \times 10^{-3}\,\mathrm{cm}^{-3}$ as found in §2.2.3.

2017; Drout et al. 2017; Evans et al. 2017; Kasliwal et al. 2017; Valenti et al. 2017)). The KN thermal emission does not constrain the properties of the fastest KN ejecta at $\beta > 0.3\,c$ and the velocity structure $E_k^{KN}(\Gamma\beta)$ of the KN outflow. The kinetic

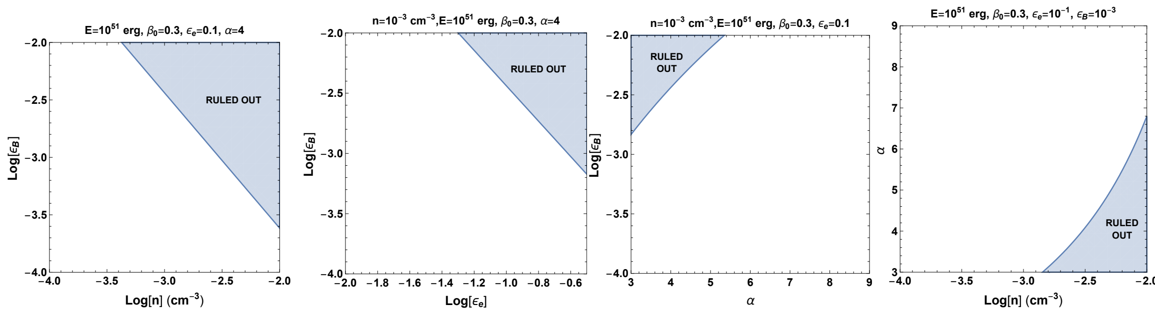

Figure 2.5 Allowed (white) and ruled out (shaded) parameter space of the KN afterglow of GW 170817 based on the fact that no re-brightening of the X-ray or radio emission was detected at ~ 2 yrs after the merger (Fig. 2.1). Two parameters are varied in each plot while the rest are kept fixed to values indicated in the plot title. The radio data set drives our conclusions and disfavors shallow stratification indexes $\alpha \leq 6$. Future observations will further constrain the parameter space of the KN afterglow.

energy profile $E_k^{KN}(\Gamma\beta)$ of the kilonova outflow carries direct information about the merger dynamics and, potentially, on the nature of the compact object remnant (e.g. Hotokezaka et al. 2018; Radice et al. 2018a; Radice et al. 2018d; Fernández et al. 2019).

We parameterize the kinetic energy of the fastest KN ejecta as a power-law in specific momentum $\Gamma\beta$ with index α: $E_k^{KN}(\Gamma\beta) \propto (\Gamma\beta)^{-\alpha}$ with a minimum outflow velocity v_0 motivated by thermal KM models. Following Kathirgamaraju et al. 2019 we generated a set of broad-band KN afterglow light-curves with the typical parameters inferred for the afterglow of short gamma-ray bursts (GRBs): $v_0 = 0.3\,c$, total kinetic energy $\sim 10^{51}$ erg, $p = 2.2$, $\epsilon_e = 0.1$, $\epsilon_B = [10^{-4}–10^{-2}]$, $n = [10^{-4}–10^{-2}]\,\mathrm{cm}^{-3}$ ((Fong et al. 2015)), and with $\alpha = [3–9]$ (Radice et al. 2018a; Radice et al. 2018d), which are shown in Fig.2.1 along with the best-fitting off-axis structured jet models.

We use the lack of evidence for emission from the KN afterglow to constrain the properties of the KN ejecta and its environment, as in (Kathirgamaraju et al. 2019). The results are displayed in Fig. 2.5, which shows that current radio observations disfavor shallow stratification indices $\alpha \leq 6$. [8] Future observations at $\delta t \geq 1000$ days are more sensitive to the KN fastest ejecta tail and will probe a larger portion of the parameter space (Fig.2.1).

2.6. Summary and Conclusions

We present deep X-ray and radio observations of GW 170817 that extend to ∼2 yrs after the neutron-star merger, a homogeneous analysis of the entire X-ray data set, and a new method to independently constrain the density of the merger environment based on diffuse X-ray emission from hot plasma in the host galaxy. These observations offer a complete view of the evolution of the broad-band afterglow of an off-axis structured jet launched by the neutron star merger from its first detection at ∼10 days, peak at ∼160 days and steep decline until the present epoch, and place the first constraints on the properties of the kilonova (KN) afterglow. Our main results can be summarized as follows:

- Our analysis reveals no evidence for broad-band spectral evolution or temporal variability of the X-ray emission at any time. The radio-to-X-ray data are well described by a simple-power law spectrum $F_\nu \propto \nu^{-\beta}$ with

[8] We note that the KN afterglow and the jet afterglow do not necessarily share the same microphysical parameters ϵ_e, ϵ_B, and p as the physical properties of the shocks launched by the two outflows are different.

$\beta = 0.575 \pm 0.007$. The highest statistical significance of short-term temporal X-ray variability is at the level of $2.5\,\sigma$.

- From the analysis of diffuse X-ray emission from hot plasma in the host galaxy of GW 170817 we infer a density limit on the NS merger environment $n \leq 9.6 \times 10^{-3}\,\mathrm{cm}^{-3}$. We note however that our analysis does not capture small-scale variations in density.
- After ~2 yrs of monitoring GW 170817, we conclude that the non-thermal emission from the binary neutron-star merger has been dominated at all times by a jetted outflow with angular structure viewed off-axis (Fig.2.1). Modeling the afterglow emission without (with) the density constraint results in $\theta_{obs} = 33.2^{+11.5}_{-5.2}\,\mathrm{deg}$ ($\theta_{obs} = 30.4^{+4.0}_{-3.4}\,\mathrm{deg}$). The outflow carries $\mathrm{E} = 2.1^{+38}_{-1.9} \times 10^{50}\,\mathrm{erg}$ ($\mathrm{E} = 1.5^{+3.6}_{-1.1} \times 10^{49}\,\mathrm{erg}$) of energy and contains a core of collimated ultra-relativistic material (i.e. a jet) with inferred opening angle $\theta_0 = 6.7^{+2.5}_{-1.3}\,\mathrm{deg}$ ($\theta_0 = 5.9^{+1.0}_{-0.7}\,\mathrm{deg}$) and characteristic Lorentz factor $\Gamma_j = 139^{+39}_{-44}$ ($\Gamma_j = 163^{+23}_{-43}$). We infer an environment density of $n = 7.3^{+129}_{-6.9} \times 10^{-2}\,\mathrm{cm}^{-3}$ ($n = 2.5^{+4.1}_{-1.9} \times 10^{-3}\,\mathrm{cm}^{-3}$). We note that the values of opening angle, θ_0 and spectral index, ‘p’, of the electron distribution are the same in both scenarios.
- The lack of evidence of departure from the off-axis structured jet emission allows us to constrain the properties of the yet-to-be detected KN afterglow. We find that for fiducial values of the parameters of the KN ejecta kinetic

energy distribution $E_k^{KN}(\Gamma\beta) \propto (\Gamma\beta)^{\alpha}$, current radio data disfavor shallow stratification indices $\alpha \leq 6$.

Future X-ray and radio observations of GW 170817 have the potential to detect the very first electromagnetic signature of non-thermal emission from the deceleration of the fastest ejecta from a kilonova. Simulations show that the fastest KN ejecta is launched by a shock when the merger remnant bounces back after merger (e.g. (Radice et al. 2018a)). The detection of emission from a fast KN outflow would (i) confirm that a high-mass neutron star was formed that was temporarily stable to collapse, ruling out prompt black hole formation; (ii) directly provide a constraint on the neutron star equation of state at higher densities than those probed by current LIGO/Virgo constraints on tidal deformability (as the process of "bounce" happens at higher densities and temperatures).

CHAPTER 3

Evidence for X-ray emission in excess to the jet afterglow decay 3.5 yrs after the binary neutron star merger GW 170817: a new emission component

This thesis chapter originally appeared in the literature as

Hajela, A., Margutti, R., Bright, J. S., Alexander, K. D., Metzger, B. D., Nedora, V., Kathirgamaraju, A., Margalit, B., Radice, D., Guidorzi, C., Berger, E., MacFadyen, A., Giannios, D., Chornock, R., Heywood, I., Sironi, L., Gottlieb, O., Coppejans, D., Laskar, T., Cendes, Y., Duran, R. B., Eftekhari, T., Fong, W., McDowell, A., Nicholl, M., Xie, X., Zrake, J., Bernuzzi, S., Broekgaarden, F. S., Kilpatrick, C. D., Terreran, G., Villar, V. A., Blanchard, P. K., Gomez, S., Hosseinzadeh, G., Matthews, D. J., & Rastinejad, J. C. (2022), ApJ, 927, L17.

ABSTRACT

For the first $\sim$ 3 years after the binary neutron star merger event GW 170817 the radio and X-ray radiation has been dominated by emission from a structured relativistic off-axis jet propagating into a low-density medium with $n < 0.01\,\mathrm{cm}^{-3}$.

We report on observational evidence for an excess of X-ray emission at $\delta t > 900$ days after the merger. With $L_x \approx 5 \times 10^{38}\,\mathrm{erg\,s^{-1}}$ at 1234 days, the recently detected X-ray emission represents a $\geq 3.2\,\sigma$ (Gaussian equivalent) deviation from the universal post jet-break model that best fits the multi-wavelength afterglow at earlier times. In the context of `JetFit` afterglow models, current data represent a departure with statistical significance $\geq 3.1\,\sigma$, depending on the fireball collimation, with the most realistic models showing excesses at the level of $\geq 3.7\,\sigma$. A lack of detectable 3 GHz radio emission suggests a harder broad-band spectrum than the jet afterglow. These properties are consistent with the emergence of a new emission component such as synchrotron radiation from a mildly relativistic shock generated by the expanding merger ejecta, i.e. a kilonova afterglow. In this context, we present a set of ab-initio numerical-relativity BNS merger simulations that show that an X-ray excess supports the presence of a high-velocity tail in the merger ejecta, and argues against the prompt collapse of the merger remnant into a black hole. Radiation from accretion processes on the compact-object remnant represents a viable alternative. Neither a kilonova afterglow nor accretion-powered emission have been observed before, as detections of BNS mergers at this phase of evolution are unprecedented.

3.1. Introduction

The binary neutron-star (BNS) merger GW 170817 is the first celestial object from which both gravitational waves (GWs) and light have been detected (Abbott et al. 2017b), enabling unprecedented insight on the pre-merger (GWs) and post-merger (light) physical properties of these phenomena (Nakar 2020; Margutti et al. 2021 and references therein). GWs from GW 170817 were detected on 17 August 2017 at 12:41:04 (UT) by Advanced LIGO and Advanced Virgo (Abbott et al. 2017a). The event was rapidly localized to reside in a nearby galaxy at a distance of 40.7 Mpc (Cantiello et al. 2018) thanks to the identification of its electromagnetic counterpart across the spectrum (γ-rays to radio, Abbott et al. 2017b). During the first ~ 70 days, the electromagnetic spectrum of GW 170817 consisted of a combination of thermal emission partially powered by the radioactive decay of heavy chemical elements freshly synthesized in the merger ejecta (i.e. the "kilonova") and non-thermal synchrotron emission dominating in the X-ray and radio bands. The spectrum and flux evolution of the kilonova emission from GW 170817 was in agreement with theoretical predictions (Metzger 2017) demonstrating that mergers of neutron stars are one of the major sources of heavy elements in our Universe (e.g., Rosswog et al. 2018). Modeling of the UV-Optical-NIR thermal emission from the kilonova allowed estimates of the bulk velocities and masses of the slower-moving ejecta powering the kilonova: $v \sim 0.1 - 0.3c$ and total ejecta mass $M_{\rm ej} \sim 0.06\,{\rm M}_{\odot}$, carrying a kinetic energy of $\approx 10^{51}$ erg (Cowperthwaite et al. 2017; Drout et al. 2017; Kilpatrick et al. 2017; Villar et al. 2017; Arcavi 2018; Waxman et al. 2018; Bulla et al. 2019; Nicholl et al. 2021).

In the first ≈ 900 days since merger, the non-thermal spectrum of GW 170817 has been dominated by synchrotron emission from an ultra-relativistic structured jet initially pointing $\theta_{\mathrm{obs}} \sim 15-25$ degrees away from our line of sight (Mooley et al. 2018c; Ghirlanda et al. 2019; Hotokezaka et al. 2019; Nathanail et al. 2021). Radio-to-X-ray data did not show any evidence for spectral evolution across nine orders of magnitude of frequency for 900 days (Fong et al. 2019; Hajela et al. 2019; Troja et al. 2020) and the emission was well characterized as originating from an optically thin synchrotron source with a power-law spectrum $F_{\nu} \propto \nu^{-(p-1)/2}$ with best-fitting $p = 2.166 \pm 0.026$ (Fong et al. 2019), where p is the index of the distribution of relativistic electrons responsible for the emission $dN_{\mathrm{e}}/d\gamma_{\mathrm{e}} \propto \gamma_{\mathrm{e}}^{-p}$, and γ_{e} is the electron Lorentz factor above some minimum Lorentz factor γ_{min}. Modeling of the multi-wavelength off-axis jet afterglow emission enabled tight constraints on some of the system and environment parameters (or their combination): for example, the jet kinetic energy to environment density ratio was constrained to $E_{\mathrm{k}}/n \approx (1-2) \times 10^{53}\,\mathrm{erg\,cm^{3}}$ (Mooley et al. 2018c; Ghirlanda et al. 2019; Hotokezaka et al. 2019) with a credible density range of $10^{-4}\,\mathrm{cm^{-3}} \leq n \leq 10^{-2}\,\mathrm{cm^{-3}}$ (Hajela et al. 2019) and the inferred ultra-relativistic jet opening angle is $\theta_{\mathrm{jet}} \approx 2-5$ degrees (Mooley et al. 2018c; Ghirlanda et al. 2019; Hotokezaka et al. 2019; Nathanail et al. 2021). A robust prediction of the off-axis afterglow model post-peak (i.e. after radiation from the core of the jet enters the observer's line of sight) is that of a universal asymptotic light-curve decay with flux $F_{\nu}(t) \propto t^{-p}$ (Sari et al. 1999). For the best-fitting jet-environment parameters of GW 170817 no broadband spectral evolution is expected, leading to $F_{\nu}(\nu, t) \propto$

$\nu^{-(p-1)/2}t^{-p}$ (we call this "universal post jet-break model"). Until ≈ 900 days post-merger, panchromatic observations of the jet afterglow of GW 170817 satisfied these expectations.

Here we present the results from our multi-wavelength campaign of GW 170817 at X-ray and radio frequencies extending to 1273 days since merger, which was designed to constrain the emergence of the kilonova afterglow. These observations provide the first statistically significant evidence for an excess of X-ray emission that is consistent with the emergence of a new X-ray component of emission that is physically distinct from the jet afterglow. This chapter is organized as follows. In §3.2, we present the detailed analysis of the recent X-ray observations taken at $\delta t = 1234$ days and a re-analysis of the observations at $\delta t \sim 939$ days and earlier. Newly acquired VLA and MeerKAT observations around $\delta t = 1234$ days are presented in §3.3. We calculate the statistical evidence for the observed excess of emission in X-rays in §3.4. We discuss the inferences of the observed excess in X-rays and a lack of detection in radio on the broadband spectrum in §3.5. We discuss the possibility of different scenarios leading to an excess in X-rays without an accompanying radio emission as the observations suggest in §3.6-§3.8. We draw our conclusions in §3.9.

3.2. X-ray Observations

We present *Chandra X-ray Observatory* (*CXO*) observations of the X-ray emission from GW 170817 acquired at $\delta t = 1209 - 1258$ days since merger (combined X-ray image in the left panel in Figure 1) and a complete and homogeneous analysis

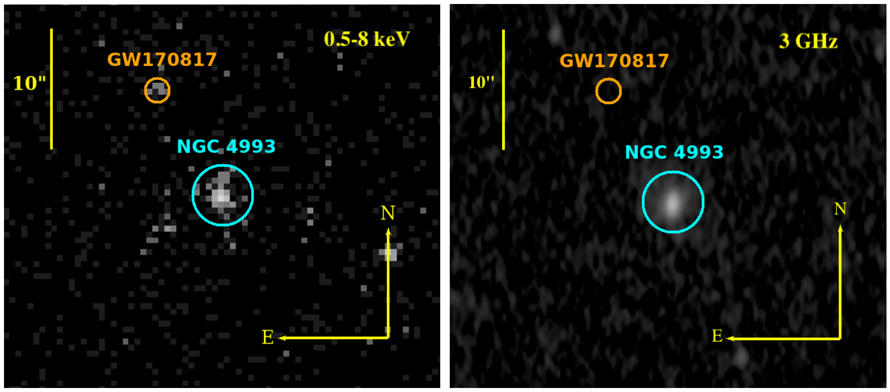

Figure 3.1 *Left Panel*: Combined X-ray image consisting of *CXO* observations spanning $\delta t = 1209 - 1258$ days in the $0.5 - 8\,\mathrm{keV}$ energy range. An X-ray source is clearly detected at the location of GW 170817 with statistical significance of $7.2\,\sigma$ (Table 3.1). *Right Panel*: Combined radio image comprising VLA 3 GHz observations acquired in the time range $\delta t = 1216 - 1265$ days. No radio emission is detected at the location of GW 170817. The RMS noise around the location of the BNS merger is $\sim 1.7\,\mu$Jy (§3.3.1). In both panels the orange and light-blue regions have a $1''$ and $2.5''$ radius, respectively, and mark the location of the BNS merger and its host galaxy.

of the entire *CXO* data set. Results from *CXO* observations of the jet afterglow of GW 170817 in the time range $\delta t = 2.33 - 939.31$ days have already been published in the literature (Haggard et al. 2017; Margutti et al. 2017; Alexander et al. 2018; Margutti et al. 2018; Nynka et al. 2018; Pooley et al. 2018; Ruan et al. 2018; Troja et al. 2018; Hajela et al. 2019; Piro et al. 2019; Troja et al. 2019; Hajela et al. 2020; Makhathini et al. 2020; Troja et al. 2020). With respect to previous data reductions: (1) when possible, we do not assume a spectral model for the X-ray count-to-flux calibration, which allows us to test for spectral evolution; (2) we align all the X-ray images to a common astrometric solution, significantly improving on the *CXO* relative astrometry; (3) for each observation we extract a spectrum and we perform a flux calibration that utilizes the complete information on the instrumental response at the time of the observation (as opposed to using averaged instrumental responses); (4) we jointly fit spectra from observations acquired close in time (i.e. around the same "epoch") as opposed to merging the files into an average spectrum; (5) we implement an accurate point-spread function (PSF) correction; (6) we calculate the model parameter uncertainties (including the unabsorbed fluxes) with MCMC simulations that self-consistently account for the low-count statistics and the deviation from Gaussian statistics. At $\delta t > 900$ days, the low number statistics of the detected X-rays does not allow us to independently constrain the spectral model and we thus offer a flux calibration that *assumes* the jet-afterglow spectral parameters.

3.2.1. CXO Source Count Rates

We observed GW 170817 with the *CXO* from December 09, 2020 at 00:05:21 UT through December 13, 2020 at 14:02:43 UT, and further between January 18, 2021 at 09:43:15 UT and January 27, 2021 at 08:49:13 UT, spanning $\delta t = 1209 - 1258$ days after the merger. The observation was taken in seven distinct exposures (Obs ID 22677, 24887, 24888, 24889, 23870, 24923, and 24924; PI Margutti; programs #21510449 and #22510329, publicly available on the *CXO* archive) for a total exposure time of 189.1 ks.

We reprocessed the entire *CXO* dataset using the `repro` task within `CIAO` (v4.13.0, Fruscione et al. 2006) with standard ACIS data filtering and using the latest calibration database (`CALDB, v4.9.4`). We used `wcs_match` and `wcs_update` to realign all the IDs to a common astrometric solution using as a reference the list of X-ray point-source positions generated with `wavdetect` run on our longest exposure observation (Obs ID 20860). In ID 20860 the X-ray emission from GW 170817 is detected with high significance at sky coordinates RA=$13^h09^m48^s.061 \pm 0.049^s$ and dec=-23°:22′:52.88″ $\pm$ 0.034″ (J2000). After having realigned the images, for each ID we extracted source count-rates and spectra using a 1″ region centered at the coordinates above. Table 3.1 lists the inferred $0.5 - 8\,\mathrm{keV}$ net count-rates and the associated targeted-detection significance. For source detection, we employed a 1″ source region and we filtered in the energy range $0.5 - 8\,\mathrm{keV}$ to minimize the background contribution. For reference, a 1″ region contains $\gtrsim 90\%$ of the PSF at 1 keV.

Focusing on the data at $\delta t > 900\,\mathrm{days}$, we find that an X-ray source is clearly detected at the location of GW 170817 at $\delta t = 939\,\mathrm{days}$ with a statistical significance of $5.4\,\sigma$ (Gaussian equivalent), corresponding to a net count-rate of $(7.53 \pm 2.93)\times10^{-5}\,\mathrm{ct\,s^{-1}}$ ($0.5 - 8\,\mathrm{keV}$). For *CXO* observations acquired at $\delta t = 1209 - 1214\,\mathrm{days}$, we infer an observed net count-rate of $(1.13 \pm 0.36)\times10^{-4}\,\mathrm{ct\,s^{-1}}$ ($6.3\,\sigma$ detection significance), whereas for the remaining observations acquired between $\delta t = 1250 - 1258\,\mathrm{days}$, the observed net count-rate is $(4.31 \pm 2.28)\times10^{-5}\,\mathrm{ct\,s^{-1}}$ and an X-ray source is detected at a significance level of $3.4\,\sigma$. Being temporally close, we combined the latter two sets of observations spanning $1205 - 1258$ days and we infer a net count-rate of $(7.68 \pm 2.12)\times10^{-5}\,\mathrm{ct\,s^{-1}}$, where an X-ray source is detected with a $7.2\,\sigma$ statistical significance.

3.2.2. CXO Spectral Analysis

For each re-aligned Obs ID we extracted a spectrum using a $1''$ circular source region centered at the location of the X-ray counterpart of GW 170817 indicated above and a source-free background region of $22''$. We used `specextract`, setting the `refcoord` parameter to the center of the source region to ensure an accurate PSF correction to the inferred fluxes. This procedure furthermore ensures that the appropriate instrumental ARF (Auxiliary Response File) and RMF (Redistribution Matrix File) response files are generated for each Obs ID. We note that not setting `refcoord` parameter explicitly leads to an overestimate of the PSF correction by an average factor of $\approx 1.2 - 1.5$ for a source region of $1''$. We fitted the data with an absorbed power-law spectral model (`tbabs*ztbabs*cflux(pow)` within *Xspec* (v12.9.1). We adopted a Galactic neutral hydrogen column density in the direction of GW 170817 of $\mathrm{NH_{gal}} = 7.84 \times 10^{20}\,\mathrm{cm}^{-2}$ (Kalberla et al. 2005a). Consistent with results from previous analysis (Margutti et al. 2017; Alexander et al. 2018; Margutti et al. 2018; Hajela et al. 2019; Makhathini et al. 2020), we did not find evidence for intrinsic absorption and we thus assumed no intrinsic absorption in the following analysis. For $\delta t < 750$ days, we jointly fitted the observations acquired around the same epoch since merger leaving the spectral photon index, Γ, and the unabsorbed $0.3 - 10$ keV flux as free parameters. We fitted the data in the $0.3 - 10$ keV energy range. We note that filtering the data in the $0.5 - 8$ keV energy range before fitting does not lead to significantly different inferences. We used Cash statistics and we employed a chain of 10^5 MCMC simulations to estimate the parameter uncertainties to account for the deviation from Gaussian statistics in the regime of low counts. The results from our X-ray spectral modeling are reported in Table 3.1. We find no evidence for X-ray spectral evolution of the source at $\delta t < 745$ days. From a joint spectral fit of all *CXO* observations at $\delta t < 745$ days with the same Γ we infer a best-fitting $\Gamma = 1.603^{+0.102}_{-0.076}$, consistent with our previous analysis of these observations in (Hajela et al. 2019) which used a previous `CALDB` v4.8.3 and a $1.5''$ source region.

We now consider the *CXO* observations acquired at $\delta t > 745$ days. These *CXO* observations were acquired in two epochs at $\delta t = 939$ and $\delta t = 1234$ days since merger. The low-count statistics of 6 and 12 photons, respectively, available for model fitting after *Xspec* filtering in the $0.3 - 10$ keV energy range leads to poorly constrained spectral photon indexes $\Gamma = 1.16^{+1.38}_{-1.39}$ and $\Gamma = 1.92^{+2.53}_{-0.65}$. We thus proceeded by freezing the spectral photon index to $\Gamma = 1.603$ (i.e. the best-fit value inferred from the joint fit of all the *CXO* data collected at $\delta t < 745$ days) for the purpose of count-to-flux calibration. The inferred unabsorbed $0.3 - 10$ keV flux is $F_{\rm x} = 1.81^{+0.79}_{-0.94} \times 10^{-15}\,\rm erg\,cm^{-2}\,s^{-1}$ at $\delta t = 939$ days, and $F_{\rm x} = 2.31^{-0.81}_{+0.57} \times 10^{-15}\,\rm erg\,cm^{-2}\,s^{-1}$ at $\delta t = 1234$ days, corresponding to luminosities of $L_{\rm x} \approx (3-5) \times 10^{38}\,\rm erg\,s^{-1}$ (Table 3.1). These recent observations when visually examined against the jet afterglow model that best-fitted the multiwavelength data at $\delta t < 745$ days (Figure 2) show slight deviations from the expectations. We quantify this deviation in Section 4.

We end by addressing the possibility of X-ray spectral evolution at $\delta t > 745$ days. We assessed the statistical evidence for X-ray spectral evolution in two ways. First, from a joint spectral modeling of all *CXO* data acquired at $\delta t > 745$ days with a power-law spectrum, we infer $\Gamma = 1.54^{+0.83}_{-0.75}$. Compared to $\Gamma = 1.603^{+0.102}_{-0.076}$ of the earlier X-ray data reported above, we find that there is no evidence for statistically significant X-ray spectral evolution from this analysis. Second, we generated 10^6 synthetic spectra of $N = 12$ photons (as observed at $\delta t = 1234$ days in the 0.3 – 10 keV energy range after *Xspec* filtering) by randomly sampling the probability density distribution associated with an incoming $\Gamma = 1.6$ spectrum with $\mathrm{NH_{gal}} = 7.84 \times 10^{20}\,\mathrm{cm}^{-2}$ convolved with the *CXO* instrumental response. We applied the non-parametric distribution-free Epps–Singleton two-sample test to each sample and the parent distribution and we found that 52% of the synthetic samples have a p-value at least as extreme as the one associated with the observed photon distribution, leading to no statistical evidence of a departure of the detected photon distribution at $\delta t > 745$ days from earlier X-ray data. We conclude that there is no statistically significant evidence for the evolution of the X-ray spectrum at $\delta t > 745$ days.

Finally, we compare the results from our X-ray analysis with previous results that appeared in the literature, and specifically with the analyses by Troja et al. 2020 (for $\delta t = 582 - 945$ days), Makhathini et al. 2020 (for $\delta t = 9 - 745$ days) and Troja et al. 2021. The analysis by (Makhathini et al. 2020) cannot be used to test for X-ray spectral evolution of the source because the final count-to-flux calibration is performed by assuming a spectral photon index. We find that the central values of the X-ray fluxes reported by (Makhathini et al. 2020) using a $1''$ source region are systematically larger than our fluxes (by a factor of up to 30%). Discrepancy remains even after adopting the same $\Gamma = 1.57$ for the count-to-flux calibration. We are able to reproduce the (Makhathini et al. 2020) X-ray fluxes by removing the `refcoord` parameter setting from `specextract`, which leads to artificially inflated PSF corrections of $\approx 20 - 50\%$, as previously noted. Our X-ray fluxes in the time range $\delta t = 582 - 945$ days are consistent with those reported by (Troja et al. 2020) within 1-σ uncertainties. We found that we could reproduce the (Troja et al. 2020) fluxes by using the online Portable Interactive Multi-Mission Simulator (PIMMS) for the count-rate to flux calibration. In contrast, our spectral analysis and count-to-flux calibration is based on ARFs and RMFs generated from each individual Obs ID to best account for the instrumental response at the time and in the conditions of the observation, as opposed to the proposal planning tool PIMMS.[1]

We finally compare our results with the recent work of (Troja et al. 2021), which appeared after our first submission to the archive, where their fiducial X-ray fluxes are calculated by adopting a photon index $\Gamma = 1.585$ derived from their modeling of the broadband radio-to-X-ray afterglow spectrum, differently from our jet afterglow *model-independent* analysis. The count-to-flux calibration by (Troja et al. 2021) is done by using the hardness ratio (HR) of observed counts in the $0.5 - 2$ keV energy range and the $2 - 7$ keV energy range to infer a spectral photon index, as opposed to the full spectral extraction and analysis that we perform here. The HR method does not account for and does not self-consistently model the uncertainty that affects the energy of each event on the detector. It is furthermore based on

[1]https://cxc.harvard.edu/ciao/why/pimms.html

averaged instrumental responses (one for each epoch), instead of using the accurate instrumental information from each obs ID, which our joint spectral analysis does. While we emphasize that there is no tension between the derived $0.3 - 10\,\mathrm{keV}$ fluxes of the two methods and the fluxes are consistent to within 1-σ uncertainties[2] (Figure B1), here we note the following: (i) as there is no evidence of the latest radio and X-ray observations at $\delta t = 1234\,\mathrm{days}$ lying on the same power-law segment of the spectrum, no such assumption is made for the flux calibration of the X-ray data. (ii) We self-consistently propagate the uncertainties during the spectral calibration. (iii) The X-ray upper limit at 2 days is computed using pure Poisson statistics and represents the 3σ deviation from the background, as we detail in (Margutti et al. 2017). The difference in the flux limit is partially a result of the different photon indexes assumed by (Troja et al. 2021) ($\Gamma = 1.585$) and (Margutti et al. 2017) ($\Gamma = 2$) for the spectral calibration of the count-rate upper limit. Unsurprisingly, models with harder assumed photon indices lead to greater $0.3 - 10\,\mathrm{keV}$ fluxes.

[2]For observations taken at $\delta t = 1234$ day, assuming $\mathrm{NH_{gal}} = 1.1 \times 10^{21}\,\mathrm{cm^{-2}}$ and $\Gamma = 1.585$, as in (Troja et al. 2021), we find an unabsorbed 0.3-10 keV flux of $1.8^{+0.4}_{-0.5} \times 10^{-15}\,\mathrm{erg\,cm^{-2}\,s}$ when using an averaged instrumental response, which is entirely consistent with $F_x = 1.6^{+0.5}_{-0.5} \times 10^{-15}\,\mathrm{erg\,cm^{-2}\,s}$ reported by (Troja et al. 2021) for the same model parameters. Instead, using the more accurate approach of jointly fitting the observations, each with its own instrumental response, and using the same parameters $\mathrm{NH_{gal}} = 1.1 \times 10^{21}\,\mathrm{cm^{-2}}$ and $\Gamma = 1.585$, we find an unabsorbed flux of $2.51^{+0.66}_{-0.92} \times 10^{-15}\,\mathrm{erg\,cm^{-2}\,s}$, which is consistent to our value. All errors are quoted at 68% confidence level.

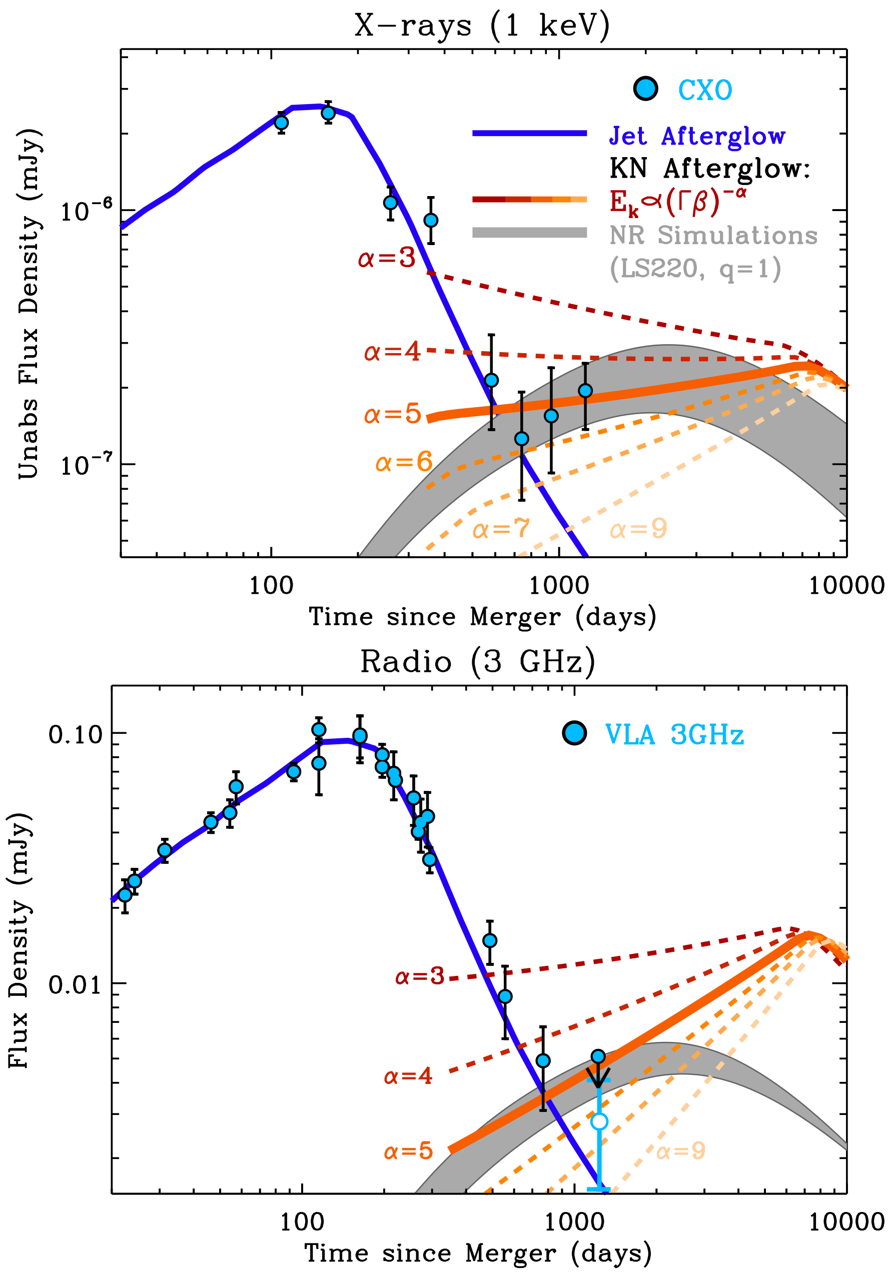
X−rays (1 keV)
CXO
Jet Afterglow
KN Afterglow:
$E_k \propto (\Gamma\beta)^{-\alpha}$
NR Simulations
(LS220, q=1)
α=3
α=4
α=5
α=6
α=7
α=9
Unabs Flux Density (mJy)
10^{-6}
10^{-7}
100
1000
10000
Time since Merger (days)
Radio (3 GHz)
VLA 3GHz
Flux Density (mJy)
0.10
0.01

Figure 3.2

Figure 3.2 X-ray (*upper panel*) and radio (3 GHz, *lower panel*) evolution of the emission from GW 170817 as detected by the *CXO* and the VLA (light-blue circles). Open circle: peak pixel flux value within one synthesized beam at the location of GW 170817 from (Balasubramanian et al. 2021). At $\delta t > 900$ days the X-ray emission shows an excess compared to the off-axis jet afterglow model (solid blue line, §3.4 and §3.6) that indicates the emergence of a new emission component. Red-to-orange dashed lines: synchrotron radiation from the kilonova afterglow calculated using semi-analytical models (Kathirgamaraju et al. 2019) where we parametrized the kilonova kinetic energy distribution as $E_{\rm k} \propto (\Gamma\beta)^{-\alpha}$ for $\beta \geq 0.35$ and we used a total kilonova kinetic energy of 10^{51} erg. These models require $p < 2.15$ to avoid violating our radio upper limit. Here we use $p = 2.05$ and we emphasize with a solid thick line the $\alpha = 5$ model. Other kilonova afterglow parameters assumed: $\epsilon_{\rm B} = 0.001$, $\epsilon_{\rm e} = 0.1$, $n = 0.001\,{\rm cm}^{-3}$. Grey shaded area: synchrotron emission calculated from kilonova kinetic ejecta profiles derived from ab-initio numerical relativity simulations using a neutron-star mass-ratio $q = 1$ and the LS220 equation of state (§3.7). These simulations emphasize the contribution from the merger's dynamical ejecta. The shaded area corresponds to values $p_{KN} = 2.05 - 2.15$, $n = 6 \times 10^{-3}\,{\rm cm}^{-3}$, $\epsilon_{\rm e} = 0.1$ and $\epsilon_{\rm B} = 0.01$.

3.3. Radio Observations

3.3.1. VLA Data Analysis

We initiated late-time S and Ku-band Karl G. Jansky Very Large Array (VLA) observations of GW 170817 as part of our joint *CXO*-VLA proposals #21510449 and #22510329 (PI Margutti). GW 170817 was observed for a total of 10.21 hours on source at S-band spread between three observations occurring on 15$^{\rm th}$ December 2020 (δt = 1216.08), 27$^{\rm th}$ December 2020 (δt = 1228.02) and 2$^{\rm nd}$ February 2021 (δt = 1264.95). All three observations were conducted while the VLA was in A-configuration and at a central frequency of 3 GHz using a 2 GHz bandwidth. Additionally, we conducted a single observation at Ku-band on 10$^{\rm th}$ February 2021

(δt=1272.88) for a total of 2.74 hours on source. The observation was conducted with the VLA in A-configuration and at a central frequency of 15 GHz using a 6 GHz bandwidth. These data are publicly available on the VLA archive under project IDs SL0449 and SM0329. Details of each observation are given in Table 3.2.

Each individual observation was independently calibrated using the VLA calibration pipeline version 2020.1.0.36 as part of CASA (v6.1.2.7, McMullin et al. 2007a), with 3C286 used as the flux density and bandpass calibrator and J1258-2219 used to calibrate the time-varying complex gains. We then manually inspected and validated the output and re-ran the pipeline after flagging additional radio frequency interference (RFI). Additional RFI flagging was performed on the results of the second pipeline run. In order to achieve maximum sensitivity we combined the three epochs of S-band data into a single measurement set (right panel in Figure 1) using the CASA task CONCAT. We imaged the concatenated data using `wsclean` (Offringa et al. 2014; Offringa et al. 2017), creating a 16384$\times$16384 pixel image with a single pixel corresponding to 0.08$''$. The synthesised beam is 1.19$'' \times$ 0.66$''$ with a position angle of -5.57 degrees. In order to account for spectral variation introduced for sources far from the phase center (we are imaging well beyond the half power point of the primary beam in order to ensure complete deconvolution, and to produce an accurate sky model for self-calibration) we fit a third order polynomial (`fit-spectral-pol 4`) over eight output channels (`channels-out 64`). No time or frequency averaging was performed when imaging in order to avoid bandwidth or temporal smearing of sources far from the phase center ensuring the best possible deconvolution. We performed one round of phase-only self-calibration using a sky-model produced from our phase reference calibrated data.

We do not detect any significant emission at the position of GW 170817. The root-mean-square (RMS) noise at the edge of the image in a region free of sources is $\sim 1.2\,\mu$Jy while in a circular region with 25 pixel radius centered on the position of GW 170817 we measure an RMS noise of $\sim 1.7\,\mu$Jy.

The single Ku-band epoch was calibrated using the VLA calibration pipeline version 2020.1.0.36 as part of CASA version 6.1.2.7 and validated by NRAO as part of the Science Ready Data Products project. We imaged the calibrated measure set using the CASA task `tclean` with a user defined mask. We created a 2048×2048 pixel image with a cell size of $0.02''$. We do not detect any significant emission at the location of GW 170817 and measure an RMS noise of $1.7\,\mu$Jy in a 30×30 pixel region centred on the position of GW 170817.

3.3.2. MeerKAT Data Analysis

We conducted a single observation of the field of GW 170817 with the MeerKAT radio interferometer on the 3$^{\rm rd}$ January 2021 as part of a DDT request (DDT-20201218-JB-01). These data are available publicly on the SARAO archive. Data were recorded for a total of 7.56 hours (resulting in 7.24 hours on source) with an 8 s dump time at the UHF band between 544 MHz and 1088 MHz with a central frequency of 816 MHz using 4096 frequency channels. Details of the observation are given in Table 3.2.

Data reduction was performed using OXKAT (Heywood 2020), a suite of semi-automated scripts to reduce MeerKAT UHF and L-band data. First, phase reference calibration (1GC) is carried out using CASA, with flagging performed with Tricolour (a variant of the SARAO Science Data Processing flagging software). B0407−65 was observed to calibrate the flux and bandpass of the instrument and 3C283 was used to calibrate the time variable complex gains. Second, we used WSCLEAN to image the field and the resulting sky model was used to perform phase and delay self-calibration (2GC) using CUBICAL (Kenyon et al. 2018). Images created throughout this process are 10240×10240 pixels with a robust weighting of -0.5 and pixel size of $1.7''$. The phase calibrator, 3C283, is a bright off-axis source when observing GW 170817 with MeerKAT at the UHF band and leaves strong imaging artefacts after 2GC calibration. Strong sources away from the phase center of an interferometer have their apparent spectral shape modified by the time and frequency dependent primary beam, and for a sufficiently wide field of view one set of gain solutions (direction-dependent) is not appropriate to properly calibrate the data. These issues result in a corrupted point spread function that will not vanish under deconvolution. The primary beam can be corrected for either by providing a model of the primary beam for the array, or by using higher order polynomials when fitting the spectral variation when cleaning (OXKAT employs the latter). To correct for direction-dependent gains across the wide MeerKAT field of view ($\sim 2\,\mathrm{deg}^2$ at UHF) we 'peel' the source 3C283, and performed faceted direction dependent self-calibration on the residual data. The peeling stage was performed using CUBICAL, and the facet based direction dependent calibration was carried out using KILLMS with DDFACET (Tasse et al. 2018) used to image the corrected data. To enhance the resolution we image the final data-set with a Briggs robustness parameter -1.

The RMS noise at the edge of the image in a region free of sources is $8.5\,\mu$Jy. Due to the extremely high source brightness sensitivity of MeerKAT the region around the phase center has a very high density of sources, making it difficult to estimate the phase center noise. We opt to fit the entire image for significant emission using PyBDSF (Mohan et al. 2015) using island and pixel thresholds of 3σ and 5σ, respectively, with adaptive RMS thresholding turned on. We identify extended (resolved) emission from the host galaxy of GW 170817 (NGC 4993) and emission from a source. We identify no significant emission at the position of GW 170817. Using a 40×40 pixel region centered on the position of GW 170817 we measure an RMS noise of $\sim 13\,\mu$Jy.

3.4. Statistical Evidence for an X-ray Excess of Emission

In this section, we calculate the significance of a deviation, *if any*, of the latest X-ray observations from jet afterglow models. We perform our statistical analysis in the count phase-space to fully account for the Poissonian nature of the process. Our results and conclusions do not depend on the specific flux calibration of the latest epochs of data at > 900 days that we present in Table 3.1 with the purpose of offering to the reader a flux scale, and we explain the reasons as follows. Our goal is to test for the presence of a departure from the expectations of jet afterglow models, which have

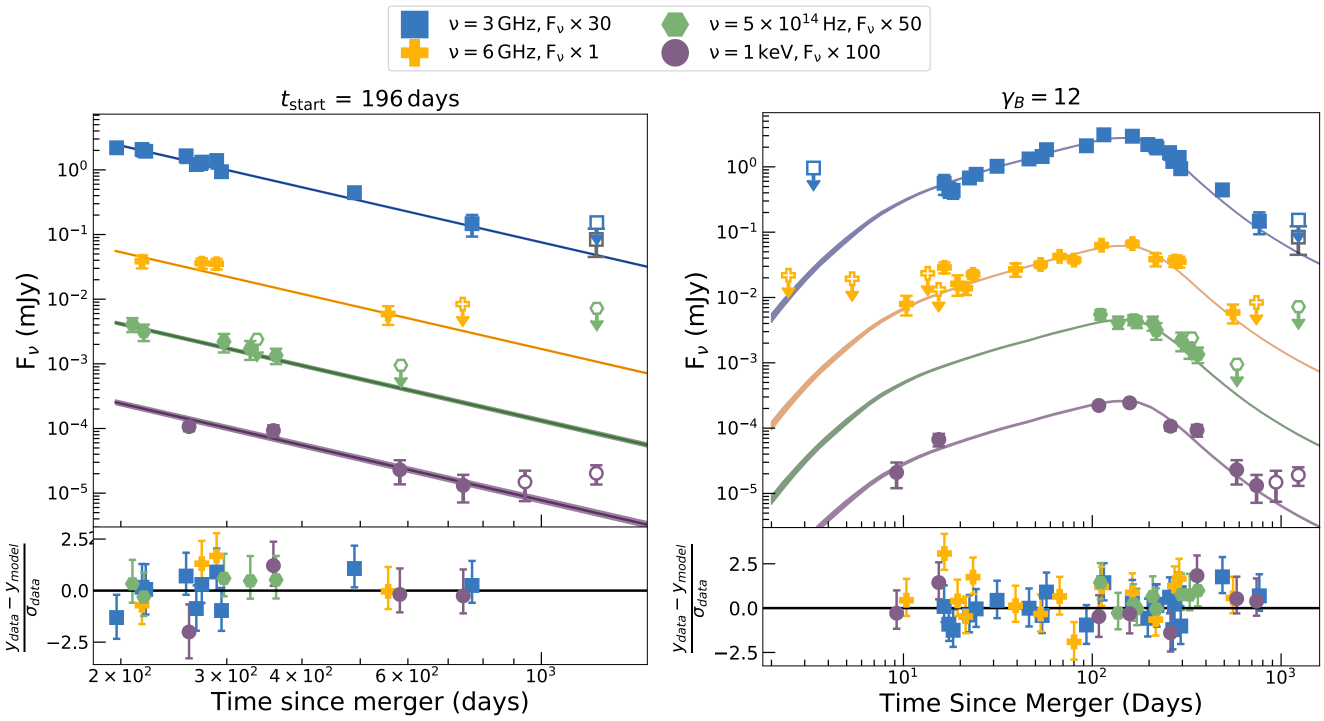

Figure 3.3 *Left Panel:* Non-thermal emission from GW 170817 across the electromagnetic spectrum and best fitting universal post jet-break model, as explained in §3.4, with $t_{\rm start} = 196$ days. *Right Panel:* Non-thermal emission from GW 170817 and best fitting jet-afterglow model computed with `JetFit` for $n = 0.01\,{\rm cm}^{-3}$, $\epsilon_{\rm e} = 0.1$, and $\gamma_{\rm B} = 12$ fixed. In both panels empty symbols were not included in the fitting procedure but are shown here for completeness adopting a flux calibration consistent with the afterglow models. Colored bands identify the 68% flux confidence interval. The grey empty square symbol is the peak pixel value within one synthesized beam at the location of GW 170817 at 3 GHz from (Balasubramanian et al. 2021). The bottom subplots show the the difference between observations and the best-fitting models as derived from the model posteriors, and expressed in units of 1σ data uncertainties for displaying purposes.

solid predictions both in terms of temporal behavior and in terms of spectral behavior of the data at $\delta t > 900$ days. Jet models can be violated spectrally, temporally, or both spectrally and temporally. The X-ray data at $\delta t > 900$ days provide no useful

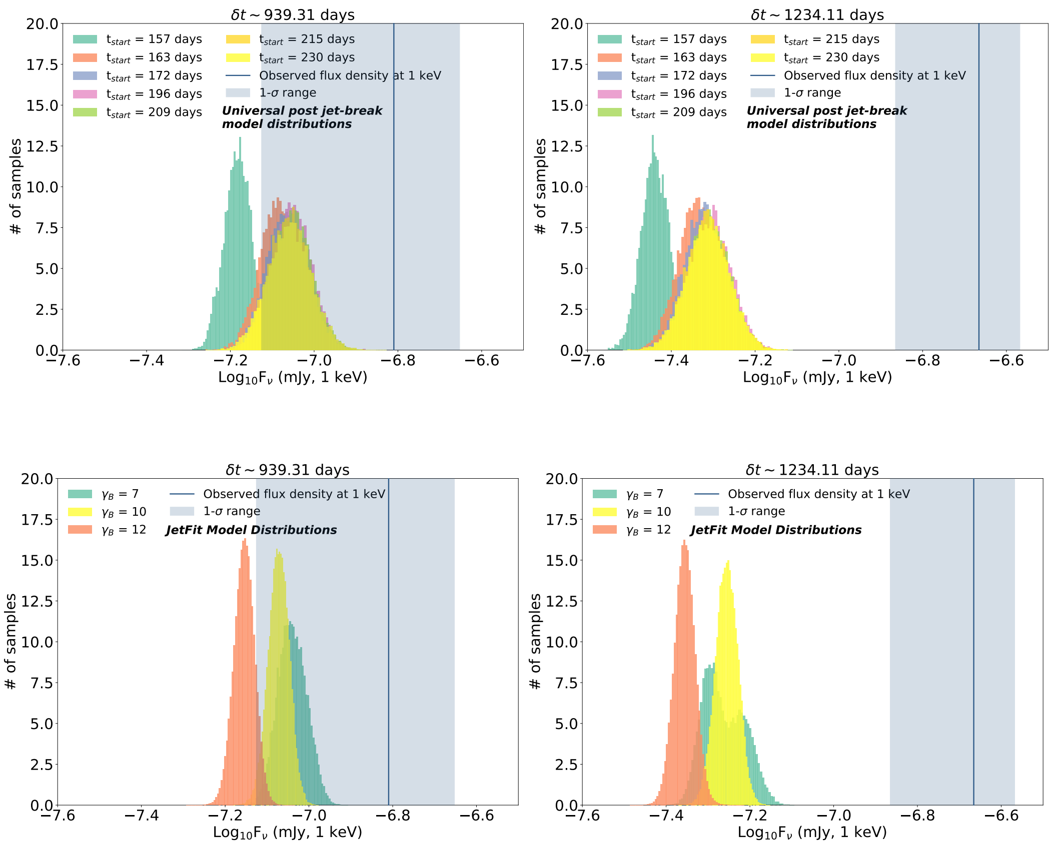

Figure 3.4 *Top Panel:* Universal post jet-break model distributions. Expected 1-keV flux density distributions at 939.31 and 1234.11 days (histograms in color) derived from fitting the post-peak multi-wavelength afterglow of GW170817 in the post jet-break regime with $F_\nu \propto \nu^{-\beta} t^{-\alpha}$ (where $\beta = (p-1)/2$ and $\alpha = p$) in the time range $t_{\rm start} < \delta t < 900$ days for a variety of choices of $t_{\rm start}$. *Bottom Panel:* `JetFit` model distributions. Expected 1-keV flux density distributions at 939.31 and 1234.11 days (histograms in color) derived from the fitting of the multi-wavelength afterglow of GW170817 in the time range $2 < \delta t < 900$ days using the code `JetFit` (using different values of $\gamma_{\rm B}$). *Both Panels:* Vertical blue thick line and shaded area: observed X-ray flux density at the corresponding epoch and $\pm 1\sigma$ confidence range, for which the flux calibration was performed by conservatively assuming a jet-afterglow spectrum (§3.2.2- §3.4).

spectral constraint (§3.2.2). At this point we face two options: (i) we can perform a flux calibration of the X-ray count-rates at $\delta t > 900$ days assuming a spectral model that is *not* consistent with jet afterglows. This clearly violates jet afterglow models and implies that these models can be rejected at late times, and that the late-time X-rays come from a different source of emission; or (ii) we conservatively assume that the late-time X-rays have a spectrum that is consistent with jet afterglow models and we use the range of spectral models that are statistically allowed by jet afterglows to convert the predicted fluxes into observed count-rates on the CXO detector. We adopt approach (ii). This approach is conservative, in the sense that we are *assuming* that the late-time X-ray spectrum is exactly as expected based on jet afterglow models, while in fact this might not be true. With this assumption, we then address the question: what is the probability of detecting a number of X-ray photons at least as large as the one observed at $\delta t > 900$ days as a result of a statistical fluctuation of the model and background?

In the following we first adopt a jet-structure model agnostic approach, and use the universal post jet-break model to assess the potential deviation of the late-time X-ray data (§3.4.1). Second, we use the off-axis structured jet afterglow models as computed by `JetFit` (§3.4.2). Finally, we address in detail potential sources of systematic uncertainties and the performance of other numerical afterglow models. For the remainder of this section we note that including or not including in the initial jet afterglow fitting procedure the X-ray data at $\delta t > 900$ days leads to differences that are smaller than the quoted level of precision of the statistical significances of the departure of the data from the models. This is a direct consequence of the limited number of X-ray photons at $\delta t > 900$ days, which leaves the X-ray flux fundamentally unconstrained (§3.2.2). We elected to fit the data at $\delta t < 900$ days, which has the advantage of preserving the statistical independence of the data acquired at $\delta t > 900$ days from the models we are testing. We end by noting that from a statistical perspective we are not comparing two sets of models. Instead, we are assessing the potential departure of a sub-sample of data from models of jet afterglow emission.

3.4.1. Jet afterglows from the universal post jet-break model

We first assessed the statistical evidence of an excess of X-ray emission with respect to the off-axis jet afterglow model by fitting the post-peak multi-wavelength afterglow decay with the following model $F_\nu \propto \nu^{-\beta} t^{-\alpha}$. The X-ray to radio emission of GW 170817 is powered by synchrotron radiation in the optically thin regime (Margutti et al. 2018; Fong et al. 2019) for which $\beta = (p-1)/2$. Standard closure relations (e.g., Lamb et al. 2018) in the post jet break phase, which apply to the post-peak afterglow evolution, imply $\alpha = p$ (Sari et al. 1999). Our "universal post jet-break model" is thus: $F_\nu \propto \nu^{-(p-1)/2} t^{-p}$. The multi-wavelength jet afterglow of GW 170817 peaked at $t_{\rm pk} \approx 160$ days (Alexander et al. 2017; Dobie et al. 2018; Mooley et al. 2018b).

We fitted the multi-wavelength post-peak jet afterglow evolution with the model above in the time range $t_{\rm start} < \delta t < 900$ days for several choices of start time $t_{\rm start} = 157, 163, 172, 196, 209, 215, 230$ days. We selected a range of $t_{\rm start}$ times starting from

t_{pk} to account for the unknown onset time of the asymptotic post-peak post jet-break power-law decay. We used VLA observations at 3 and 6 GHz compiled from (Alexander et al. 2017; Hallinan et al. 2017; Alexander et al. 2018; Dobie et al. 2018; Margutti et al. 2018; Mooley et al. 2018a; Mooley et al. 2018c; Hajela et al. 2019); *Hubble Space Telescope* (*HST*) observations at optical wavelengths from (Fong et al. 2019); and *CXO* observations at 1 keV from this work. As an example, we show the plot of the best-fitting model, and the corresponding 68% confidence interval, obtained assuming $t_{\rm start} = 196\,$days in Figure 3.3. We assess the statistical significance of the departure of the late-time X-ray data for each choice of $t_{\rm start}$.

We employed MCMC sampling with a Python module, `emcee` (Foreman-Mackey et al. 2013). For each choice of $t_{\rm start}$ we sampled 10^5 times the expected X-ray flux density distribution at 1 keV ($F_{1\,\rm keV}$) at the times of the last two *CXO* epochs at $t_1 = 939.31$ days and $t_2 = 1234.11\,$days (Table3.1, top panel in Figure 3.4). For each MCMC sample we converted the predicted 1-keV flux densities ($F_{1\,\rm keV,1} \equiv F_{1\,\rm keV}(t_1)$ and $F_{1\,\rm keV,2} \equiv F_{1\,\rm keV}(t_2)$) into observed $0.5-8\,$keV total (i.e. source plus background) counts in a $1''$ region (c_1 and c_2) using the respective exposure times, the count-to-flux conversion factors derived from *Xspec* and the observed background. We computed for each MCMC sample i the probabilities $P_{\rm i,1} \equiv {\rm Pois(c \geq N_{obs,1}|c_1)}$ and $P_{\rm i,2} \equiv {\rm Pois(c \geq N_{obs,2}|c_2)}$, which represent the probability of each sample to produce a number of X-ray photons larger or equal to those observed at t_1 and t_2 after *Xspec* filtering in the $0.5-8$ keV energy band ($N_{\rm obs,1} = 6$ and $N_{\rm obs,2} = 12$, as noted in §3.2.2) as a result of a Poissonian fluctuation. For each model defined by the choice of t_{start}, the total probability to lead to a deviation at least as prominent as the one observed at t_1 and t_2 is the re-normalized sum of the sample probabilities: $P_1 = \frac{1}{N_{\rm sample}} \sum_i P_{\rm i,1}$ and $P_2 = \frac{1}{N_{\rm sample}} \sum_i P_{\rm i,2}$. We find that the resulting P_1 and P_2 vary in the range $P_1 = 0.060 - 0.139$ and $P_2 = 2.61 \times 10^{-4} - 1.53 \times 10^{-3}$ depending on the choice of $t_{\rm start}$. The observed X-rays at 1234 days thus correspond to a $3.2\,\sigma - 3.7\,\sigma$ (Gaussian equivalent, 99.8626% - 99.9784%)[3] deviation from the off-axis jet model. $P_1 \times P_2$ thus lies in the range $P_1 \times P_2 = 1.73 \times 10^{-5} - 2.50 \times 10^{-4}$, where the range of probabilities reported reflect the assumed $t_{\rm start}$ (Table 3.3). Finally, the combined probability to obtain deviations from the universal post-jet break off-axis model at 939.31 days and 1234.11 days can be conservatively estimated as $P_{\rm combined} \equiv \frac{1}{N_{\rm sample}} \sum_i {\rm Pois}({\rm c} \geq ({\rm N_{obs,2}} + {\rm N_{obs,1}}) | ({\rm c_{1,i}} + {\rm c_{2,i}}))$. We find $P_{\rm combined} = 9.51 \times 10^{-5} - 1.37 \times 10^{-3}$ (3.2-3.9σ, Gaussian equivalent, depending on the choice of $t_{\rm start}$). We conclude that the observed X-rays at $\delta t > 900$ days represent a statistical deviation from the expectations of the universal post jet-break models that best fit earlier observations of GW 170817 with statistical significance $\geq 3.2\sigma$. The chance probabilities as a function of $t_{\rm start}$ are reported in Table 3.3.

3.4.2. Jet afterglows computed with `JetFit`

We further performed a similar statistical study to test the excess of X-ray emission with respect to the off-axis structured jet light-curves modeled with `JetFit` (Duffell et al. 2013; Ryan et al. 2015; Wu et al. 2018). `JetFit` fits the afterglow light

[3]Probabilities in the form of % added as per referee#2 request.

curves for arbitrary viewing angles using a 'boosted-fireball' structured jet model to compute the jet dynamics as it spreads. It naturally accommodates a diverse range of outflows from mildly-relativistic quasi-spherical outflows to ultra-relativistic highly collimated jets. `JetFit` uses the python package `emcee` to explore the full parameter space formed by eight parameters: the explosion energy, E_0; the ambient density, n; the asymptotic Lorentz factor, η_0; the boost Lorentz factor, $\gamma_{\rm B}$; the spectral index of the electron distribution, p; the electron energy fraction, $\epsilon_{\rm e}$; the magnetic energy fraction, $\epsilon_{\rm B}$; and viewing angle $\theta_{\rm obs}$; and finds the best-fitting values and their posterior distributions. Because the broadband SED (spectral energy distribution) of GW 170817, from $\delta t = 2 - 745$ days, is best explained by a simple power-law, some of these parameters are highly degenerate and the problem is under-constrained. Hence, we fixed $\epsilon_{\rm e} = 0.1$, as predicted from the simulations of particle acceleration by relativistic shocks (Sironi et al. 2013b), $n = 0.01\,{\rm cm}^{-3}$, the upper-limit on the ambient density inferred from the study of the host X-ray thermal emission (Hajela et al. 2019), and we computed the best-fitting models assuming three values of $\gamma_{\rm B} = 7, 10$, and 12. We selected these $\gamma_{\rm B}$ values based on the VLBI measurements of the angular displacement of the radio emission with time, which constrained the jet Lorentz factor $\Gamma \approx 4$ at the time of the afterglow peak (or $\theta_{\rm obs} - \theta_{\rm j} \approx 1/\Gamma \approx 1/4$, Mooley et al. 2018c).[4] We use `JetFit` to fit the multi-wavelength afterglow light-curves at 3 GHz, 6 GHz, optical and at 1 keV frequencies acquired at $2 < \delta t < 900$ days. The jet opening angle $\theta_{\rm j}$ of GW 170817 has been estimated to be of the order

[4] `JetFit` can reliably predict the afterglow from boosted fireballs with $\gamma_{\rm B} \leq 12$, which translates into $\theta_{\rm j} \approx 1/\gamma_{\rm B} \geq 4.8°$

of a few degrees (Mooley et al. 2018c; Ghirlanda et al. 2019; Nathanail et al. 2021), and we thus consider the $\gamma_{\rm B} = 12$ boosted fireball model as our fiducial case. The best-fitting light curves for the $\gamma_{\rm B} = 12$ are shown in Figure 3.3, while the one- and two-dimensional projections of the posterior distribution of the free parameters for $\gamma_{\rm B} = 12$ are provided in Appendix C, Figure C1.

We use the full posterior distribution of all the free parameters to compute the distribution of flux density at 1 keV at t_1 and t_2 for each choice of $\gamma_{\rm B}$. Similar to the above statistical analysis, we convert these flux densities to the total counts in the 0.5 – 8 keV energy range in a $1''$ region, calculate the probability of each sample, i, $P_{\rm i,j} = {\rm Pois}({\rm c} \geq {\rm N}_{\rm obs,j}|{\rm c}_{\rm j})$, where ${\rm j} \in 1, 2$ for the two epochs respectively, and finally compute the cumulative probabilities, $P_{\rm j}$, to lead to a deviation at least as prominent as the one observed at $t_{\rm j}$ (bottom panel, Figure 3.4). For different values of $\gamma_{\rm B}$, we find $P_{\rm j}$ in the range $P_1 = 0.07 - 0.15$ and $P_2 = 7.36 \times 10^{-4} - 2.82 \times 10^{-3}$, corresponding to a $2.9\,\sigma - 3.4\,\sigma$ (Gaussian equivalent, 99.6268% - 99.9326%) deviation of the observed X-rays at 1234 days from the light-curve modeled by the off-axis structured jet model. We further find $P_1 \times P_2 = 5.59 \times 10^{-5} - 4.69 \times 10^{-4}$ ($3.5\,\sigma - 4.0\,\sigma$ Gaussian equivalent, 99.9535% - 99.9937%), and $P_{\rm combined} = 2.62 \times 10^{-4} - 2.10 \times 10^{-3}$ ($3.1\,\sigma - 3.7\,\sigma$, where the range reflects the assumed values of $\gamma_{\rm B}$ used) to obtain deviations from the off-axis structured jet model at least as prominent as those observed at both epochs t_1 and t_2. Larger $\gamma_{\rm B}$ values imply a higher level of collimation of the jet, and hence a faster post-peak transition to the asymptotic power-law decay, which explains the highest significance of the excess associated to the $\gamma_{\rm B} = 12$ model (bottom panel,

Figure 3.4). Since for GW 170817 $\theta_j \leq 5°$ (e.g., (Mooley et al. 2018c; Ghirlanda et al. 2019)) and our most collimated model has $\gamma_{\rm B} = 12$ (i.e. $\theta_j \approx 5°$), in this sense the probabilities derived with this approach are conservative. For the same reason, $\gamma_{\rm B} = 12$ is our baseline model and for this set of models the probabilities associated with $\gamma_{\rm B} = 12$ should be considered the most realistic estimates (i.e. P of chance deviation corresponding to 3.7σ). The chance probabilities as a function of $\gamma_{\rm B}$ are reported in Table 3.3.

From Figure, right panel, 3.4, the $\gamma_{\rm B} = 12$ best fitting model lies slightly above the central value of the data points at $\delta t > 300$ days, but it is well within the 1σ error bars of the data at $\delta t > 600$ days and always within the 2σ range. For this model the $\chi^2/dof = 1.03$. We further tested the departure from a random distribution of the signs of the residuals implementing a Runs test for randomness. Our data set contains 54 data points and the number of runs is 24. The chance probability of obtaining the observed distribution of runs is 26%. It follows that the hypothesis of random distribution of the model's residuals cannot be rejected.

3.4.3. General Considerations

Both statistical approaches detailed above (i.e. the jet afterglow light-curve models and the universal post jet-break power-law decay) independently lead to the conclusion of the presence of an X-ray excess of emission at $\delta t > 900$ days with statistical confidence $\geq 3.1\,\sigma$. Observations acquired around 940 days alone do not provide any statistically significant evidence of a deviation from the expectations of an off-axis jet model as we reported in Hajela et al. 2020 (see also Troja et al. 2020). The statistical significance of the excess of X-ray emission is driven by our most recent epoch of *CXO* data at 1234 days. We also note that we do *not* claim a re-brightening of the X-ray flux, but a statistically significant deviation from the existing models that best fit the afterglow at < 900 days, which points to the emergence of a new X-ray component. Our approach is agnostic with regard to the spectral and temporal properties of any additional emission component. The statistical tests that we carried out have been explicitly designed to avoid any dependency on any assumed property of the additional component and instead test for a deviation compared to expectations from the jet afterglow emission.

We note that systematic uncertainties on the relative flux calibration of *Chandra*/ACIS-S between observations acquired at $\delta t < 900$ days and $\delta t >$900 days have minimal impact on our conclusions. We use the `JetFit` models with $\gamma_B = 12$ here as an example to quantify this effect. Specifically, adopting a systematic RMS flux variation of $< 3.4\%$ (Chandra calibration team, private communication) on *Chandra*/ACIS-S fluxes, and assuming that fluxes at $\delta t > 900$ days have been systematically overestimated by that RMS factor, we find evidence for a $3.97\,\sigma$ (Gaussian equivalent) deviation of the X-rays emission at $\delta t > 900$ days from the best fitting model. Similar results hold for the universal post-jet break afterglow models. Finally, we note that correcting or not correcting for PSF-losses the count-rates at $\delta t > 900$ days induces changes in the stated statistical significances of the excess of $\lesssim 0.1\,\sigma$

(Gaussian equivalent), demonstrating that the choice of the aperture size of $1''$ does not drive our conclusions.

We end by addressing the difference between our conclusions and the claim of a statistical significance of the X-ray excess of $\lesssim 3\,\sigma$ that appeared in (Troja et al. 2021). The main source of difference between our analysis and the one presented in (Troja et al. 2021), which drives the different conclusions about the statistical evidence for an X-ray excess, is related to the statistical treatment of the data, to the Poisson nature of the X-ray signal at $t > 900$ days, and to the specific jet model chosen as a reference. Specifically, the use of a jet model presented in their work that is *not* in tension with the VLBI measurements would have led to the inference of a significantly larger discrepancy between X-ray observations at $\delta t > 900$ days and expectations as we demonstrate in Figure B1 in Appendix B. The X-ray flux calibration plays a negligible statistical role, as we show in Figure B1 and Appendix B. Our statistical tests self-consistently account for the Poisson nature of the process, using jet models that are *not* in violation of the VLBI constraints. To the extent of the authors' knowledge, there is no jet model that does not violate the VLBI constraints and can naturally reproduce the late time X-rays of GW 170817.

3.5. Inferences on the Broadband Spectrum at 1234 days

The broadband X-ray-to-radio non-thermal emission from the jet afterglow of GW 170817 at $\delta t < 900$ days is well fitted by a simple power-law spectral model $F_\nu \propto \nu^{-\beta}$ with $\beta = 0.583 \pm 0.013$ (Fong et al. 2019), or equivalently, $F_\nu \propto \nu^{-(p-1)/2}$

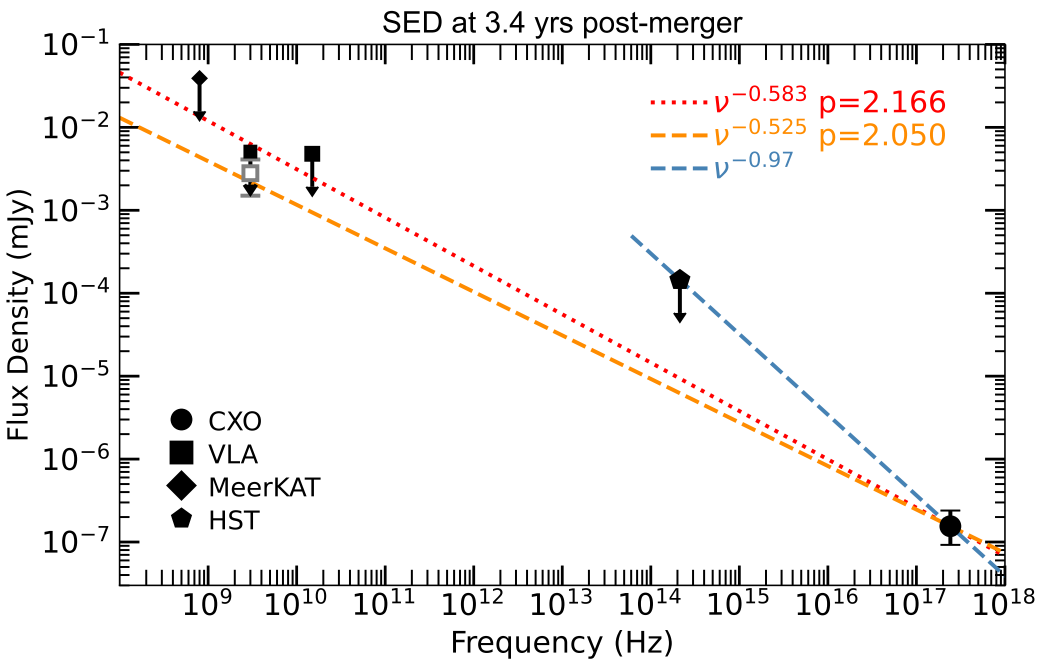

Figure 3.5 Broad-band spectral energy distribution acquired around $\delta t \approx$3.4 years post-merger, including CXO X-ray data (filled circle), VLA upper limits at 3 and 15 GHz (filled squares), MeerKAT flux limit (filled diamond) and *HST*/F140W flux limit (filled hexagon). Grey open square: 3 GHz peak flux pixel value of 2.8 μJy (with RMS of 1.3 μJy) within one synthesized beam at the location of GW 170817 from (Balasubramanian et al. 2021). Red dotted line: $F_\nu \propto \nu^{-(p-1)/2}$ spectrum with $p = 2.166$ that best fitted the jet-afterglow data (Fong et al. 2019). The VLA 3 GHz limit suggests a shallower spectrum (§3.5). Orange dashed line: $F_\nu \propto \nu^{-(p-1)/2}$ with $p = 2.05$. *HST* observations imply a NIR-to-X-ray spectral slope steeper than ≈ 1.

with $p = 2.166 \pm 0.026$ in the optically thin synchrotron regime. In this section we compute the constraints on the spectral slope at $=$ 1234 days that are imposed by the X-ray detection (§3.2) and the 3 GHz radio limits (§3.3.1) under the assumption that the broadband spectrum is still described by a simple power-law model. Radio limits at 15 GHz and 0.8 GHz (§3.3.1-3.3.2), and *HST* observations (Kilpatrick et al. 2021) do not provide additional constraints on the simple power-law model (Figure

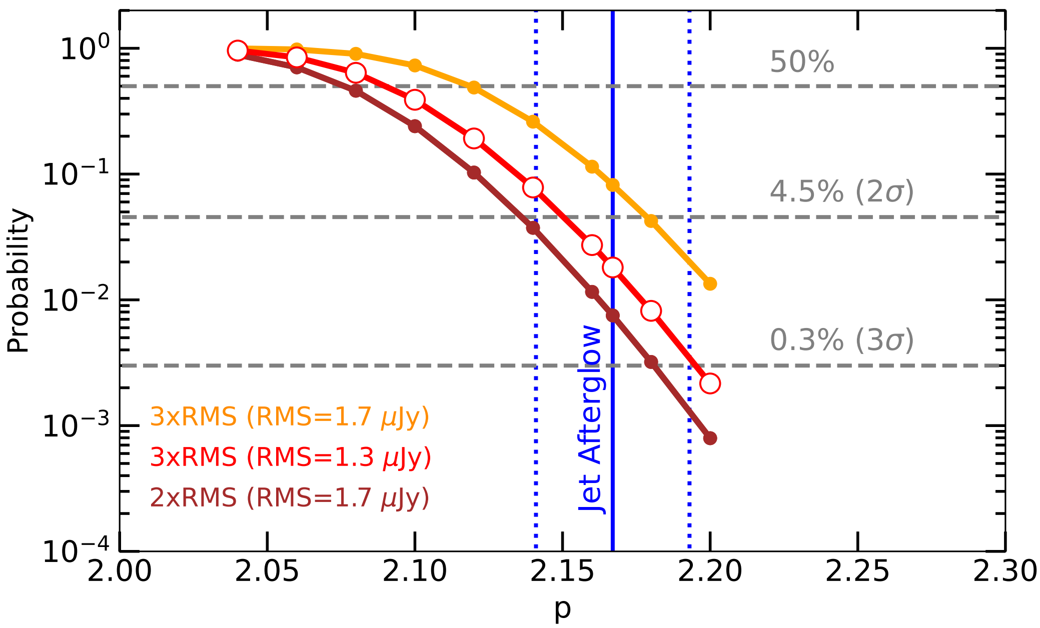

Figure 3.6 Probability of simple power-law $F_\nu = \text{Norm} \times \nu^{-(\text{p}-1)/2}$ spectral models at 1234 days that do not violate the 3×RMS (orange), and 2×RMS (brown) flux density of our 3 GHz image at the location of GW 170817 as a function of p, where RMS=1.7 μJy inferred from this work. Red line and open symbols: results for RMS=1.3 μJy inferred by (Balasubramanian et al. 2021), Norm is drawn from the posterior probability distribution of the 0.3 – 10 keV unabsorbed X-ray flux at 1234 days as derived from MCMC sampling within *Xspec*. Horizontal grey dashed lines mark the 0.3%, 4.5% and 50% probability levels. Vertical blue thick and dotted lines: best fitting p parameter and 1 σ range for the jet afterglow as derived from broad-band SED fitting of the non-thermal emission of GW 170817 at $\delta t < 900$ days (Fong et al. 2019). This analysis suggests a hardening of the non-thermal spectrum of GW 170817 at 1234 days to values of $p <$ than the best-fitting value from the earlier jet afterglow at statistical confidence $\geq 92\% - 99.2\%$.

3.5). We used MCMC sampling within *Xspec* as described in §3.2.2 and we sampled 10^6 times the posterior probability distribution of the unabsorbed 0.3 – 10 keV flux derived from fitting the *CXO* data at 1234 days employing Cash-statistics. This method accounts for deviations from Gaussian statistics that manifest in the regime of low spectral counts. We then computed as a function of p the probability associated with spectral models $F_\nu \propto \nu^{-(p-1)/2}$ that would not lead to a radio detection, here defined as a 3 GHz radio flux density above 3×, or alternatively 2×, the flux density root mean square – RMS – of our image around the location of GW 170817, where RMS $= 1.7\,\mu Jy$.

Our results are shown in Figure 3.6. We find that values of $p > 2.166$, i.e. larger than the best fitting value of the jet-afterglow at $\delta t < 900$ days are ruled out with statistical confidence $\geq 92\% - 99.2\%$. These results suggest the evolution of the broadband spectrum towards lower values of p and constitute the first indication of spectral evolution of the non-thermal emission from GW 170817. This conclusion is strengthened by using the RMS $= 1.3\,\mu$Jy at 3 GHz from (Balasubramanian et al. 2021). We end by noting that *HST* observations acquired on $\delta t =$1236.5 days since merger at $\nu = 2.13 \times 10^{14}$ Hz (Kilpatrick et al. 2021) imply an optical to X-ray spectral index $\beta_{\rm OX} \lesssim 0.97$ (where $F_\nu \propto \nu^{-\beta_{\rm OX}}$). Finally, our VLA observations at 15 GHz reach a similar depth as our 3 GHz observations and rule out an optically thick $F_\nu \propto \nu^2$ radio source with flux density $F_\nu \geq 0.06\,\mu$Jy at $\nu = 3$ GHz.

3.6. Late time evolution of the emission from off-axis jet afterglows

In the context of synchrotron emission from an ultra-relativistic off-axis jet, a post-peak late-time flattening of the light-curve can be the result of: (i) the jet encounter with an over-density in the environment; (ii) energy injection; (iii) time-varying shock microphysical parameters $\epsilon_{\rm B}$ and $\epsilon_{\rm e}$; (iv) transition into the sub-relativistic phase; and (v) emergence of the counter-jet emission (Nakar et al. 2011; Granot et al. 2018).

The universal post jet-break light-curve evolution for an observed frequency ν above the synchrotron self-absorption frequency $\nu_{\rm sa}$ and for $\nu_m < \nu < \nu_c$ (where $\nu_{\rm m}$ is the synchrotron frequency and ν_c is the cooling frequency) is (Granot et al. 2018):

$$F_\nu(\nu, t) \propto \epsilon_{\rm e}^{p-1} \epsilon_{\rm B}^{\frac{p+1}{4}} n^{\frac{3-p}{12}} E_k^{\frac{p+3}{3}} t^{-p} \nu^{\frac{1-p}{2}} \tag{3.1}$$

where E_k is the jet energy and n is the circum-burst density. The observed X-ray emission at 1234 days is a factor ≈ 4 above the extrapolation of the off-axis jet afterglow models (Figure 3.2). Explaining this excess of emission as a result of an over-density in the environment would require an exceedingly steep density gradient with n increasing by a factor of $(4)^{\frac{12}{3-p}} \approx 3 \times 10^8$ (Eq. 3.1) over $\Delta r/r \approx 1$ at $r \approx 1$ pc. The characteristic size of the bow-shock cavity inflated by a pulsar wind (*if* any of the NS progenitors of GW 170817 was a pulsar) scales as $R_s \propto n_{\rm ext}^{-1/2}$, where $n_{\rm ext}$ external medium density probed by the wind (Ramirez-Ruiz et al. 2019).

Following Ramirez-Ruiz et al. 2019, their equation 4, R_s is expected to be a factor $\gtrsim 3-8$ smaller than the the shock radius at this time if the density probed by the jet $n = 10^{-4} - 10^{-2}\,\mathrm{cm}^{-3}$ is representative of the density in the evacuated region (as it is reasonable to expect $n_{\mathrm{ext}} > n$). Additionally, for a density contrast $\approx 10^8$ the implied amount of mass at $r \approx 1$ pc within the jet angle is $\geq 10\,\mathrm{M}_{\odot}$. We thus consider the jet encounter with the edge of an associated pulsar wind bubble unlikely to occur at the time of our monitoring. Deep *HST* observations of the host galaxy environment of GW 170817 rule out the presence of a globular cluster (GC) at the location of BNS merger (Blanchard et al. 2017b; Levan et al. 2017; Pan et al. 2017; Fong et al. 2019; Lamb et al. 2019). The gravitational potential well of a GC might otherwise provide a physical reason for an abrupt change in the external gas density on the scale probed by the afterglow. We thus do not consider the over-density scenario any further.

Following a similar line of reasoning, an excess of emission can be produced if the shock is re-freshed by the deposition of new energy (e.g. (Sari et al. 2000; Laskar et al. 2015)). From Eq. 3.1, a flux ratio of ≈ 4 requires the late-time deposition of a large amount of additional energy similar to the jet energy E_k. There is no plausible energy source that can power the sudden energy release of an amount of energy equivalent to the jet energy at late times and we consider this scenario unlikely. Finally, a sharp variation of the shock microphysical parameters ϵ_{e} and ϵ_{B} with time can in principle lead to larger fluxes. This scenario would require an ad hoc evolution of ϵ_{e} and ϵ_{B} to explain the X-ray observations and we thus consider this model not physically motivated. Additionally, the deceleration of the shock is expected to lead to smaller ϵ_e values, while larger ϵ_e values would be needed to explain a flatter light-curve. In addition to the arguments above, we end by noting that all the models discussed so far do not naturally explain the harder radio-to-X-ray spectrum with a reduced value of p (§3.5).

In the absence of energy injection, environment over-densities and variations in the shock microphysical parameters, the transition of the blast wave dynamics to the sub-relativistic phase at $t_{\rm NR} \approx 1100(E_{\rm k,iso,53}/n)^{1/3}$ days (Piran 2004) is expected to lead to a smooth transition to a less steeply decaying light-curve $F_\nu \propto t^{-3(p-1)/2+3/5}$ at $\nu_m < \nu < \nu_c$ (Equation 97, Piran 2004) or $F_\nu \propto t^{-3(p-1)/2+1/2}$ at $\nu > \nu_c$ (equation A20, Frail et al. 2000). For $p = 2.05 - 2.15$ we expect the light-curve to decay as $F_\nu \propto t^{-1.2} - t^{-1.0}$ in the non-relativistic regime. For the jet-environment parameters of GW 170817 ((Mooley et al. 2018c; Ghirlanda et al. 2019; Hotokezaka et al. 2019; Ryan et al. 2020) , Figure 3.3) the full transition to the non-relativistic regime and the appearance of the counter jet is expected at $t_{\rm NR} \geq 5000$ days, significantly later than our current epoch of observation, with the start of the "deep Newtonian phase" being at even later times. In the deep Newtonian phase $F_\nu \propto t^{-3(1+p)/10}$ or $F_\nu \propto t^{-0.9}$ for $p = 2.05 - 2.15$ (Sironi et al. 2013a). A smooth transition to the sub-relativistic regime, accompanied by a slower light-curve decay, might start to be noticeable at earlier epochs, and possibly now, as the jet-core bulk Lorentz factor is $\Gamma(t) \approx 4(t/100\,\text{days})^{-3/8} \approx 1.6$ at the current epoch (still in the Blandford-McKee regime, no jet spreading) or $\Gamma(t) \propto t^{-1/2}$ leading to $\Gamma(t) \approx 1.1$ for exponential jet spreading (Rhoads 1999). These estimates are based on the inferred $\Gamma \approx 4$ at ≈ 100 days (Mooley et al. 2018c). In both cases the light-curve evolution is expected to be achromatic and the emission is expected to become dimmer with time as $F_\nu \propto t^{-1}$ or steeper. No excess can be explained within the non-relativistic jet transition scenario and no spectral evolution is expected unless we invoke an ad hoc temporal evolution of p from $p = 2.15$ to $p = 2.0$ in the time range $900 - 1200$ days (i.e. well before the full transition to the non-relativistic phase) as the shock decelerates. The theoretical predictions from the Fermi process of particle acceleration in shocks would support this trend of evolution, as they predict $p = 2$ at non-relativistic shock speeds (Bell 1978; Blandford et al. 1978; Blandford et al. 1987) and $p \approx 2.22$ at ultra-relativistic velocities in the test particle limit (Kirk et al. 2000; Achterberg et al. 2001; Keshet et al. 2005; Sironi et al. 2013b). However, here the challenge is represented by having a shock where the index of the non-thermal electron distribution p changes with time as a result of the shock deceleration, without having a substantial drop in the electron acceleration efficiency $\epsilon_{\rm e}$ when compared to the earlier ultra-relativistic regime (Crumley et al. 2019). Finally, the emergence of the counter-jet emission is expected to lead to a flatter light-curve at $\delta t > t_{\rm NR}$, or $\delta t > 5000$ days for the parameters of GW 170817.

To summarize, the late time evolution of the jet does not naturally account for the brightness, spectrum and flattening of the X-ray light-curve at $\delta t \approx 1200$ days. Specifically: (i) the steep density gradient of a factor of $\approx 10^8$ over a pc scale required to explain the X-ray excess of emission implies an extremely large shell mass $\geq 10 M_\odot$

within the jet angle at $\approx 1\,\mathrm{pc}$, making the scenario of a jet encounter with the edge of an associated pulsar-wind bubble unlikely; (ii) similarly, the large amount of energy required to be injected to produce a X-ray excess is equivalent to the energy of the jet itself and there is no plausible source to power such an energy release at these late-times; (iii) a sudden variation of the shock microphysical parameters is not physically motivated at this epoch; (iv) the shock transition to the Newtonian regime is expected to happen at significantly later times $t_{\mathrm{NR}\geq 5000}$ days and no effect related to the Newtonian transition can thus be invoked to explain the late-time excess of X-ray emission; (v) lastly, the counter-jet is also expected to emerge at $\delta t > 5000$ days.

3.7. Kilonova Afterglow Models and Numerical Relativity Simulations of BNS Mergers

NS merger simulations predict the ejection of neutron-rich and neutron-poor matter due to a variety of mechanisms operating over different timescales before, during and after the merger (Shibata et al. 2019). These mass outflows shock the circumbinary medium producing synchrotron radiation that peaks on the deceleration time scale t_{dec} (Nakar et al. 2011). The direct implication is that heavier mass outflows like those associated with the kilonova ejecta will produce non-thermal emission that will peak later in time than the emission associated with the significantly faster but also significantly lighter jet. For the inferred kilonova ejecta properties of GW 170817 ($M_{\mathrm{ej}} \approx 0.06\,\mathrm{M}_{\odot}$, $n \approx 0.01 - 0.001\,\mathrm{cm}^{-3}$ and $\beta \approx 0.1 - 0.3$; Cowperthwaite et al. 2017;

Drout et al. 2017; Kilpatrick et al. 2017; Villar et al. 2017; Arcavi 2018; Waxman et al. 2018; Bulla et al. 2019; Nicholl et al. 2021), $t_{\rm dec} \approx 10^4$ days. However, the deceleration of the fastest-moving tail of these ejecta is expected to contribute to non-thermal emission on significantly shorter timescales of months to years after the merger (Nakar et al. 2011; Kyutoku et al. 2014; Takami et al. 2014; Hotokezaka et al. 2015; Hotokezaka et al. 2018; Kathirgamaraju et al. 2019; Margalit et al. 2020) that are relevant now (while the bulk of slower-moving ejecta powered the UV/optical/IR kilonova at $\delta t < 70$ days).

This kilonova afterglow will appear as an excess of emission compared to the off-axis jet afterglow. Being powered by a different shock and by a different electron population than the jet's forward shock, the synchrotron emission from the kilonova afterglow does not necessarily inherit the same microphysical parameters $\epsilon_{\rm e}$, $\epsilon_{\rm B}$, as well as the electron index p. In this respect, the lower p value indicated by our observations (Figure 3.6) would be a natural outcome and would be consistent with the $p < 2.2$ theoretical expectation of shocks that are non-relativistic (Bell 1978; Blandford et al. 1978; Blandford et al. 1987).

The luminosity and time evolution of the kilonova afterglow from a BNS merger depends on (and is a tracer of) the intrinsic parameters that include how the ejecta energy is partitioned in the velocity space $E_{\rm KN}(\Gamma\beta)$, which ultimately depends on the neutron star equation of state (EoS) and the binary mass ratio q, and also the extrinsic parameters that include those that regulate the kilonova shock microphysics (fraction of post-shock energy density in relativistic electrons, $\epsilon_{\rm e,KN}$, and in magnetic field, $\epsilon_{\rm B,KN}$ and $p_{\rm KN}$), and the environment density n. We first adopt in §3.7.1 an analytical parametrization of $E_{\rm KN}(\Gamma\beta)$ to explore the large parameter space of the kilonova afterglow parameters while being agnostic to the ejecta type (e.g. winds vs. dynamical etc.). In the second part (§3.7.2) we employ a set of numerical relativity simulations of BNS mergers to emphasize the dependency of the observed kilonova afterglow on intrinsic parameters of the NS binary, like the binary mass ratio or the NS EoS. We note that the potential early emergence of the kilonova afterglow a few years after the merger, at a time when the jet has yet to effectively become spherical (§3.6) implies that the kilonova shock is expanding into a medium that is mostly unperturbed (i.e., not shocked by the jet shock) and that effects related to the jet evacuating the circum-merger medium (Margalit et al. 2020) are unlikely to play a major role.

3.7.1. Kilonova afterglow models from Kathirgamaraju et al. 2019

We parameterized the kinetic energy distribution of the kilonova ejecta as a power-law in specific momentum $\Gamma\beta$ for $\beta > \beta_0$: $E_{\rm KN} \propto (\Gamma\beta)^{-\alpha}$ (Kathirgamaraju et al. 2019). This parameterization captures the properties of the high-velocity tail of all types of kilonova outflows, including dynamical ejecta and disk winds that might dominate the mass of the blue kilonova component. Motivated by the results from the modeling of the thermal emission from the kilonova in the following we adopt $\beta_0 = 0.35$ as baseline

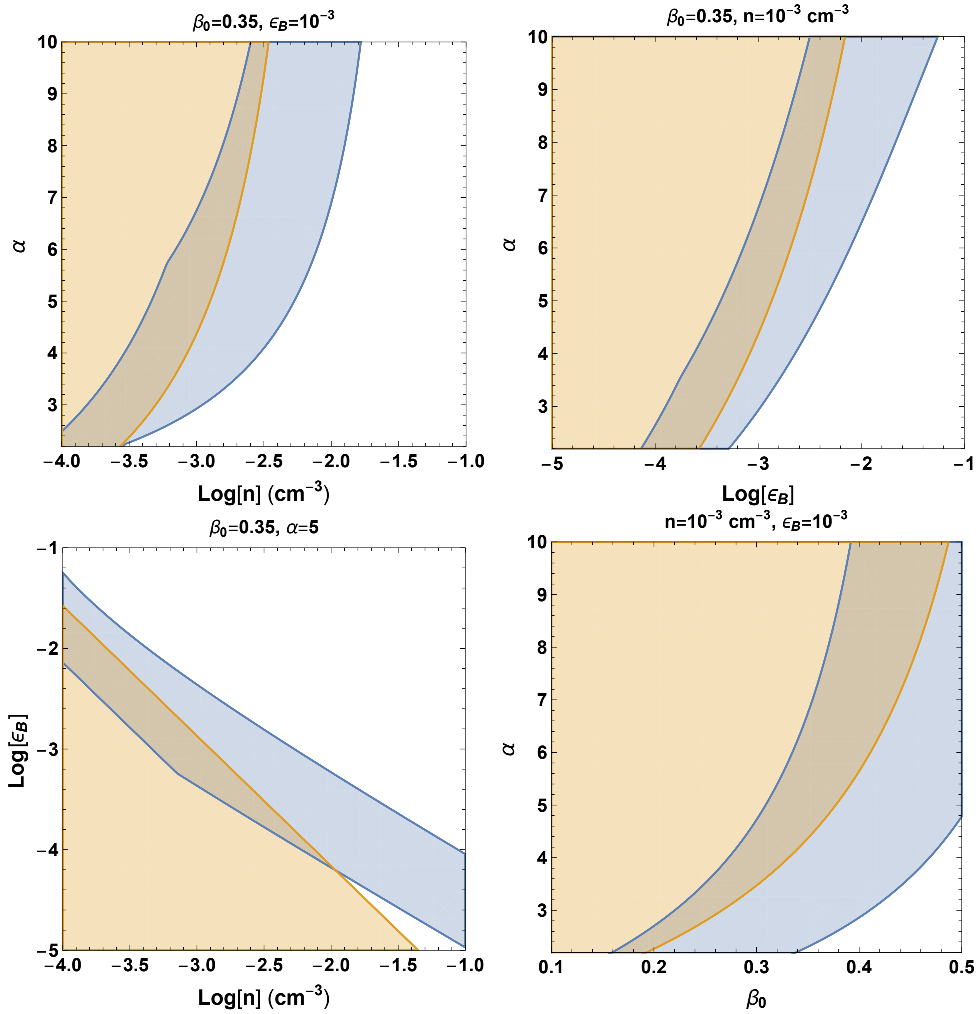

Figure 3.7 Blue shaded area: region of the parameter space consistent with the X-ray flux excess at 1234 days following the modeling described in §3.7. Orange shaded area: region of the parameter space that is consistent with our radio upper limit at 3 GHz: $F_\nu < 5.1\,\mu$Jy. The kinetic energy distribution of the kilonova ejecta in the velocity space has been parameterized as $E_{\rm KN} \propto (\Gamma\beta)^{-\alpha}$ above β_0 with $E_{\rm KN}(\Gamma_0\beta_0) = 10^{51}$ erg. The shock microphysical parameters adopted in this calculation are $p = 2.05$ (consistent with the observational findings of §3.5) and $\epsilon_e = 0.1$. Two parameters are varied in each plot while the rest are kept fixed to values indicated in the plot title.

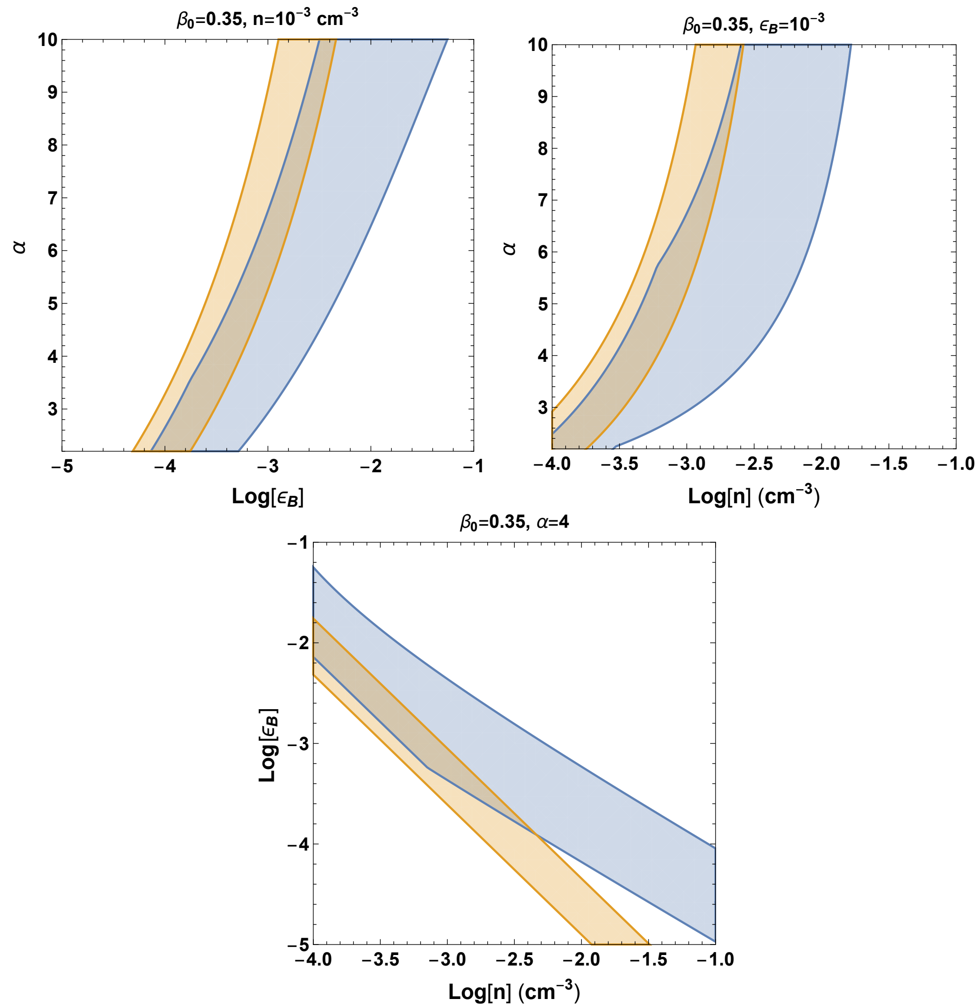

Figure 3.8 Kilonova afterglow parameter space with the same color scheme as Figure 3.7 where we used the peak pixel flux within one synthesized beam at 3 GHz from (Balasubramanian et al. 2021) ($F_\nu = 2.8 \pm 1.3\,\mu$Jy) as a constraint on the radio emission from the kilonova. As in Figure 3.7, we assume $E_{\rm KN} = 10^{51}$ erg, $\epsilon_{\rm e} = 0.1$, and $p = 2.05$. Our conclusions remain unchanged.

and a total kinetic energy of $E_{\rm KN}(\Gamma_0\beta_0) = 10^{51}$ erg. We generated a set of multi-wavelength kilonova afterglow light-curves for shock microphysical parameters $p = 2.05$ (consistent with the observational findings of §3.5), $\epsilon_{\rm e} = 0.1$, $\epsilon_{\rm B} = [10^{-4} - 10^{-2}]$

and circumbinary medium density $n = [10^{-4} - 10^{-2}]\,\mathrm{cm}^{-3}$. As a comparison, studies of the jet afterglow pointed at densities $n > 10^{-4}\,\mathrm{cm}^{-3}$ (Margutti et al. 2021) , while multiple studies (Hallinan et al. 2017; Hajela et al. 2019; Makhathini et al. 2020) of the large-scale environment of GW 170817 at X-ray and radio wavelengths argue in favor of $n \leq 10^{-2}\,\mathrm{cm}^{-3}$. Motivated by the results from numerical relativity simulations of BNS mergers described below we explore the parameter space for $\alpha = [3 - 9]$.

Our results are shown in Figure 3.7, where shaded areas highlight the regions of the parameter space that are consistent with the bright X-ray excess (blue) and the deep radio upper limit (orange). We further show a successful kilonova afterglow model for $\alpha = 5$, $n = 0.001\,\mathrm{cm}^{-3}$ and $\epsilon_{\mathrm{B}} = 0.001$ in Figure 3.2. Consistent with the results from the jet afterglow modeling, current data point to lower density environments with $n < 0.01\,\mathrm{cm}^{-3}$, but otherwise leave the multi-dimensional parameter space largely unconstrained. Specifically, we find that all values of $\alpha = [3, 10]$ are consistent with the X-ray and radio data set. This conclusion remains unchanged even if we adopt the peak pixel flux within one synthesized beam at 3 GHz from (Balasubramanian et al. 2021) ($F_\nu = 2.8 \pm 1.3\,\mu\mathrm{Jy}$) as a constraint on the radio emission from the kilonova (Figure 3.8).

Using their reduction of the multi-wavelength data set up to $\approx$ 1200 days and similar to our preliminary assessment of the properties of the kilonova ejecta properties in (Hajela et al. 2019), (Balasubramanian et al. 2021) favor $\alpha \geq 5$ kilonova ejecta profiles assuming a density and the kilonova shock microphysical parameters set to the values of the jet afterglow shock (i.e. $n \sim 10^{-2}\,\mathrm{cm}^{-3}$, $\epsilon_{\mathrm{e}} \sim 10^{-2}$, and $\epsilon_{\mathrm{B}} \sim 10^{-3}$). While for this choice of extrinsic parameters our findings qualitatively agree with the conclusions by (Balasubramanian et al. 2021), we note that there is no physical reason for the kilonova shock microphysical parameters to be the same as those of the jet afterglow shock, and relaxing these parameters leaves the problem unconstrained. Our results are consistent with those from previous analyses that did not include the latest epoch (Hajela et al. 2019; Troja et al. 2020), and constitute an important advancement with respect to these previous works that were completed before the emergence of a statistically significant new component of emission.

3.7.2. Kilonova afterglows from physically-motivated kilonova kinetic energy profiles

We consider a set of 76 numerical relativity BNS merger simulations tailored to GW 170817 (Nedora et al. 2019; Perego et al. 2019; Bernuzzi et al. 2020; Endrizzi et al. 2020; Perego et al. 2020; Nedora et al. 2021b). The simulations were performed using the `WhiskyTHC` code (Radice et al. 2012; Radice et al. 2014a; Radice et al. 2014b). The set includes simulations performed at different resolutions and employs five finite-temperature microphysical equations of state (EoSs) that span the (large) range of EoS compatible with current laboratory and astronomical constraints. The simulations self-consistently included compositional and thermal effects due to neutrino emission and re-absorption (Radice et al. 2016; Radice et al. 2018a). The general-relativistic large-eddy simulation (GRLES) method was used to capture subgrid-scale turbulent dissipation and angular momentum transport (Radice 2017; Radice 2020).

Dynamical ejecta from these simulations show the presence of a fast moving tail of ejecta, which is produced following the centrifugal bounce of the remnant taking place in the first milliseconds of the merger, unless prompt BH formation occurs, in which case there is no bounce (Radice et al. 2018a). The bounce produces a shock wave that is rapidly accelerated by the steep density gradient in the outer layers of the remnant, propels material to trans-relativistic velocities, and propagates into the circumbinary medium. Fast moving material could also be accelerated by the thermalization of mass exchange flows between the stars prior to merger (Radice et al. 2018d). However, this alternative scenario typically predicts a faster rise of the synchrotron emission than indicated by observations of GW 170817.

The deceleration of this kilonova shock into the medium produces synchrotron radiation. We compute the kilonova synchrotron light curves using the semi-analytic code `PyBlastAfterglow` (Nedora et al. 2021a). We have validated this code in the subrelativistic regime by comparing the results it produces using the ejecta profiles from (Radice et al. 2018a), which had been previously analyzed using the code of (Hotokezaka et al. 2015) and in the ultra-relativistic regime by comparing our results with those produced by `afterglowpy` (Ryan et al. 2020).

Figure 3.9 collects a representative set of X-ray light curves for three EoSs (BLh, Bernuzzi et al. 2020; Logoteta et al. 2021; LS220, Lattimer et al. 1991; and SLy4, Douchin et al. 2001; Schneider et al. 2017) and two values of the binary mass ratio

q. This figure highlights the sensitivity of the kilonova afterglow on intrinsic (EoS, q) and extrinsic (n, p, ϵ_{e}, ϵ_{B}) parameters of the binary. It is important to emphasize that the overall flux level predicted by our models is strongly dependent on assumed microphysical parameters of the shock. However, the light curve temporal evolution only depends on the structure of the ejecta and on the ISM density. Specifically, the peak time of the kilonova emission is of dynamical nature, tracing the deceleration time of the blast wave into the environment (Nakar et al. 2011) and it is thus independent from the parameters that set the level of the emitted flux (like the shock microphysical parameters).

With respect to the intrinsic binary parameters probed by our simulation, we find that binaries which do *not* undergo prompt BH formation are broadly consistent with the observations. Numerical simulations of BNS mergers by (Nedora et al. 2021a; Prakash et al. 2021) show that if prompt collapse to BH occurs in equal mass NS binaries, the kilonova afterglow is expected to be several orders of magnitude fainter than the observed X-ray luminosity of GW 170817 at ≈ 1000 days (e.g. Figure 15 in (Prakash et al. 2021)). In the case of highly asymmetric NS binaries, the prompt collapse to BH is associated with afterglow light curves that peak at $\approx 10^4$ days post-merger, which is significantly later than the current epoch (see Figure 4 and 5 in (Nedora et al. 2021a)). An important conclusion is that prompt BH formation is disfavored (Bauswein et al. 2017; Margalit et al. 2017; Radice et al. 2018b), because the presence of the post-merger bounce appears to be necessary in order to produce sufficient fast and massive outflows to power the kilonova emission. Improved higher-resolution targeted simulations are needed to draw more quantitative conclusions.

In addition to the nature of the compact-object remnant, the early detection of a kilonova afterglow a few years after the merger and its future modeling can enable fundamental insight into two other still-open questions pertaining to GW 170817: the presence of a free-neutron component of ejecta, and the origin of the detected prompt γ-rays (Goldstein et al. 2017; Savchenko et al. 2017). Fast ejecta with mass $\gtrsim 10^{-4}\,M_{\odot}$ at velocity $v \geq 0.5c$ (light-blue shaded area in Figure 3.10, lower panel) are expected to lead to a freeze out of the r-process (Metzger et al. 2015b), as most neutrons will avoid capture, leaving behind free neutrons that can power a short-lived (i.e. $\approx$hrs) but luminous UV/optical transient. Additionally, kilonova ejecta profiles extending to velocities $v \geq 0.6\,c$ (light-green shaded area in Figure 3.10, lower panel) provide the necessary conditions to produce γ-rays from a shock breakout of a wide-angle outflow (i.e. the cocoon) inflated by the jet from the merger ejecta (Bromberg et al. 2018; Gottlieb et al. 2018). Being sensitive to the presence and properties of the fast kilonova ejecta, the kilonova afterglow is thus a probe of the merger dynamics and nature of the compact object remnant.

We conclude by remarking that a general, robust and testable prediction of the kilonova afterglow models is that of a persistent source of emission across the electromagnetic spectrum, which is not expected to become fainter for thousands of days, and might even become brighter during this period of time. Eventually, the kilonova afterglow will appear as a detectable source in the radio sky and might even be detectable via deep optical observations from space.

3.8. Emission from a Compact-Object Remnant

An alternative explanation of rising X-rays without accompanying bright radio emission is that of central-engine powered radiation, i.e. radiation powered by an energy release associated with the compact-object remnant either in the form of accretion (for a BH remnant) or spin-down energy (for a long-lived NS remnant). The nature of the compact-object remnant of GW 170817 is a fundamentally open question that directly relates to the NS EoS. While post-merger GWs were inconclusive, the observational evidence for (i) a blue kilonova component associated with a large mass of lanthanide-free ejecta and kinetic energy $\approx 10^{51}$ erg (Cowperthwaite et al. 2017; Evans et al. 2017; Villar et al. 2017; Bulla et al. 2019; Nicholl et al. 2021), and (ii) the uncontroversial evidence for a successful relativistic jet (Alexander et al. 2018; Mooley et al. 2018c; Ghirlanda et al. 2019) together with energetics arguments strongly disfavor either a prompt collapse to a BH or a long-lived NS remnant. These arguments and observations argue in favor of a hypermassive NS that collapsed to a BH within a second or so after the merger (Granot et al. 2017; Margalit et al. 2017; Shibata et al. 2017; Metzger et al. 2018; Rezzolla et al. 2018; Gill et al. 2019; Ciolfi 2020; Murguia-Berthier et al. 2021). While the most likely scenario is that of a BH remnant at the current time of the observations, in the following we also consider the less-likely case of a spinning-down NS for completeness (see however Piro et al. 2019).

3.8.1. Accreting BH remnant scenario

The Eddington luminosity for accretion onto a remnant BH of mass $M_\bullet \sim 2.5 M_\odot$ (Abbott et al. 2019) of GW 170817 is given by

$$L_{\rm Edd} = \frac{4\pi G M_\bullet c}{\kappa_{\rm es}} \approx 8 \times 10^{38} \left(\frac{M_\bullet}{2.5 M_\odot}\right) {\rm erg\,s^{-1}}, \tag{3.2}$$

where $\kappa_{\rm es} = Y_e \sigma_{\rm T}/m_p \approx 0.16~{\rm cm^2~g^{-1}}$ is the approximate electron scattering opacity for fully ionized matter comprised of heavy elements (electron fraction $Y_e \simeq 0.4$).

From hydrodynamical simulations of BNS mergers, the rate of fall-back accretion is $\dot{M}|_{t_0} \sim 2 \times 10^{-4} M_\odot~{\rm s^{-1}}$ on a timescale of $t_0 \sim 1$ s after the merger (Rosswog 2007). A more important source of fall-back material may arise from the accretion disk outflows (Fernández et al. 2013), which likely dominated the kilonova ejecta in GW 170817 (Radice et al. 2020). If a few tens of percent of the total ejecta mass $\approx 0.06 M_\odot$ inferred for GW 170817 (Cowperthwaite et al. 2017; Villar et al. 2017; Arcavi 2018; Waxman et al. 2018; Nicholl et al. 2021) were to fall back to the BH on a timescale comparable to the predicted accretion disk lifetime ~ 1 s, the mass fall-back rate would be orders of magnitude higher, $\dot{M}|_{\rm t_0} \sim 10^{-2} M_\odot~{\rm s^{-1}}$.

Based on the expectation that $\dot{M} \simeq \dot{M}_{t_{\rm fb}}(t/t_0)^{-5/3}$ at times $t \gg t_0$ for marginally bound material (Rees 1988), the total X-ray accretion luminosity is given by

$$
\begin{aligned}
L_{\rm X} &\approx \frac{\eta}{f_{\rm b}}\dot{M}c^2 \approx 10^{39}\,{\rm erg\,s^{-1}}\left(\frac{{\rm f_b}}{0.1}\right)^{-1} \\
&\times \left(\frac{\eta}{0.1}\right)\left(\frac{\dot{M}|_{t_0}}{10^{-2}M_{\odot}\,{\rm s}^{-1}}\right)\left(\frac{t}{1000\,{\rm days}}\right)^{-5/3}, \qquad (3.3)
\end{aligned}
$$

where the radiative efficiency η has been normalized to that of a thin disk orbiting a BH of dimensionless spin $a \approx 0.6 - 0.8$ (Novikov et al. 1973), as expected for the remnant of a BNS merger. Here $f_{\rm b}$ is the geometric beaming fraction of the X-ray emission. We expect $f_{\rm b} \ll 1$ for sources at or near the Eddington luminosity (e.g., Ultraluminous X-ray sources, ULXs, (Walton et al. 2018)) due to powerful disk outflows that generate a narrow accretion funnel (King 2009). We have normalized $f_{\rm b}$ to a lower limit based on the observer's viewing angle (Mooley et al. 2018c; Ghirlanda et al. 2019; Hotokezaka et al. 2019) $\theta_{\rm obs} \approx 0.4$ with respective to the original binary axis ($\simeq$ accretion disk angular momentum axis): $f_{\rm b,min} \approx \theta_{\rm obs}^2/2 \sim 0.1$.

In analogy with X-ray binaries in the “ultra luminous" state (Gladstone et al. 2009) the spectra of stellar mass BHs accreting close to the Eddington rate are satisfactorily modeled by a thermal accretion disk plus power-law component with a high-energy exponential break. Ignoring relativistic terms and color corrections, the effective temperature of the disk emission can be estimated as

$$2\pi R_{\rm isco}^2 \sigma T_{\rm eff}^4 = f_{\rm b} L_{\rm X}, \qquad (3.4)$$

where $R_{\rm isco} \approx 3GM_{\bullet}/c^2$ is the innermost radius of the disk for a BH of spin $a \approx 0.6 - 0.8$. This gives

$$
\begin{aligned}
kT_{\rm eff} &\simeq 2\,{\rm keV}\left(\frac{f_{\rm b}}{0.1}\right)^{1/4} \\
&\times \left(\frac{L_{\rm X}}{5\times 10^{38}{\rm erg\,s^{-1}}}\right)^{1/4}\left(\frac{M_{\bullet}}{2.5M_{\odot}}\right)^{-1/2},
\end{aligned} \tag{3.5}
$$

i.e. in the range of the *CXO* sensitivity window for the observed $L_{\rm X} \approx 5\times 10^{38}{\rm erg\,s^{-1}}$ at 1234 days (Table 3.1).

We now consider the question of the observability of this X-ray emission. The X-ray rise time will be determined by the maximum of two timescales. The first is the timescale for the accretion rate to drop sufficiently that the beaming fraction $f_{\rm b} \propto (\dot{M}/\dot{M}_{\rm Edd})^{-2} \propto t^{10/3}$ (King 2009) increases to the point that the angle of the accretion funnel $\theta_{\rm b} \propto f_{\rm b}^{1/2} \propto t^{5/3}$ enters the observer's viewing angle $\theta_{\rm obs} \approx 0.4$. Given that $L_{\rm X}$ at the present epoch is $\lesssim L_{\rm Edd}$ (Eq. 3.2), we conclude that this effect may still play a role in generating a rising X-ray luminosity.

A second timescale for the X-rays to be able to reach the observer is that required for the kilonova ejecta to become transparent to the X-rays. Assuming that the r-process ejecta have a bound-free opacity to photons of energy $\sim$ 1 keV which is similar to that of iron group elements $\kappa_{\rm X} \approx 10^4$ cm^{-2} g^{-1}, this will take place after a time

$$
\begin{aligned}
t_{\rm thin} &= \left(\frac{3M_{\rm ej}\kappa_{\rm X}}{4\pi v_{\rm ej}^2}\right)^{1/2} \\
&\approx 2000\,{\rm days}\left(\frac{v_{\rm ej}}{0.1{\rm c}}\right)^{-1} \\
&\times \left(\frac{\kappa_{\rm X}}{10^4\,{\rm cm^2\,g^{-1}}}\right)^{1/2}\left(\frac{M_{\rm ej}}{0.06M_{\odot}}\right)^{1/2}, \qquad (3.6)
\end{aligned}
$$

where we have normalized the ejecta mass $M_{\rm ej}$ and velocity $v_{\rm ej}$ to characteristic values for the (dominant) red/purple ejecta component inferred by modeling the optical/IR kilonova of GW 170817 (Cowperthwaite et al. 2017; Drout et al. 2017; Kilpatrick et al. 2017; Villar et al. 2017).

Given that the ejecta density may be lower than average for our high altitude viewing angle $\theta_{\rm obs} \approx 0.4$, and hence $t_{\rm thin}$ somewhat over-estimated, we conclude that $t_{\rm thin}$ is also likely to be comparable to the present epoch. Figure 3.11 shows the evolution of the accretion-powered fall-back X-ray luminosity on a BH remnant, both intrinsic (orange solid line) and observed (red dashed line), i.e. with a correction for absorption by the kilonova ejecta of the form $\propto (1 - e^{-(t/t_{\rm thin})^2})$, where we used $t_{\rm thin} \approx 1000$ days, as the time when the ejecta becomes optically thin. An absorption cause for the X-ray rise could in principle be tested by a strong suppression of soft X-ray photons due to the rapidly increasing bound-free opacity towards lower-energy X-rays. However, due to faintness of the X-ray source (which leads to very low-count statistics, §3.2.2) combined with the progressive loss of sensitivity of the *CXO* at soft X-ray energies, this effect cannot be tested at present with any statistically meaningful confidence.

One potential constraint on this scenario comes from earlier IR/optical observations, since at earlier epochs the absorbed X-rays would be reprocessed to IR/optical radiation. For instance, to explain $L_x \sim 5 \times 10^{38}$ erg s^{-1} at $t_{\rm now} \sim 10^3$ days, the accretion power on a timescale of $t_{\rm KN} \sim 1$ week after the merger would be higher by a factor $\sim (t_{\rm now}/t_{\rm KN})^{5/3} \approx 4000$, or $\sim 2 \times 10^{42}$ erg s^{-1}. The bolometric UV/optical/IR emission (Cowperthwaite et al. 2017; Arcavi 2018; Waxman et al. 2018) from the kilonova of GW 170817 reached $L \approx 10^{41}\,{\rm erg\,s^{-1}}$. The accretion power would thus exceed the bolometric output of the kilonova on this timescale by a factor $\gtrsim 10$. Even more stringently, extrapolating back to the last *HST* optical detection of GW 170817 at ≈ 360 days since merger leads to values $\approx 10^2$ times larger than the observed *HST* luminosity. At 360 days the optical flux density inferred from *HST* observations is perfectly consistent with the power-law spectrum that extends from the radio band to the X-rays (Fong et al. 2019) and it is thus dominated by jet-afterglow emission.

However, there are two effects that act to alleviate these constraints. Firstly, at these earlier epochs the fall-back rate is highly super-Eddington. The efficiency with which the fall-back material reaches the central black hole may be drastically reduced at these early times due to the inability of the super-Eddington accretion to radiatively cool (Rossi et al. 2009). Furthermore, the radiative efficiency η of highly super-Eddington accretion flows may be substantially reduced relative to the near or sub-Eddington accretion rate which characterizes the present epoch. Finally, it is unclear if most of the reprocessed power will emerge in the optical/NIR bands; if lanthanide-series atoms dominate the cooling of the gas in the nebular phase then much of the reprocessed emission may emerge in the mid-IR bands (Hotokezaka et al. 2021). On the other hand, *Spitzer* observations (Villar et al. 2018; Kasliwal et al. 2019) revealed the 4.5μm luminosity to be $\sim 10^{38}$ erg s^{-1} on a timescale ≈ 74 days after the merger, at which time the fall-back accretion rate would be a factor ~ 100 higher than at present epoch. Thus we conclude that the reprocessing into the IR band is not a viable option, and would have to rely instead on the reduced accretion efficiency of the fall-back material onto the BH.

We end by commenting on the expected broadband spectrum. If the GW 170817 remnant is accreting at or close to the Eddington limit, it is valuable to contrast its observational properties with those of the ultra-luminous X-ray sources (ULXs), which accrete at or above the Eddington limit for compact objects at $\sim 1\,M_{\odot}$. Radio observations of ULX sources place upper limits on the radio power of $L_{\rm R} \lesssim 10^{24}\,{\rm erg\,s^{-1}\,Hz^{-1}}$ (Körding et al. 2005), corresponding to a flux density limit of $\lesssim 1\,\mu$Jy at the distance of GW 170817, which is below the level of our latest radio upper limit of $\approx 5\,\mu$Jy (3×RMS, §3.3.1) and comparable to the local image RMS in our deep VLA observations at 3 GHz. The lack of a radio counterpart of GW 170817 is consistent with observations of XRBs in the "soft" state, which can accrete at a significant fraction of the Eddington rate and have no associated persistent radio emission (Fender et al. 2004). Similarly, if GW 170817 is accreting in a "hard" state (associated with an X-ray spectrum peaking at higher energies compared to the soft state), where the X-ray and radio emission are strongly coupled (Corbel et al. 2003), we would only expect a radio flux density of $\sim 10^{22}\,\mathrm{erg\,s^{-1}\,Hz^{-1}}$ based on our measured *CXO* luminosity and the radio X-ray correlation derived from an ensemble of 24 X-ray binaries in the hard state (Gallo et al. 2014). Typically, X-ray binaries are only in the hard state while in quiescence (accreting at some small fraction of the Eddington rate) or while in outburst where they typically make the hard to soft state transition (Dunn et al. 2010) at around $\sim 0.01\,L_{\rm Edd}$ to $\sim 0.1\,L_{\rm Edd}$. However, high X-ray luminosity hard states have been observed in the XRB GRS 1915+105 (Rushton et al. 2010; Motta et al. 2021), but the associated radio emission would still be well below our detection threshold. We conclude by emphasizing that a solid expectation from this scenario is that of a different radio-to-X-ray spectrum than the jet afterglow, with less luminous radio emission than expected based on the jet-afterglow spectral slope. This is consistent with our observational findings (§3.5). Differently from the kilonova afterglow (§3.7, Figure 3.9), in the BH fall-back accretion scenario the X-ray luminosity is expected to to be continuously decreasing with time (Figure 3.11).

To conclude, an accretion-powered origin of the emerging component of X-ray emission is a potentially viable explanation and would naturally account for the broadband spectrum *if* the efficiency of the super-Eddington fall-back matter reaching the black hole is suppressed sufficiently to prevent the accretion luminosity from violating the observed kilonova luminosity at earlier times.[5] This scenario is further supported by α-viscosity hydrodynamical simulations presented in (Metzger et al. 2021).

3.8.2. Spinning-down magnetar scenario

Alternatively, the additional X-ray component could be powered by spin-down energy from a long-lived magnetar remnant[6] ((Piro et al. 2019; Troja et al. 2020),see however (Radice et al. 2018c)). While there are theoretical arguments against the long-lived magnetar remnant scenario (Margalit et al. 2017), we consider this scenario here for completeness.

The massive NS remnant created by a BNS merger will in general have more than sufficient angular momentum to be rotating near break-up (Radice et al. 2018c). A NS of mass $M_{\rm ns}$ rotating near its mass-shedding limit possesses a rotational energy

$$\begin{aligned} E_{\rm rot} = \frac{1}{2}I\Omega^2 &\simeq 1\times 10^{53}\left(\frac{I}{I_{\rm LS}}\right) \\ &\times \left(\frac{M_{\rm ns}}{2.5M_\odot}\right)^{3/2}\left(\frac{P}{0.7{\rm ms}}\right)^{-2} {\rm erg}, \end{aligned} \tag{3.7}$$

where $P = 2\pi/\Omega$ is the rotational period and I is the NS moment of inertia, which we have normalized to an approximate value for a relatively wide class of nuclear equations of state $I_{\rm LS} \approx 1.3\times 10^{45}(M_{\rm ns}/1.4M_\odot)^{3/2}$ g cm^2 (Lattimer et al. 2005).

[5]We note that a similar scenario has been proposed by (Ishizaki et al. 2021), which was released a few days after a first version of this chapter appeared on the arXiv.

[6]We note that the thermal X-ray luminosity of a cooling NS at this epoch is expected to be $\lll L_{\rm X,obs} \approx 5\times 10^{38}\,{\rm erg s^{-1}}$ (see Figure 9 in (Beznogov et al. 2020)).

The spin-down luminosity $L_{\rm sd}$ of an aligned dipole rotator of surface field strength B with $I = I_{\rm LS}$ is (Philippov et al. 2015)

$$
\begin{aligned}
L_{\rm sd} &= 7\times 10^{50}\,{\rm erg\,s^{-1}}\left(\frac{B}{10^{15}\,{\rm G}}\right)^{2} \\
&\times \left(\frac{P_0}{0.7\,{\rm ms}}\right)^{-4}\left(1+\frac{t}{t_{\rm sd}}\right)^{-2}
\end{aligned}
\tag{3.8}
$$

where we have taken $R_{\rm ns} = 12\,{\rm km}$ as the NS radius, and

$$
\begin{aligned}
t_{\rm sd} = & \left.\frac{E_{\rm rot}}{L_{\rm sd}}\right|_{t=0} \\
& \simeq 150\,{\rm s}\left(\frac{I}{I_{\rm LS}}\right)\left(\frac{B}{10^{15}\,{\rm G}}\right)^{-2}\left(\frac{P_0}{0.7\,{\rm ms}}\right)^{2}
\end{aligned}
\tag{3.9}
$$

is the characteristic spin-down time over which an order unity fraction of the rotational energy is removed, where P_0 is the initial spin-period and we have assumed a remnant mass of $M = 2.3 M_\odot$.

The natural spin-down timescale, $t_{\rm sd}$, of $\sim$ 150 seconds (Equation 3.9), is $\sim$ 6 orders of magnitude shorter than the observed $\sim$ 1000 day timescale for the emergence of excess X-ray emission. Accommodating $t_{\rm sd}$ to much-increased $\sim$ 1000 day timescale implies an a-priori unlikely reduction in the magnetic field, an increase of the initial spin period, or both. From Eq. 3.8:

$$
\begin{aligned}
L_{\rm sd} \simeq & \\
7 & \times 10^{50}\,{\rm erg\,s^{-1}}\left(\frac{I}{I_{\rm LS}}\right)\left(\frac{B}{10^{15}\,{\rm G}}\right)^{2}\left(\frac{P_0}{0.7\,{\rm ms}}\right)^{-4}
\end{aligned}
\tag{3.10}
$$

Matching the observed excess X-ray luminosity $L_{\rm X} \sim 5 \times 10^{38}$ erg s^{-1} would require an extremely weak magnetic field, $B \sim 10^{9}$ G. While this value is in the range of B inferred for recycled pulsars, this magnetic field is much smaller than the field strength $\gtrsim 10^{16}$ G expected to be amplified inside the remnant during the merger processes (Kiuchi et al. 2015). The calculations above do not include the effects related to gravitational-wave losses that have been proposed in the context of the long-lived NS remnant scenario to dominate the magnetar spin-down at early times to avoid violating the inferred kilonova energy. However, it would still require fine-tuning to match $L_{\rm sd}$ to the observed $L_{\rm X}$ for a more physical value of B. Furthermore, unlike the BH case (Eq. 3.5), there is no reason *a priori* to expect the magnetar emission to be largely confined to the X-ray range.

3.9. Summary and Conclusions

We presented the results from our coordinated *CXO*, VLA and MeerKAT campaign of GW 170817 at $\delta t = 900 - 1273$ days (March 2020 to February 2021). Our observations are public and have been partially presented by (Troja et al. 2020) (for data at $\delta t < 950$ days), (Balasubramanian et al. 2021), and (Troja et al. 2021). Our X-ray observations at $\delta t = 940$ and 1234 days provide the first evidence for a statistically significant deviation from the off-axis jet model and the emergence of a new X-ray component of emission.[7] Our detailed observational findings can be summarized as follows:

[7] We note that the $\delta t = 940$ day dataset would not on its own establish a statistically-significant excess over prior extrapolations.

- We found evidence for bright X-ray emission from GW 170817 with a statistical significance of $7.2\,\sigma$ (§3.2.1) at $\delta t \approx 1234$ days with luminosity of $\sim 5\times10^{38}\,\mathrm{erg\,s^{-1}}$. This emission is a factor ≈ 4 larger than the extrapolation of the structured-jet model to the present epoch (Figure 3.2). We employed two independent approaches to estimate the statistical significance of the X-ray excess. For both approaches the statistical tests are performed in the count-rate phase space to minimize the role of any effect related to the flux calibration and self-consistently account for the Poisson nature of the process. The first approach utilizes multi-wavelength jet afterglow light-curves generated with `JetFit`, while the second approach is jet-model agnostic and adopts an achromatic simple power-law flux decay. Based on these two independent tests we conclude that the *CXO* observations at $\delta t > 900$ days support the evidence of an excess of X-ray emission compared to the predictions from the earlier broad-band evolution with statistical significance in the range $3.1\,\sigma$ – $3.9\,\sigma$
- In contrast to the X-rays, we find no evidence for significant radio emission at the location of GW 170817 (Figure 3.2, lower panel, and Figure 3.1), and we place $3\,\sigma$ flux density upper limits of 39, 5.1, and 5.1 μJy at mean frequencies of 0.8, 3 and 15 GHz, respectively, with MeerKAT and the VLA ($3 \times$ RMS, §3.3.1 and §3.3.2).
- While there is no evidence for X-ray spectral evolution using the X-ray data alone, the lack of detectable radio emission at the time of the X-ray excess

suggests hardening of the non-thermal emission from GW 170817 (Figure 3.5) compared to jet afterglow with a statistical confidence $\geq 92\% - 99.2\%$ (Figure 3.6). Therefore, these results suggest the evolution of the radio-to-X-ray broadband spectrum towards lower values of p (where the spectrum is $F_\nu \propto \nu^{-(p-1)/2}$) and constitute the first indication of spectral evolution of the non-thermal emission from GW 170817 (Figure 3.5). The radio flux density recently reported by (Balasubramanian et al. 2021) further strengthens these conclusions (Figure 3.6).

A number of factors could in principle lead to a late-time X-ray light-curve flattening as the observations suggest. We discuss the late-time evolution of the jet in §3.6 as one of the potential scenarios and conclude that to explain the excess of emission it would require an ad hoc evolution of key physical parameters of the system and is thus disfavored. We propose two alternative explanations: (i) the emergence the kilonova afterglow; (ii) emission from accretion processes on the compact-object remnant.

The emergence of the kilonova afterglow, which originates from a quasi-spherical shock that is different from the jet afterglow shock, can naturally explain the observed broadband spectral evolution of the radiation, as the value of p may be different in the two shocks. In this context the lower value of p suggested by our observations is consistent with the expectations from the the theory of Fermi acceleration in the test particle limit (Bell 1978; Blandford et al. 1978; Blandford et al. 1987) for mildly relativistic shocks, such as that produced by the kilonova. From our exploration of the kilonova afterglow emission with analytical kinetic energy profiles ($E_{KN}(\Gamma\beta) \propto (\Gamma\beta)^{-\alpha}$, §3.7.1) and physically-motivated $E_{KN}(\Gamma\beta)$ (§3.7.2, Figure 3.10) we find that ejecta profiles with $\alpha = 4 - 6$ can reasonably account for observations at $\delta t > 900$ day (Figure 3.2). However, as discussed in §3.7.1, the parameter space is currently poorly constrained (Figure 3.7). Similarly, we find that a variety of NS EoS and binary mass ratios can accommodate our observations (also see Nedora et al. 2021a). However, a common ingredient of successful models is binaries that do *not* undergo prompt black hole (BH) collapse.Finally, the presence of a very fast kilonova ejecta component (Figure 3.10) has important implications on still-open questions pertaining to the existence a free-neutron component of the ejecta possibly powering a short-lived luminous UV/optical transient, and the origin of subluminous gamma-rays produced in GRB 170817A from the breakout of the cocoon shock from the merger ejecta.

Radiation powered by an energy release associated with the compact-object remnant in the form of accretion on a BH remnant offers an alternative explanation to the presence of an X-ray excess that is not accompanied by bright radio emission (§3.8.1). The detected X-ray luminosity $L_x \sim 5 \times 10^{38}\,\mathrm{erg\,s^{-1}}$ is $\approx L_{\mathrm{Edd}}$ for a compact-object with mass of a few $\mathrm{M}_{\odot}$. A long-lived NS cannot be entirely ruled out, but we conclude that it is an unlikely scenario based on the exceedingly low magnetic field $B \approx 10^9\,\mathrm{G}$ necessary to match the observed X-ray luminosity (§3.8.2). In analogy to stellar-mass compact-objects accreting close to or above the Eddington rate, i.e. X-ray binaries (XRBs) in the "soft" state and ultra-luminous X-ray (ULXs) sources significant suppression of the radio emission can be expected. Unlike the kilonova afterglow, where the radio emission is expected to brighten with time (Figure 3.2), this accretion model predicts a constant or declining X-ray emission *without* accompanying bright radio emission.

Observations of GW 170817 are mapping an uncharted territory of the BNS merger phenomenology and have far-reaching theoretical implications. Measuring the time of peak of the kilonova afterglow, which probed the ejecta dynamics independent of shock microphysics, would offer a unique opportunity to do calorimetry of the kilonova's fastest ejecta. Alternatively, the detection of a constant (or declining) source of X-ray emission in the next thousands of days that is not accompanied by bright radio emission will unveil how accretion processes work on a compact-object remnant of a BNS merger a few years after its birth.

Table 3.1 Observed and inferred properties of the X-ray counterpart of GW 170817 as constrained by a spectral analysis of *CXO* data with model `tbabs*ztbabs*cflux(pow)` within *Xspec*. The net count-rate is computed for $1''$ region, using source and background counts from `ds9`. We adopted a Galactic neutral hydrogen column density in the direction of the transient of $\mathrm{NH_{gal}} = 0.0784 \times 10^{22}\,\mathrm{cm^{-2}}$ and no intrinsic absorption. The uncertainties on the X-ray spectral parameters (photon index Γ and unabsorbed 0.3- 10 keV flux) have been computed with MCMC sampling and are reported at the $1\,\sigma$ c.l.. Upper limits are reported at the $3\,\sigma$ c.l. We provide two flux calibrations for the latest two epochs at $\delta t \sim 939$ and 1234 days for which the photon statistics is too limited to constrain the photon index: first we assume a photon index that is the best fitting value from the joint spectral fitting of all CXO observations $\Gamma = 1.603$ (see §3.2.2). Second, we provide a flux calibration that assumes a spectral model consistent with a jet afterglow origin of the detected X-rays. From the posterior distribution of the p parameter of models presented in §3.4, we infer $\Gamma = 1.565 \pm 0.025$.

δt[1] (days)	Significance[2] (σ)	Exposure (ks)	Net count-rate[3] (10^{-4} ct/s) (0.5-8 keV)	Γ[4]	Unabsorbed Flux ($10^{-15}\,\mathrm{erg\,cm^{-2}\,s^{-1}}$) (0.3-10 keV)	Luminosity[5] ($10^{38}\,\mathrm{erg\ s^{-1}}$) (0.3-10 keV)	PI
2.33[6]	–	24.60	< 1.2	1.4	< 1.9	< 3.75	Fong
9.19	> 8	49.41	2.36 ± 0.70	$0.78^{+0.67}_{-0.56}$	$6.80^{+2.82}_{-2.92}$	$13.5^{+5.59}_{-5.79}$	Troja
15.39	> 8	96.1	2.95 ± 0.56	$2.05^{+0.49}_{-0.33}$	$5.32^{+1.42}_{-0.99}$	$10.6^{+2.81}_{-1.97}$	Haggard, Troja
108.39	> 8	98.83	13.5 ± 1.17	$1.58^{+016}_{-0.16}$	$25.6^{+2.49}_{-2.34}$	$50.8^{+4.93}_{-4.65}$	Wilkes
157.76	> 8	104.85	13.7 ± 1.14	$1.64^{+0.15}_{-0.18}$	$26.7^{+2.90}_{-2.33}$	$52.8^{+5.74}_{-4.63}$	Wilkes
259.67	> 8	96.78	6.85 ± 0.85	$1.47^{+0.23}_{-0.22}$	$13.9^{+2.13}_{-2.01}$	$27.6^{+4.22}_{-3.98}$	Wilkes
358.61	> 8	67.16	3.94 ± 0.77	$2.02^{+0.44}_{-0.34}$	$7.67^{+1.76}_{-1.46}$	$15.2^{+3.50}_{-2.89}$	Troja
581.82	> 8	98.76	1.44 ± 0.39	$1.19^{+0.89}_{-0.61}$	$3.88^{+1.97}_{-1.40}$	$7.68^{+3.90}_{-2.77}$	Margutti
741.48	6.5	98.86	1.03 ± 0.34	$0.92^{+0.91}_{-0.77}$	$3.32^{+1.75}_{-1.42}$	$6.58^{+3.46}_{-2.81}$	Troja
939.31	5.4	96.60	0.75 ± 0.29	1.603	$1.81^{+0.79}_{-0.94}$	$3.59^{+1.57}_{-1.86}$	Margutti
1234.11	7.2	189.06	0.77 ± 0.21	1.603	$2.31^{+0.57}_{-0.81}$	$4.57^{+1.13}_{-1.61}$	Margutti
939.31				1.565 ± 0.025	$2.14^{+0.74}_{-1.35}$	$4.23^{+1.46}_{-2.69}$	Margutti
1234.11				1.565 ± 0.025	$2.33^{+0.60}_{-0.85}$	$4.62^{+1.19}_{-1.69}$	Margutti

[1] Exposure-time weighted average time since merger of all the observations within an epoch.

The obsIDs within each epoch are as follows: 9 days: 19294; 15 days: 18988, 20728; 108 days: 20860, 28061; 158 days: 20936, 20937, 20938, 20939, and 20945; 260d: 21080, and 21090; 359 days: 21371; 582 days: 21322, 22157, and 22158; 742 days: 21372, 22736, and 22737; 939 days: 21323, 23183, 23184, and 23185; and 1234 days: 22677, 24887, 24888, 24889,2 3870, 24923, and 24924.

[2] Gaussian equivalent.

[3] Inferred from `dmcopy` and energy filtering in channels 500-8000.

[4] Spectral photon index, where $F_\nu \propto \nu^{-\beta}$ and $\Gamma = \beta + 1$.

[5] Calculated using a distance of 40.7 Mpc (Cantiello et al. 2018)

[6] From Margutti et al. 2018.

Table 3.2. Radio Observations Log. Time on source for the VLA observations was calculated using the CASA analysis utilities task `timeOnSource`.

Start Date UTC	δt (days)	Observatory	Program /Project	On Source Time (minutes)	Mean Frequency (GHz)	Frequency Range (GHz)
15-Dec-2020	1216.08	VLA	SL0449	204.23	3	2-4
27-Dec-2020	1228.02	VLA	SL0449	204.23	3	2-4
02-Feb-2021	1264.95	VLA	SM0329	204.27	3	2-4
10-Feb-2021	1272.88	VLA	SM0329	164.40	15	12-18
03-Jan-2021	1234.66	MeerKAT	DDT-20201218-JB-01	434.40	0.816	0.544-1.088

Table 3.3. Chance probability of measuring a number of X-ray photon counts at least as extreme as the one observed at t_1, t_2 and combined, as a result of a stochastic fluctuation of the source and background. See §3.4 for details.

t_{start} (days)	P_1	P_2	$P_1 \times P_2$	$P_{combined}$
157.	6.0×10^{-2}	2.6×10^{-4}	1.7×10^{-5}	9.5×10^{-5}
163.	1.1×10^{-1}	9.7×10^{-4}	1.2×10^{-4}	6.7×10^{-4}
172.	1.2×10^{-1}	1.2×10^{-3}	1.8×10^{-4}	9.5×10^{-4}
196.	1.4×10^{-1}	1.5×10^{-3}	2.5×10^{-4}	1.4×10^{-4}
209.	1.4×10^{-1}	1.5×10^{-3}	2.5×10^{-4}	1.3×10^{-4}
215.	1.3×10^{-1}	1.5×10^{-3}	2.4×10^{-4}	1.2×10^{-4}
230.	1.4×10^{-1}	1.5×10^{-3}	2.4×10^{-4}	1.3×10^{-4}
γ_B	P_1	P_2	$P_1 \times P_2$	$P_{combined}$
7	1.5×10^{-1}	2.8×10^{-3}	4.7×10^{-4}	2.1×10^{-3}
10	1.2×10^{-1}	2.7×10^{-3}	3.4×10^{-4}	1.4×10^{-3}
12	7.2×10^{-2}	7.4×10^{-4}	5.6×10^{-5}	2.6×10^{-4}

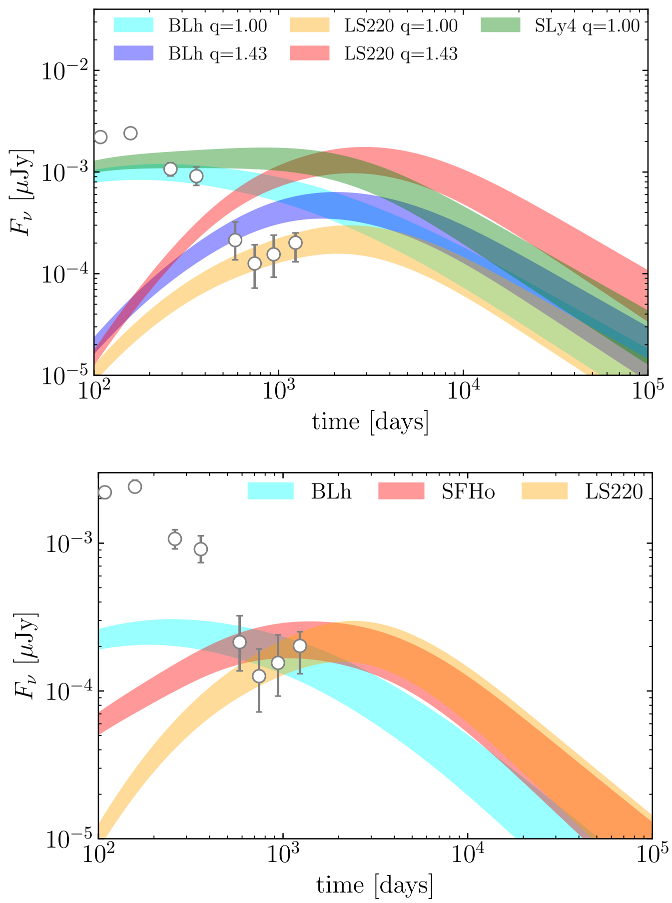

Figure 3.9 *Upper Panel:* Kilonova afterglows from a set of ab-initio numerical relativity BNS merger simulations. In these simulations the kilonova ejecta is of dynamical nature, with resulting kinetic energy profiles shown in Figure 3.10. Different colors correspond to different EoSs (BLh, LS220, and SLy4) and NS mass ratios q. Good quantitative agreement between the numerical relativity predictions and the observation is obtained. The light curves are computed assuming an ISM density of $n_{\rm ISM} = 6 \times 10^{-3}$ cm^{-3}, and microphysical parameters, $\epsilon_{\rm e} = 10^{-1}$, $\epsilon_{\rm B} = 10^{-2}$. *Lower Panel:* Effect of the extrinsic parameters (i.e. density and shock microphysics) on the kilonova afterglow emission from equal-mass NS binaries (i.e., $q \approx 1$ that is typical of the Galactic population) and different EoSs. For LS220, BLh and SFHo current observations are consistent with $n \sim 6 \times 10^{-3}, 5 \times 10^{-3}, 5 \times 10^{-3}\,{\rm cm}^{-3}$ and $\epsilon_{\rm B} \sim 10^{-2}, 2 \times 10^{-3}, 10^{-3}$, respectively, for a fiducial $\epsilon_{\rm e} = 0.1$. In both panels the viewing angle is assumed to be 30° from the polar axis. The bands correspond to light curves with the electron distribution power-law index p varying between 2.05 and 2.15.

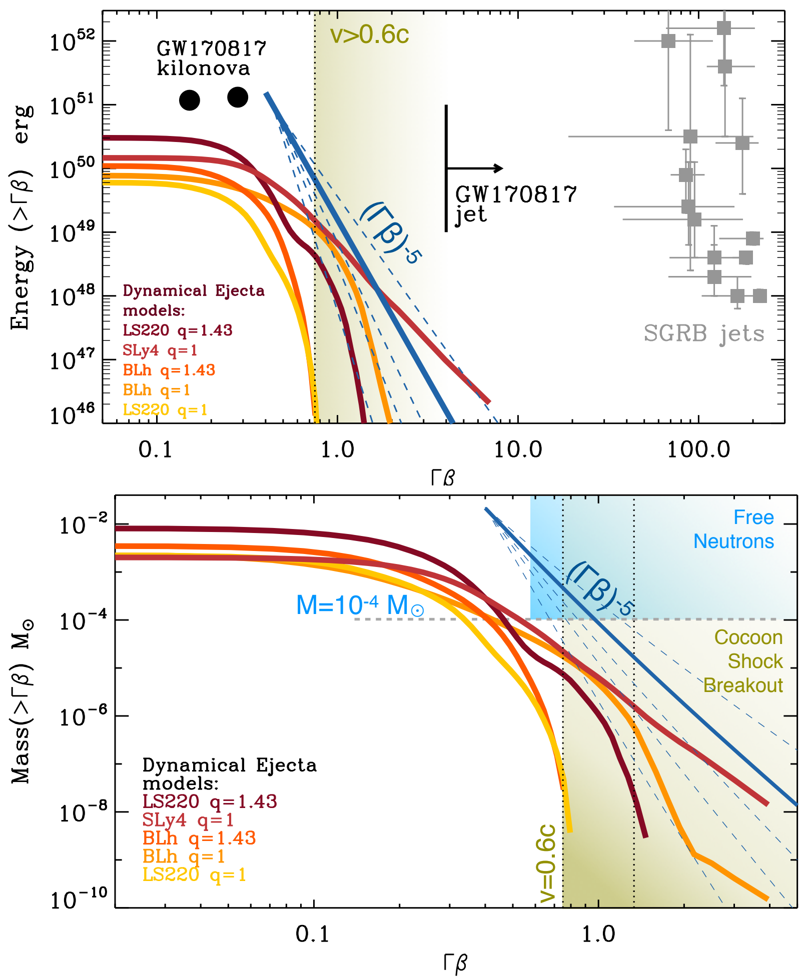

Figure 3.10 *Upper Panel:* Colored lines: kinetic energy profile of the fastest kilonova ejecta as a function of specific momentum $\Gamma\beta$. Dark-red to orange shade: dynamical ejecta profiles as inferred from ab-initio numerical-relativity simulations described in §3.7 for different EoS and NS mass ratios q. Blue lines: $E_{\rm KN}(>\Gamma\beta) \propto (\Gamma\beta)^{-\alpha}$ analytical profiles that include the contributions from all types of kilonova ejecta for $\alpha = 4, 5, 6, 7, 9$. Black filled circles: kinetic energy inferred from the modeling of the UV/optical/NIR kilonova emission (Villar et al. 2017). Grey squares: SGRB jets (Wu et al. 2019). *Lower Panel:* kilonova ejecta profiles in the mass phase-space. Green colored area: region of the parameter space consistent with a cocoon shock breakout origin of GRB 170817A (Gottlieb et al. 2018). Blue colored area: region of the parameter space which is suggestive of a free-neutron component of the ejecta expected to power a short-lived UV/optical transient.

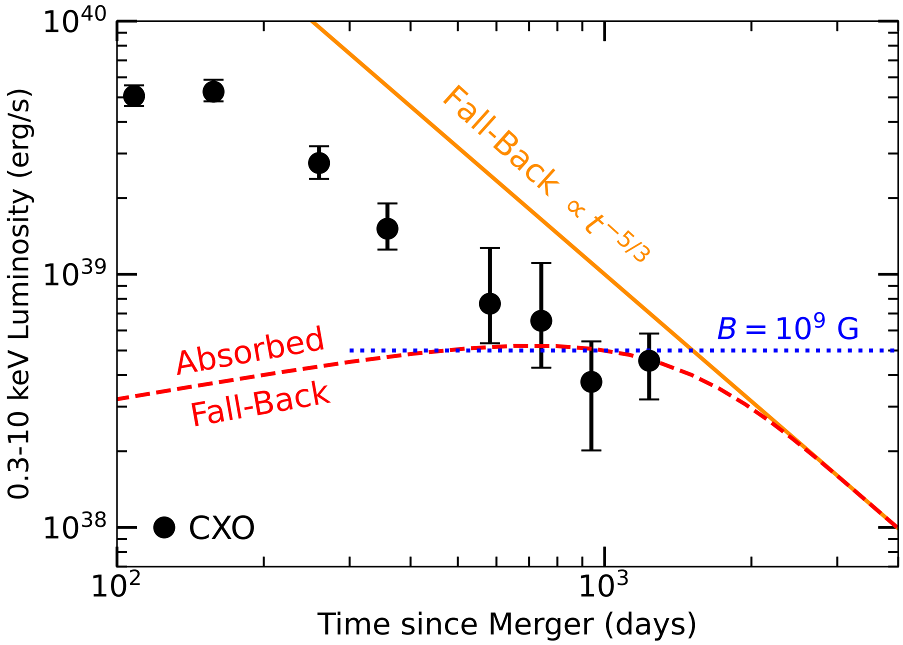

Figure 3.11 Observed 0.3 – 10 keV X-ray luminosity (black filled circles) compared to two sources of energy to power the X-ray excess in the compact-object powered scenario: (1) accretion-powered fall-back luminosity, both intrinsic (orange solid line) and observed (red dashed line), i.e. with a correction for absorption by the kilonova ejecta of the form $\propto (1 - e^{-(t/t_{\rm thin})^2})$, where $t_{\rm thin} \approx 1000$ days (Eq.3.6). And, (2) magnetar spin-down luminosity (Eq. 3.10, dotted blue line) for $B \sim 10^9$ G to match the level of the observed X-ray emission.

CHAPTER 4

ASASSN-15oi: An Unusual TDE with Unprecedented Multiple Radio Flares

At the time of writing this thesis, this chapter is still a work in progress. I have tried to gather as much information possible on this unusual event to shine light on its unique behavior with the help of multiwavelength observations.

4.1. Introduction

When a star strays too close to a supermassive black hole (SMBH) in the center of a galaxy, the strong tidal forces of the black hole shred the star apart powering an energetic and short-lived transient event known as a tidal disruption event (TDE). TDEs provide an exclusive window to study the previously dormant SMBHs and the make up of the environment in the central regions of the galaxies. However, the complex physical processes that occur when a star gets tidally disrupted are still largely unexplored. While the early–time optical and soft X-ray wavelengths probe the thermal emission tracing the fallback accretion of the disrupted material towards the center of the event, radio wavelengths probe the regions away from the center where the outflows launched during the disruption interact with the surrounding medium. Existing observations of TDEs have already displayed a broad underlying diversity in these events. For e.g., *Swift* J1644+57 with its extremely bright $\gamma-$ray, X-ray and radio emission was the first TDE to reveal the presence of an ultra-relativistic jet (e.g. Berger et al. 2012; Eftekhari et al. 2018). We have now observed a few other TDEs with a jet observed on-axis. On the other hand, broadband observations of TDEs such as ASASSN-14li showed only the presence of a non-relativistic outflow component (Alexander et al. 2016). The number of TDEs detected have exponentially increased because of growing number of sensitive time-domain surveys in the past decade, but so has the puzzling diversity of this class of events.

More recently, a few TDEs (Horesh et al. 2021a; Horesh et al. 2021b), that were discovered with no early–time radio emission have instead shown late–time flaring in radio $\sim$ months – years post–discovery. ASASSN-15oi was one of them whose unusual radio behavior was first reported in Horesh et al. 2021a. Independently from the campaigns that resulted in the discovery of the "first" delayed flare at $\delta t \sim 180$ days in ASASSN-15oi, our team identified an unprecedented "second" flare–up in ASASSN-15oi in the archival images of the VLA Sky Survey data at $\delta t \sim 4$ years making it unique among the class of TDEs with late–time radio flaring.

ASASSN-15oi was optically discovered on August 14, 2015 (Brimacombe et al. 2015; all times are measured in reference to this date) at a distance of ~ 216 Mpc (Holoien et al. 2016a; Gezari et al. 2017) with the All-Sky Automated Survey for SuperNovae (ASAS-SN; Shappee et al. 2014). The early time observations of ASASSN-15oi are reported in Holoien et al. 2016a, Gezari et al. 2017 and Holoien et al.

2018. The optical observations showed a very rapid evolution in the spectral features (e.g., the blue continnum and the emission lines) that disappeared on much shorter timescales (Holoien et al. 2018) than what is typical for other TDEs. The observations at $\delta t < 100$ days declined steeply as $F \propto t^{-5/3}$, as expected in the fall-back accretion regime, but later leveled off as a plateau at the host galaxy level. While the optical wavelengths were dominated by the host galaxy at later times, the transient was still dominating UV wavelengths above the host galaxy level. The X-rays on the other hand were much weaker at the beginning compared to other TDEs in the literature, brightening by a factor of ~ 6 between $\delta t \sim 80$ and ~ 230 days. This behavior was also reported in Gezari et al. 2017. They concluded that the X-ray brightening is an evidence for a delay in the formation of an accretion disk in the TDE (as also postulated by Lodato 2012; Piran et al. 2015), and therefore, interpreted the optical/UV flare at the time of discovery as originating in stream–stream collisions. All the previous interpretations of ASASSN-15oi have been single wavelength specific, and furthermore do not include the study of second radio flare. In this work, we report the results of our multiwavelength campaign to monitor the second flare, along with a homogeneous analysis and interpretation of the existing broadband observations in context of both the radio flares together.

4.2. Observations and Data Analysis

ASASSN-15oi has been densely monitored in UV (*Swift*-UVOT, Holoien et al. 2016a; Gezari et al. 2017; Holoien et al. 2018; Hinkle et al. 2020), in the X-rays

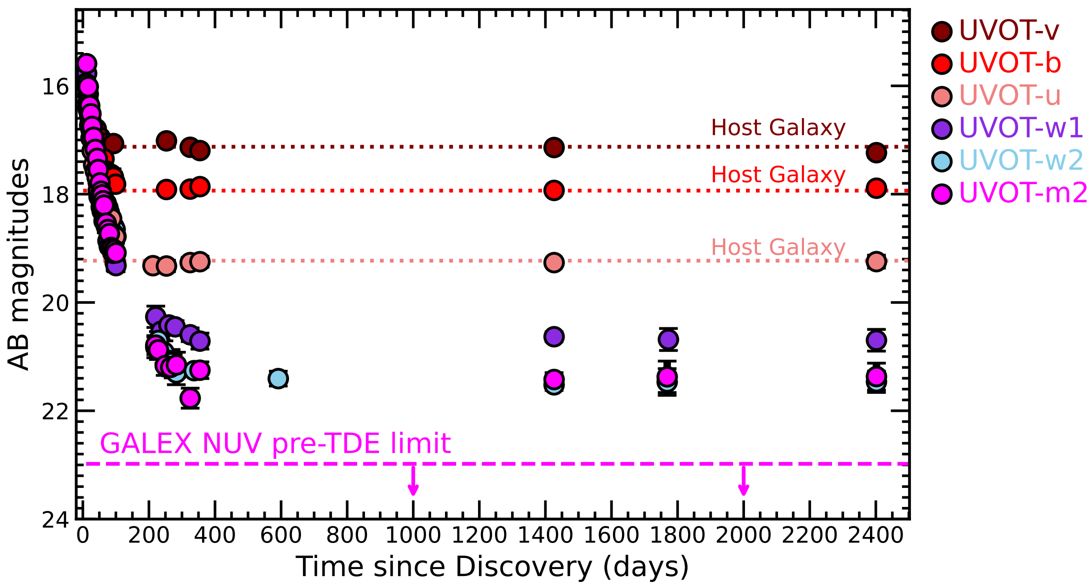

Figure 4.1 Long-term evolution of ASASSN-15oi as captured by *Swift*-UVOT. Filled circles mark the total emission (i.e. TDE + host galaxy) at the location of ASASSN-15oi. While at $\delta t \gtrsim 200\,\mathrm{d}$ the optical emission is dominated by the host galaxy light (horizontal dotted lines as determined by Hinkle et al. 2021), the UV emission at the location of ASASSN-15oi remains bright and does not relax to the pre-TDE UV flux levels (horizontal dashed line). Magnitudes have been corrected for Galactic extinction.

(*Swift*-XRT and *XMM-Newton*; Holoien et al. 2016a; Gezari et al. 2017; Holoien et al. 2018) and in the radio bands with the Very Large Array, VLA (Horesh et al. 2021a). Here we report on our late-time UV, X-ray and radio campaigns that followed, which include *Swift*-UVOT, *Swift*-XRT, *XMM-Newton*, VLA as well as Very Long Baseline Interferometry (VLBI) observations at $\delta t > 600\,\mathrm{d}$. For *Swift*-XRT data we provide a self-consistent flux calibration of the entire data set that accounts for the spectral evolution of the source.

4.2.1. UV: *Swift*-UVOT

Swift-UVOT (Gehrels et al. 2004; Roming et al. 2005) started observing ASASSN-15oi on August 23, 2015 until March 12, 2022, covering the evolution of the TDE during in the interval $\delta t = 8 - 2402\,\mathrm{d}$. We analyzed the *Swift*-UVOT photometric data following the prescriptions of Brown et al. 2009, with the updated calibration files (Poole et al. 2008; Breeveld et al. 2010). All the photometry has been extracted using a $5''$ radius aperture and a $36''$ region free of sources for the background. When possible, we merged observations to achieve a minimal source detection significance of $\approx 10\,\sigma$. For observations at $\delta t < 500\,\mathrm{d}$ we find excellent agreement with the photometry presented in Hinkle et al. 2021. Finally, we corrected for Galactic extinction assuming the Fitzpatrick 1999 reddening law and $R_{\mathrm{V}} = 3.1$.[1] The resulting extinction corrections are $A_v = 0.185$ mag, $A_b = 0.245$ mag, $A_u = 0.294$ mag, $A_{w1} = 0.377$ mag, $A_{w2} = 0.551$ mag, $A_{m2} = 0.547$ mag. The long-term UV evolution of ASASSN-15oi is shown in Figure 4.1.

In stark contrast with the X-ray and radio emissions that show dramatic temporal variability on short time scales (§4.2.2, §4.2.3, §4.2.4), the late-time *Swift*-UVOT photometry at $\delta t > 600\,\mathrm{d}$ is consistent with constant flux (Figure 4.1). We find no significant evidence for fading at $\delta t \approx 500 - 2400\,\mathrm{d}$ in any of the *Swift*-UVOT filters. However, while at optical wavelengths (i.e. *Swift*-UVOT u, b, and v filters) the flux

[1] Hinkle et al. 2021 adopt a Cardelli et al. 1989 reddening law. Here we adopt the Fitzpatrick 1999 reddening law following the findings by Schlafly et al. 2011. For the $R_{\mathrm{V}} = 3.1$ curves the difference in the A_λ values of *Swift*-UVOT filters are ≤ 0.015 mag.

is consistent with the pre-TDE host galaxy level as determined by the updated host-galaxy modeling of Hinkle et al. 2021, at UV wavelengths (i.e. *Swift*-UVOT $w1$, $w2$, and $m2$ filters) we confirm the presence of an excess of emission that was reported by Holoien et al. 2018 using data at earlier epochs $\delta t \approx 250 - 600\,\mathrm{d}$. As of $\delta t = 2400\,\mathrm{d}$, with $m_{w1} \approx 21\,\mathrm{mag}$, $m_{w2} \approx 22\,\mathrm{mag}$ and $m_{m2} \approx 22\,\mathrm{mag}$ (observed mags, AB system), ASASSN-15oi is $\approx 0.7\,\mathrm{mag}$, $\approx 1.5\,\mathrm{mag}$ and $\approx 0.9\,\mathrm{mag}$ brighter, respectively, than the best-fitting pre-TDE host-galaxy model of Hinkle et al. 2021. From a completely observational perspective that is independent from the host-galaxy light modeling, pre-TDE *Galaxy Evolution Explorer* (*GALEX*) observations constrain the UV emission of the host-galaxy as $m_{NUV} > 22.98\,\mathrm{mag}$ (Holoien et al. 2018; Hinkle et al. 2021). For a black-body spectrum with $T \sim 2 \times 10^4\,\mathrm{K}$ that best fits the late-time UVOT data, the *GALEX* NUV to *Swift*-UVOT $m2$ filter correction term is $\delta mag \approx 0.05$ mag, which implies that at $\approx 2400\,\mathrm{d}$ after the TDE, the UV emission is ≈ 2.3 times brighter than in the pre-TDE era.

Finally, we note the presence of an unrelated optical/UV source at $\approx 10''$ from ASASSN-15oi (S1 hereafter).

4.2.2. X-rays: *Swift*-XRT

We analyzed *Swift*-XRT data (Gehrels et al. 2004; Burrows et al. 2005) using the online tools[2] (Evans et al. 2009) and custom `IDL` scripts following the prescriptions in Margutti et al. 2013. *Swift*-XRT has observed ASASSN-15oi starting on August

[2]The Swift-XRT data products generator, https://www.swift.ac.uk/user_objects/docs.php

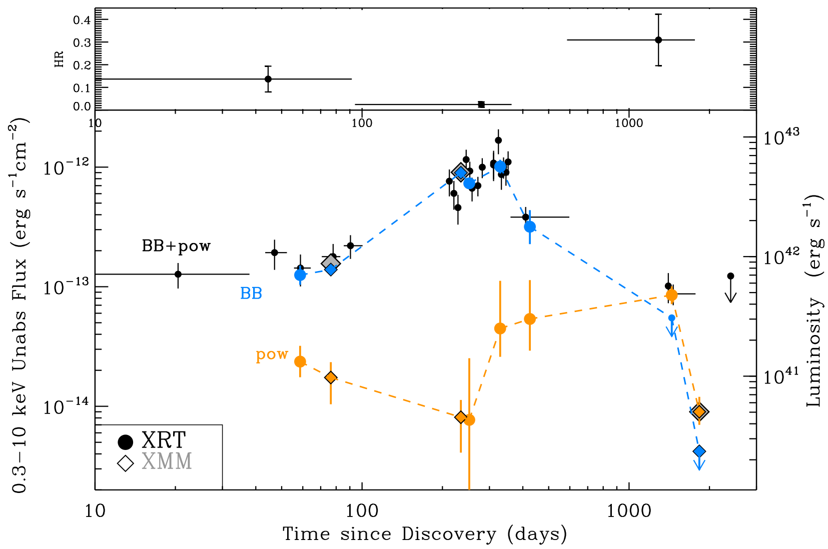

Figure 4.2 Evolution of the 0.3-10 keV X-ray emission from ASASSN-15oi as constrained with observations by *Swift*-XRT (circles) and *XMM-Newton* (diamonds). The data have been corrected for Galactic absorption. The rise of the X-ray emission at $\delta t \leq 350\,\mathrm{d}$ is dominated by the black-body component (blue), while the power-law spectral component dominates the emission at $\delta t \geq 1400\,\mathrm{d}$. The last two X-ray detections at $\delta t \approx 1400\,\mathrm{d}$ and $\delta t \approx 1833\,\mathrm{d}$ imply a remarkably steep decay with $F_x \propto t^{-8.5}$ *if* the outflow was launched at the time of the optical discovery of the transient. This analysis shows that X-ray emission is dominated by the non-thermal component when the second radio flare appears at $\delta t \gtrsim 1000\,\mathrm{d}$. *Upper Panel:* temporal evolution of the Hardness Ratio (HR) here defined as the ratio of the *Swift*-XRT counts in the 0.3-1.5 keV to the 1.5-10. keV energy bands. The very soft emission around the time of the light-curve peak is followed by hardening as the black-body component subsides.

23, 2015 ($\delta t \approx 8\,\mathrm{d}$). Observations acquired under IDs 00033999 and 00095141 extend until 2020 June 21 ($\delta t \approx 1773\,\mathrm{d}$) and showed a progressive brightening (accompanied by spectral softening) of the source until $\delta t \approx 350\,\mathrm{d}$, followed by rapid fading of a factor ≈ 10 in luminosity by $\delta t \approx 600\,\mathrm{d}$, Figure 4.2 (originally presented in Gezari et al. 2017, their Fig. 3; Holoien et al. 2018, their Fig. 6). Additional XRT observations of ASASSN-15oi acquired at $\approx 1400-1460\,$d showed fainter but persistent X-ray emission. A final epoch of *Swift*-XRT data was acquired on 2022 March 11 ($\delta t \approx 2401\,$d) under ID 00096018. No X-ray source is detected at the location of the transient and we infer a count-rate $3\,\sigma$ upper limit of $4.3\times10^{-3}\mathrm{c\,s^{-1}}$ (exposure of 7.2 ks, 0.3-10 keV).

We extracted five spectra (Table 4.1). Following the findings by Holoien et al. 2016a; Gezari et al. 2017; Holoien et al. 2018, we fitted the spectra in the 0.3-10 keV energy range with an absorbed two-component model featuring a power-law and a black-body, i.e. `tbabs*(cflux*pow+cflux*bbody)` within `XSPEC` v12.12.1. We found no evidence for intrinsic absorption and we thus assumed $N_{\mathrm{H,int}} = 0\,\mathrm{cm^{-2}}$. The Galactic neutral hydrogen column density in the direction of the transient is $N_{\mathrm{H,gal}} = 5.6\times10^{20}\,\mathrm{cm^{-2}}$ (Kalberla et al. 2005b). The best-fitting results are reported in Table 4.1: consistent with Holoien et al. 2016a; Holoien et al. 2018 and Gezari et al. 2017, we find that the brightening of the source at $\delta \leq 350\,$d is due the progressive strengthening of the soft emission of the black-body component that dominates over the non-thermal power-law component. Differently from Holoien et al. 2018, we find that a spectral power-law component is needed to account for the harder photons at all times,[3] and dominates the spectrum at $\delta t \approx 1400\,$d. The black-body component shows rapid fading $F_x \propto t^{-4.5}$ between 330-425 d and becomes undetectable by the time of the following *Swift*-XRT observation at $\delta t \approx 1400\,$d. The temperature T

[3]This discrepancy is likely the result of the use of the restricted 0.3-5 keV energy range by Holoien et al. 2016a; Holoien et al. 2018 to fit the X-ray spectra, which leads to reduced sensitivity to harder spectral components.

of the black-body and the index of the power-law component Γ show no significant evolution with time.

The temporal evolution of the relative strength of the thermal and non-thermal spectral components in ASASSN-15oi implies a time-varying count-to-flux conversion factor. Following Margutti et al. 2013, we used the results from the time-resolved spectral analysis to perform a self-consistent flux calibration of the count-rate light-curve. Specifically, we derived a count-to-flux conversion as a function of time since discovery by linearly interpolating in the log space the count-to-flux conversion factors derived from the five spectra of Table 4.1. The 0.3-10 keV unabsorbed flux light-curve of ASASSN-15oi is shown in Figure 4.2. Since optical discovery, this transient has radiated $\sim 2 \times 10^{50}$ erg in X-ray emission in the 0.3-10 keV band.

4.2.3. X-rays: *XMM-Newton*

Following the prominent re-brigthening of ASASSN-15oi at radio frequencies at $\delta t \gtrsim 1000\,\mathrm{d}$ (Horesh et al. 2021a; §4.2.4, Figure 4.4) we acquired deep X-ray observations with the X-ray Multi-Mirror Mission Newton (*XMM-Newton*; Jansen et al. 2001) on 08 October, 2020 ($\delta t = 1830\,\mathrm{d}$, exposure time $\approx$ $23.6, 23.8, \mathrm{and} 12.5\,\mathrm{ks}$ for MOS1, MOS2, and PN cameras, respectively ; observation ID 0872390301; PI Hajela). The results from the analysis of the first two *XMM-Newton* observations (PI Gezari) were reported in Gezari et al. 2017 and Holoien et al. 2018. For consistency, we re-reduce these data here along with our latest epoch of observations.

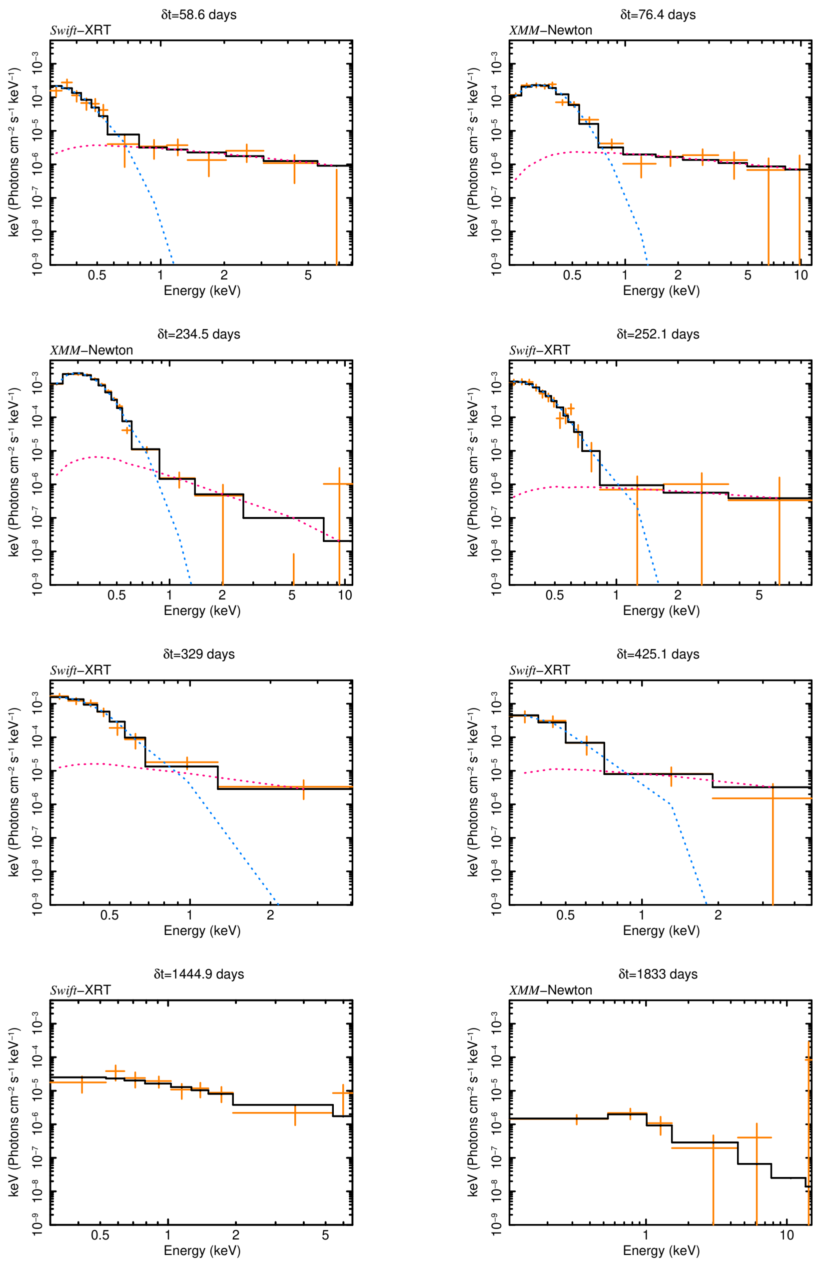

Figure 4.3 Unfolded *XMM-Newton* and *Swift*-XRT spectra of ASASSN-15oi at $\delta t =$ 76.4 d (left), 234.5 d (central) and 1833 d (right) in the 0.2-12 keV energy range. Blue (pink) dashed line: black-body (power-law) component. For the three plots the y-axis covers the same dynamical range. At late times the black-body component that was responsible for the source brightening until $\delta t \approx 350$ d becomes undetectable and the spectrum consists of an absorbed sinple power-law.

All *XMM-Newton* observations were performed with the European Photon Imaging Camera (EPIC) detector in full-frame mode with the thin filter. We processed all the observations using standard routines in the Scientific Analysis System (SASversion–1.3) software package and the corresponding calibration files. Filtering out time intervals with high background flaring activity results in net exposure times reported in Table 4.1. [4] An X-ray source is clearly detected in all three *XMM-Newton* observations at the position of the radio/optical transient. We extracted a spectrum from a circular region of 15″ (300 pixels) radius centered at the source position using a nearby 75″ source-free background region. Similarly to Gezari et al. 2017, we perform the spectral analysis of the earlier two observations using only the EPIC-pn data (given the relatively larger number of counts observed in the pn channel). For the latest observation, however, we perform a joint spectral analysis of the data from all three EPIC cameras (MOS1, MOS2, and pn).

We fit the data in 0.2–12 keV energy range with the same two-component model that we used for *Swift*-XRT data: an absorbed (thermal) blackbody (BB) component + an absorbed (non-thermal) power-law (PL) component, `tbabs*ztbabs*(cflux *bbody +cflux*pow)` within *XSPEC* (v.12.12.1). As for *Swift*-XRT, we used $N_{\rm H,gal} = 5.6 \times 10^{20}\,{\rm cm}^{-2}$ and $N_{\rm H,int} = 0\,{\rm cm}^{-2}$ as we found no evidence for intrinsic absorption. For each epoch, the best-fitting BB temperature, photon index (Γ), unabsorbed fluxes corresponding to respective components are reported in Table 4.1. The unfolded spectra are shown in Figure 4.3. Our results for the first two epochs are broadly

[4] We note that the slightly different net exposure times reported by Gezari et al. 2017 for the first two observations likely result from different filtering criteria.

consistent with those reported in Gezari et al. 2017. For the third epoch at $\delta t \approx$ 1833 d, we find that a black-body component is not required to explain the *XMM-Newton* observations, which are instead consistent with a non-thermal power-law spectrum only (Figure 4.3). This result is consistent with our findings from the *Swift*-XRT spectrum at $\delta t \approx 1400$ d, which we found to be dominated by the power-law spectral component (§4.2.2). We plot the temporal evolution of the total unabsorbed X-ray flux as well as the black-body and the power-law components in Figure 4.2.

4.2.4. Radio: VLA

Horesh et al. 2021a started monitoring ASASSN-15oi with the Very Large Array (VLA) $\delta t \approx 8$ d after optical discovery, reporting a first radio detection at $\delta t \approx 182$ d that provided evidence for a significant brightening of the source compared to earlier upper limits (Figure 4.4). This first radio brightening was followed by a second, even more dramatic radio re-brightening at $\delta t > 1000$ d that constitutes the focus of this study.

ASASSN-15oi's second radio flare was discovered in data from the VLA Sky Survey (VLASS, Lacy et al. 2020). ASASSN-15oi was observed as part of regular survey operations on 2019 July 1, revealing that the flux density at 3 GHz had increased by a factor of ~ 3000 compared to the previous observation in 2017 (Horesh et al. 2021a). To further explore the nature of this second radio flare, we obtained multi-frequency observations with the VLA under the DDT program 20A-492 (PI: Alexander). The data were taken when the array was in its C configuration. The data were reduced and imaged using standard procedures in CASA (McMullin et al. 2007b). ASASSN-15oi is detected as a very bright radio source at all frequencies. We measured the flux density of ASASSN-15oi using the `imtool` package within `pwkit` (Williams et al. 2017b) and report the results in Table 4.2.

To monitor the spectral and temporal evolution of the second radio flare in ASASSN-15oi, we initiated further broadband observations with the VLA under program VLA/21A-303 (PI Hajela). ASASSN-15oi was observed in a standard phase referencing mode for 18-20 minutes at the mean frequencies of 1.5 GHz (L-band), 3 GHz (S-band), 6 GHz (C-band), and 10 GHz (X-band), for a total time of 1.2 hours. We used 3-bit samplers for C and X bands and 8-bit samplers for L and S bands. The observations were conducted in B-configuration.

We used the VLA calibration pipeline packaged with CASA v.6.2.1.7, with 3C48 as the flux calibrator, and ICRF J210101.6−293327 (PKS J2101−2933) as the complex gain calibrator. After manually inspecting the data, we further flagged antennas with bad solutions and some additional weak RFI and re-ran the pipeline. To densely sample the spectral energy distribution (SED), we divided the data-set in every observing band further into 4 sub-bands, and imaged each sub-band individually. We imaged the data using `CLEAN` algorithm using Briggs weighting with a robust factor of 0.5. We measured the flux densities using PyBDSF (Python Blob Detection and Source Finder) with an elliptical Gaussian fixed to the dimensions of the `CLEAN` beam. Since the flux density scale calibration has an accuracy of 3% – 5% for our observing bands, we add a 5% systematic uncertainty to our measurements. All the radio flux densities are tabulated in Table 4.2. We show the evolution of the radio SED of ASASSN-15oi in the top panel of Figure 4.4.

4.2.5. Radio: VLBI

We observed ASASSN-15oi with the Very Long Baseline Array (VLBA) of the National Radio Astronomy Observatory (NRAO), using all antennas except Brewster, under observing code BH238. The total observing time was 5.5 h, with a midpoint of 2022 Feb. 22.75 (UT; MJD = 59632.75). We recorded a total bandwidth of 512 MHz, centered on 8.30 GHz, in two polarization, using a total bitrate of 4096 Mbps. The VLBI data were correlated with NRAO's VLBA processor, and the analysis carried out with NRAO's AIPS. The initial flux density calibration was done through measurements of the system temperature at each telescope, and then improved through self-calibration of the reference source. A correction was made for the dispersive delay due to the ionosphere using the AIPS task TECOR, although the effect at our frequency is not large. We phase-referenced the observations of ASASSN-15oi to PMN J2036$-$2830, using a ~ 3.7 min cycle, of which ~ 2.5 min were on ASASSN-15oi.

We show the VLBI image of ASASSN-15oi in Fig. 4.5, made using the CLEAN algorithm. The total CLEANed flux density was 1.2 mJy, and the image background rms was 140 μJy beam^{-1}. For an ideal, unresolved source, the peak brightness should also be 1.2 mJy, however, the peak peak brightness in the image was somewhat larger 1.5 mJy beam^{-1} so the relatively low-dynamic-range image allows only an approximate determination of the flux density. The image dynamic range was 11:1.

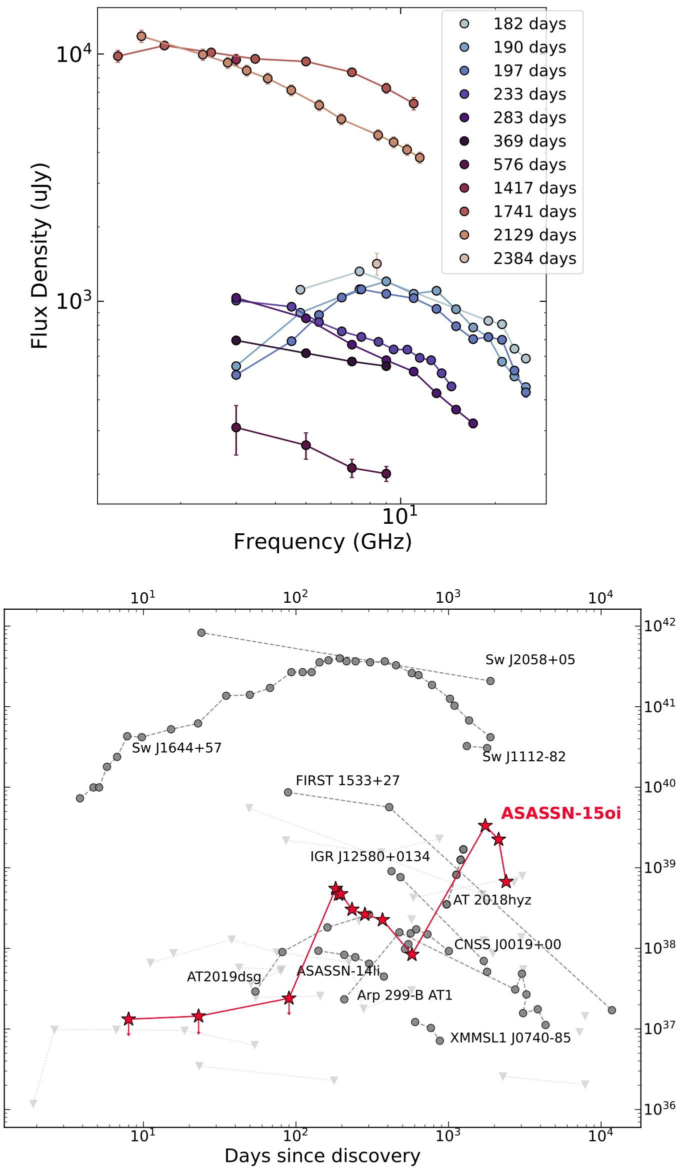

Figure 4.4 *Top panel*: Evolution of the emission from ASASSN-15oi across the radio spectrum from the time of the first radio detection at $\delta t = 182\,\mathrm{d}$ until $\delta t = 2384\,\mathrm{d}$. Observations at $\delta t \leq 1417\,\mathrm{d}$ have been presented in Horesh et al. 2021a, while data at $\delta t \geq 1741\,\mathrm{d}$ are presented here for the first time. All the flux densities are also reported in Table 4.2.
Bottom panel: Temporal evolution of the radio luminosity νL_ν of ASASSN-15oi (red stars) in the context of all radio observations of TDEs. For ASASSN-15oi we use observations carried out in the frequency range 6.5–8.5 GHz, while for the TDE comparison sample we use $\nu = 3 - 9$ GHz. At $\delta t \approx 1700\,\mathrm{d}$, ASASSN-15oi is the most luminous known radio TDE among those not associated with relativistic jets (i.e., Sw J1644+57, Sw J2058+05 and Sw J1112-82). References: Alexander et al. 2016; Alexander et al. 2020; Anderson et al. 2020; Cendes et al. 2021b; Horesh et al. 2021a; Cendes et al. 2022

ASASSN-15oi is not resolved at our FWHM resolution of 2.47×0.78 mas at p.a. $-5°$.

For marginally resolved sources, such as ASASSN-15oi, the best values for the flux density and source size come from fitting models directly to the visibility data (e.g. Bietenholz et al. 2010), rather than from imaging. Fitting a circular Gaussian to the visibilities by least squares (AIPS task OMFIT), we find that the best fit has a FWHM size of 0 ± 1 mas and a flux density or 1.38 ± 0.3 mJy, with the caveat that the fitted size is positively correlated with the fitted flux density.

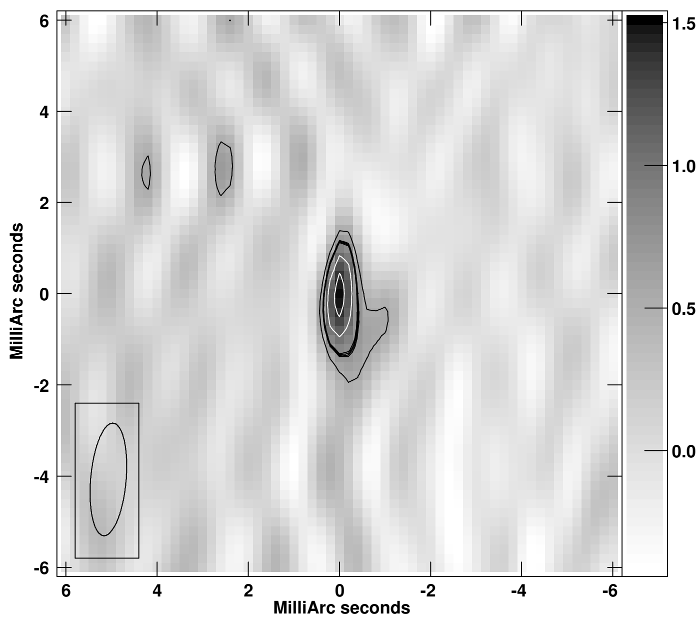

Figure 4.5 A VLBI image of ASASSN-15oi on 2022 Feb. 22 ($\delta t = 2384$ d), at 8.3 GHz. The peak brightness was 1.5 mJy beam^{-1}, and the image background rms brightness was 140 μJy beam^{-1}. The greyscale is labelled in mJy beam^{-1}. The contours are drawn at -35, 35, **50** (emphasized), 70 and 90% of the peak brightness. The FWHM resolution is shown at lower left, and was 2.47×0.78 mas at p.a. $-5°$. North is up and east to the left.

4.3. Radio Data Modeling

The radio spectral evolution of ASASSN-15oi (left panel of Figure 4.4) is unlike any other TDE observed to date. We first attempt to fit these observations with a standard synchrotron model that is commonly used in the TDE literature, where a spherical blastwave moving at relativistic or sub-relativistic speeds interacts with the surrounding cold medium and accelerates electrons into a power–law (PL) distribution with $N_e(\gamma) \propto \gamma^{-p}$ for $\gamma \geq \gamma_m$ (where p is the electron power–law index, and γ is the electron Lorentz factor). The resulting population of electrons gyrate in the amplified magnetic field and radiate synchrotron emission. By studying the evolution of synchrotron spectra across both the flares, we can derive fundamental physical parameters such as the shock energy (U), the size of the emitting region (R), the strength of the magnetic field (B) and the density of the ambient medium (n).

To begin, we fit the radio SEDs of both flares with either a broken power–law or a simple power-law spectral model as appropriate. For example, a turnover is clearly observed in the first three SEDs at $\delta t \sim 182 - 197$ days associated with the first radio flare (Figure 4.4). We fit these SEDs together using a broken power–law of the form:

$$F_\nu = F_{\rm pk}\left[\left(\frac{\nu}{\nu_{\rm pk}}\right)^{\frac{\alpha_1}{s}} + \left(\frac{\nu}{\nu_{\rm pk}}\right)^{\frac{\alpha_2}{s}}\right]^s, \tag{4.1}$$

where s is a smoothing parameter (the smaller the value of s, the sharper is the turnover in the curve), $F_{\rm pk}$ is the spectral peak flux where the asymptotic power–laws intersect (this form of $F_{\rm pk}$ is used in the treatment of synchrotron emission model in the non-relativistic regime as defined by Chevalier 1998) as opposed to the peak that lies on the SED itself, and $\nu_{\rm pk}$ is the peak frequency. $\alpha_{1,2}$ are the power–law slopes on either side of the SED spectral peak. For a standard synchrotron model in the relevant spectral regime here, $\nu_{\rm pk}$ can be interpreted as the synchrotron self-absorption frequency, ν_{sa}, above which the optically-thin spectrum follows $F_\nu \propto \nu^{-(p-1)/2} \propto \nu^{\alpha_2}$ and therefore $p \equiv 1-2\alpha_2$. All the other SEDs that follow in time are best–fitted by a simple PL instead. We find that the first three SEDs have a best-fitting optically-thin spectral index, $\alpha_2 = -1.01{\pm}0.13$, which implies $p = 3.02{\pm}0.26$. However, the rest of the SEDs associated with the first flare show a shallower spectral decay with an $\alpha_2 = -0.53{\pm}0.03$, and $p = 2.06{\pm}0.06$, consistent with the findings from Horesh et al. 2021a. The simple PL radio SEDs associated with the second radio flare at $\delta t \geq 1400\,$d are also well fitted with $\alpha_2 \sim -0.6$. These results suggest that the optically thin part of the spectrum might have been dominated by two distinct physical components: one that dominated the emission of the first radio flare, and a second one associated with the second radio flare.

Following Chevalier 1998 we use the best–fitting values of p, $F_{\rm pk}$, and $\nu_{\rm pk}$ for the broken PLs and constraints on these observables in the case of simple PL spectra to infer properties of the emitting region. Specifically, we assume equipartition of energy between relativistic electrons and the post-shock magnetic field [5] and we use the equations presented in DeMarchi et al. 2022 to constrain the post-shock

[5] In order to break the degeneracy between the synchrotron model parameters in absence of other constraints, equipartition is commonly assumed in the literature with $\epsilon_e = \epsilon_B = 0.1$, where the $\epsilon_{e,B}$ are the shock microphysics parameters describing the fraction of post-shock energy in relativistic electrons and magnetic field, respectively.

magnetic field B, the radius of the emitting region R and the shock energy $U \equiv B^2/(\epsilon_B 8\pi) \times (4/3\pi R^3 f)$ as follows:

$$B = (2.50 \times 10^9)\left(\frac{\nu_{\rm pk}}{5\,{\rm GHz}}\right)\left(\frac{1}{c_1}\right)\left[\frac{4.69 \times 10^{-23}(\frac{E_l}{\rm erg})^{2(2-p)}\epsilon_B^2 c_5 \sin(\theta)^{\frac{1}{2}(-5-2p)}}{(p-2)^2(\frac{D}{\rm Mpc})^2\epsilon_e^2(\frac{f}{0.5})^2(\frac{F_{\rm pk}}{\rm Jy})c_6^3}\right]^{\frac{2}{13+2p}} {\rm G}, \tag{4.2}$$

$$R = (2.50 \times 10^9)^{-1} c_1 \left(\frac{\nu_{\rm pk}}{5\,{\rm GHz}}\right)^{-1}\Bigg[12\epsilon_B c_5^{-(6+p)} c_6^{(5+p)} (9.52 \times 10^{25})^{(6+p)} \sin^2\theta \pi^{-(5+p)} \left(\frac{D}{\rm Mpc}\right)^{2(6+p)}\left(\frac{E_l}{\rm erg}\right)^{(2-p)}\left(\frac{F_{\rm pk}}{\rm Jy}\right)^{(6+p)}\left(\epsilon_e(p-2)\left(\frac{f}{0.5}\right)\right)^{-1}\Bigg]^{1/(13+2p)} {\rm cm}, \tag{4.3}$$

$$U = c_1(3.33 \times 10^{-11})\epsilon_B^{-1} 10^{\frac{75(6+p)}{13+2p}}\left(\frac{f}{0.5}\right)\left(\frac{\nu_{\rm brk}}{5\,{\rm GHz}}\right)^{-1}\Bigg[3.086^{6(6+p)} 4.411 \times 10^{-96} \left(\frac{D}{\rm Mpc}\right)^{28+6p}\left(\frac{F_{\rm brk}}{\rm Jy}\right)^{14+3p}\pi^{-3(1+p)}\sin\theta^{-4(1+p)} c_5^{-(14+3p)} c_6^{3(1+p)} \left(2\epsilon_B\epsilon_e^{-1}(p-2)^{-1}\left(\frac{E_l}{\rm erg}\right)^{2-p}\left(\frac{f}{0.5}\right)^{-1}\right)^{11}\Bigg]^{1/(13+2p)} {\rm erg}, \tag{4.4}$$

where f is a volume filling factor that represents the fraction of a sphere of radius R that is emitting synchrotron radiation; c_1, $c_5(p)$ and $c_6(p)$ are synchrotron coefficients (see e.g., DeMarchi et al. 2022, their Appendix A). These equations from DeMarchi et al. 2022 generalize those originally presented in Chevalier 1998 for an arbitrary value of p. Following Chevalier 1998 we further adopt $f = 0.5$, $\sin(\theta) \approx 1$ and $\gamma_m = 1$, which is $E_l = m_e c^2$.

4.4. Preliminary Discussion

4.4.1. X-rays

Taken together, the *Swift*-XRT and *XMM-Newton* campaigns lead to the following observational results: (i) For $\delta t \lesssim 430\,\mathrm{d}$ the soft X-ray spectrum consists of a mixture of a thermal black-body component with $kT_{\mathrm{bb}} \sim 0.05\,\mathrm{keV}$ and a non-thermal power-law component of emission with $\Gamma \sim 2$, i.e., $F_\nu \propto \nu^{-1}$ (Figure 4.3). (ii) The source brightening of a factor ≈ 10 in the time interval $\delta t \approx 10 - 350\,\mathrm{d}$ is due to the flux increase of the black-body component (Figure 4.2). During this time there is only a hint for an increase of the black-body temperature, which implies that the effective black-body radius increases with time, from 2.33×10^{11} cm to 1.32×10^{12} cm. Results (i)+(ii) confirm the findings by Holoien et al. 2016a; Gezari et al. 2017; Holoien et al. 2018. (iii) Differently from Holoien et al. 2018, we find that the thermal component rapidly shuts off around $\delta t \approx 350$ days as $F_x \propto t^{-4.5}$, and fades below detection by $\delta t \approx 430\,\mathrm{d}$. (iv) A non-thermal power-law component is always present in the spectra and dominates the emission for $\delta t \geq 1000\,\mathrm{d}$. The inferred spectral index is consistent with no variation, however the power-law flux does vary with time reaching a minimum at 235 d followed by a brightening by a factor ~ 10 at $\sim 1400\,\mathrm{d}$. (v) The non-thermal power-law flux abruptly decays by a similar factor over a time scale of ~ 1 yr, implying a remarkably steep decay with $F_x \propto t^{-8.5}$ *if* timescales are measured since the optical discovery of the transient. In the context of TDEs, similarly steep decays of the X-ray emission have been observed in SwiftJ1644+57 and have been interpreted as observational manifestations of the TDE jets shutting off.

We end by noting that Gezari et al. 2017 associated the power-law spectral component to the presence of a weak AGN (i.e. unrelated to the transient). Pre-TDE *ROSAT* observations of the host galaxy 2MASX J20390918–3045201 provide no useful constraint: Holoien et al. 2018 report a pre-TDE X-ray flux limit of $F_x < 1.9 \times 10^{-12}\,\mathrm{erg\,cm^{-2}s^{-1}}$ (0.1-2.4 keV), which is larger than the measured fluxes for ASASSN-15oi.

4.4.2. Radio Observations of ASASSN-15oi in context of other TDEs

In Figure 4.6, we have plotted the shock energy involved in the different TDEs. The phase space is divided at $\Gamma\beta = 1$, which defines the boundary between non-relativistic and relativistic outflows. While *Swift*J1644+57 and *Swift*J2058+05 had clear evidence of relativistic outflows, they had energies similar to those observed in GRBs. The non–relativistic TDEs, however, are less energetic than GRBs but more energetic than Type Ib/c supernova. We calculate the shock energy of all the non-relativistic TDEs using the modeling prescription in Chevalier 1998. The observations of the first flare of ASASSN-15oi show energies and outflow velocities similar to other TDEs, however, the second radio flare contains energy comparable to the jetted–TDEs. This, in addition to the evidence found in Section 4.3 of the radio emission in the two radio flares originating from a separate population of electrons hint at two complete different origins of these radio flares.

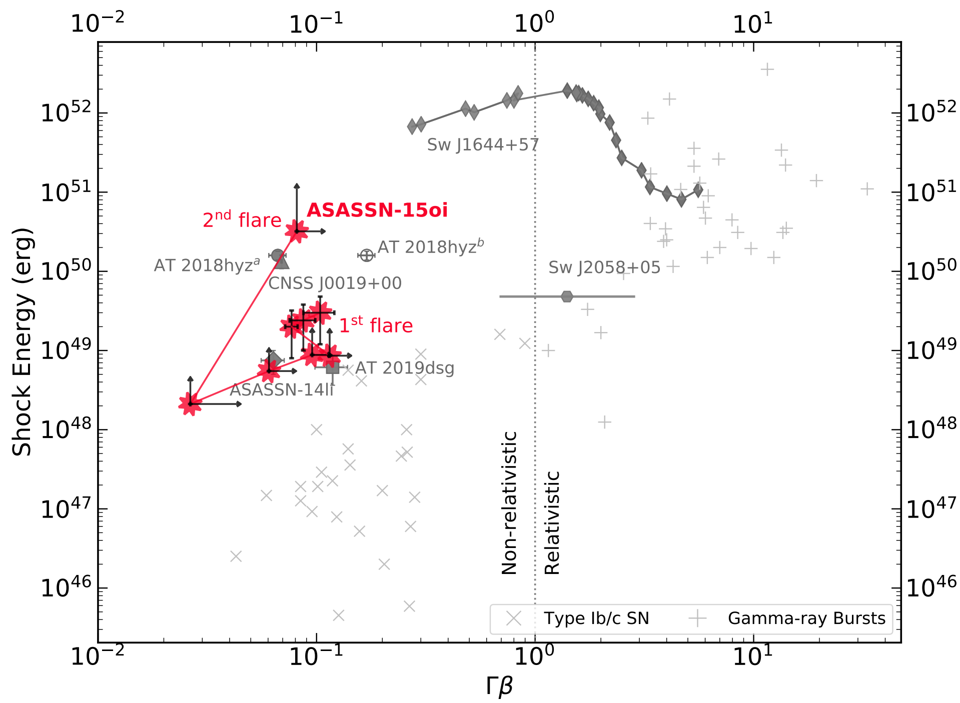

Figure 4.6 Radio energetics from Alexander et al. 2016 and Cendes et al. 2021a: the first flare of ASASSN-15oi fits nicely in the upper part of the non-relativistic TDEs, while the second flare is as energetic as jetted TDEs, with lower limit on the expansion speed. The two At 2018hyz points come from the different assumptions of the launch time of the outflow. Cendes et al. 2022 *in prep* considers a launch time of $\delta t \sim 700$ days post–discovery and the corresponding velocity is plotted with an empty grey symbol here, where if the time of launch of the outflow were considered to be the as the epoch of discovery, we would get a velocity as shown with the filled grey circle.

We finally plot the multi–band luminosities measured for ASASSN-15oi in this work at all times since the discovery. We specifically plot the two components of X–rays separately so as to determine any correlation that exists between any individual component to any other across the different observing bands. We note that the

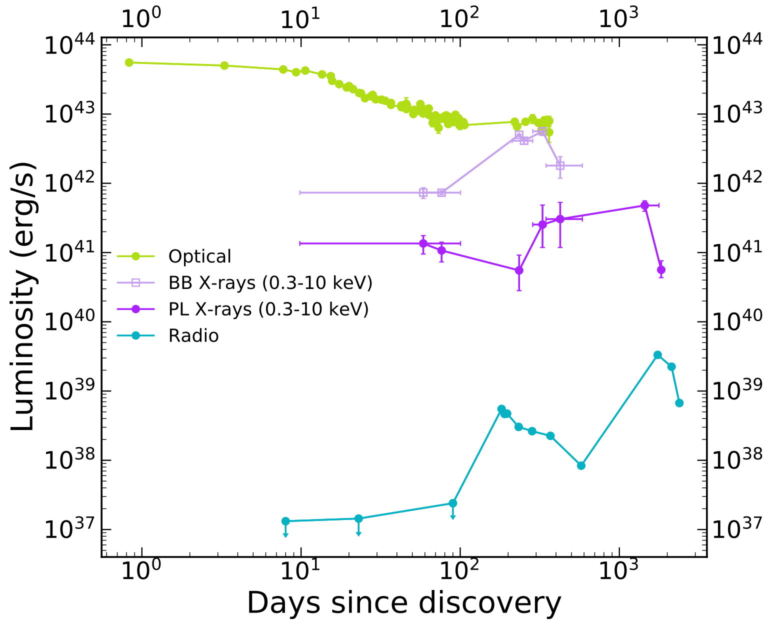

Figure 4.7 Multi-band light-curve evolution of ASASSN-15oi in the optical (νL_ν at $\nu = 7.5\times10^{14}$ Hz), X-rays (0.3–10 keV) and radio (νL_ν at $\nu \approx 7.5$ GHz) from the time of discovery until ~ 2400 days. For the X-rays we plot the 0.3–10 keV luminosity of the power–law component (dark purple filled circles) and the black-body component (light purple open squares). separately.

optical luminosity is behaving independently of the other two wavelengths, whereas following the peak of the first radio flare, we see the power–law component of the X-rays also rise, remain constant when the flare is fading, and finally we see a sharp decline in the power–law luminosity of the X–rays when the radio emission from ASASSN-15oi re–brightened at $\delta t \sim 4$ years. This clearly shows that there is at least a slight correlation between the X–rays and radio emission at these late–times. While this work is in progress, we can still appreciate the exciting prospect of these observations in ASASSN-15oi at late–times which might be hinting at something entirely new for the first time.

Table 4.1 Best-fitting results from the time-resolved X-ray spectral analysis of ASASSN-15oi using *Swift*-XRT (upper part) and *XMM-Newton* (lower part). The data require two components of emission using a spectral model of the form `tbabs*(cflux*pow+cflux*bbody)` within `XSPEC`. We adopted $N_{\rm H,gal} = 5.59 \times 10^{20}\,{\rm cm}^{-2}$, $N_{\rm H,int} = 0\,{\rm cm}^{-2}$, redshift, $z = 0.0484$. *XMM-Newton* (*Swift*-XRT) observations are fitted in 0.2–12 keV (0.3–10 keV) energy range. Fluxes are reported in the 0.3–10 keV energy range, uncertainties are reported at 68% confidence ($1\,\sigma$) level, and upper limits are reported at $3\,\sigma$ confidence level. Γ is the power-law photon index, and kT_{bb} is the observed black-body temperature in keV units. For *XMM-Newton* we report the EPIC-pn exposure times after removal of the time intervals affected by high background.

δt^a	Expo		PL		BB	Source
		Γ	Unabs. Flux	kT$_{bb}$	Unabs. Flux	
(days)	(ks)		($\times10^{-14}$ erg/cm^2/s)	($\times10^{-2}$ keV)	($\times10^{-13}$ erg/cm^2/s)	
				Swift-XRT		
58.6	61.7	$1.7^{+0.49}_{-0.46}$	$2.4^{+0.72}_{-0.71}$	$4.5^{+0.50}_{-0.58}$	$1.3^{+0.23}_{-0.23}$	This Work
252.1	31	$1.5^{+8.02}_{-2.25}$	$0.77^{+0.91}_{-1.8}$	$4.9^{+0.31}_{-0.63}$	$7.3^{+0.74}_{-0.74}$	This Work
329.0	11.7	$2.5^{+1.4}_{-1.2}$	$4.5^{+4.1}_{-2.4}$	$5.0^{+0.47}_{-0.52}$	$10^{+1.3}_{-1.3}$	This Work
425.1	6.1	$1.9^{+1.3}_{-1.2}$	$5.4^{+4.0}_{-3.3}$	$5.4^{+1.3}_{-1.3}$	$3.2^{+1.0}_{-1.1}$	This Work
1444.9	25.3	$2.3^{+0.29}_{-0.28}$	$8.5^{+1.4}_{-1.5}$	–	< 0.55	This Work
				XMM-Newton[b]		
76.4	10.3	$2.5^{+0.8}_{-0.8}$	–[c]	$4.7^{+0.2}_{-0.2}$	1.6	Gezari et al. 2017
76.4	12.4	$1.7^{+1.0}_{-0.8}$	$2.3^{+0.8}_{-0.8}$	6.2^{+6}_{-6}	$1.2^{+0.5}_{-0.5}$	Holoien et al. 2018
76.4	9.7	$1.5^{+0.53}_{-0.44}$	$1.9^{+0.6}_{-0.6}$	$5.1^{+0.3}_{-0.3}$	$1.3^{+0.08}_{-0.08}$	This Work
234.5	12.0	3.3±1.3	–	$4.2^{+0.07}_{-0.07}$	18	Gezari et al. 2017
234.5	14.0	$2.8^{+2.6}_{-1.2}$	$1.5^{+0.8}_{-0.8}$	5.3^{+2}_{-2}	Holoien et al. 2018	
234.5	10.9	$3.1^{+1.2}_{-0.89}$	$0.98^{+0.65}_{-0.48}$	$4.2^{+0.06}_{-0.06}$	$8.9^{-0.19}_{+0.18}$	This Work
1833	12.5[d]	$2.0^{+0.33}_{-0.30}$	$1.0^{+0.35}_{-0.23}$	–	$< 4.2 \times 10^{-2}$	This Work

Note. — [a] For *Swift*-XRT we list the mean time of arrival of photons. From the top to the bottom, the interval of times of extraction of the spectra are $9.8 - 100.5$ d, $212.2 - 285.5$ d, $285.5 - 346.4$ d, $346.4 - 585.7$ d and $1394.9 - 1774.2$ d.

[b] For XMM, we provide the numbers reported in the earlier works of Gezari et al. 2017, and Holoien et al. 2018 for the purpose of comparison.

[c] The columns with no values (–) were not reported in the previously published works. The empty columns in the last XMM and XRT observations where we report the values from this work are because of the unconstrained nature of the BB component at these epochs.

[d] For this epoch of XMM, we performed a joint–fit of MOS1, MOS2 and PN data. The exposure time reported in the table is the net exposure time after filtering out for the high-energy flaring events in PN data only. The net exposure times for MOS1 and MOS2 are 23.6 and 23.8 ks, respectively.

Table 4.2 Radio Observations of the TDE ASASSN-15oi. A $3-5\%$ systematic error is added to the uncertainties of all the flux densities measured in this work. The upper limits are reported as $3 \times$ RMS values obtained for the corresponding image.

Date	Observatory	Project	ν (GHz)	F_ν (mJy)	Source
			$\delta t = 8$ days		
2015-Aug-22	VLA	16A-422	6.1	<0.03	Horesh et al. 2021a
		(PI: Horesh)	7.1	<0.03	
			22	<0.06	
			$\delta t = 23$ days		
2015-Sep-06	VLA	16A-422	6.1	<0.034	Horesh et al. 2021a
		(PI: Horesh)	7.1	<0.04	
			22	<0.07	
			$\delta t = 90$ days		
2015-Nov-12	VLA	16A-422	6.1	<0.06	
		(PI: Horesh)	7.1	<0.06	
			22	<0.03	
			$\delta t = 182$ days		
2016-Feb-12	VLA	16A-422	4.8	1.114 ± 0.013	Horesh et al. 2021a
		(PI: Horesh)	7.4	1.321 ± 0.011	
			19	0.834 ± 0.025	
			21	0.808 ± 0.020	
			23	0.643 ± 0.014	
			25	0.587 ± 0.025	
			$\delta t = 190$ days		
2016-Feb-20	VLA	16A-422	3	0.547 ± 0.005	Horesh et al. 2021a
		(PI: Horesh)	4.8	0.899 ± 0.019	
			7.4	1.119 ± 0.028	
			9	1.204 ± 0.014	
			11	1.073 ± 0.022	
			13	1.103 ± 0.021	
			15	0.929 ± 0.016	
			17	0.784 ± 0.014	
			19	0.717 ± 0.013	
			21	0.570 ± 0.014	
			23	0.497 ± 0.018	
			25	0.450 ± 0.012	

Table 4.2 (cont'd)

Date	Observatory	Project	ν (GHz)	F_ν (mJy)	Source
			$\delta t = 197$ days		
2016-Feb-27	VLA	16A-422	3	0.504 ± 0.006	Horesh et al. 2021a
		(PI: Horesh)	4.5	0.690 ± 0.005	
			5.5	0.881 ± 0.008	
			6.5	1.036 ± 0.011	
			7.5	1.118 ± 0.011	
			9	1.072 ± 0.014	
			11	1.030± 0.016	
			13	0.932 ± 0.012	
			15	0.793 ± 0.013	
			17	0.703 ± 0.014	
			19	0.717 ± 0.014	
			21	0.699 ± 0.017	
			23	0.525 ± 0.021	
			25	0.429 ± 0.020	
			$\delta t = 233$ days		
2016-Apr-03	VLA	16A-422	3	1.007 ± 0.024	Horesh et al. 2021a
		(PI: Horesh)	4.5	0.951 ± 0.011	
			5.5	0.824 ± 0.011	
			6.5	0.756 ± 0.017	
			7.5	0.718 ± 0.010	
			8.5	0.686 ± 0.013	
			9.5	0.639 ± 0.012	
			10.5	0.638 ± 0.012	
			11.5	0.591 ± 0.014	
			12.5	0.578 ± 0.015	
			13.5	0.512 ± 0.013	
			14.5	0.453 ± 0.013	

Table 4.2 (cont'd)

Date	Observatory	Project	ν (GHz)	F_{ν} (mJy)	Source
			$\delta t = 283$ days		
2016-May-23	VLA	16A-422	3	1.033 ± 0.020	Horesh et al. 2021a
		(PI: Horesh)	5	0.854 ± 0.012	
			7	0.668 ± 0.010	
			9	0.578 ± 0.010	
			11	0.520 ± 0.011	
			13	0.425 ± 0.011	
			15	0.365 ± 0.012	
			17	0.321 ± 0.013	
			$\delta t = 369$ days		
2016-Aug-17	VLA	16A-422	3	0.695 ± 0.020	Horesh et al. 2021a
		(PI: Horesh)	5	0.617 ± 0.017	
			7	0.571 ± 0.017	
			9	0.547 ± 0.014	
			$\delta t = 576$ days		
2017-March-12	VLA	16A-422	3	0.309 ± 0.070	Horesh et al. 2021a
		(PI: Horesh)	5	0.262 ± 0.032	
			7	0.212 ± 0.018	
			9	0.201 ± 0.014	
			$\delta t = 1417$ days		
2019-Jul-01	VLA	VLASS	3	9.49±0.48	
			$\delta t = 1714$ days		
2020-May-20	VLA	20A-492	1.26	9.802 ± 0.544	This Work
		(PI: Alexander)	1.78	1.08 ±0.191	
			2.5	1.01 ±0.108	
			3.45	9.554 ±0.099	
			5	9.327 ±0.132	
			7	8.436 ±0.166	
			9	7.275 ±0.336	
			11	6.305 ±0.368	

Table 4.2 (cont'd)

Date	Observatory	Project	ν (GHz)	F_ν (mJy)	Source
		$\delta t = 2129\,\mathrm{days}$			
2021-Jun-08	VLA	21A-303	1.5	11.8 ± 0.34	This Work
		(PI: Hajela)	2.35	9.94 ± 0.552	
			2.82	9.22 ± 0.466	
			3.24	8.57 ± 0.430	
			3.78	7.96 ± 0.402	
			4.49	7.140± 0.358	
			5.51	6.210± 0.312	
			6.48	5.450± 0.274	
			8.48	4.700 ± 0.237	
			9.5	4.400 ± 0.226	
			10.48	4.100 ± 0.211	
			11.5	3.810 ± 0.197	
		$\delta t = 2384\,\mathrm{days}$			
2022-Feb-22	VLBI	BH238	8.3	1.38 ± 0.3	This Work
		(PI: Hajela)			

CHAPTER 5

A GMRT 150 MHz Search for Variables and Transients in Stripe 82

This thesis chapter originally appeared in the literature as

Hajela, A., Mooley, K. P., Intema, H. T., & Frail, D. A. (2019), MNRAS, 490, 4898.

We have carried out a dedicated transient survey of 300 deg^2 of the SDSS Stripe 82 region using the Giant Meterwavelength Radio Telescope (GMRT) at 150 MHz. Our multi-epoch observations, together with the TGSS survey, allow us to probe variability and transient activity on four different timescales, beginning with 4 hours, and up to 4 years. Data calibration, RFI flagging, source finding and transient search were carried out in a semi-automated pipeline incorporating the SPAM recipe. This has enabled us to produce superior-quality images and carry out reliable transient search over the entire survey region in under 48 hours post-observation. Among the few thousand unique point sources found in our 5σ single-epoch catalogs (flux density thresholds of about 24 mJy, 20 mJy, 16 mJy and 18 mJy on the respective timescales), we find <0.08%, 0.01%, <0.06% and 0.05% to be variable (beyond a significance of 4σ and fractional variability of 30%) on timescales of 4 hours, 1 day, 1 month and 4

years respectively. This is substantially lower than that in the GHz sky, where $\sim$1% of the persistent point sources are found to be variable. Although our survey was designed to probe a superior part of the transient phase space, our transient sources did not yield any significant candidates. The transient (preferentially extragalactic) rate at 150 MHz is therefore <0.005 on timescales of 1 month and 4 years, and <0.002 on timescales of 1 day and 4 hours, beyond 7σ detection threshold. We put these results in the perspective with the previous studies and give recommendations for future low-frequency transient surveys.

5.1. Introduction

Our understanding of the dynamic radio sky on timescales >1s has relied heavily on the radio follow up of transients discovered through synoptic surveys at optical, X-ray, or gamma-ray wavelengths. However, a significant fraction of transients, such as the ones residing in dust-obscured environments, those powered by coherent emission processes, and unbeamed phenomena, are missed by these synoptic surveys. Blind radio searches have the exceptional ability to access this population of transients, thus giving an unbiased rate of these events.

There has been significant progress made with blind searches at GHz frequencies over the past few years. Since the transient rates are low (e.g. Frail et al. 2012), these searches have highlighted the use of widefield observations together with near-real-time data processing and extensive follow up observations in order to maximize the transient yield and identification (Mooley et al. 2016). Only a few percent of the persistent radio sources are found to be variable, with AGN dominating this sample (e.g. Frail et al. 1994; Carilli et al. 2003; de Vries et al. 2004; Croft et al. 2010; Bannister et al. 2011; Ofek et al. 2011; Thyagarajan et al. 2011; Williams et al. 2013; Bell et al. 2015; Hancock et al. 2016; Mooley et al. 2016). Widefield surveys have led to the discovery of several AGN showing renewed jet activity on timescales of ∼40,000 years, stellar explosions, a tidal disruption event, and flares from Galactic sources (Gal-Yam et al. 2006; Bannister et al. 2011; Thyagarajan et al. 2011; Mooley et al. 2016). Radio transient surveys such as the VLA Sky Survey (Lacy et al. in prep) with the Karl G. Jansky Very Large Array (VLA), the ThunderKAT program on the MeerKAT telescope (Fender et al. 2016) and the ASKAP Survey for Variables and Slow Transients (VAST; Murphy et al. 2013) program, will substantially increase the number of radio transients (at GHz frequencies) in the coming years.

On the other hand, blind searches for transients at MHz frequencies have had limited success. With modest sensitivities, the vast majority of these surveys[1] have probed mainly the Jansky-level population, and the transient yield has been low. The majority of the transients that were found have ambiguous or unknown classification due to the searches being carried out in archival data and untimely follow-up observations.

Nevertheless, the transients discovered thus far assure a rich phase space of the dynamic MHz sky. (Hyman et al. 2005; Hyman et al. 2007; Hyman et al. 2009)

[1]A fairly complete compilation of radio transient surveys carried out till date can be found at http://www.tauceti.caltech.edu/kunal/radio-transient-surveys/index.html.

discovered three "Galactic Center Radio Transients (GCRTs)", with peak flux densities ranging from of tens to thousands of mJy, among which one was a flaring X-ray binary and two transients were of unknown origin (but one likely a coherent emitter; Ray et al. 2007; Polisensky et al. 2016). (Jaeger et al. 2012) reported a 2.1 mJy transient in the SWIRE Deep Field 1046+59 at 340 MHz with the VLA, with no known counterparts. Another transient, possibly Galactic in origin and lasting for $<$10 min with a peak flux density of about 20 Jy, was discovered in $\sim$400 hours of LOFAR 30 MHz data towards the North Celestial Pole at 60 MHz (Stewart et al. 2016). (Obenberger et al. 2014) discovered two transients at 30 MHz, having peak flux densities of about 3 kJy, and lasting for 75–100 seconds with evidence for polarization or dispersion. (Murphy et al. 2017) recently found a transient, having a peak flux density of 180 mJy and timescale between 1–3 years, while comparing the TGSS-ADR (Intema et al. 2017) and GLEAM (Hurley-Walker et al. 2017) catalogs.

The MHz transient sky is expected to be different from the GHz sky. On timescales of $>$1 s, the GHz sky is illuminated primarily by (incoherent) synchrotron-driven transients arising from astrophysical shocks, such as supernovae, gamma-ray bursts, tidal disruption events, AGN, X-ray binaries, etc., and from astrophysical plasma accelerated in stellar magnetic fields observed in the form of stellar flares, magnetar flares, etc (e.g. Mooley et al. 2016). Being brightness-temperature limited, these transients evolve on timescales of days–months (extragalactic; more luminous) or hours–weeks (Galactic; less luminous), as noted by (Pietka et al. 2015). Most classes of incoherent synchrotron transients are self-absorbed at MHz frequencies at early times, pushing these events to much longer timescales of years to decades and lower peak flux densities compared to GHz frequencies. Consequently, their rates are lower, and they are harder to identify in transient surveys (Metzger et al. 2015a). On the other hand, transients powered by coherent emission (such as pulsars and brown dwarfs) may be more abundant at MHz frequencies.

Likewise, we expect the variable MHz sky to be different as well. Rather than the substantial intrinsic variability observed in the GHz sky, variability at MHz frequencies will be dominated by refractive interstellar scintillation (e.g. Rickett 1986). Interplanetary scintillation (Clarke 1964; Morgan et al. 2018), caused due to local density fluctuations in the ionised medium in the ecliptic plane, will dominate the extrinsic variability close to the ecliptic.

Given the yield of transients at ∼Jansky flux densities in the low-frequency sky, one would expect a multifold increase in the yield by probing deeper, at milliJanky flux densities. Motivated by this, and the need for systematic exploration of the mJy-level dynamic sub-GHz sky, we have carried out a dedicated survey over 220 deg^2 of the SDSS Stripe 82 region with the GMRT at 150 MHz. GMRT offers both good sensitivity and ∼arcsec localization; the latter is essential for associating radio variable/transient sources with their optical counterparts. The choice of our survey region is motivated by the presence of the abundance of deep multiwavelength archival data in Stripe 82, which aids our search for the progenitors/host galaxies of transients. Using the dataset, we are able to probe timescales between ∼hours and ∼1 month. The observing frequency of 150 MHz allows us to take advantage of the existing TGSS survey and extend our transient search to a timescale of ∼4 years. In §5.2 we describe the observations, the calibration and source cataloging procedures. In §5.3 and §5.4 we detail the variability and transient search. The summary and discussion are given in §5.5.

5.2. Observations and Data Processing

5.2.1. Observations

Stripe 82 is an equatorial strip on the sky, spanning 2.5 degrees in declination between ±1.25 degrees, and 109 degrees in right ascension between −50 degrees and +59 degrees. Since the half-power beamwidth (HPBW) of GMRT at 150 MHz is 186 arcmin, we were able to cover the declination range of Stripe 82 in a single pointing. In right ascension, the pointings were spaced by HPBW/2 to get a fairly uniform sensitivity across Stripe 82.

We observed two regions, R1 and R2, in November–December 2014 and June–September 2015 under project codes 27_032 and 28_082 respectively. Twenty seven pointings centred on declination of 0 degrees and spanning 0–40 degrees in right ascension were used for region R1. Thirty pointings centred on declination of 0 degrees and spanning 310–355 degrees in right ascension were used for region R2. Data was recorded in full polarization mode every 8 seconds, in 256 frequency channels across 16 MHz of bandwidth (140–156 MHz). We observed each region in two epochs, 1 month apart, with each epoch being split over two observing sessions usually spread over two consecutive days. In a single session, typically 15–30 pointings (covering an area of 50–100 deg^2), with each pointing observed for 20–40 minutes split over 2 scans (each scan was 10–20 minutes long) spaced out in time (about 4 hours) to improve the UV-coverage. The flux calibrator, 3C48, was observed in the middle and beginning/end of each session. Due to the presence of in-beam calibrators and the use of the SPAM recipe for direction-dependent calibration (Intema et al. 2009), no phase calibration scans were obtained. An overview of all GMRT observations used for the variability and transient search is given in Table 5.1.

5.2.2. RFI Flagging, Calibration and Imaging using the SPAM recipe

After each observation, the data were downloaded from the GMRT archive within 12 hours onto the computer cluster at the NRAO in Socorro, and processed with a fully automated pipeline based on the SPAM recipe (Intema et al. 2009; Intema et al. 2017). The pipeline incorporates direction-dependent calibration and modeling of ionospheric effects, generally yielding high-quality images. In brief, the pipeline consists of two parts: a pre-processing part that converts the raw data from individual observing sessions into pre-calibrated visibility data sets for all observed pointings, and a main pipeline part that converts each pre-calibrated visibility data set per pointing into a Stokes I continuum image. Both parts run as independent processes on the multi-node, multi-core compute cluster, allowing for parallel processing of many observations and pointings. A detailed description of the processing pipeline

Table 5.1 GMRT Observing Log

No.	Date (UT)	Region/Epoch	LST (h)	RMS[a] (mJy/beam)
Archival Data: TGSS				
0	2010 Dec 15[b]	R1&2E0	–	~ 3.5
G1STS Observations				
1	2014 Nov 10	R1E1a	19–06	3.8
2	2014 Nov 11	R1E1b	19–06	4.1
3	2014 Dec 27	R1E2a	16–01	4.8
4	2014 Dec 28	R1E2b	17–01	6.6
5	2015 Jun 29	R2E1a	22–09	2.8
6	2015 Jun 30	R2E1b	23–09	2.6
7	2015 Aug 31	R2E2a	20–05	2.5
8	2015 Sep 02	R2E2b	20–05	2.4

[a]RMS refers to the median single-pointing RMS noise achieved during the given observing run.

[b]This is the median epoch of TGSS survey. The TGSS observations were taken over two years from April 2010 to March 2012.

is given in (Intema et al. 2017). With this pipeline, we were able to calibrate and image each GMRT observation within 10 hours after retrieval.

In addition to imaging each pointing per observing run, we also imaged each pointing for every scan (typically two scans per observing run; see §5.2.1) and every epoch (E1/E2; combining the visibility data from the observing runs on consecutive days).

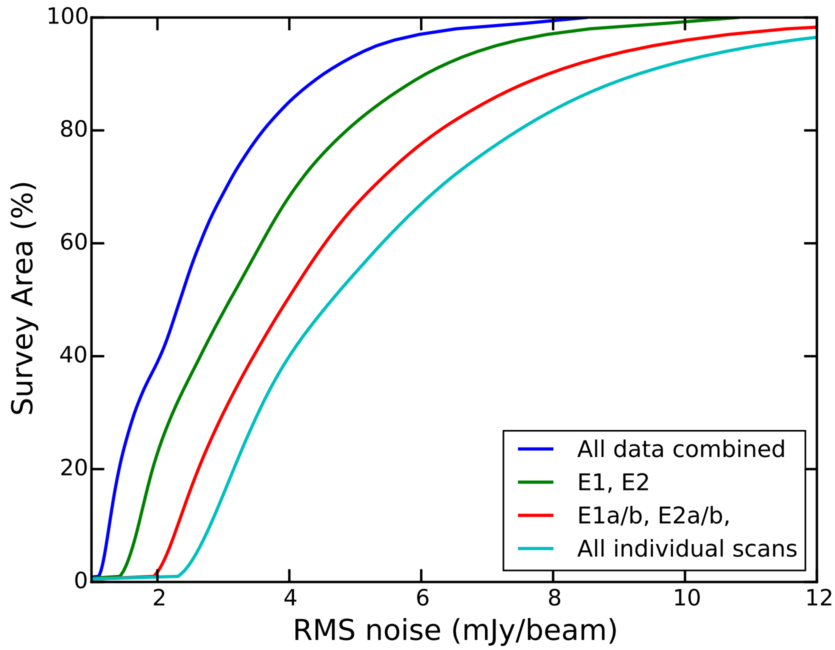

Figure 5.1 Cumulative plot of the RMS noise for each timescale probed by the GMRT data. See §5.2.1and Table 5.1 for details.

5.2.3. Image Mosaicing and Source Cataloging

Once the single-pointing images were produced by the SPAM pipeline, we combined them into mosaics using the AIPS task FLATN. The RMS noise of the image mosaics generated for each scan, each observing run, each epoch and all data combined, are shown in Figure 5.1, and the median values for each observing run are reported in Table 5.1.

We used PyBDSF[2], a Python module, to decompose images for every observing run, the corresponding scans and the epochs into sources and generate a 5σ catalog.

[2](Mohan et al. 2015)

We used `process_image` task of PyBDSF to process and find sources above a user-defined threshold in each individual image. `process_image` offers a user-defined parameter, `rms_box`, which was used to calculate the mean and the rms of the image using two inputs, the first fixed the rms-box size to calculate the mean and the rms and the second input fixed the step-size by which the box moved across the image. For this work, we used an rms box which was 20 times the size of the synthesized beam of the image (Hancock et al. 2012; Mooley et al. 2013) and moved it by 10 pixels (i.e. the step-size) for the next measurement. We used the module-default values for `thresh_pix` = 5.0 and `thresh_isl` = 3.0. The combination of these two parameters set the threshold for source detection in the images. `thresh_isl` defined the threshold to select the regions or islands to which Gaussian is fitted and `thresh_pix` defines the threshold for individual pixels to be included in that island. We wrote down all the detected sources and their properties in a catalog using `write_catalog` task of PyBDSF.

The $\sim$300 deg^2 co-added image mosaics and the corresponding 5σ source catalog containing 12,703 sources above 10.5 mJy is available via the Caltech Stripe 82 Portal[3].

[3] http://www.tauceti.caltech.edu/stripe82/

5.2.4. Archival Data

The Stripe 82 region is also covered by the 150 MHz GMRT sky survey TGSS[4] with a very similar sensitivity ($\sim$ 3.5 mJy/beam). The TGSS observations were performed over 2 years, from April 2010 to March 2012 with a median epoch of about 2010 Dec 15. We have used the publicly available data products from the TGSS-ADR to construct a 5σ catalog of the same area in Stripe 82, which provides an extra epoch for our transient search (on $\sim$4 yr timescale).

5.3. Variability Search

From our GMRT observations of Stripe 82 alone, we can probe (via "two-epoch" comparisons) variability on three timescales: 4 hours, 1 day and 1 month. As alluded to in §5.2, each of the eight observations listed in Table 5.1 was carried out using two scans separated by approximately four hours. Hence, in order to study the variability on this four hour timescale, we compared the 5-sigma source catalogs of the two scans[5]. To study variability on a timescale of 1 day, we compared observation E1a with E1b, and observation E2a with E2b (cf. Table 5.1). For the 1 month timescale, we compared E1 and E2 (obtained by combining E1a+E1b and E2a+E2b respectively, for regions R1 and R2; see §5.2.2). For the 4 year timescale, we compared our full combined dataset (all eight observations listed in Table 5.1 combined into a single deep mosaic) with the TGSS ADR1. It should be noted that if a source is

[4]Details of the Alternative Data Release (TGSS-ADR) can be found in (Intema et al. 2017) and at `http://tgssadr.strw.leidenuniv.nl/`

[5]We excluded E1b from our analysis due to missing data and presence of substantial RFI.

found to be variable between two epochs, its variability timescale is generally smaller than the separation between the two epochs and larger than the duration of each of the two epochs. For example, when comparing individual scans of each observation, we are probing a timescale of <4 hours (and $\gtrsim$30 min).

A variable source will be unresolved at our angular resolution of $\sim 19''$, unless that source is very nearby ($\ll$ 1 pc) and expanding extremely rapidly (superluminal motion). Therefore, in order to shortlist point-like (unresolved) sources, and to avoid potential false sources/imaging artifacts, we applied the constraints listed below to the 5σ catalogs:

- **Search area bounds.** Due to very low sensitivity beyond ~1.75 degrees from the GMRT 150 MHz beam center, the edges of our image mosaics of regions R1 and R2 are noisy. Hence we retained only those sources satisfying -1.75 deg < Dec < 1.75 deg, -1.25 deg < RA < 41.25 deg and 308.75 deg < RA < 356.25 deg.
- **Flux density ratio.** Following (Mooley et al. 2016) and (Frail et al. 2018), we keep sources having S/P < 1.5 (SNR<15) and S/P < 1.1 (SNR≥15), where S is the total flux density and P is peak flux density of the source.
- **Source size.** We retained sources having `BMAJ`/1.5<MAJ<1.5×`BMAJ` and `BMIN`/1.5<MIN<1.5×`BMIN`, where `BMAJ` and `BMIN` are the major and minor axis of the synthesized beam and MAJ, MIN are the major and minor axis of the Gaussian fitted by PyBDSF. We further

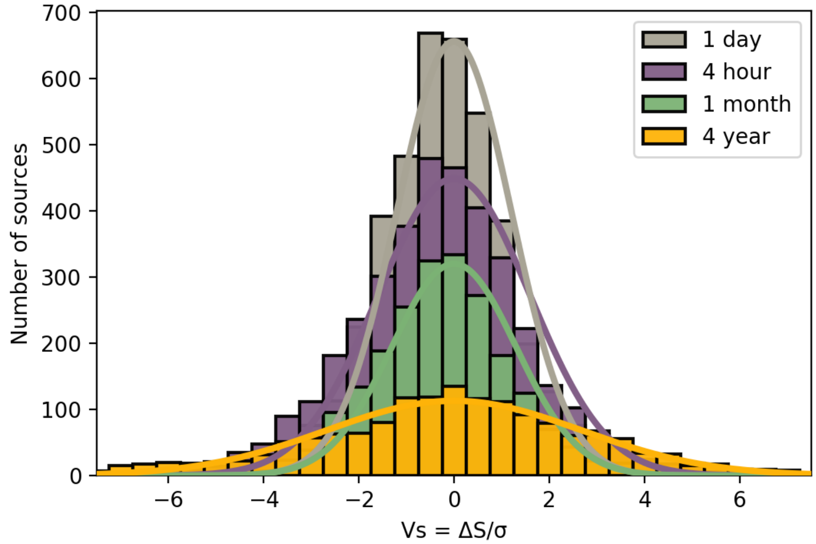

Figure 5.2 The histograms of variability statistic V_s corresponding to all timelines. V_s is calculated after applying all the constraints to the single-epoch catalogs. Histograms are fit by the Gaussians of same color. Standard deviations, `std`, of the fitted Gaussians for 4 hour timescale: 1.6, for 1 day timescale: 1.2, for 1 month timescale: 1.3 and for 4 year timescale: 2.7

imposed MAJ $>$ 1.1$\times$`BMAJ`, MIN $>$ 1.1$\times$`BMIN` for sources detected at a high significance (SNR $\geq$ 15) (e.g. Mooley et al. 2016).

- **Proximity to bright sources.** To avoid any potential imaging artifacts around bright sources, we removed fainter sources (sources with total flux density $\ll$ 500 mJy) lying within 3 arcmin of all $>$ 500 mJy sources.

Following the application of the constraints mentioned above to our 5σ PyBDSF catalogs (for each individual image mosaic described above), we used `TOPCAT` (Tool for OPerations on Catalogues And Tables, v4.6-1; Taylor 2005) to perform a two-epoch comparative study at every timescale. Given the synthesized beam of GMRT

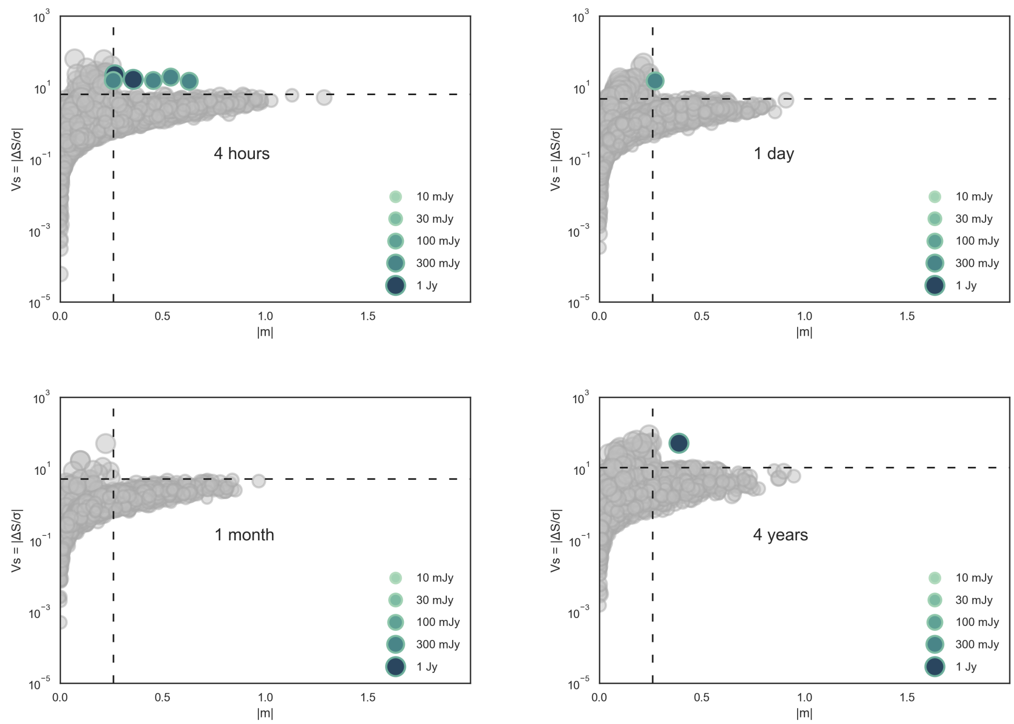

Figure 5.3 The variability statistic, Vs, as a function of modulation index, m, for all timescales probed in this work: <4 hours, <1 day, <1 month and <4 years. The dashed lines correspond to final selection criteria i.e. limits on m and Vs. The green-to-blue circles are sources which are finally shortlisted as variables after visual inspection. The size of the circle denotes the mean flux density of the source in two epochs. We find 18, 2 and 12 variables on timescales of 4 hours, 1 day, and 4 years.

at 150 MHz, $19'' \times 15''$, we used a search radius of $\sqrt{\mathtt{BMAJ} \times \mathtt{BMIN}}/2 = 9''$ to find the counterparts between any two epochs. The following 'two-epoch' comparisons were successfully performed under the aforementioned conditions:

- 4 yr timescale: 2132 two-epoch comparisons (2132 unique sources were matched) between our combined survey data and TGSS-ADR

- 1 month timescale: 4686 two-epoch comparisons (4686 unique sources matched) between E1 and E2
- 1 day timescale: 6987 two-epoch comparisons (among which 4389 unique sources were matched) for E1a vs. E1b and E2a vs. E2b.
- 4 hour timescale: 7134 two-epoch comparisons (among which 6689 unique sources were matched) for E1a scan1 vs. scan2, E2a scan1 vs. scan2, and E2b scan1 vs. scan2.

For every source catalog comparison made, we applied a suitable correction factor to ensure that the ratio of the source flux densities between the two epochs (S1/S2) is unity. The median of S1/S2 was taken to be the correction factor and applied to (divided out from) source flux densities and the associated uncertainties in the (fiducial) first comparison epoch (S1). The correction factors ranged between 0.85 (4 hr timescale) and 0.98 (4 yr timescale). We then used the corrected source flux densities with the corrected uncertainties to calculate two statistical measures, the variability statistic (V_s) and the modulation index (m), to distinguish between true variables and false positives. Following (Mooley et al. 2016), we compared the flux densities of a source between two different epochs using the $V_s = (S_1 - S_2)/\sqrt{{\sigma_1}^2 + {\sigma_2}^2} = \Delta S/\sigma$. The null hypothesis is that the sources are selected from the same distribution and are hence non-variable. Under this hypothesis, V_s follows a Student-t distribution. However, in our case we find that the distribution is Gaussian (see Figure 5.2). This may be explained by ionospheric effects in the low-frequency sky, other systematic effects in the amplitude calibration, cleaning artifacts etc. Nevertheless, we are able to fit Gaussian functions to the V_s distributions, for the four timescales probed, and we consider a source as a true variable if it has V_s lie beyond 4σ in the distribution (see Mooley et al. 2016). Our criterion for selecting a true variable source is therefore:

$$V_s = \left| \frac{\Delta S}{\sigma} \right| > 4 \times \texttt{std} \tag{5.1}$$

where `std` is the standard deviation of the V_s distribution (see Figure 5.2). Modulation index, m, is a measure of variability defined as difference of flux densities of a source between two epochs divided by the mean of the two flux densities, $\overline{S}$

$$m = \frac{\Delta S}{\overline{S}} = 2 \times \frac{S_1 - S_2}{S_1 + S_2} \tag{5.2}$$

Given the uncertainties in flux calibration, ionospheric effects and the like, we consider a source as a true variable only if the fractional variability is more than or equal to 30% (i.e. a modulation index of $|m| > 0.26$; see also Mooley et al. 2016).

We shortlisted the variable candidates using the above criteria. Then we visually inspected the image cutouts (from our survey as well as archival data from NVSS and FIRST) of these candidates and removed the potentially resolved sources. We thus found 1 variable for the 4 year timescale, no variables for the 1 month timescale, 1 variable for the 1 day timescale and 6 variables for the 4 hour timescale. These variables are shown in Figure 5.3 (variability statistic against modulation index plots for each timescale probed) and their details are tabulated in Table 5.2. The typical

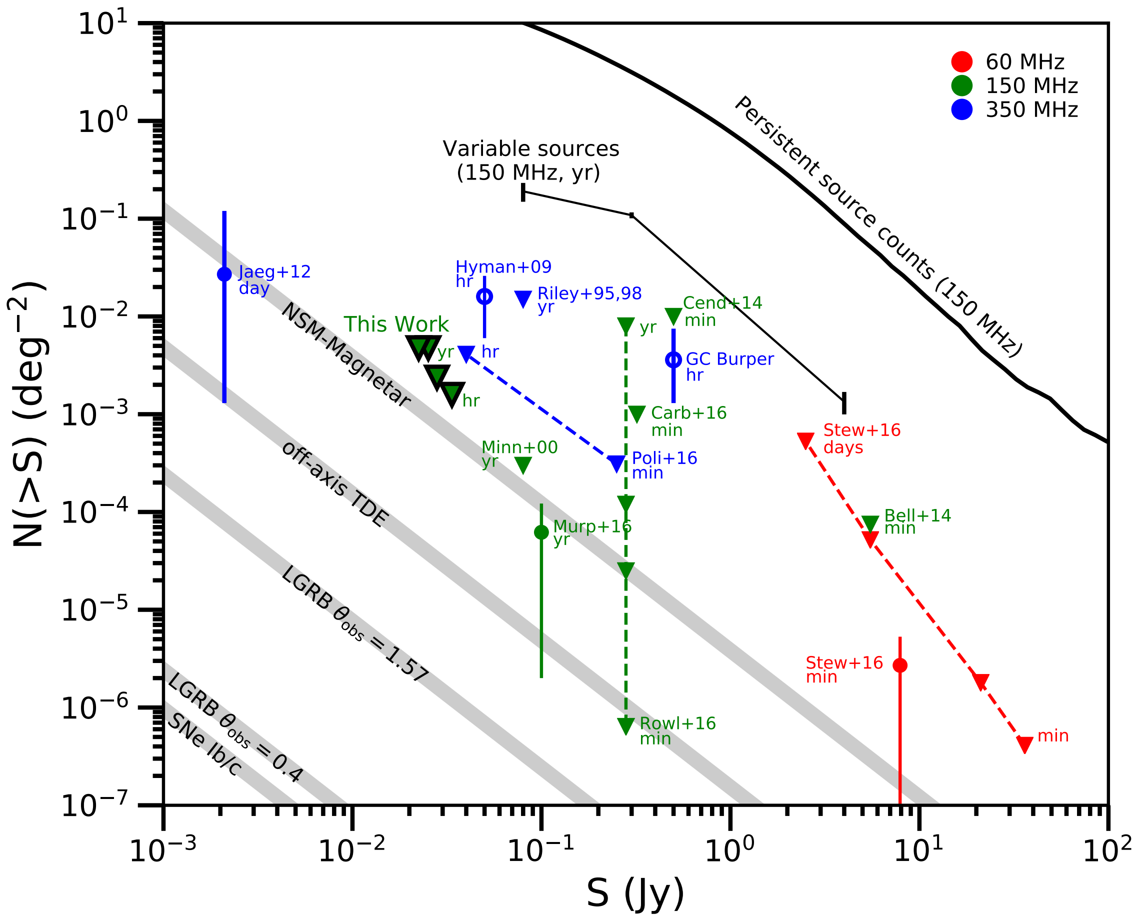

Figure 5.4 The log(N)–log(S) phase space of low-frequency radio transients. The 2σ upper limits to the transient rates from previous radio surveys (see the compilation at http://www.tauceti.caltech.edu/kunal/radio-transient-surveys/index.html) are shown as triangles. Rates from the same survey are joined by dashed lines. The rates derived from radio transient detections are shown as 2σ errorbars. The extragalactic transient rates, at 150 MHz, from (Metzger et al. 2015a) are shown with thick gray lines. The symbols are color-coded according to observing frequency. The source counts for persistent (from the TGSS-ADR; Intema et al. 2017) and variable sources ($m \gtrsim 0.1$ at 150 MHz, based on McGilchrist et al. 1990; Riley 1993; Minns et al. 2000; Bell et al. 2019) are shown with black lines. Timescale corresponding to each transient detection or upper limit is denoted as min (minute), hr (hour), day (day), mo (month) or yr (year). References: (Riley et al. 1995; Riley et al. 1998; Bell et al. 2014; Cendes et al. 2014; Carbone et al. 2016; Polisensky et al. 2016; Rowlinson et al. 2016) (other references are cited in the text). Upper limits from (Feng et al. 2017), at 182 MHz and on timescales between minutes and months, lie in the region similar to the (Polisensky et al. 2016) limits and are not shown on this plot. Transient rate upper limits from our survey, on timescales of 4 hr, 1 day, 1 month and 4 years, are shown as thick green triangles.

modulation index is 0.3–0.4. Identification of the variable sources and estimation of the variability fraction of the 150 MHz sky is done in §5.5.

5.4. Transient Search

For our transient search, we chose a higher detection threshold than the 5σ used for the variability search. Considering an average, $\sim$18 arcsec, synthesized beam for our survey, and searching effectively across $\sim$4200 sq deg (300 sq deg survey area $\times$ 14 observations searched), implies 50 Million synthesized beams searched. Hence, in order to keep the number of false positives, due to noise, down to $<$1, we chose a 7σ source detection threshold for transient search (following the recommendation of Frail et al. 2012).

We used the same point-source constraints defined above, for the variables case, to perform the transient search. The cumulative number of sources in our resulting point-source catalogs is 68,964 sources. We compared the source catalogs as in the above case of variables, probing timescales of 4 yr, 1 month, 1 day and 4 hours. For each single-epoch catalog pair compared (using `TOPCAT`), we searched for those sources present in one epoch and absent in the other. For the resulting transient candidates, we further verified their absence in the combined deep mosaics from our survey, and from archival images from the TGSS, NVSS and FIRST surveys. All of these candidates were SNR$<$15 and were either imaging artifacts (due to the presence of nearby bright sources) or appeared to be resolved sources in the archival radio images. We thus find no evidence for any transient sources in our data.

5.5. Summary & Discussion

With the aim of probing deeper into the phase space of transients in the low-frequency radio sky, we observed the SDSS Stripe 82 region at 150 MHz at multiple epochs with the GMRT. Our survey region spans 300 sq. deg (uniformity of RMS noise shown in Figure 5.1) and the observations are tabulated in Table 5.1. Using our observations in addition to the archival data from the TGSS-ADR, we were able to perform “two-epoch" comparisons, to find transients and variables, on four different timescales: 4 hours, 1 day, 1 month and 4 years. Using 5σ source catalogs for each timescale, we generated catalogs of point-like sources using a set of constraints, as described in Section 5.3.

We found 6, 1, 0 and 1 sources satisfying our variability criteria (significance greater than 4σ and fractional variability larger than 30%; see §5.3) on timescales of 4 hours, 1 day, 1 month and 4 years respectively. We note that the results for the 4 hour timescale are most uncertain due to modest UV coverage and larger flux calibration uncertainty. This is also the timescale for which we found the largest number of false positives (imaging artifacts), compared to our analysis for other timescales. Hence, the number of true variables on the 4 hour timescale is likely to be far less than 6.

Table 5.2 lists the variable sources that we found, along with their fluxes from the TGSS-ADR, NVSS and FIRST catalogs, the spectral indices with respect to the NVSS source catalog, and the magnitudes and spectroscopic redshifts of their optical counterparts. We also performed source identification (noted in Table 5.2) based on published optical spectra or WISE colors. We find that all the variable sources are AGN. The spectral indices calculated using the flux density in the NVSS survey are consistent with the typical AGN spectral index of -0.8 with the exception of J012528+000505, found on the 4 year timescale, and J022609+012929, found on the 4 hour timescale, which have a flat or inverted radio spectra. Comparison of the 150 MHz flux density of J012528+000505 with recently-published 1.4 GHz flux density ($\sim$800 mJy; (Heywood et al. 2016)) suggests that the source is consistent with being flat-spectrum, and its 1.4 GHz flux density has decreased by a factor of two with respect to the FIRST and NVSS surveys (observed in the 1990s).

5.5.1. Variability of the 150 MHz sky

We calculate the fraction of persistent sources that are variable as following: On a timescale of 4 hours, we found 6 significant variables out of a total of 7134 independent “two-epoch" comparisons (see §5.3). This implies that 0.08% of the persistent sources are variable, having a fractional variability $\geq$30%. Due to the UV coverage and flux calibration issues noted above for the 4 hour timescale, we consider this fraction as an upper limit. A single variable source was found in each of the 1 day and 4 year timescales, among a total of 6987 (0.01% of the persistent sources) and 2132 (0.05% of the persistent sources) “two-epoch" comparisons, respectively. No variables were found on the 1 month timescale (among 4686 "two-epoch" comparisons), and if we assume three sources as the 2σ upper limit (Gehrels 1986), then we get the variability fraction as <0.06% of the persistent sources.

Variability in these sources, listed in Table 5.2, is most likely extrinsic rather than being intrinsic to the sources themselves[6]. One of the suspects could be the ionosphere, but the SPAM pipeline (see §5.2.2) is expected to minimize this factor. Interstellar scintillation, on the other hand, is expected to be the dominant factor. Brightness temperature constraints ($T_b \lesssim 10^{12}$ K for synchrotron emission; (Kellermann et al. 1969; Readhead 1994)) place strong limits on the source size of the radio emitting region. Assuming that the source size is comparable to the light travel time $c\tau$, the variability in flux density at 150 MHz is constrained as follows, unless relativistic beaming is involved.

$$\Delta S \lesssim 0.03\,\mathrm{mJy}\,(\tau/1\,\mathrm{yr})^2 (D_A/1.5\,\mathrm{Gpc})^{-2} \tag{5.3}$$

where τ is the variability timescale, and D_A is the angular diameter distance. Therefore, any intrinsic component to the variability will be limited to sub-mJy flux densities. None of the variable sources (having optical counterparts) show any evidence of blazar activity in their optical spectra, and therefore we do not expect relativistic beaming. We thus find extrinsic variability (refractive interstellar scintillation or RISS; consistent with Rickett 1986) to be the most probable explanation of the flux density changes seen in our sources.

[6]Incoherent emission sets a limit on the brightness temperature, as we discuss below. We do not attribute variability of our sources (all of which are AGN) due to coherent emission since this would require invoking new physics in AGN, which we believe is unlikely.

These results are also consistent with previous variability surveys. For example, (McGilchrist et al. 1990), (Riley 1993) and (Minns et al. 2000) carried out observations of several extragalactic fields with the Rile telescope at 150 MHz, and found 2/811 sources, 21/1050 and 207/6000 sources brighter than $\sim$100 mJy, respectively, to be variable at the $\gtrsim$10% level on timescales of $\geq$1 yr. (Riley 1993) noted enhanced variability in flat-spectrum sources and in steep spectrum sources whose spectra turn over at about 400 MHz. A similar conclusion was derived by (Bell et al. 2019), who recently studied the variability of 944 sources brighter than 4 Jy at 154 MHz with the MWA. They found 15 sources (1.6% of the sources monitored) to be variable on a timescale longer than 2.8 years, and noted enhanced variability in sources having peaked spectral energy distributions. All these studies have attributed the source variability to RISS. In our sample of variable source, we find 1–2 sources are flat spectrum, while the others are steep spectrum (we cannot exclude the possibility of the latter having spectra peaking at $\sim$100 MHz.) We mark the variable source counts[7] from (McGilchrist et al. 1990), (Riley 1993), (Minns et al. 2000) and (Bell et al. 2019) in Figure 5.4.

The variability of the low-frequency radio sky is substantially lower than that of the GHz sky. A number of studies of the dynamic GHz sky (e.g. Carilli et al. 2001; Bannister et al. 2011; Croft et al. 2011; Thyagarajan et al. 2011; Mooley et al. 2013; Williams et al. 2013; Bell et al. 2015; Mooley et al. 2016) have shown that $\sim$1% of the persistent sources at frequencies of 1–few GHz are variable beyond the $\sim$30%

[7] These denote sources varying beyond the $\gtrsim$10% level. Source counts from our search are much lower, since we considered sources varying only beyond 30%.

level, on timescales ranging from days to years. At 150 MHz, the fraction of variables among persistent sources is less by a factor of 10 or more.

We have attributed the variability of our sources to extrinsic factors, likely RISS. It is possible that interplanetary scintillation (IPS) may be playing a role, since the Stripe 82 region lies along the ecliptic. In their study of IPS at 162 MHz, (Morgan et al. 2018) find modulation indices of $\gtrsim$0.5 for radio sources lying along or in the vicinity of the ecliptic, and m$\lesssim$0.25 for sources lying away from the ecliptic. Indeed some of the variable sources on 4 hour timescale may also be due to IPS, although the flux scale for this timescale is most uncertain. Future surveys carried out with the LOFAR, the MWA and the SKA-low will find significant variability resulting from IPS.

5.5.2. Transient rates at low frequencies

We now calculate the upper limits to the transient rate from our survey. Using Poissonian statistics, we take the 2σ upper limit to the number of transients as 3. Since we have carried out 6, 4, 2 and 2 two-epoch comparisons on timescales of 4 hours, 1 day, 1 month and 4 years respectively, we calculate the upper limits[8] as 1.6×10^{-3} deg^{-2}, 2.4×10^{-3} deg^{-2}, 4.8×10^{-3} deg^{-2} and 4.8×10^{-3} deg^{-2} respectively (these are the instantaneous snapshot rates). The quoted upper limits to the transient rate are for 7σ flux density thresholds, i.e. 28 mJy, 34 mJy, 22 mJy and 25 mJy respectively.

[8]This is calculated as 3/(Area $\times$ epochs), where we take the survey area to be 315 deg^2.

In Figure 5.4 we show the log N(>S)-log S phase space of the dynamic low-frequency radio sky (S is the flux density and N is the number of radio sources). Persistent source counts from the TGSS-ADR are shown as a thick black line. The transient rate upper limits (including those from our survey) and detections from past blind searches below 400 MHz are plotted as triangles and errorbars. For reference, the rates of extragalactic transients considered by (Metzger et al. 2015a), assumed to follow a Euclidean $N(>S) \propto S^{-1.5}$ distribution, are plotted as grey shaded areas. The symbols are color coded to represent observing frequency. Searches that were primarily extragalactic are shown with filled symbols and those that were primarily Galactic (mainly towards the Galactic Center) are shown with unfilled symbols.

5.5.3. Investigation the radio transient phase space and recommendations for future low-frequency transient surveys

We make the following observations from Figure 5.4 and make recommendations for maximizing the yield of transients at low radio frequencies.

Firstly, the rate of Galactic Center transients, such as the "burper" (Hyman et al. 2005; Kulkarni et al. 2005) and the X-ray binary found by (Hyman et al. 2009), is significantly larger than the rate of extragalactic transients. The rate is higher by a factor of $\gtrsim$10. This suggests that low-frequency radio surveys of the Galactic Center, Galactic bulge or the Galactic plane will be lucrative.

Secondly, although we have sampled a competitive part of the phase space (where the population(s) uncovered by (Jaeger et al. 2012), (Murphy et al. 2017) and (Stewart et al. 2016) reside(s), assuming $N \propto S^{-1.5}$ distribution) with our medium-deep medium-wide GMRT Stripe 82 survey, we have not recovered any transients[9]. This suggests that a multi-epoch survey covering $\gtrsim$1000 deg^2 may be required to find any transient, in extragalactic fields, at the $\sim$10 mJy sensitivity level.

Our survey together with the transient rate upper limits on minutes/hour timescales from (Rowlinson et al. 2016) (both surveys carried out at around 150 MHz) suggest that the transient class detected by (Stewart et al. 2016) (at 60 MHz; assuming that the source is astrophysical) either 1) does not follow a Euclidean distribution or 2) has a steep spectrum or narrowband emission. Otherwise, we would have expected to find at least a few such transients in the 150 MHz surveys. We define null probability as the probability of not detecting any transients (of a particular class) in our survey. Assuming Poisson statistics and Euclidean distribution, we derive a null probability for Stewart et al. 2016-like transients of $\ll$1%. It is possible that such events may be caused by variability (intrinsic or extrinsic) of compact Galactic sources (for which we speculate that the source counts are flat ($N(>S) \propto S^{-1}$ or $\propto S^{-0.5}$) because the source density falls off substantially beyond a distance of a few kpc. In this case, we expect the rate of such events to be high close to or within the Galactic plane, and this possibility can be explored with Galactic plane transient surveys at low

[9]Our transient search on the <4 hour timescale is capable of finding transients similar to the one found by (Stewart et al. 2016) (which had a timescale of a few minutes timescale), since each of our observations, that were compared, was 10–20 minutes long. This of course assumes that the emission is broadband and the spectral index of the transient between 60 MHz and 150 MHz is not very steep.

radio frequencies. If we attribute the absence of these transients in our survey and in (Rowlinson et al. 2016) purely to steep spectral index (while assuming $N \propto S^{-1.5}$), then we calculate the spectral index constraint to be $\alpha \lesssim -4$.

The implied rate of the transients like the one found by (Jaeger et al. 2012) is N(>1 mJy)=0.1 deg^{-2}. In the GHz sky, the only transient class known to have such a high rate is active stars and binaries (e.g. Mooley et al. 2016). Hence, we advocate that the Jaeger et al. 2012 transient is a stellar flare, otherwise a different emission mechanism needs to be invoked. A stellar flare interpretation is also consistent with the (Murphy et al. 2017) transient, whose implied snapshot rate per deg^2 is similar to the Jaeger et al. 2012 transient, and was found at low Galactic latitude. This is in line with the M dwarf counterpart/candidate ($d \sim 1.5$ kpc in Gaia; Gaia Collaboration et al. 2018, (Bailer-Jones et al. 2018)) proposed by Murphy et al. 2017. The null probabilities of finding transients, like the ones uncovered by Jaeger et al. 2012 and Murphy et al. 2017, in our survey are approximately 2% and 40% respectively.

As discussed earlier in this section, the transient upper limits from our GMRT survey advocate Galactic searches or very widefield extragalactic searches. We therefore provide recommendations for maximizing transient discovery using existing low-frequency radio interferometers. Considering their modest fields of view ($\ll$100 deg^2), widefield surveys will be expensive to execute with telescopes such as the GMRT, LOFAR, especially given the computing time/cost for data processing. Hence, we recommend surveys of the Galactic plane or Galactic Center for these telescopes. The geographical location and the recent upgrade of the GMRT makes the observatory uniquely situated to carry out sensitive surveys of the Galactic Center with arcsecond localization capability. Although extragalactic transients will be challenging to find with such telescopes, searching for the radio afterglows of neutron star mergers (detected as gravitational wave sources) over tens of square degree localization regions may be worthwhile, especially since reference images can now be provided by the LoTSS (Shimwell et al. 2019) and TGSS-ADR (Intema et al. 2017).

Widefield surveys with the MWA or with the VLA (VCSS, currently being undertaken alongside the VLASS) may be useful for finding old, optically thin extragalactic transients (the transient found by Murphy et al. 2017 may be one such event) and constraining the rates of such transients. All-sky imagers like the LWA1 and OVRO-LWA will be excellent for finding big samples of transients similar to Obenberger et al. 2014, thus identifying these transients with a known class of objects, as well as for detecting coherent emission from Galactic sources and the mergers of neutrons stars. Eventually, SKA-low will be able to routinely survey the low-frequency sky and provide a complete census of the dynamic Galactic and extragalactic sky.

Table 5.2 Summary of variables sources.

Name (G1STS J...)	RA (deg)	DEC (deg)	S1 (mJy)	S2 (mJy)	m	Vs	S_{TGSS} (mJy)	S_{NVSS} (mJy)	S_{FIRST} (mJy)	$\alpha_{0.15}^{1.4}$	Ident.	r (mag)	spec-z
Timescale < 4 years													
012528+000505	21.3699	-0.0990	493 ± 3	731 ± 3	0.39	-52.0	731	1540	1401	0.41	QSO	16.5	1.08
Timescale < 1 month													
None													
Timescale < 1 day													
004608+000505	11.5355	0.0935	478 ± 5	627 ± 8	0.27	15.6	519	96	87	-0.78	QSO	20.3	1.44
Timescale < 4 hours*													
022109+002525	35.2893	-0.4296	343±5	445±3	0.26	15.8	331	335	313	-0.07	AGN	20.5	0.48
022609+012929	36.5402	1.4906	1111 ± 12	776 ± 15	0.36	16.9	1247	363	340	-0.43	QSO	18.5	1.37
013227+002828	23.1165	-0.4766	293 ± 5	153 ± 7	0.63	15.2	316	66	50	-0.54	AGN	24.6	-
012205+000808	20.5248	0.1497	1073 ± 6	820 ± 9	0.27	22.7	1309	172	156	-0.76	AGN	-	-
225224+012626	343.1039	1.4394	225 ± 6	390 ± 6	0.54	-19.5	382	52	49	-0.79	AGN	-	-
223908+012020	339.7868	1.3410	185 ± 5	294 ± 4	0.45	-15.9	237	51	44	-0.68	AGN	21.3	0.53

*The flux scale is most uncertain for this timescale. Many of these variable candidates may be false positives. See §5.5.

CHAPTER 6

Concluding Remarks

In the recent years, owing to the advancements in the development of highly sensitive astronomical observatories, we have unveiled several peculiar transients that are rare, or that were never observed before. The upcoming decade will see even more of an explosion in the numbers of new discoveries. We are still far away from understanding the true nature of cosmos, but there is an urgent need to systematically investigate any new discovery that might come our way. In this work, I have demonstrated the importance of multiwavelength observations of near-by extragalactic transients, as opposed to the conventional single wavelength studies, and how the information unique to every wavelength can form a truly complete picture of a phenomenon. Focusing on near-by objects help us understand the true demographics within a class of events as only the brightest transients occurring at higher redshift are selectively observed (due to sensitivity of the telescopes), whereas no such bias exists in the nearby Universe. Furthermore, this work signifies the importance of extremely late–time observations of the transient events. While many astronomers have observational campaigns in place to follow the events immediately after the discovery, this work motivates us to pursue a long–term monitoring program to uncover new and different physical processes occurring during the lifetime of a transient event.

In Chapters 2 – 3, I extensively studied GW 170817 – the first ever multi-messenger event, and the first binary neutron star merger to be ever observed – both in X-rays and radio at late–times. One of the most exciting developments that I discuss in this work is the plausibility of the kilonova afterglow to be the newly emerging X–ray component, as the jet afterglow fades $\sim$ 3.4 years post–merger, which if true, will be the first ever detection of one. Tracing the kilonova afterglow would give us direct ways of measuring the EoS of the neutron star. Information from EM observations also complements the information from GW signal and together we can use them to test general relativity and the fundamental physics, and make improvements on the measurements of the cosmological Hubble constant.

Our team has recently uncovered a population of TDEs through systematic searches in the archival images of the VLA Sky Survey (VLASS) data to have a delayed emerging radio component ($\sim$ years post–discovery). As discussed in Chapter 4, this could confirm the presence of long–eluded off–axis jets in the TDEs, or a possibility of a new and previously unexplored phase during a TDE's lifetimes.

Lastly, the importance of making efforts to sift through archival survey data is presented in Chapter 5. While targeted observational campaigns are the most effective means to obtain information, many transients can be easily missed. However transients that evolve over $\sim$ months – years timescales can still be discovered in the archival images. Extragalactic synchrotron transients are especially suited for such explorations at low frequencies.

We can extend on the work presented in this dissertation to systematically explore and interpret the multiwavelength data of any new future discoveries to form a complete understanding of the event. A lot remains unexplored in the fields of multi–messenger astronomy and TDEs, especially in unraveling the demographics of these class of transients. For e.g., with more observations 1) of BNS and BH–NS mergers, we will understand the diversity in the outflows that are launched in these systems, and the nature of the merger remnant and its dependence on the intrinsic properties of the progenitor system; 2) of TDEs at late–times will reveal if ASASSN-15oi is typical of a larger population of TDEs with delayed jet launch or formation.

Bibliography

[1] Abbott, B. P., Abbott, R., Abbott, T. D., et al. "GW170817: Observation of Gravitational Waves from a Binary Neutron Star Inspiral". In: *Physical Review Letters* 119.16, 161101 (Oct. 2017), p. 161101. DOI: 10.1103/PhysRevLett.119.161101. arXiv: 1710.05832 [gr-qc].

[2] Abbott, B. P., Abbott, R., Abbott, T. D., and other. "Multi-messenger Observations of a Binary Neutron Star Merger". In: ApJ 848.2, L12 (Oct. 2017), p. L12. DOI: 10.3847/2041-8213/aa91c9. arXiv: 1710.05833 [astro-ph.HE].

[3] Abbott, B. P., Abbott, R., Abbott, T. D., et al. "Properties of the Binary Neutron Star Merger GW170817". In: *Physical Review X* 9.1, 011001 (Jan. 2019), p. 011001. DOI: 10.1103/PhysRevX.9.011001. arXiv: 1805.11579 [gr-qc].

[4] Achterberg, A., Gallant, Y. A., Kirk, J. G., and Guthmann, A. W. "Particle acceleration by ultrarelativistic shocks: theory and simulations". In: MNRAS 328.2 (Dec. 2001), pp. 393–408. DOI: 10.1046/j.1365-8711.2001.04851.x. arXiv: astro-ph/0107530 [astro-ph].

[5] Alexander, K. D., Berger, E., Guillochon, J., Zauderer, B. A., and Williams, P. K. G. "Discovery of an Outflow from Radio Observations of the Tidal

Disruption Event ASASSN-14li". In: ApJ 819.2, L25 (Mar. 2016), p. L25. DOI: 10.3847/2041-8205/819/2/L25. arXiv: 1510.01226 [astro-ph.HE].

[6] Alexander, K. D., Berger, E., Fong, W., et al. "The Electromagnetic Counterpart of the Binary Neutron Star Merger LIGO/Virgo GW170817. VI. Radio Constraints on a Relativistic Jet and Predictions for Late-time Emission from the Kilonova Ejecta". In: *The Astrophysical Journal* 848.2, L21 (Oct. 2017), p. L21. DOI: 10.3847/2041-8213/aa905d. arXiv: 1710.05457 [astro-ph.HE].

[7] Alexander, K. D., Margutti, R., Blanchard, P. K., et al. "A Decline in the X-Ray through Radio Emission from GW170817 Continues to Support an Off-axis Structured Jet". In: ApJ 863, L18 (Aug. 2018), p. L18. DOI: 10.3847/2041-8213/aad637. arXiv: 1805.02870 [astro-ph.HE].

[8] Alexander, K. D., van Velzen, S., Horesh, A., and Zauderer, B. A. "Radio Properties of Tidal Disruption Events". In: Space Sci. Rev. 216.5, 81 (June 2020), p. 81. DOI: 10.1007/s11214-020-00702-w. arXiv: 2006.01159 [astro-ph.HE].

[9] Anderson, M. M., Mooley, K. P., Hallinan, G., et al. "Caltech-NRAO Stripe 82 Survey (CNSS). III. The First Radio-discovered Tidal Disruption Event, CNSS J0019+00". In: ApJ 903.2, 116 (Nov. 2020), p. 116. DOI: 10.3847/1538-4357/abb94b. arXiv: 1910.11912 [astro-ph.HE].

[10] Arcavi, I., Hosseinzadeh, G., Howell, D. A., et al. "Optical emission from a kilonova following a gravitational-wave-detected neutron-star merger". In:

Nature 551 (Nov. 2017), pp. 64–66. DOI: 10.1038/nature24291. arXiv: 1710.05843 [astro-ph.HE].

[11] Arcavi, I. "The First Hours of the GW170817 Kilonova and the Importance of Early Optical and Ultraviolet Observations for Constraining Emission Models". In: ApJ 855, L23 (Mar. 2018), p. L23. DOI: 10.3847/2041-8213/aab267. arXiv: 1802.02164 [astro-ph.HE].

[12] Asplund, M., Grevesse, N., Sauval, A. J., and Scott, P. "The Chemical Composition of the Sun". In: ARA&A 47.1 (Sept. 2009), pp. 481–522. DOI: 10.1146/annurev.astro.46.060407.145222. arXiv: 0909.0948 [astro-ph.SR].

[13] Bailer-Jones, C. A. L., Rybizki, J., Fouesneau, M., Mantelet, G., and Andrae, R. "Estimating Distance from Parallaxes. IV. Distances to 1.33 Billion Stars in Gaia Data Release 2". In: AJ 156.2, 58 (Aug. 2018), p. 58. DOI: 10.3847/1538-3881/aacb21. arXiv: 1804.10121 [astro-ph.SR].

[14] Balasubramanian, A., Corsi, A., Mooley, K. P., et al. "Continued radio observations of GW170817 3.5 years post-merger". In: *arXiv e-prints*, arXiv:2103.04821 (Mar. 2021), arXiv:2103.04821. arXiv: 2103.04821 [astro-ph.HE].

[15] Bannister, K. W., Murphy, T., Gaensler, B. M., Hunstead, R. W., and Chatterjee, S. "A 22-yr southern sky survey for transient and variable radio sources using the Molonglo Observatory Synthesis Telescope". In: MNRAS 412.1 (Mar. 2011), pp. 634–664. DOI: 10.1111/j.1365-2966.2010.17938.x. arXiv: 1011.0003 [astro-ph.CO].

[16] Bauswein, A., Goriely, S., and Janka, H. .-. "Systematics of Dynamical Mass Ejection, Nucleosynthesis, and Radioactively Powered Electromagnetic Signals from Neutron-star Mergers". In: ApJ 773.1, 78 (Aug. 2013), p. 78. DOI: 10.1088/0004-637X/773/1/78. arXiv: 1302.6530 [astro-ph.SR].

[17] Bauswein, A., Just, O., Janka, H.-T., and Stergioulas, N. "Neutron-star Radius Constraints from GW170817 and Future Detections". In: ApJ 850.2, L34 (Dec. 2017), p. L34. DOI: 10.3847/2041-8213/aa9994. arXiv: 1710.06843 [astro-ph.HE].

[18] Bell, A. R. "The acceleration of cosmic rays in shock fronts - I." In: MNRAS 182 (Jan. 1978), pp. 147–156. DOI: 10.1093/mnras/182.2.147.

[19] Bell, M. E., Murphy, T., Kaplan, D. L., et al. "A survey for transients and variables with the Murchison Widefield Array 32-tile prototype at 154 MHz". In: MNRAS 438.1 (Feb. 2014), pp. 352–367. DOI: 10.1093/mnras/stt2200. arXiv: 1311.2989 [astro-ph.GA].

[20] Bell, M. E., Huynh, M. T., Hancock, P., et al. "A search for variable and transient radio sources in the extended Chandra Deep Field South at 5.5 GHz". In: MNRAS 450.4 (July 2015), pp. 4221–4232. DOI: 10.1093/mnras/stv882. arXiv: 1504.06371 [astro-ph.GA].

[21] Bell, M. E., Murphy, T., Hancock, P. J., et al. "The Murchison Widefield Array Transients Survey (MWATS). A search for low-frequency variability in a bright Southern hemisphere sample". In: MNRAS 482.2 (Jan. 2019), pp. 2484–2501. DOI: 10.1093/mnras/sty2801. arXiv: 1810.10152 [astro-ph.GA].

[22] Berger, E., Zauderer, A., Pooley, G. G., et al. "Radio Monitoring of the Tidal Disruption Event Swift J164449.3+573451. I. Jet Energetics and the Pristine Parsec-scale Environment of a Supermassive Black Hole". In: ApJ 748.1, 36 (Mar. 2012), p. 36. DOI: 10.1088/0004-637X/748/1/36. arXiv: 1112.1697 [astro-ph.HE].

[23] Bernuzzi, S., Breschi, M., Daszuta, B., et al. "Accretion-induced prompt black hole formation in asymmetric neutron star mergers, dynamical ejecta, and kilonova signals". In: MNRAS 497.2 (Sept. 2020), pp. 1488–1507. DOI: 10.1093/mnras/staa1860. arXiv: 2003.06015 [astro-ph.HE].

[24] Beznogov, M. V., Page, D., and Ramirez-Ruiz, E. "Thermal Evolution of Neo-neutron Stars. I. Envelopes, Eddington Luminosity Phase, and Implications for GW170817". In: ApJ 888.2, 97 (Jan. 2020), p. 97. DOI: 10.3847/1538-4357/ab5fd6. arXiv: 1908.04888 [astro-ph.HE].

[25] Bietenholz, M., Bartel, N., Rupen, M. P., et al. "Radio Imaging of SN1993J: The Story Continues". In: *10th European VLBI Network Symposium and EVN Users Meeting: VLBI and the New Generation of Radio Arrays*. 2010, 57. arXiv: 1103.1783 [astro-ph.CO].

[26] Blanchard, P. K., Nicholl, M., Berger, E., et al. "PS16dtm: A Tidal Disruption Event in a Narrow-line Seyfert 1 Galaxy". In: ApJ 843.2, 106 (July 2017), p. 106. DOI: 10.3847/1538-4357/aa77f7. arXiv: 1703.07816 [astro-ph.HE].

[27] Blanchard, P. K., Berger, E., Fong, W., et al. "The Electromagnetic Counterpart of the Binary Neutron Star Merger LIGO/Virgo GW170817. VII. Properties of the Host Galaxy and Constraints on the Merger Timescale". In: ApJ 848.2, L22 (Oct. 2017), p. L22. DOI: 10.3847/2041-8213/aa9055. arXiv: 1710.05458 [astro-ph.HE].

[28] Blandford, R. D. and Ostriker, J. P. "Particle acceleration by astrophysical shocks." In: ApJ 221 (Apr. 1978), pp. L29–L32. DOI: 10.1086/182658.

[29] Blandford, R. and Eichler, D. "Particle acceleration at astrophysical shocks: A theory of cosmic ray origin". In: Phys. Rep. 154.1 (Oct. 1987), pp. 1–75. DOI: 10.1016/0370-1573(87)90134-7.

[30] Bloom, J. S., Giannios, D., Metzger, B. D., et al. "A Possible Relativistic Jetted Outburst from a Massive Black Hole Fed by a Tidally Disrupted Star". In: *Science* 333.6039 (July 2011), p. 203. DOI: 10.1126/science.1207150. arXiv: 1104.3257 [astro-ph.HE].

[31] Breeveld, A. A., Curran, P. A., Hoversten, E. A., et al. "Further calibration of the Swift ultraviolet/optical telescope". In: MNRAS 406.3 (Aug. 2010), pp. 1687–1700. DOI: 10.1111/j.1365-2966.2010.16832.x. arXiv: 1004.2448 [astro-ph.IM].

[32] Brimacombe, J., Brown, J. S., Holoien, T. W. .-., et al. "ASAS-SN Discovery of A Probable Supernova in 2MASX J20390918-3045201". In: *The Astronomer's Telegram* 7910 (Aug. 2015), p. 1.

[33] Bromberg, O., Tchekhovskoy, A., Gottlieb, O., Nakar, E., and Piran, T. “The γ-rays that accompanied GW170817 and the observational signature of a magnetic jet breaking out of NS merger ejecta”. In: MNRAS 475.3 (Apr. 2018), pp. 2971–2977. DOI: 10.1093/mnras/stx3316. arXiv: 1710.05897 [astro-ph.HE].

[34] Brown, G. C., Levan, A. J., Stanway, E. R., et al. “Late-time observations of the relativistic tidal disruption flare candidate Swift J1112.2-8238”. In: MNRAS 472.4 (Dec. 2017), pp. 4469–4479. DOI: 10.1093/mnras/stx2193. arXiv: 1708.09668 [astro-ph.HE].

[35] Brown, P. J., Holland, S. T., Immler, S., et al. “Ultraviolet Light Curves of Supernovae with the Swift Ultraviolet/Optical Telescope”. In: AJ 137.5 (May 2009), pp. 4517–4525. DOI: 10.1088/0004-6256/137/5/4517. arXiv: 0803.1265 [astro-ph].

[36] Bulla, M., Covino, S., Kyutoku, K., et al. “The origin of polarization in kilonovae and the case of the gravitational-wave counterpart AT 2017gfo”. In: *Nature Astronomy* 3 (Mar. 2019), pp. 99–106. DOI: 10.1038/s41550-018-0593-y. arXiv: 1809.04078 [astro-ph.HE].

[37] Burrows, D. N., Hill, J. E., Nousek, J. A., et al. “The Swift X-Ray Telescope”. In: Space Sci. Rev. 120 (Oct. 2005), pp. 165–195. DOI: 10.1007/s11214-005-5097-2. eprint: arXiv:astro-ph/0508071.

[38] Burrows, D. N., Kennea, J. A., Ghisellini, G., et al. “Relativistic jet activity from the tidal disruption of a star by a massive black hole”. In: Nature 476.7361

(Aug. 2011), pp. 421–424. DOI: 10.1038/nature10374. arXiv: 1104.4787 [astro-ph.HE].

[39] Cantiello, M., Jensen, J. B., Blakeslee, J. P., et al. "A Precise Distance to the Host Galaxy of the Binary Neutron Star Merger GW170817 Using Surface Brightness Fluctuations". In: ApJ 854, L31 (Feb. 2018), p. L31. DOI: 10.3847/2041-8213/aaad64. arXiv: 1801.06080.

[40] Carbone, D., van der Horst, A. J., Wijers, R. A. M. J., et al. "New methods to constrain the radio transient rate: results from a survey of four fields with LOFAR". In: MNRAS 459.3 (July 2016), pp. 3161–3174. DOI: 10.1093/mnras/stw539. arXiv: 1411.7928 [astro-ph.IM].

[41] Cardelli, J. A., Clayton, G. C., and Mathis, J. S. "The relationship between infrared, optical, and ultraviolet extinction". In: ApJ 345 (Oct. 1989), pp. 245–256. DOI: 10.1086/167900.

[42] Carilli, C. L., Bertoldi, F., Rupen, M. P., et al. "A 250 GHz Survey of High-Redshift Quasars from the Sloan Digital Sky Survey". In: ApJ 555.2 (July 2001), pp. 625–632. DOI: 10.1086/321519. arXiv: astro-ph/0103252 [astro-ph].

[43] Carilli, C. L., Ivison, R. J., and Frail, D. A. "Variability of Submillijansky Radio Sources". In: ApJ 590.1 (June 2003), pp. 192–196. DOI: 10.1086/375005. arXiv: astro-ph/0302528 [astro-ph].

[44] Cendes, Y., Wijers, R. A. M. J., Swinbank, J. D., et al. "LOFAR Observations of Swift J1644+57 and Implications for Short-Duration Transients". In: *arXiv*

e-prints, arXiv:1412.3986 (Dec. 2014), arXiv:1412.3986. arXiv: 1412.3986 [astro-ph.HE].

[45] Cendes, Y., Alexander, K. D., Berger, E., et al. "Radio Observations of an Ordinary Outflow from the Tidal Disruption Event AT2019dsg". In: ApJ 919.2, 127 (Oct. 2021), p. 127. DOI: 10.3847/1538-4357/ac110a. arXiv: 2103.06299 [astro-ph.HE].

[46] Cendes, Y., Alexander, K. D., Berger, E., et al. "Radio Observations of an Ordinary Outflow from the Tidal Disruption Event AT2019dsg". In: ApJ 919.2, 127 (Oct. 2021), p. 127. DOI: 10.3847/1538-4357/ac110a. arXiv: 2103.06299 [astro-ph.HE].

[47] Cendes, Y., Berger, E., Alexander, K., et al. "A Mildly Relativistic Outflow Launched Two Years after Disruption in the Tidal Disruption Event AT2018hyz". In: *arXiv e-prints*, arXiv:2206.14297 (June 2022), arXiv:2206.14297. arXiv: 2206.14297 [astro-ph.HE].

[48] Cenko, S. B., Krimm, H. A., Horesh, A., et al. "Swift J2058.4+0516: Discovery of a Possible Second Relativistic Tidal Disruption Flare?" In: ApJ 753, 77 (July 2012), p. 77. DOI: 10.1088/0004-637X/753/1/77. arXiv: 1107.5307 [astro-ph.HE].

[49] Chevalier, R. A. "Synchrotron Self-Absorption in Radio Supernovae". In: ApJ 499 (May 1998), pp. 810–819. DOI: 10.1086/305676.

[50] Chornock, R., Berger, E., Kasen, D., et al. "The Electromagnetic Counterpart of the Binary Neutron Star Merger LIGO/Virgo GW170817. IV. Detection of

Near-infrared Signatures of r-process Nucleosynthesis with Gemini-South". In: ApJ 848.2, L19 (Oct. 2017), p. L19. DOI: 10.3847/2041-8213/aa905c. arXiv: 1710.05454 [astro-ph.HE].

[51] Ciolfi, R. "Collimated outflows from long-lived binary neutron star merger remnants". In: MNRAS 495.1 (June 2020), pp. L66–L70. DOI: 10.1093/mnrasl/slaa062. arXiv: 2001.10241 [astro-ph.HE].

[52] Clarke, M. E. "The determination of the positions of 88 radio sources". In: MNRAS 127 (Jan. 1964), p. 405. DOI: 10.1093/mnras/127.5.405.

[53] Corbel, S., Nowak, M. A., Fender, R. P., Tzioumis, A. K., and Markoff, S. "Radio/X-ray correlation in the low/hard state of GX 339-4". In: A&A 400 (Mar. 2003), pp. 1007–1012. DOI: 10.1051/0004-6361:20030090. arXiv: astro-ph/0301436 [astro-ph].

[54] Coulter, D., Foley, R., Kilpatrick, C., et al. "Swope Supernova Survey 2017a (SSS17a), the optical counterpart to a gravitational wave source". In: *Science* (2017), eaap9811.

[55] Cowperthwaite, P. S., Berger, E., Villar, V. A., et al. "The Electromagnetic Counterpart of the Binary Neutron Star Merger LIGO/Virgo GW170817. II. UV, Optical, and Near-infrared Light Curves and Comparison to Kilonova Models". In: ApJ 848, L17 (Oct. 2017), p. L17. DOI: 10.3847/2041-8213/aa8fc7.

[56] Croft, S., Bower, G. C., Ackermann, R., et al. "The Allen Telescope Array Twenty-centimeter Survey—A 690 deg^2, 12 Epoch Radio Data Set. I. Catalog

and Long-duration Transient Statistics". In: ApJ 719.1 (Aug. 2010), pp. 45–58. DOI: 10.1088/0004-637X/719/1/45. arXiv: 1006.2003 [astro-ph.CO].

[57] Croft, S., Bower, G. C., Keating, G., et al. "The Allen Telescope Array Twenty-centimeter Survey—A 700-square-degree, Multi-epoch Radio Data Set. II. Individual Epoch Transient Statistics". In: ApJ 731.1, 34 (Apr. 2011), p. 34. DOI: 10.1088/0004-637X/731/1/34. arXiv: 1102.2227 [astro-ph.CO].

[58] Crumley, P., Caprioli, D., Markoff, S., and Spitkovsky, A. "Kinetic simulations of mildly relativistic shocks - I. Particle acceleration in high Mach number shocks". In: MNRAS 485.4 (June 2019), pp. 5105–5119. DOI: 10.1093/mnras/stz232. arXiv: 1809.10809 [astro-ph.HE].

[59] D'Avanzo, P., Campana, S., Salafia, O. S., et al. "The evolution of the X-ray afterglow emission of GW 170817/ GRB 170817A in XMM-Newton observations". In: A&A 613, L1 (May 2018), p. L1. DOI: 10.1051/0004-6361/201832664. arXiv: 1801.06164 [astro-ph.HE].

[60] de Vries, W. H., Becker, R. H., White, R. L., and Xanthopoulos, E. "Demographics of Double Lobed Radio Quasars". In: *American Astronomical Society Meeting Abstracts*. Vol. 205. American Astronomical Society Meeting Abstracts. Dec. 2004, 143.01, p. 143.01.

[61] DeMarchi, L., Margutti, R., Dittman, J., et al. "Radio Analysis of SN 2004C Reveals an Unusual CSM Density Profile as a Harbinger of Core Collapse". In: *arXiv e-prints*, arXiv:2203.07388 (Mar. 2022), arXiv:2203.07388. arXiv: 2203.07388 [astro-ph.HE].

[62] Dobie, D., Kaplan, D. L., Murphy, T., et al. "A Turnover in the Radio Light Curve of GW170817". In: ApJ 858, L15 (May 2018), p. L15. DOI: 10.3847/2041-8213/aac105.

[63] Douchin, F. and Haensel, P. "A unified equation of state of dense matter and neutron star structure". In: A&A 380 (Dec. 2001), pp. 151–167. DOI: 10.1051/0004-6361:20011402. arXiv: astro-ph/0111092 [astro-ph].

[64] Drout, M., Piro, A., Shappee, B., et al. "Light curves of the neutron star merger GW170817/SSS17a: Implications for r-process nucleosynthesis". In: *Science* (2017), eaaq0049.

[65] Duffell, P. C. and MacFadyen, A. I. "A "Boosted Fireball" Model for Structured Relativistic Jets". In: ApJ 776.1, L9 (Oct. 2013), p. L9. DOI: 10.1088/2041-8205/776/1/L9. arXiv: 1308.1731 [astro-ph.HE].

[66] Dunn, R. J. H., Fender, R. P., Körding, E. G., Belloni, T., and Cabanac, C. "A global spectral study of black hole X-ray binaries". In: MNRAS 403.1 (Mar. 2010), pp. 61–82. DOI: 10.1111/j.1365-2966.2010.16114.x. arXiv: 0912.0142 [astro-ph.HE].

[67] Eftekhari, T., Berger, E., Zauderer, B. A., Margutti, R., and Alexander, K. D. "Radio Monitoring of the Tidal Disruption Event Swift J164449.3+573451. III. Late-time Jet Energetics and a Deviation from Equipartition". In: ApJ 854.2, 86 (Feb. 2018), p. 86. DOI: 10.3847/1538-4357/aaa8e0. arXiv: 1710.07289 [astro-ph.HE].

[68] Eichler, D., Livio, M., Piran, T., and Schramm, D. N. "Nucleosynthesis, neutrino bursts and γ-rays from coalescing neutron stars". In: Nature 340.6229 (July 1989), pp. 126–128. DOI: 10.1038/340126a0.

[69] Eichler, D. and Waxman, E. "The Efficiency of Electron Acceleration in Collisionless Shocks and Gamma-Ray Burst Energetics". In: ApJ 627.2 (July 2005), pp. 861–867. DOI: 10.1086/430596. arXiv: astro-ph/0502070 [astro-ph].

[70] Einstein, A. "Näherungsweise Integration der Feldgleichungen der Gravitation". In: *Sitzungsberichte der Königlich Preußischen Akademie der Wissenschaften (Berlin* (Jan. 1916), pp. 688–696.

[71] Endrizzi, A., Perego, A., Fabbri, F. M., et al. "Thermodynamics conditions of matter in the neutrino decoupling region during neutron star mergers". In: *European Physical Journal A* 56.1, 15 (Jan. 2020), p. 15. DOI: 10.1140/epja/s10050-019-00018-6. arXiv: 1908.04952 [astro-ph.HE].

[72] Evans, P. A., Beardmore, A. P., Page, K. L., et al. "Methods and results of an automatic analysis of a complete sample of Swift-XRT observations of GRBs". In: MNRAS 397.3 (Aug. 2009), pp. 1177–1201. DOI: 10.1111/j.1365-2966.2009.14913.x. arXiv: 0812.3662 [astro-ph].

[73] Evans, P. A., Cenko, S. B., Kennea, J. A., et al. "Swift and NuSTAR observations of GW170817: Detection of a blue kilonova". In: *Science* 358.6370 (Dec. 2017), pp. 1565–1570. DOI: 10.1126/science.aap9580. arXiv: 1710.05437 [astro-ph.HE].

[74] Fender, R., Woudt, P. A., Corbel, S., et al. "ThunderKAT: The MeerKAT Large Survey Project for Image-Plane Radio Transients". In: *MeerKAT Science: On the Pathway to the SKA*. Jan. 2016, 13, p. 13. arXiv: 1711.04132 [astro-ph.HE].

[75] Fender, R. P., Belloni, T. M., and Gallo, E. "Towards a unified model for black hole X-ray binary jets". In: MNRAS 355.4 (Dec. 2004), pp. 1105–1118. DOI: 10.1111/j.1365-2966.2004.08384.x. arXiv: astro-ph/0409360 [astro-ph].

[76] Feng, L., Vaulin, R., Hewitt, J. N., et al. "A Matched Filter Technique for Slow Radio Transient Detection and First Demonstration with the Murchison Widefield Array". In: AJ 153.3, 98 (Mar. 2017), p. 98. DOI: 10.3847/1538-3881/153/3/98. arXiv: 1701.03557 [astro-ph.HE].

[77] Fernández, R. and Metzger, B. D. "Delayed outflows from black hole accretion tori following neutron star binary coalescence". In: MNRAS 435.1 (Oct. 2013), pp. 502–517. DOI: 10.1093/mnras/stt1312. arXiv: 1304.6720 [astro-ph.HE].

[78] Fernández, R., Tchekhovskoy, A., Quataert, E., Foucart, F., and Kasen, D. "Long-term GRMHD simulations of neutron star merger accretion discs: implications for electromagnetic counterparts". In: MNRAS 482.3 (Jan. 2019), pp. 3373–3393. DOI: 10.1093/mnras/sty2932. arXiv: 1808.00461 [astro-ph.HE].

[79] Fitzpatrick, E. L. "Correcting for the Effects of Interstellar Extinction". In: PASP 111.755 (Jan. 1999), pp. 63–75. DOI: 10.1086/316293. arXiv: astro-ph/9809387 [astro-ph].

[80] Fong, W., Berger, E., Margutti, R., and Zauderer, B. A. "A Decade of Short-duration Gamma-Ray Burst Broadband Afterglows: Energetics, Circumburst Densities, and Jet Opening Angles". In: ApJ 815, 102 (Dec. 2015), p. 102. DOI: 10.1088/0004-637X/815/2/102. arXiv: 1509.02922 [astro-ph.HE].

[81] Fong, W., Berger, E., Blanchard, P. K., et al. "The Electromagnetic Counterpart of the Binary Neutron Star Merger LIGO/Virgo GW170817. VIII. A Comparison to Cosmological Short-duration Gamma-Ray Bursts". In: ApJ 848, L23 (Oct. 2017), p. L23. DOI: 10.3847/2041-8213/aa9018. arXiv: 1710.05438 [astro-ph.HE].

[82] Fong, W., Blanchard, P. K., Alexander, K. D., et al. "The Optical Afterglow of GW170817: An Off-axis Structured Jet and Deep Constraints on a Globular Cluster Origin". In: ApJ 883.1, L1 (Sept. 2019), p. L1. DOI: 10.3847/2041-8213/ab3d9e. arXiv: 1908.08046 [astro-ph.HE].

[83] Foreman-Mackey, D., Hogg, D. W., Lang, D., and Goodman, J. "emcee: The MCMC Hammer". In: PASP 125.925 (Mar. 2013), p. 306. DOI: 10.1086/670067. arXiv: 1202.3665 [astro-ph.IM].

[84] Frail, D. A., Kulkarni, S. R., Hurley, K. C., et al. "A Search for the Radio Counterpart to the 1994 March 1 Gamma-Ray Burst". In: ApJ 437 (Dec. 1994), p. L43. DOI: 10.1086/187678. arXiv: astro-ph/9409025 [astro-ph].

[85] Frail, D. A., Waxman, E., and Kulkarni, S. R. "A 450 Day Light Curve of the Radio Afterglow of GRB 970508: Fireball Calorimetry". In: ApJ 537.1 (July 2000), pp. 191–204. DOI: 10.1086/309024. arXiv: astro-ph/9910319 [astro-ph].

[86] Frail, D. A., Kulkarni, S. R., Ofek, E. O., Bower, G. C., and Nakar, E. "A Revised View of the Transient Radio Sky". In: ApJ 747.1, 70 (Mar. 2012), p. 70. DOI: 10.1088/0004-637X/747/1/70. arXiv: 1111.0007 [astro-ph.HE].

[87] Frail, D. A., Ray, P. S., Mooley, K. P., et al. "An image-based search for pulsars among Fermi unassociated LAT sources". In: MNRAS 475.1 (Mar. 2018), pp. 942–954. DOI: 10.1093/mnras/stx3281. arXiv: 1712.06609 [astro-ph.HE].

[88] Fruscione, A., McDowell, J. C., Allen, G. E., et al. "CIAO: Chandra's data analysis system". In: *Society of Photo-Optical Instrumentation Engineers (SPIE) Conference Series*. Ed. by Silva, D. R. and Doxsey, R. E. Vol. 6270. Society of Photo-Optical Instrumentation Engineers (SPIE) Conference Series. June 2006, 62701V, p. 62701V. DOI: 10.1117/12.671760.

[89] Gaia Collaboration and al., et. "Gaia Data Release 2. Summary of the contents and survey properties". In: A&A 616, A1 (Aug. 2018), A1. DOI: 10.1051/0004-6361/201833051. arXiv: 1804.09365 [astro-ph.GA].

[90] Gal-Yam, A., Ofek, E. O., Poznanski, D., et al. "Radio and Optical Follow-up Observations of a Uniform Radio Transient Search: Implications for Gamma-Ray Bursts and Supernovae". In: ApJ 639.1 (Mar. 2006), pp. 331–339. DOI: 10.1086/499157. arXiv: astro-ph/0508629 [astro-ph].

[91] Gallo, E., Miller-Jones, J. C. A., Russell, D. M., et al. "The radio/X-ray domain of black hole X-ray binaries at the lowest radio luminosities". In: MNRAS 445.1 (Nov. 2014), pp. 290–300. DOI: 10.1093/mnras/stu1599. arXiv: 1408.3130 [astro-ph.HE].

[92] Gao, H., Lei, W.-H., Zou, Y.-C., Wu, X.-F., and Zhang, B. "A complete reference of the analytical synchrotron external shock models of gamma-ray bursts". In: New A Rev. 57.6 (Dec. 2013), pp. 141–190. DOI: 10.1016/j.newar.2013.10.001. arXiv: 1310.2181 [astro-ph.HE].

[93] Gehrels, N. "Confidence Limits for Small Numbers of Events in Astrophysical Data". In: ApJ 303 (Apr. 1986), p. 336. DOI: 10.1086/164079.

[94] Gehrels, N., Chincarini, G., Giommi, P., et al. "The Swift Gamma-Ray Burst Mission". In: ApJ 611 (Aug. 2004), pp. 1005–1020. DOI: 10.1086/422091.

[95] Gezari, S., Chornock, R., Rest, A., et al. "An ultraviolet-optical flare from the tidal disruption of a helium-rich stellar core". In: Nature 485.7397 (May 2012), pp. 217–220. DOI: 10.1038/nature10990. arXiv: 1205.0252 [astro-ph.CO].

[96] Gezari, S., Cenko, S. B., and Arcavi, I. "X-Ray Brightening and UV Fading of Tidal Disruption Event ASASSN-15oi". In: ApJ 851.2, L47 (Dec. 2017), p. L47. DOI: 10.3847/2041-8213/aaa0c2. arXiv: 1712.03968 [astro-ph.HE].

[97] Ghirlanda, G., Salafia, O. S., Paragi, Z., et al. "Compact radio emission indicates a structured jet was produced by a binary neutron star merger". In: *Science* 363.6430 (Mar. 2019), pp. 968–971. DOI: 10.1126/science.aau8815. arXiv: 1808.00469 [astro-ph.HE].

[98] Gill, R., Nathanail, A., and Rezzolla, L. "When Did the Remnant of GW170817 Collapse to a Black Hole?" In: ApJ 876.2, 139 (May 2019), p. 139. DOI: 10.3847/1538-4357/ab16da. arXiv: 1901.04138 [astro-ph.HE].

[99] Gladstone, J. C., Roberts, T. P., and Done, C. "The ultraluminous state". In: MNRAS 397.4 (Aug. 2009), pp. 1836–1851. DOI: 10.1111/j.1365-2966.2009.15123.x. arXiv: 0905.4076 [astro-ph.CO].

[100] Goldstein, A., Veres, P., Burns, E., et al. "An Ordinary Short Gamma-Ray Burst with Extraordinary Implications: Fermi-GBM Detection of GRB 170817A". In: ApJ 848.2, L14 (Oct. 2017), p. L14. DOI: 10.3847/2041-8213/aa8f41. arXiv: 1710.05446 [astro-ph.HE].

[101] Gottlieb, O., Nakar, E., Piran, T., and Hotokezaka, K. "A cocoon shock breakout as the origin of the γ-ray emission in GW170817". In: MNRAS 479.1 (Sept. 2018), pp. 588–600. DOI: 10.1093/mnras/sty1462. arXiv: 1710.05896 [astro-ph.HE].

[102] Graham, M. J., Ford, K. E. S., McKernan, B., et al. "Candidate Electromagnetic Counterpart to the Binary Black Hole Merger Gravitational-Wave Event S190521g*". In: Phys. Rev. Lett. 124.25, 251102 (June 2020), p. 251102. DOI: 10.1103/PhysRevLett.124.251102. arXiv: 2006.14122 [astro-ph.HE].

[103] Granot, J. and Sari, R. "The Shape of Spectral Breaks in Gamma-Ray Burst Afterglows". In: ApJ 568 (Apr. 2002), pp. 820–829. DOI: 10.1086/338966. eprint: astro-ph/0108027.

[104] Granot, J., Guetta, D., and Gill, R. "Lessons from the Short GRB 170817A: The First Gravitational-wave Detection of a Binary Neutron Star Merger". In: ApJ 850.2, L24 (Dec. 2017), p. L24. DOI: 10.3847/2041-8213/aa991d. arXiv: 1710.06407 [astro-ph.HE].

[105] Granot, J., Gill, R., Guetta, D., and De Colle, F. "Off-axis emission of short GRB jets from double neutron star mergers and GRB 170817A". In: MNRAS 481.2 (Dec. 2018), pp. 1597–1608. DOI: 10.1093/mnras/sty2308. arXiv: 1710.06421 [astro-ph.HE].

[106] Haggard, D., Nynka, M., Ruan, J. J., et al. "A Deep Chandra X-Ray Study of Neutron Star Coalescence GW170817". In: ApJ 848, L25 (Oct. 2017), p. L25. DOI: 10.3847/2041-8213/aa8ede.

[107] Hajela, A., Margutti, R., Alexander, K. D., et al. "Two Years of Nonthermal Emission from the Binary Neutron Star Merger GW170817: Rapid Fading of the Jet Afterglow and First Constraints on the Kilonova Fastest Ejecta". In: ApJ 886.1, L17 (Nov. 2019), p. L17. DOI: 10.3847/2041-8213/ab5226. arXiv: 1909.06393 [astro-ph.HE].

[108] Hajela, A., Margutti, R., Kathirgamaraju, A., et al. "X-Ray Emission from GW170817 ~2.5 years After the Merger". In: *Research Notes of the American*

Astronomical Society 4.5, 68 (May 2020), p. 68. DOI: 10.3847/2515-5172/ab9229.

[109] Hallinan, G., Corsi, A., Mooley, K. P., et al. "A radio counterpart to a neutron star merger". In: *Science* 358 (Dec. 2017), pp. 1579–1583. DOI: 10.1126/science.aap9855.

[110] Hancock, P. J., Murphy, T., Gaensler, B. M., Hopkins, A., and Curran, J. R. "Compact continuum source finding for next generation radio surveys". In: MNRAS 422.2 (May 2012), pp. 1812–1824. DOI: 10.1111/j.1365-2966.2012.20768.x. arXiv: 1202.4500 [astro-ph.IM].

[111] Hancock, P. J., Drury, J. A., Bell, M. E., Murphy, T., and Gaensler, B. M. "Radio variability in the Phoenix Deep Survey at 1.4 GHz". In: MNRAS 461.3 (Sept. 2016), pp. 3314–3321. DOI: 10.1093/mnras/stw1486. arXiv: 1606.05953 [astro-ph.GA].

[112] Heywood, I., Bannister, K. W., Marvil, J., et al. "Wide-field broad-band radio imaging with phased array feeds: a pilot multi-epoch continuum survey with ASKAP-BETA". In: MNRAS 457.4 (Apr. 2016), pp. 4160–4178. DOI: 10.1093/mnras/stw186. arXiv: 1601.05857 [astro-ph.IM].

[113] Heywood, I. *oxkat: Semi-automated imaging of MeerKAT observations*. Sept. 2020. ascl: 2009.003.

[114] Hinkle, J. T., Holoien, T. W. .-., Shappee, B. J., et al. "Peak-Luminosity/Decline-Rate Relationship for Tidal Disruption Events". In: *arXiv e-prints*, arXiv:2001.08215 (Jan. 2020), arXiv:2001.08215. arXiv: 2001.08215 [astro-ph.HE].

[115] Hinkle, J. T., Holoien, T. W. .-., Shappee, B. J., and Auchettl, K. "A Swift Fix for Nuclear Outbursts". In: ApJ 910.2, 83 (Apr. 2021), p. 83. DOI: 10.3847/1538-4357/abe4d8. arXiv: 2012.08521 [astro-ph.HE].

[116] Holoien, T. W. .-., Kochanek, C. S., Prieto, J. L., et al. "ASASSN-15oi: a rapidly evolving, luminous tidal disruption event at 216 Mpc". In: MNRAS 463.4 (Dec. 2016), pp. 3813–3828. DOI: 10.1093/mnras/stw2272. arXiv: 1602.01088 [astro-ph.HE].

[117] Holoien, T. W. .-., Kochanek, C. S., Prieto, J. L., et al. "Six months of multiwavelength follow-up of the tidal disruption candidate ASASSN-14li and implied TDE rates from ASAS-SN". In: MNRAS 455.3 (Jan. 2016), pp. 2918–2935. DOI: 10.1093/mnras/stv2486. arXiv: 1507.01598 [astro-ph.HE].

[118] Holoien, T. W. .-., Brown, J. S., Auchettl, K., et al. "The unusual late-time evolution of the tidal disruption event ASASSN-15oi". In: MNRAS 480.4 (Nov. 2018), pp. 5689–5703. DOI: 10.1093/mnras/sty2273. arXiv: 1804.00006 [astro-ph.HE].

[119] Horesh, A., Cenko, S. B., and Arcavi, I. "Delayed radio flares from a tidal disruption event". In: *Nature Astronomy* 5 (Jan. 2021), pp. 491–497. DOI: 10.1038/s41550-021-01300-8. arXiv: 2102.11290 [astro-ph.HE].

[120] Horesh, A., Sfaradi, I., Fender, R., et al. "Are Delayed Radio Flares Common in Tidal Disruption Events? The Case of the TDE iPTF 16fnl". In: ApJ 920.1, L5 (Oct. 2021), p. L5. DOI: 10.3847/2041-8213/ac25fe. arXiv: 2109.10921 [astro-ph.HE].

[121] Hotokezaka, K., Nakar, E., Gottlieb, O., et al. "A Hubble constant measurement from superluminal motion of the jet in GW170817". In: *Nature Astronomy* 3 (July 2019), pp. 940–944. DOI: 10.1038/s41550-019-0820-1. arXiv: 1806.10596 [astro-ph.CO].

[122] Hotokezaka, K., Kiuchi, K., Kyutoku, K., et al. "Mass ejection from the merger of binary neutron stars". In: Phys. Rev. D 87.2, 024001 (Jan. 2013), p. 024001. DOI: 10.1103/PhysRevD.87.024001. arXiv: 1212.0905 [astro-ph.HE].

[123] Hotokezaka, K. and Piran, T. "Mass ejection from neutron star mergers: different components and expected radio signals". In: MNRAS 450.2 (June 2015), pp. 1430–1440. DOI: 10.1093/mnras/stv620. arXiv: 1501.01986 [astro-ph.HE].

[124] Hotokezaka, K., Kiuchi, K., Shibata, M., Nakar, E., and Piran, T. "Synchrotron Radiation from the Fast Tail of Dynamical Ejecta of Neutron Star Mergers". In: ApJ 867.2, 95 (Nov. 2018), p. 95. DOI: 10.3847/1538-4357/aadf92. arXiv: 1803.00599 [astro-ph.HE].

[125] Hotokezaka, K., Tanaka, M., Kato, D., and Gaigalas, G. "Nebular Emission from Lanthanide-rich Ejecta of Neutron Star Merger". In: *arXiv e-prints*, arXiv:2102.07879 (Feb. 2021), arXiv:2102.07879. arXiv: 2102.07879 [astro-ph.HE].

[126] Huang, Y. F. and Cheng, K. S. "Gamma-ray bursts: optical afterglows in the deep Newtonian phase". In: MNRAS 341.1 (May 2003), pp. 263–269. DOI: 10.1046/j.1365-8711.2003.06430.x. arXiv: astro-ph/0301387 [astro-ph].

[127] Hulse, R. A. and Taylor, J. H. "Discovery of a pulsar in a binary system." In: ApJ 195 (Jan. 1975), pp. L51–L53. DOI: 10.1086/181708.

[128] Hurley-Walker, N., Callingham, J. R., Hancock, P. J., et al. "GaLactic and Extragalactic All-sky Murchison Widefield Array (GLEAM) survey - I. A low-frequency extragalactic catalogue". In: MNRAS 464.1 (Jan. 2017), pp. 1146–1167. DOI: 10.1093/mnras/stw2337. arXiv: 1610.08318 [astro-ph.GA].

[129] Hyman, S. D., Lazio, T. J. W., Kassim, N. E., et al. "A powerful bursting radio source towards the Galactic Centre". In: Nature 434.7029 (Mar. 2005), pp. 50–52. DOI: 10.1038/nature03400. arXiv: astro-ph/0503052 [astro-ph].

[130] Hyman, S. D., Roy, S., Pal, S., et al. "A Faint, Steep-Spectrum Burst from the Radio Transient GCRT J1745-3009". In: ApJ 660.2 (May 2007), pp. L121–L124. DOI: 10.1086/518245. arXiv: astro-ph/0701098 [astro-ph].

[131] Hyman, S. D., Wijnands, R., Lazio, T. J. W., et al. "GCRT J1742-3001: A New Radio Transient Toward the Galactic Center". In: ApJ 696.1 (May 2009), pp. 280–286. DOI: 10.1088/0004-637X/696/1/280. arXiv: 0811.1972 [astro-ph].

[132] Intema, H. T., van der Tol, S., Cotton, W. D., et al. "Ionospheric calibration of low frequency radio interferometric observations using the peeling scheme. I. Method description and first results". In: A&A 501.3 (July 2009), pp. 1185–1205. DOI: 10.1051/0004-6361/200811094. arXiv: 0904.3975 [astro-ph.IM].

[133] Intema, H. T., Jagannathan, P., Mooley, K. P., and Frail, D. A. "The GMRT 150 MHz all-sky radio survey. First alternative data release TGSS ADR1". In: A&A 598, A78 (Feb. 2017), A78. DOI: 10.1051/0004-6361/201628536. arXiv: 1603.04368 [astro-ph.CO].

[134] Ishizaki, W., Ioka, K., and Kiuchi, K. "Fallback Accretion Model for the Years-to-Decades X-ray Counterpart to GW170817". In: *arXiv e-prints*, arXiv:2104.04433 (Apr. 2021), arXiv:2104.04433. arXiv: 2104.04433 [astro-ph.HE].

[135] Jaeger, T. R., Hyman, S. D., Kassim, N. E., and Lazio, T. J. W. "Discovery of a Meter-wavelength Radio Transient in the SWIRE Deep Field: 1046+59". In: AJ 143.4, 96 (Apr. 2012), p. 96. DOI: 10.1088/0004-6256/143/4/96. arXiv: 1201.6290 [astro-ph.HE].

[136] Jansen, F., Lumb, D., Altieri, B., et al. "XMM-Newton observatory. I. The spacecraft and operations". In: A&A 365 (Jan. 2001), pp. L1–L6. DOI: 10.1051/0004-6361:20000036.

[137] Jansky, K. G. "Radio Waves from Outside the Solar System". In: Nature 132.3323 (July 1933), p. 66. DOI: 10.1038/132066a0.

[138] Kalberla, P. M. W., Burton, W. B., Hartmann, D., et al. "The Leiden/Argentine/Bonn (LAB) Survey of Galactic HI. Final data release of the combined LDS and IAR surveys with improved stray-radiation corrections". In: A&A 440 (Sept. 2005), pp. 775–782. DOI: 10.1051/0004-6361:20041864. eprint: astro-ph/0504140.

[139] Kalberla, P. M. W., Burton, W. B., Hartmann, D., et al. "The Leiden/Argentine/Bonn (LAB) Survey of Galactic HI. Final data release of the combined LDS and IAR surveys with improved stray-radiation corrections". In: A&A 440 (Sept. 2005), pp. 775–782. DOI: 10.1051/0004-6361:20041864. eprint: arXiv:astro-ph/0504140.

[140] Kasliwal, M. M., Kasen, D., Lau, R. M., et al. "Spitzer Mid-Infrared Detections of Neutron Star Merger GW170817 Suggests Synthesis of the Heaviest Elements". In: MNRAS (Jan. 2019), p. L14. DOI: 10.1093/mnrasl/slz007. arXiv: 1812.08708 [astro-ph.HE].

[141] Kasliwal, M., Nakar, E., Singer, L., et al. "Illuminating gravitational waves: A concordant picture of photons from a neutron star merger". In: *Science* (2017), eaap9455.

[142] Kathirgamaraju, A., Tchekhovskoy, A., Giannios, D., and Barniol Duran, R. "EM counterparts of structured jets from 3D GRMHD simulations". In: MNRAS 484.1 (Mar. 2019), pp. L98–L103. DOI: 10.1093/mnrasl/slz012. arXiv: 1809.05099 [astro-ph.HE].

[143] Kellermann, K. I. and Pauliny-Toth, I. I. K. "The Spectra of Opaque Radio Sources". In: ApJ 155 (Feb. 1969), p. L71. DOI: 10.1086/180305.

[144] Kenyon, J. S., Smirnov, O. M., Grobler, T. L., and Perkins, S. J. "CUBICAL - fast radio interferometric calibration suite exploiting complex optimization". In: MNRAS 478.2 (Aug. 2018), pp. 2399–2415. DOI: 10.1093/mnras/sty1221. arXiv: 1805.03410 [astro-ph.IM].

[145] Keshet, U. and Waxman, E. "Energy Spectrum of Particles Accelerated in Relativistic Collisionless Shocks". In: Phys. Rev. Lett. 94.11, 111102 (Mar. 2005), p. 111102. DOI: 10.1103/PhysRevLett.94.111102. arXiv: astro-ph/0408489 [astro-ph].

[146] Kilpatrick, C. D., Foley, R. J., Kasen, D., et al. "Electromagnetic evidence that SSS17a is the result of a binary neutron star merger". In: *Science* 358.6370 (Dec. 2017), pp. 1583–1587. DOI: 10.1126/science.aaq0073. arXiv: 1710.05434 [astro-ph.HE].

[147] Kilpatrick, C. D., Fong, W., Hajela, A., et al. "GW170817: HST observations at 3.4 years from merger". In: *GRB Coordinates Network* 29263 (Jan. 2021), p. 1.

[148] King, A. R. "Masses, beaming and Eddington ratios in ultraluminous X-ray sources". In: MNRAS 393.1 (Feb. 2009), pp. L41–L44. DOI: 10.1111/j.1745-3933.2008.00594.x. arXiv: 0811.1473 [astro-ph].

[149] Kirk, J. G., Guthmann, A. W., Gallant, Y. A., and Achterberg, A. "Particle Acceleration at Ultrarelativistic Shocks: An Eigenfunction Method". In: ApJ 542.1 (Oct. 2000), pp. 235–242. DOI: 10.1086/309533. arXiv: astro-ph/0005222 [astro-ph].

[150] Kiuchi, K., Cerdá-Durán, P., Kyutoku, K., Sekiguchi, Y., and Shibata, M. "Efficient magnetic-field amplification due to the Kelvin-Helmholtz instability in binary neutron star mergers". In: Phys. Rev. D 92.12, 124034 (Dec.

2015), p. 124034. DOI: 10.1103/PhysRevD.92.124034. arXiv: 1509.09205 [astro-ph.HE].

[151] Komossa, S. and Bade, N. “The giant X-ray outbursts in NGC 5905 and IC 3599:() hfill Follow-up observations and outburst scenarios”. In: A&A 343 (Mar. 1999), pp. 775–787. arXiv: astro-ph/9901141 [astro-ph].

[152] Körding, E., Colbert, E., and Falcke, H. “A radio monitoring survey of ultra-luminous X-ray sources”. In: A&A 436.2 (June 2005), pp. 427–436. DOI: 10.1051/0004-6361:20042452. arXiv: astro-ph/0502265 [astro-ph].

[153] Kulkarni, S. R. and Phinney, E. S. “Astronomy: Blasts from the radio heavens”. In: Nature 434.7029 (Mar. 2005), pp. 28–29. DOI: 10.1038/434028a.

[154] Kyutoku, K., Ioka, K., and Shibata, M. “Ultrarelativistic electromagnetic counterpart to binary neutron star mergers”. In: MNRAS 437.1 (Jan. 2014), pp. L6–L10. DOI: 10.1093/mnrasl/slt128. arXiv: 1209.5747 [astro-ph.HE].

[155] Lacy, M., Baum, S. A., Chandler, C. J., et al. “The Karl G. Jansky Very Large Array Sky Survey (VLASS). Science Case and Survey Design”. In: *Publications of the Astronomical Society of the Pacific* 132.1009 (Jan. 2020), p. 035001. DOI: 10.1088/1538-3873/ab63eb. URL: https://doi.org/10.1088/1538-3873/ab63eb.

[156] Lamb, G. P., Mandel, I., and Resmi, L. “Late-time evolution of afterglows from off-axis neutron star mergers”. In: MNRAS 481 (Dec. 2018), pp. 2581–2589. DOI: 10.1093/mnras/sty2196. arXiv: 1806.03843 [astro-ph.HE].

[157] Lamb, G. P., Lyman, J. D., Levan, A. J., et al. "The Optical Afterglow of GW170817 at One Year Post-merger". In: ApJ 870.2, L15 (Jan. 2019), p. L15. DOI: 10.3847/2041-8213/aaf96b. arXiv: 1811.11491 [astro-ph.HE].

[158] Laskar, T., Berger, E., Margutti, R., et al. "Energy Injection in Gamma-Ray Burst Afterglows". In: ApJ 814.1, 1 (Nov. 2015), p. 1. DOI: 10.1088/0004-637X/814/1/1. arXiv: 1504.03702 [astro-ph.HE].

[159] Lattimer, J. M. and Swesty, D. F. "A generalized equation of state for hot, dense matter". In: Nucl. Phys. A 535.2 (Dec. 1991), pp. 331–376. DOI: 10.1016/0375-9474(91)90452-C.

[160] Lattimer, J. M. and Schutz, B. F. "Constraining the Equation of State with Moment of Inertia Measurements". In: ApJ 629.2 (Aug. 2005), pp. 979–984. DOI: 10.1086/431543. arXiv: astro-ph/0411470 [astro-ph].

[161] Lazzati, D., Perna, R., Morsony, B. J., et al. "Late Time Afterglow Observations Reveal a Collimated Relativistic Jet in the Ejecta of the Binary Neutron Star Merger GW170817". In: Phys. Rev. Lett. 120.24, 241103 (June 2018), p. 241103. DOI: 10.1103/PhysRevLett.120.241103. arXiv: 1712.03237 [astro-ph.HE].

[162] Levan, A. J., Tanvir, N. R., Cenko, S. B., et al. "An Extremely Luminous Panchromatic Outburst from the Nucleus of a Distant Galaxy". In: *Science* 333.6039 (July 2011), p. 199. DOI: 10.1126/science.1207143. arXiv: 1104.3356 [astro-ph.HE].

[163] Levan, A. J., Lyman, J. D., Tanvir, N. R., et al. "The Environment of the Binary Neutron Star Merger GW170817". In: ApJ 848.2, L28 (Oct. 2017), p. L28. DOI: 10.3847/2041-8213/aa905f. arXiv: 1710.05444 [astro-ph.HE].

[164] Lodato, G. "Challenges in the modeling of tidal disruption events lightcurves". In: *European Physical Journal Web of Conferences*. Vol. 39. European Physical Journal Web of Conferences. Dec. 2012, 01001, p. 01001. DOI: 10.1051/epjconf/20123901001. arXiv: 1211.6109 [astro-ph.HE].

[165] Logoteta, D., Perego, A., and Bombaci, I. "Microscopic equation of state of hot nuclear matter for numerical relativity simulations". In: A&A 646, A55 (Feb. 2021), A55. DOI: 10.1051/0004-6361/202039457. arXiv: 2012.03599 [nucl-th].

[166] Lyman, J. D., Lamb, G. P., Levan, A. J., et al. "The optical afterglow of the short gamma-ray burst associated with GW170817". In: *Nature Astronomy* 2 (July 2018), pp. 751–754. DOI: 10.1038/s41550-018-0511-3. arXiv: 1801.02669 [astro-ph.HE].

[167] Makhathini, S., Mooley, K. P., Brightman, M., et al. "The Panchromatic Afterglow of GW170817: The full uniform dataset, modeling, comparison with previous results and implications". In: *arXiv e-prints*, arXiv:2006.02382 (June 2020), arXiv:2006.02382. arXiv: 2006.02382 [astro-ph.HE].

[168] Margalit, B. and Metzger, B. D. "Constraining the Maximum Mass of Neutron Stars from Multi-messenger Observations of GW170817". In: ApJ 850.2, L19

(Dec. 2017), p. L19. DOI: 10.3847/2041-8213/aa991c. arXiv: 1710.05938 [astro-ph.HE].

[169] Margalit, B. and Piran, T. "Shock within a shock: revisiting the radio flares of NS merger ejecta and gamma-ray burst-supernovae". In: MNRAS 495.4 (July 2020), pp. 4981–4993. DOI: 10.1093/mnras/staa1486. arXiv: 2004.13028 [astro-ph.HE].

[170] Margutti, R., Zaninoni, E., Bernardini, M. G., et al. "The prompt-afterglow connection in gamma-ray bursts: a comprehensive statistical analysis of Swift X-ray light curves". In: MNRAS 428 (Jan. 2013), pp. 729–742. DOI: 10.1093/mnras/sts066. arXiv: 1203.1059 [astro-ph.HE].

[171] Margutti, R., Berger, E., Fong, W., et al. "The Electromagnetic Counterpart of the Binary Neutron Star Merger LIGO/Virgo GW170817. V. Rising X-Ray Emission from an Off-axis Jet". In: ApJ 848, L20 (Oct. 2017), p. L20. DOI: 10.3847/2041-8213/aa9057.

[172] Margutti, R., Alexander, K. D., Xie, X., et al. "The Binary Neutron Star Event LIGO/Virgo GW170817 160 Days after Merger: Synchrotron Emission across the Electromagnetic Spectrum". In: ApJ 856, L18 (Mar. 2018), p. L18. DOI: 10.3847/2041-8213/aab2ad. arXiv: 1801.03531 [astro-ph.HE].

[173] Margutti, R. and Chornock, R. "First Multimessenger Observations of a Neutron Star Merger". In: ARA&A 59 (Sept. 2021). DOI: 10.1146/annurev-astro-112420-030742. arXiv: 2012.04810 [astro-ph.HE].

[174] McGilchrist, M. M. and Riley, J. M. "The 7C survey of radio sources at 151 MHz : a search for low-frequency variability." In: MNRAS 246 (Sept. 1990), p. 123.

[175] McMullin, J. P., Waters, B., Schiebel, D., Young, W., and Golap, K. "CASA Architecture and Applications". In: *Astronomical Data Analysis Software and Systems XVI*. Ed. by Shaw, R. A., Hill, F., and Bell, D. J. Vol. 376. Astronomical Society of the Pacific Conference Series. Oct. 2007, p. 127.

[176] McMullin, J. P., Waters, B., Schiebel, D., Young, W., and Golap, K. "CASA Architecture and Applications". In: *Astronomical Data Analysis Software and Systems XVI*. Ed. by Shaw, R. A., Hill, F., and Bell, D. J. Vol. 376. Astronomical Society of the Pacific Conference Series. Oct. 2007, p. 127.

[177] Metzger, B. D., Williams, P. K. G., and Berger, E. "Extragalactic Synchrotron Transients in the Era of Wide-field Radio Surveys. I. Detection Rates and Light Curve Characteristics". In: ApJ 806.2, 224 (June 2015), p. 224. DOI: 10.1088/0004-637X/806/2/224. arXiv: 1502.01350 [astro-ph.HE].

[178] Metzger, B. D., Bauswein, A., Goriely, S., and Kasen, D. "Neutron-powered precursors of kilonovae". In: MNRAS 446.1 (Jan. 2015), pp. 1115–1120. DOI: 10.1093/mnras/stu2225. arXiv: 1409.0544 [astro-ph.HE].

[179] Metzger, B. D. "Kilonovae". In: *Living Reviews in Relativity* 20, 3 (May 2017), p. 3. DOI: 10.1007/s41114-017-0006-z.

[180] Metzger, B. D., Thompson, T. A., and Quataert, E. “A Magnetar Origin for the Kilonova Ejecta in GW170817”. In: ApJ 856.2, 101 (Apr. 2018), p. 101. DOI: 10.3847/1538-4357/aab095. arXiv: 1801.04286 [astro-ph.HE].

[181] Metzger, B. D. and Fernandez, R. “From Neutrino- to Photon-Cooled in Three Years: Can Fallback Accretion Explain the X-ray Excess in GW170817?” In: *arXiv e-prints*, arXiv:2106.02052 (June 2021), arXiv:2106.02052. arXiv: 2106.02052 [astro-ph.HE].

[182] Minns, A. R. and Riley, J. M. “Compact radio sources variable at 151MHz - I. Catalogue of sources”. In: MNRAS 315.4 (July 2000), pp. 839–855. DOI: 10.1046/j.1365-8711.2000.03506.x.

[183] Mohan, N. and Rafferty, D. *PyBDSF: Python Blob Detection and Source Finder*. Astrophysics Source Code Library, record ascl:1502.007. Feb. 2015. ascl: 1502.007.

[184] Mooley, K. P., Frail, D. A., Ofek, E. O., et al. “Sensitive Search for Radio Variables and Transients in the Extended Chandra Deep Field South”. In: ApJ 768.2, 165 (May 2013), p. 165. DOI: 10.1088/0004-637X/768/2/165. arXiv: 1303.6282 [astro-ph.CO].

[185] Mooley, K. P., Hallinan, G., Bourke, S., et al. “The Caltech-NRAO Stripe 82 Survey (CNSS). I. The Pilot Radio Transient Survey In 50 $\deg^2$”. In: ApJ 818.2, 105 (Feb. 2016), p. 105. DOI: 10.3847/0004-637X/818/2/105. arXiv: 1601.01693 [astro-ph.HE].

[186] Mooley, K. P., Nakar, E., Hotokezaka, K., et al. "A mildly relativistic wide-angle outflow in the neutron-star merger event GW170817". In: Nature 554 (Feb. 2018), pp. 207–210. DOI: 10.1038/nature25452. arXiv: 1711.11573 [astro-ph.HE].

[187] Mooley, K. P., Frail, D. A., Dobie, D., et al. "A Strong Jet Signature in the Late-time Light Curve of GW170817". In: ApJ 868, L11 (Nov. 2018), p. L11. DOI: 10.3847/2041-8213/aaeda7. arXiv: 1810.12927 [astro-ph.HE].

[188] Mooley, K. P., Deller, A. T., Gottlieb, O., et al. "Superluminal motion of a relativistic jet in the neutron-star merger GW170817". In: Nature 561 (Sept. 2018), pp. 355–359. DOI: 10.1038/s41586-018-0486-3. arXiv: 1806.09693 [astro-ph.HE].

[189] Morgan, J. S., Macquart, J. .-., Ekers, R., et al. "Interplanetary Scintillation with the Murchison Widefield Array I: a sub-arcsecond survey over 900 deg^2 at 79 and 158 MHz". In: MNRAS 473.3 (Jan. 2018), pp. 2965–2983. DOI: 10.1093/mnras/stx2284. arXiv: 1709.00312 [astro-ph.IM].

[190] Motta, S. E., Kajava, J. J. E., Giustini, M., et al. "Observations of a radio-bright, X-ray obscured GRS 1915+105". In: MNRAS 503.1 (May 2021), pp. 152–161. DOI: 10.1093/mnras/stab511. arXiv: 2101.01187 [astro-ph.HE].

[191] Murguia-Berthier, A., Ramirez-Ruiz, E., De Colle, F., et al. "The Fate of the Merger Remnant in GW170817 and Its Imprint on the Jet Structure". In: ApJ 908.2, 152 (Feb. 2021), p. 152. DOI: 10.3847/1538-4357/abd08e. arXiv: 2007.12245 [astro-ph.HE].

[192] Murphy, T., Chatterjee, S., Kaplan, D. L., et al. "VAST: An ASKAP Survey for Variables and Slow Transients". In: PASA 30, e006 (Feb. 2013), e006. DOI: 10.1017/pasa.2012.006. arXiv: 1207.1528 [astro-ph.IM].

[193] Murphy, T., Kaplan, D. L., Croft, S., et al. "A search for long-time-scale, low-frequency radio transients". In: MNRAS 466.2 (Apr. 2017), pp. 1944–1953. DOI: 10.1093/mnras/stw3087. arXiv: 1611.08354 [astro-ph.GA].

[194] Nakar, E. and Piran, T. "Detectable radio flares following gravitational waves from mergers of binary neutron stars". In: Nature 478 (Oct. 2011), pp. 82–84. DOI: 10.1038/nature10365. arXiv: 1102.1020 [astro-ph.HE].

[195] Nakar, E. "The electromagnetic counterparts of compact binary mergers". In: Phys. Rep. 886 (Nov. 2020), pp. 1–84. DOI: 10.1016/j.physrep.2020.08.008. arXiv: 1912.05659 [astro-ph.HE].

[196] Narayan, R., Paczynski, B., and Piran, T. "Gamma-ray bursts as the death throes of massive binary stars". In: ApJ 395 (Aug. 1992), pp. L83–L86. DOI: 10.1086/186493. eprint: astro-ph/9204001.

[197] Nathanail, A., Gill, R., Porth, O., Fromm, C. M., and Rezzolla, L. "3D magnetized jet break-out from neutron-star binary merger ejecta: afterglow emission from the jet and the ejecta". In: MNRAS 502.2 (Apr. 2021), pp. 1843–1855. DOI: 10.1093/mnras/stab115. arXiv: 2009.09714 [astro-ph.HE].

[198] Nedora, V., Bernuzzi, S., Radice, D., et al. "Spiral-wave Wind for the Blue Kilonova". In: ApJ 886.2, L30 (Dec. 2019), p. L30. DOI: 10.3847/2041-8213/ab5794. arXiv: 1907.04872 [astro-ph.HE].

[199] Nedora, V., Radice, D., Bernuzzi, S., et al. "Dynamical ejecta synchrotron emission as possible contributor to the rebrightening of GRB170817A". In: *arXiv e-prints*, arXiv:2104.04537 (Apr. 2021), arXiv:2104.04537. arXiv: 2104.04537 [astro-ph.HE].

[200] Nedora, V., Bernuzzi, S., Radice, D., et al. "Numerical Relativity Simulations of the Neutron Star Merger GW170817: Long-term Remnant Evolutions, Winds, Remnant Disks, and Nucleosynthesis". In: ApJ 906.2, 98 (Jan. 2021), p. 98. DOI: 10.3847/1538-4357/abc9be. arXiv: 2008.04333 [astro-ph.HE].

[201] Nicholl, M., Berger, E., Kasen, D., et al. "The Electromagnetic Counterpart of the Binary Neutron Star Merger LIGO/Virgo GW170817. III. Optical and UV Spectra of a Blue Kilonova from Fast Polar Ejecta". In: ApJ 848, L18 (Oct. 2017), p. L18. DOI: 10.3847/2041-8213/aa9029. arXiv: 1710.05456 [astro-ph.HE].

[202] Nicholl, M., Margalit, B., Schmidt, P., et al. "Tight multi-messenger constraints on the neutron star equation of state from GW170817 and a forward model for kilonova light curve synthesis". In: *arXiv e-prints*, arXiv:2102.02229 (Feb. 2021), arXiv:2102.02229. arXiv: 2102.02229 [astro-ph.HE].

[203] Novikov, I. D. and Thorne, K. S. "Astrophysics of black holes." In: *Black Holes (Les Astres Occlus)*. Jan. 1973, pp. 343–450.

[204] Nynka, M., Ruan, J. J., Haggard, D., and Evans, P. A. "Fading of the X-Ray Afterglow of Neutron Star Merger GW170817/GRB 170817A at 260 Days".

In: ApJ 862, L19 (Aug. 2018), p. L19. DOI: 10.3847/2041-8213/aad32d. arXiv: 1805.04093 [astro-ph.HE].

[205] Obenberger, K. S., Hartman, J. M., Taylor, G. B., et al. "Limits on Gamma-Ray Burst Prompt Radio Emission Using the LWA1". In: ApJ 785.1, 27 (Apr. 2014), p. 27. DOI: 10.1088/0004-637X/785/1/27. arXiv: 1403.3674 [astro-ph.HE].

[206] Ofek, E. O., Frail, D. A., Breslauer, B., et al. "A Very Large Array Search for 5 GHz Radio Transients and Variables at Low Galactic Latitudes". In: ApJ 740.2, 65 (Oct. 2011), p. 65. DOI: 10.1088/0004-637X/740/2/65. arXiv: 1103.3010 [astro-ph.HE].

[207] Offringa, A. R., McKinley, B., Hurley-Walker, N., et al. "WSCLEAN: an implementation of a fast, generic wide-field imager for radio astronomy". In: MNRAS 444.1 (Oct. 2014), pp. 606–619. DOI: 10.1093/mnras/stu1368. arXiv: 1407.1943 [astro-ph.IM].

[208] Offringa, A. R. and Smirnov, O. "An optimized algorithm for multiscale wideband deconvolution of radio astronomical images". In: *MNRAS* 471.1 (2017), pp. 301–316. DOI: 10.1093/mnras/stx1547.

[209] Paggi, A., Fabbiano, G., Kim, D.-W., et al. "Active Galactic Nucleus Feedback in the Hot Halo of NGC 4649". In: ApJ 787.2, 134 (June 2014), p. 134. DOI: 10.1088/0004-637X/787/2/134.

[210] Pan, Y. .-., Kilpatrick, C. D., Simon, J. D., et al. “The Old Host-galaxy Environment of SSS17a, the First Electromagnetic Counterpart to a Gravitational-wave Source”. In: ApJ 848.2, L30 (Oct. 2017), p. L30. DOI: 10.3847/2041-8213/aa9116. arXiv: 1710.05439 [astro-ph.GA].

[211] Perego, A., Vescovi, D., Fiore, A., et al. “Production of very light elements in kilonovae”. In: *arXiv e-prints*, arXiv:2009.08988 (Sept. 2020), arXiv:2009.08988. arXiv: 2009.08988 [astro-ph.HE].

[212] Perego, A., Bernuzzi, S., and Radice, D. “Thermodynamics conditions of matter in neutron star mergers”. In: *European Physical Journal A* 55.8, 124 (Aug. 2019), p. 124. DOI: 10.1140/epja/i2019-12810-7. arXiv: 1903.07898 [gr-qc].

[213] Philippov, A. A., Cerutti, B., Tchekhovskoy, A., and Spitkovsky, A. “Ab Initio Pulsar Magnetosphere: The Role of General Relativity”. In: ApJ 815.2, L19 (Dec. 2015), p. L19. DOI: 10.1088/2041-8205/815/2/L19. arXiv: 1510.01734 [astro-ph.HE].

[214] Pietka, M., Fender, R. P., and Keane, E. F. “The variability time-scales and brightness temperatures of radio flares from stars to supermassive black holes”. In: MNRAS 446.4 (Feb. 2015), pp. 3687–3696. DOI: 10.1093/mnras/stu2335. arXiv: 1411.1067 [astro-ph.HE].

[215] Piran, T. “The physics of gamma-ray bursts”. In: *Reviews of Modern Physics* 76 (Oct. 2004), pp. 1143–1210. DOI: 10.1103/RevModPhys.76.1143. eprint: astro-ph/0405503.

[216] Piran, T., Svirski, G., Krolik, J., Cheng, R. M., and Shiokawa, H. "Disk Formation Versus Disk Accretion—What Powers Tidal Disruption Events?" In: ApJ 806.2, 164 (June 2015), p. 164. DOI: 10.1088/0004-637X/806/2/164. arXiv: 1502.05792 [astro-ph.HE].

[217] Piro, L., Troja, E., Zhang, B., et al. "A long-lived neutron star merger remnant in GW170817: constraints and clues from X-ray observations". In: MNRAS 483 (Feb. 2019), pp. 1912–1921. DOI: 10.1093/mnras/sty3047. arXiv: 1810.04664 [astro-ph.HE].

[218] Planck Collaboration, Ade, P. A. R., Aghanim, N., et al. "Planck 2015 results. XIII. Cosmological parameters". In: A&A 594, A13 (Sept. 2016), A13. DOI: 10.1051/0004-6361/201525830. arXiv: 1502.01589.

[219] Polisensky, E., Lane, W. M., Hyman, S. D., et al. "Exploring the Transient Radio Sky with VLITE: Early Results". In: ApJ 832.1, 60 (Nov. 2016), p. 60. DOI: 10.3847/0004-637X/832/1/60. arXiv: 1604.00667 [astro-ph.HE].

[220] Poole, T. S., Breeveld, A. A., Page, M. J., et al. "Photometric calibration of the Swift ultraviolet/optical telescope". In: MNRAS 383.2 (Jan. 2008), pp. 627–645. DOI: 10.1111/j.1365-2966.2007.12563.x. arXiv: 0708.2259 [astro-ph].

[221] Pooley, D., Kumar, P., Wheeler, J. C., and Grossan, B. "GW170817 Most Likely Made a Black Hole". In: ApJ 859, L23 (June 2018), p. L23. DOI: 10.3847/2041-8213/aac3d6. arXiv: 1712.03240 [astro-ph.HE].

[222] Prakash, A., Radice, D., Logoteta, D., et al. "Signatures of deconfined quark phases in binary neutron star mergers". In: *arXiv e-prints*, arXiv:2106.07885 (June 2021), arXiv:2106.07885. arXiv: 2106.07885 [astro-ph.HE].

[223] Radice, D. and Rezzolla, L. "THC: a new high-order finite-difference high-resolution shock-capturing code for special-relativistic hydrodynamics". In: A&A 547, A26 (Nov. 2012), A26. DOI: 10.1051/0004-6361/201219735. arXiv: 1206.6502 [astro-ph.IM].

[224] Radice, D., Rezzolla, L., and Galeazzi, F. "Beyond second-order convergence in simulations of binary neutron stars in full general relativity". In: MNRAS 437.1 (Jan. 2014), pp. L46–L50. DOI: 10.1093/mnrasl/slt137. arXiv: 1306.6052 [gr-qc].

[225] Radice, D., Rezzolla, L., and Galeazzi, F. "High-order fully general-relativistic hydrodynamics: new approaches and tests". In: *Class. & Quant. Grav.* 31.7, 075012 (Apr. 2014), p. 075012. DOI: 10.1088/0264-9381/31/7/075012. arXiv: 1312.5004 [gr-qc].

[226] Radice, D., Galeazzi, F., Lippuner, J., et al. "Dynamical mass ejection from binary neutron star mergers". In: MNRAS 460.3 (Aug. 2016), pp. 3255–3271. DOI: 10.1093/mnras/stw1227. arXiv: 1601.02426 [astro-ph.HE].

[227] Radice, D. "General-relativistic Large-eddy Simulations of Binary Neutron Star Mergers". In: ApJ 838.1, L2 (Mar. 2017), p. L2. DOI: 10.3847/2041-8213/aa6483. arXiv: 1703.02046 [astro-ph.HE].

[228] Radice, D., Perego, A., Hotokezaka, K., et al. "Binary Neutron Star Mergers: Mass Ejection, Electromagnetic Counterparts, and Nucleosynthesis". In: ApJ 869.2, 130 (Dec. 2018), p. 130. DOI: 10.3847/1538-4357/aaf054. arXiv: 1809.11161 [astro-ph.HE].

[229] Radice, D., Perego, A., Zappa, F., and Bernuzzi, S. "GW170817: Joint Constraint on the Neutron Star Equation of State from Multimessenger Observations". In: ApJ 852.2, L29 (Jan. 2018), p. L29. DOI: 10.3847/2041-8213/aaa402. arXiv: 1711.03647 [astro-ph.HE].

[230] Radice, D., Perego, A., Bernuzzi, S., and Zhang, B. "Long-lived remnants from binary neutron star mergers". In: MNRAS 481.3 (Dec. 2018), pp. 3670–3682. DOI: 10.1093/mnras/sty2531. arXiv: 1803.10865 [astro-ph.HE].

[231] Radice, D., Perego, A., Hotokezaka, K., et al. "Viscous-dynamical Ejecta from Binary Neutron Star Mergers". In: ApJ 869.2, L35 (Dec. 2018), p. L35. DOI: 10.3847/2041-8213/aaf053. arXiv: 1809.11163 [astro-ph.HE].

[232] Radice, D. "Binary Neutron Star Merger Simulations with a Calibrated Turbulence Model". In: *Symmetry* 12.8 (July 2020), p. 1249. DOI: 10.3390/sym12081249. arXiv: 2005.09002 [astro-ph.HE].

[233] Radice, D., Bernuzzi, S., and Perego, A. "The Dynamics of Binary Neutron Star Mergers and GW170817". In: *Annual Review of Nuclear and Particle Science* 70 (Oct. 2020), pp. 95–119. DOI: 10.1146/annurev-nucl-013120-114541. arXiv: 2002.03863 [astro-ph.HE].

[234] Ramirez-Ruiz, E., Andrews, J. J., and Schrøder, S. L. "Did GW170817 Harbor a Pulsar?" In: ApJ 883.1, L6 (Sept. 2019), p. L6. DOI: 10.3847/2041-8213/ab3f2c. arXiv: 1905.09179 [astro-ph.HE].

[235] Ray, P., Hyman, S. D., Lazio, J., et al. "A Bursting Radio Transient in the Direction of the Galactic Center". In: *Bursts, Pulses and Flickering: Wide-Field Monitoring of the Dynamic Radio Sky*. Jan. 2007, 8, p. 8. arXiv: 0808.1899 [astro-ph].

[236] Readhead, A. C. S. "Equipartition Brightness Temperature and the Inverse Compton Catastrophe". In: ApJ 426 (May 1994), p. 51. DOI: 10.1086/174038.

[237] Rees, M. J. "Tidal disruption of stars by black holes of 10^6-10^8 solar masses in nearby galaxies". In: Nature 333.6173 (June 1988), pp. 523–528. DOI: 10.1038/333523a0.

[238] Rezzolla, L., Most, E. R., and Weih, L. R. "Using Gravitational-wave Observations and Quasi-universal Relations to Constrain the Maximum Mass of Neutron Stars". In: ApJ 852.2, L25 (Jan. 2018), p. L25. DOI: 10.3847/2041-8213/aaa401. arXiv: 1711.00314 [astro-ph.HE].

[239] Rhoads, J. E. "The Dynamics and Light Curves of Beamed Gamma-Ray Burst Afterglows". In: ApJ 525.2 (Nov. 1999), pp. 737–749. DOI: 10.1086/307907. arXiv: astro-ph/9903399 [astro-ph].

[240] Rickett, B. J. "Refractive Interstellar Scintillations of Radio Sources". In: ApJ 307 (Aug. 1986), p. 564. DOI: 10.1086/164444.

[241] Riess, A., Casertano, S., Macri, L. M., and Yuan, W. *A Measurement of the Gaia Offset to Build a Superior Distance Ladder and Resolve the Origin of the Hubble Tension*. HST Proposal. Cycle 27, ID. #15879. June 2019.

[242] Riley, J. M. "Radio variability in a complete sample of extragalactic sources at 151 MHz." In: MNRAS 260 (Feb. 1993), p. 893. DOI: 10.1093/mnras/260.4.893.

[243] Riley, J. M. and Green, D. A. "408-MHz observations of two fields in the region 10ĥ30m, +46 deg - II. A variability study". In: MNRAS 275.2 (July 1995), pp. 527–533. DOI: 10.1093/mnras/275.2.527.

[244] Riley, J. M. and Green, D. A. "A 408-MHz variability study of two fields in the region 6ĥ30m, +45 deg". In: MNRAS 301.1 (Nov. 1998), pp. 203–209. DOI: 10.1046/j.1365-8711.1998.02029.x.

[245] Roming, P. W. A., Kennedy, T. E., Mason, K. O., et al. "The Swift Ultra-Violet/Optical Telescope". In: Space Sci. Rev. 120 (Oct. 2005), pp. 95–142. DOI: 10.1007/s11214-005-5095-4. eprint: arXiv:astro-ph/0507413.

[246] Rossi, E. M. and Begelman, M. C. "Delayed X-ray emission from fallback in compact-object mergers". In: MNRAS 392.4 (Feb. 2009), pp. 1451–1455. DOI: 10.1111/j.1365-2966.2008.14139.x. arXiv: 0808.1284 [astro-ph].

[247] Rosswog, S., Sollerman, J., Feindt, U., et al. "The first direct double neutron star merger detection: Implications for cosmic nucleosynthesis". In: A&A 615, A132 (July 2018), A132. DOI: 10.1051/0004-6361/201732117. arXiv: 1710.05445 [astro-ph.HE].

[248] Rosswog, S. “Fallback accretion in the aftermath of a compact binary merger”. In: MNRAS 376.1 (Mar. 2007), pp. L48–L51. DOI: 10.1111/j.1745-3933.2007.00284.x. arXiv: astro-ph/0611440 [astro-ph].

[249] Rowlinson, A., Bell, M. E., Murphy, T., et al. “Limits on Fast Radio Bursts and other transient sources at 182 MHz using the Murchison Widefield Array”. In: MNRAS 458.4 (June 2016), pp. 3506–3522. DOI: 10.1093/mnras/stw451. arXiv: 1602.07544 [astro-ph.HE].

[250] Ruan, J. J., Nynka, M., Haggard, D., Kalogera, V., and Evans, P. “Brightening X-Ray Emission from GW170817/GRB 170817A: Further Evidence for an Outflow”. In: ApJ 853, L4 (Jan. 2018), p. L4. DOI: 10.3847/2041-8213/aaa4f3.

[251] Rushton, A., Spencer, R. E., Pooley, G., and Trushkin, S. “A decade of high-resolution radio observations of GRS1915+105”. In: MNRAS 401.4 (Feb. 2010), pp. 2611–2621. DOI: 10.1111/j.1365-2966.2009.15838.x. arXiv: 0910.1779 [astro-ph.GA].

[252] Ryan, G., van Eerten, H., MacFadyen, A., and Zhang, B.-B. “Gamma-Ray Bursts are Observed Off-axis”. In: ApJ 799.1, 3 (Jan. 2015), p. 3. DOI: 10.1088/0004-637X/799/1/3. arXiv: 1405.5516 [astro-ph.HE].

[253] Ryan, G., van Eerten, H., Piro, L., and Troja, E. “Gamma-Ray Burst Afterglows in the Multimessenger Era: Numerical Models and Closure Relations”. In: ApJ 896.2, 166 (June 2020), p. 166. DOI: 10.3847/1538-4357/ab93cf. arXiv: 1909.11691 [astro-ph.HE].

[254] Sari, R., Piran, T., and Halpern, J. P. "Jets in Gamma-Ray Bursts". In: ApJ 519.1 (July 1999), pp. L17–L20. DOI: 10.1086/312109. arXiv: astro-ph/9903339 [astro-ph].

[255] Sari, R. and Mészáros, P. "Impulsive and Varying Injection in Gamma-Ray Burst Afterglows". In: ApJ 535.1 (May 2000), pp. L33–L37. DOI: 10.1086/312689. arXiv: astro-ph/0003406 [astro-ph].

[256] Savchenko, V., Ferrigno, C., Kuulkers, E., et al. "INTEGRAL Detection of the First Prompt Gamma-Ray Signal Coincident with the Gravitational-wave Event GW170817". In: ApJ 848, L15 (Oct. 2017), p. L15. DOI: 10.3847/2041-8213/aa8f94. arXiv: 1710.05449 [astro-ph.HE].

[257] Schlafly, E. F. and Finkbeiner, D. P. "Measuring Reddening with Sloan Digital Sky Survey Stellar Spectra and Recalibrating SFD". In: ApJ 737, 103 (Aug. 2011), p. 103. DOI: 10.1088/0004-637X/737/2/103. arXiv: 1012.4804 [astro-ph.GA].

[258] Schneider, A. S., Roberts, L. F., and Ott, C. D. "Open-source nuclear equation of state framework based on the liquid-drop model with Skyrme interaction". In: Phys. Rev. C 96.6, 065802 (Dec. 2017), p. 065802. DOI: 10.1103/PhysRevC.96.065802.

[259] Schutz, B. F. "Determining the Hubble constant from gravitational wave observations". In: Nature 323 (Sept. 1986), p. 310. DOI: 10.1038/323310a0.

[260] Sekiguchi, Y., Kiuchi, K., Kyutoku, K., Shibata, M., and Taniguchi, K. "Dynamical mass ejection from the merger of asymmetric binary neutron stars:

Radiation-hydrodynamics study in general relativity". In: Phys. Rev. D 93.12, 124046 (June 2016), p. 124046. DOI: 10.1103/PhysRevD.93.124046. arXiv: 1603.01918 [astro-ph.HE].

[261] Shappee, B., Prieto, J., Stanek, K. Z., et al. "All Sky Automated Survey for SuperNovae (ASAS-SN or "Assassin")". In: *American Astronomical Society Meeting Abstracts #223*. Vol. 223. American Astronomical Society Meeting Abstracts. Jan. 2014, 236.03, p. 236.03.

[262] Shibata, M., Fujibayashi, S., Hotokezaka, K., et al. "Modeling GW170817 based on numerical relativity and its implications". In: Phys. Rev. D 96.12, 123012 (Dec. 2017), p. 123012. DOI: 10.1103/PhysRevD.96.123012. arXiv: 1710.07579 [astro-ph.HE].

[263] Shibata, M. and Hotokezaka, K. "Merger and Mass Ejection of Neutron Star Binaries". In: *Annual Review of Nuclear and Particle Science* 69 (Oct. 2019), pp. 41–64. DOI: 10.1146/annurev-nucl-101918-023625. arXiv: 1908.02350 [astro-ph.HE].

[264] Shimwell, T. W., Tasse, C., Hardcastle, M. J., et al. "The LOFAR Two-metre Sky Survey. II. First data release". In: A&A 622, A1 (Feb. 2019), A1. DOI: 10.1051/0004-6361/201833559. arXiv: 1811.07926 [astro-ph.GA].

[265] Shiokawa, H., Krolik, J. H., Cheng, R. M., Piran, T., and Noble, S. C. "General Relativistic Hydrodynamic Simulation of Accretion Flow from a Stellar Tidal Disruption". In: ApJ 804.2, 85 (May 2015), p. 85. DOI: 10.1088/0004-637X/804/2/85. arXiv: 1501.04365 [astro-ph.HE].

[266] Sironi, L. and Giannios, D. "A Late-time Flattening of Light Curves in Gamma-Ray Burst Afterglows". In: ApJ 778.2, 107 (Dec. 2013), p. 107. DOI: 10.1088/0004-637X/778/2/107. arXiv: 1307.3250 [astro-ph.HE].

[267] Sironi, L., Spitkovsky, A., and Arons, J. "The Maximum Energy of Accelerated Particles in Relativistic Collisionless Shocks". In: ApJ 771.1, 54 (July 2013), p. 54. DOI: 10.1088/0004-637X/771/1/54. arXiv: 1301.5333 [astro-ph.HE].

[268] Stewart, A. J., Fender, R. P., Broderick, J. W., et al. "LOFAR MSSS: detection of a low-frequency radio transient in 400 h of monitoring of the North Celestial Pole". In: MNRAS 456.3 (Mar. 2016), pp. 2321–2342. DOI: 10.1093/mnras/stv2797. arXiv: 1512.00014 [astro-ph.HE].

[269] Takami, H., Kyutoku, K., and Ioka, K. "High-energy radiation from remnants of neutron star binary mergers". In: Phys. Rev. D 89.6, 063006 (Mar. 2014), p. 063006. DOI: 10.1103/PhysRevD.89.063006. arXiv: 1307.6805 [astro-ph.HE].

[270] Tasse, C., Hugo, B., Mirmont, M., et al. "Faceting for direction-dependent spectral deconvolution". In: A&A 611, A87 (Apr. 2018), A87. DOI: 10.1051/0004-6361/201731474. arXiv: 1712.02078 [astro-ph.IM].

[271] Taylor, M. B. "TOPCAT & STIL: Starlink Table/VOTable Processing Software". In: *Astronomical Data Analysis Software and Systems XIV*. Ed. by Shopbell, P., Britton, M., and Ebert, R. Vol. 347. Astronomical Society of the Pacific Conference Series. Dec. 2005, p. 29.

[272] Thyagarajan, N., Helfand, D. J., White, R. L., and Becker, R. H. "Variable and Transient Radio Sources in the FIRST Survey". In: ApJ 742.1, 49 (Nov. 2011), p. 49. DOI: 10.1088/0004-637X/742/1/49. arXiv: 1107.5901 [astro-ph.CO].

[273] Troja, E., Piro, L., Eerten, H. van, et al. "The X-ray counterpart to the gravitational-wave event GW170817". In: *Nature* 551.7678 (2017), p. 71.

[274] Troja, E., Piro, L., Ryan, G., et al. "The outflow structure of GW170817 from late-time broad-band observations". In: MNRAS 478 (July 2018), pp. L18–L23. DOI: 10.1093/mnrasl/sly061.

[275] Troja, E., van Eerten, H., Ryan, G., et al. "A year in the life of GW170817: the rise and fall of a structured jet from a binary neutron star merger". In: MNRAS (Aug. 2019), p. 2169. DOI: 10.1093/mnras/stz2248. arXiv: 1808.06617 [astro-ph.HE].

[276] Troja, E., van Eerten, H., Zhang, B., et al. "A thousand days after the merger: Continued X-ray emission from GW170817". In: MNRAS 498.4 (Nov. 2020), pp. 5643–5651. DOI: 10.1093/mnras/staa2626. arXiv: 2006.01150 [astro-ph.HE].

[277] Troja, E., O'Connor, B., Ryan, G., et al. "Accurate flux calibration of GW170817: is the X-ray counterpart on the rise?" In: *arXiv e-prints*, arXiv:2104.13378 (Apr. 2021), arXiv:2104.13378. arXiv: 2104.13378 [astro-ph.HE].

[278] Valenti, S., Sand, D. J., Yang, S., et al. "The Discovery of the Electromagnetic Counterpart of GW170817: Kilonova AT 2017gfo/DLT17ck". In: ApJ 848.2,

L24 (Oct. 2017), p. L24. DOI: 10.3847/2041-8213/aa8edf. arXiv: 1710.05854 [astro-ph.HE].

[279] van Velzen, S., Holoien, T. W. .-., Onori, F., Hung, T., and Arcavi, I. "Optical-Ultraviolet Tidal Disruption Events". In: Space Sci. Rev. 216.8, 124 (Oct. 2020), p. 124. DOI: 10.1007/s11214-020-00753-z. arXiv: 2008.05461 [astro-ph.HE].

[280] Villar, V. A., Cowperthwaite, P. S., Berger, E., et al. "Spitzer Space Telescope Infrared Observations of the Binary Neutron Star Merger GW170817". In: ApJ 862.1, L11 (July 2018), p. L11. DOI: 10.3847/2041-8213/aad281. arXiv: 1805.08192 [astro-ph.HE].

[281] Villar, V., Guillochon, J., Berger, E., et al. "The Combined Ultraviolet, Optical, and Near-infrared Light Curves of the Kilonova Associated with the Binary Neutron Star Merger GW170817: Unified Data Set, Analytic Models, and Physical Implications". In: ApJ 851.1 (2017), p. L21.

[282] Walton, D. J., Bachetti, M., Fürst, F., et al. "A Potential Cyclotron Resonant Scattering Feature in the Ultraluminous X-Ray Source Pulsar NGC 300 ULX1 Seen by NuSTAR and XMM-Newton". In: ApJ 857.1, L3 (Apr. 2018), p. L3. DOI: 10.3847/2041-8213/aabadc. arXiv: 1803.07571 [astro-ph.HE].

[283] Waxman, E., Ofek, E. O., Kushnir, D., and Gal-Yam, A. "Constraints on the ejecta of the GW170817 neutron star merger from its electromagnetic emission". In: MNRAS 481.3 (Dec. 2018), pp. 3423–3441. DOI: 10.1093/mnras/sty2441. arXiv: 1711.09638 [astro-ph.HE].

[284] Williams, P. K. G., Bower, G. C., Croft, S., et al. "ASGARD: A Large Survey for Slow Galactic Radio Transients. I. Overview and First Results". In: ApJ 762.2, 85 (Jan. 2013), p. 85. DOI: 10.1088/0004-637X/762/2/85. arXiv: 1211.1042 [astro-ph.GA].

[285] Williams, P. K. G., Clavel, M., Newton, E., and Ryzhkov, D. *pwkit: Astronomical utilities in Python*. Apr. 2017. ascl: 1704.001.

[286] Williams, P. K. G., Clavel, M., Newton, E., and Ryzhkov, D. *pwkit: Astronomical utilities in Python*. Astrophysics Source Code Library, record ascl:1704.001. Apr. 2017. ascl: 1704.001.

[287] Wu, Y. and MacFadyen, A. "Constraining the Outflow Structure of the Binary Neutron Star Merger Event GW170817/GRB170817A with a Markov Chain Monte Carlo Analysis". In: ApJ 869.1, 55 (Dec. 2018), p. 55. DOI: 10.3847/1538-4357/aae9de. arXiv: 1809.06843 [astro-ph.HE].

[288] Wu, Y. and MacFadyen, A. "GW170817 Afterglow Reveals that Short Gamma-Ray Bursts are Neutron Star Mergers". In: ApJ 880.2, L23 (Aug. 2019), p. L23. DOI: 10.3847/2041-8213/ab2fd4. arXiv: 1905.02665 [astro-ph.HE].

[289] Xie, X., Zrake, J., and MacFadyen, A. "Numerical Simulations of the Jet Dynamics and Synchrotron Radiation of Binary Neutron Star Merger Event GW170817/GRB 170817A". In: ApJ 863.1, 58 (Aug. 2018), p. 58. DOI: 10.3847/1538-4357/aacf9c. arXiv: 1804.09345 [astro-ph.HE].

[290] Zauderer, B. A., Berger, E., Soderberg, A. M., et al. "Birth of a relativistic outflow in the unusual γ-ray transient Swift J164449.3+573451". In: Nature

476.7361 (Aug. 2011), pp. 425–428. DOI: 10.1038/nature10366. arXiv: 1106.3568 [astro-ph.HE].

[291] Zauderer, B. A., Berger, E., Margutti, R., et al. "Radio Monitoring of the Tidal Disruption Event Swift J164449.3+573451. II. The Relativistic Jet Shuts Off and a Transition to Forward Shock X-Ray/Radio Emission". In: ApJ 767.2, 152 (Apr. 2013), p. 152. DOI: 10.1088/0004-637X/767/2/152. arXiv: 1212.1173 [astro-ph.HE].

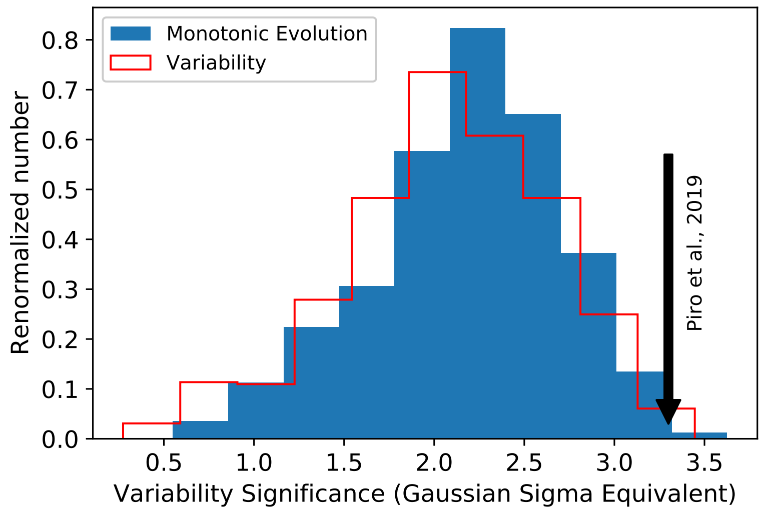

Figure A1 Distribution of statistical significance values (in units of Gaussian σ equivalent) that quantifies the evidence for deviation from the H_0 hypothesis of a source with constant count-rate between $153-164$ days in the form of temporal variability (red), or monotonic evolution of the source count-rate (blue) for 10^4 random selections of time intervals for comparison. A limited fraction of 0.3% (red) or 0.4% (blue) of randomly selected intervals show evidence for deviation from a constant count-rate at $\geq 3.3\sigma$ c.l. The typical level of significance is $\sim 2\,\sigma$.

APPENDIX A

Blind search for Temporal X-ray Variability in GW 170817 at $\delta t \sim 160$ days

We carried out a blind search for deviations from a constant source count-rate in the time interval $\delta t = 153-164$ days for which (Piro et al. 2019) report evidence for variability at the $3.3\,\sigma$ c.l. using two different approaches: (i) we divided the data set into two portions Δt_1 and Δt_2, where the dividing line is randomly chosen within the Δt of consideration, and we applied a Poissonian test to the number of detected photons N_1 and N_2. Our H_0 hypothesis is that N_1 and N_2 are randomly drawn from a Poisson distribution with expected rate $\lambda = 1.49 \times 10^{-3}\mathrm{c\,s^{-1}}$ evaluated on the effective exposure times of the CXO during Δt_1 and Δt_2 (i.e. the source count-rate is constant). We repeated the experiment 10^4 times, considering only the cases with CXO exposure times during Δt_1 and Δt_2, $\Delta t_{1,exp} \geq \Delta t_{min}$ and $\Delta t_{2,exp} \geq \Delta t_{min}$,where $\Delta t_{min} = 0.11$ d is such that the probability of obtaining zero photons by chance is less than $P(\geq 5\,\sigma)$ (i.e. $P(0) = e^{-\lambda \Delta t_{min}} < P(\geq 5\,\sigma)$). The results from this exercise are shown in Fig. A1, red histogram. We find that a random selection of time intervals to compare typically leads to a $\sim 2\,\sigma$ evidence for departure from our H_0 hypothesis of a constant count-rate, consistent with our results in Sec. 2.2.1, and that only 0.3% of choices leads to a significance larger or equal to that reported by (Piro et al. 2019). (ii) We further investigate the possibility of the presence of a monotonic evolution of the source count-rate, which would be best revealed by considering the initial and final portion of the data set only, as in (Piro et al. 2019). We followed the same procedure as above and allowed for a random selection of the duration of the initial and final time intervals to consider within $\delta t = 153 - 164$ days, with the constraint $\Delta t_{1,exp} \geq \Delta t_{min}$ and $\Delta t_{2,exp} \geq \Delta t_{min}$. Figure A1 shows that only 0.4% of the 10^4 realizations that satisfy our constraints have evidence for a deviation from a constant count-rate with significance $\geq 3.3\,\sigma$, and that the typical significance is $\sim 2.2\,\sigma$. We conclude that the claim of a $3.3\,\sigma$ deviation from a constant count-rate by (Piro et al. 2019) mostly stems from comparing a particular selection of time intervals, and that a blind search for temporal variability on the same data set leads to a reduced statistical significance of $\sim 2\,\sigma$.

APPENDIX B

Comparison of X-ray Flux calibration methods between different studies in the literature in the context of GW 170817

In this Appendix we provide additional details on the comparison between the flux calibration of the X-ray data from this work and the analysis of our data set by (Troja et al. 2021). Our X-ray data analysis and the limitations of the data treatment by (Troja et al. 2021) are described in §3.2.2. Figure B1 shows that the two flux calibrations lead to X-ray fluxes that are within $0.9\,\sigma$. There is thus no statistical tension between the two flux calibrations. We further show the best fitting jet-afterglow model that is used by (Troja et al. 2021) to compute the significance of the X-ray excess (black solid line, $\theta_{obs} = 31°$, $\theta_{jet} = 5°$), as well as the best-fitting model of the entire afterglow light-curve dataset (i.e. including the last two X-ray epochs) by (Troja et al. 2021), which has $\theta_{obs} = 38°$, $\theta_{jet} = 6°$. This model is in tension with the inferences from the VLBI observations by (Mooley et al. 2018c; Ghirlanda et al. 2019). We present with a dashed black line the model by (Ryan et al. 2020) (also presented by Troja et al. 2021, their Figure 5) that is consistent with the VLBI measurements, and that would lead to the inference of a larger discrepancy between the late-time X-ray observations and the model expectations.

As a proof of concept we have fitted the data at $\delta t < 1300$ days with `JetFit` using $\gamma_{\rm B} = 12$. First, we included the X-ray fluxes from our data reduction where we leave the photon index as a free parameter for all epochs. Even though these fits were obtained for all the flux densities derived using their respective spectral indices, for plotting purposes only, we have shown our $\delta t > 900$ days flux densities (purple points in Figure B1) that were obtained using a fixed Γ. Second, we have repeated the same exercise by including the X-ray fluxes by (Troja et al. 2021). Figure B1 shows complete overlap of the 68% confidence regions of the two best-fitting models at all times.

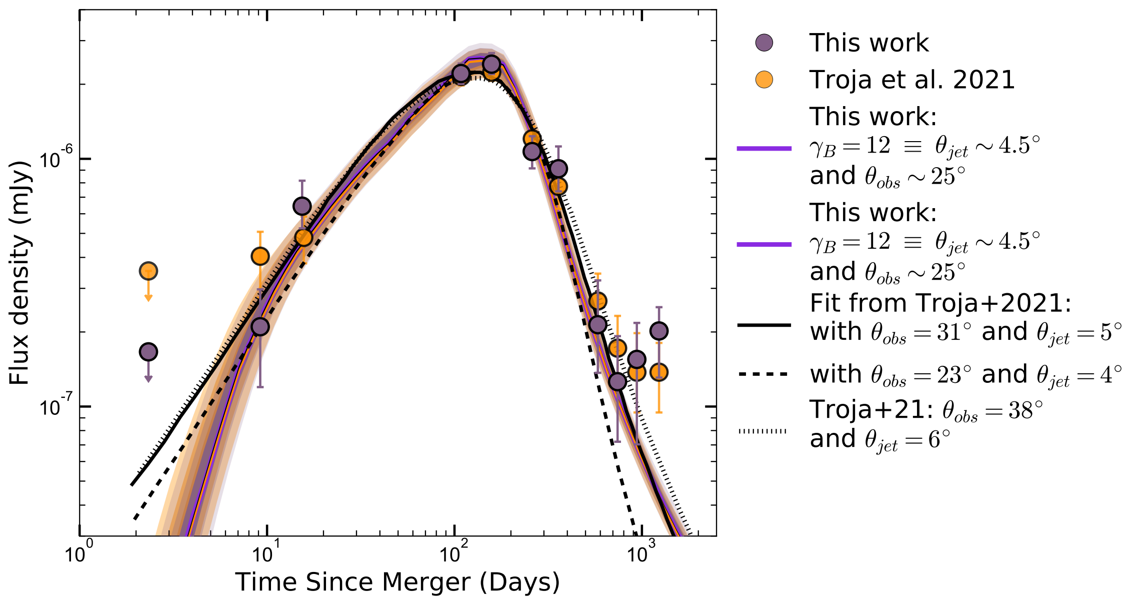

Figure B1 Comparison of 1 keV flux densities derived in this work (purple circles, derived from the fluxes reported in Table 3.1), where we do not assume a photon index based on the jet afterglow modeling, with those calculated by (Troja et al. 2021) (orange circles) where also the photon index is free for all epochs, as noted in their Table 1. We note that all the detections are consistent within $\lesssim 0.9\sigma$ uncertainties at all epochs. The colored bands are the 68%, 97.5%, and 99.8% confidence interval of the fits obtained from fitting our data including the latest epochs at $\delta t > 900$ days (purple bands, same as in Figure 3.3) and from fitting all the data from (Troja et al. 2021) (in orange) using `JetFit`, with $\gamma_{\rm B} = 12$, $n = 0.01\,{\rm cm}^{-3}$, and $\epsilon_{\rm e} = 0.1$ fixed. Even though these fits were obtained for all the flux densities derived using their respective spectral indices, for plotting purposes only, we have shown our $\delta t > 900$ days flux densities (in purple) that were obtained using a fixed Γ. The best-fits derived in this work using `JetFit` with $\gamma_{\rm B} = 12$ and $\gamma_{\rm B} = 10$ fixed as discussed in §3.4 are represented by solid and dashed purple lines, respectively. The best-fits obtained in Troja et al. 2021 are plotted in black lines.

APPENDIX C

Posterior distribution of `JetFit` model parameters that best–fit the multiwavelength dataset of GW 170817 until $\delta t \sim 900$ days

In this paper, we have calculated the significance of a deviation of the observed X-rays using two different approaches - a jet-model dependent analysis, and a more universal, jet-model independent analysis. Both analyses independently result in an excess of X-ray emission with $\geq 3.5\sigma$ (Gaussian equivalent) confidence level. In Figure C1, we show the best-fitting universal post jet-break model. As mentioned in §3.4, the fitting included the observations taken between $t_{\rm start} < t < 900$ days. As seen from Figure C1, and the residual plot in the top panel of Figure 3.3, the fits start gradually diverging (although not to any significant level) from the data at $t > 300$ days. This further strengthens our argument on the emergence of a new component of emission as it is likely to gradually manifest with time, as opposed to an abrupt appearance at some point in time, as the jet afterglow fades away.

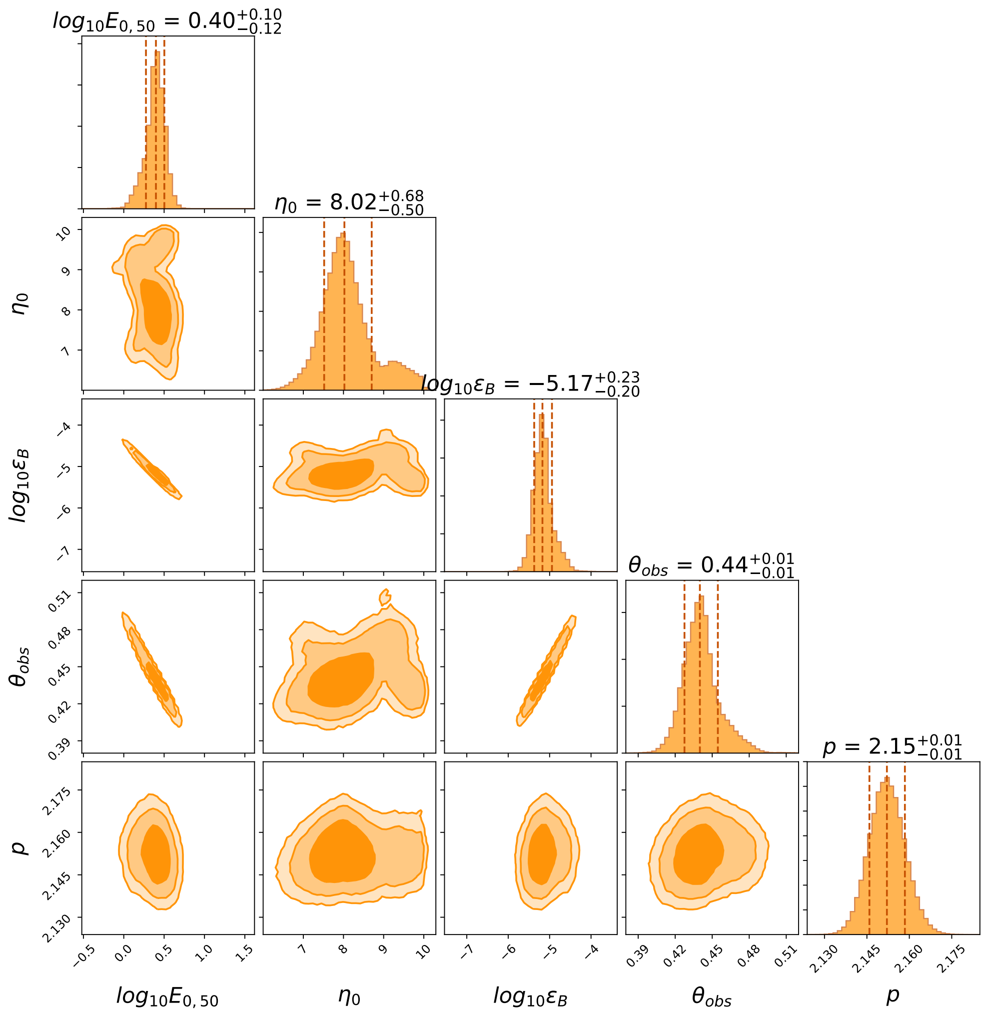

Figure C1 One- and two-dimensional projections of the posterior distributions of the model's free parameters. Vertical dashed lines mark the 16$^{\text{th}}$, 50$^{\text{th}}$, and 84$^{\text{th}}$ percentiles of the marginalized distributions (i.e. the median and 1-σ range). The contours are drawn at 68%, 95%, and 99% credible levels.